ESA DUE DIVERSITY II

Supporting the Convention on Biological Diversity

D5.1 Algorithm Theoretic Baseline Document (ATBD)

Version 2.4
20 October 2015

Table of Contents

1 Scope of the Document 12

2 Introduction 13

3 Pre-Processing 14

3.1 Improved Geolocation using Amorgos 14

3.2 Radiometric Correction 16

3.2.1 Improved Calibration 16

3.2.2 Coherent Noise Equalisation 17

3.2.3 Smile Correction 18

3.3 Cloud Screening 19

3.3.1 Background 19

3.3.2 Categorisation of Cloud Detection Methods 21

3.3.3 Theoretical description 21

3.3.4 Practical considerations 22

3.3.5 Cloud shadow and cloud edge detection 24

3.3.6 Validation of the cloud screening using PixBox 25

3.4 Land and Water Separation 26

3.5 Identification of optically shallow Water 28

3.5.1 Bottom reflected Radiance 28

3.5.2 Shallow Water Identification Algorithm Development 29

3.5.3 Assessment and validation of the shallow water indicator 32

3.6 Atmospheric Correction 34

3.6.1 Theoretical Background 34

3.6.2 Candidate algorithms for atmospheric correction over water 38

3.6.3 Validation of atmospheric correction over water 42

3.7 Drylands Auxiliary Data pre-processing 51

3.7.1 Soil Moisture Data 52

3.7.2 Hydro-Meteorological Data and Pre-processing 52

3.7.3 AVHRR NDVI 58

3.7.4 Modelled NPP data based on BETHY/DLR 58

4 Algorithms Lakes Processing 60

4.1 Water Quality Retrieval 60

4.1.1 Optical Water Types Identification 60

4.1.2 Theoretical background of Water Constituent Retrieval 61

4.1.3 Candidate Algorithms for Water Constituent Retrieval 62

4.1.4 Validation of Water Constituent Retrieval Algorithms 65

4.1.5 Lakes Water Temperature 71

4.2 Water Quantity Auxiliary Data and Algorithms 71

4.2.1 Landcover CCI Water Bodies 72

4.2.2 SRTM Water Body Dataset 72

4.2.3 LEGOS Hydroweb Lake Water Level 73
5 Algorithms Drylands Processing 73
5.1 Vegetation Indices for NPP 74
5.1.1 Ratio-based Vegetation Indices 74
5.1.2 Physical Modelling Approaches 74
5.1.3 Choice of Vegetation Indices 75
5.1.4 fAPAR Calculation 76
5.1.5 Validation of the JRC MERIS fAPAR 77
5.1.6 NDVI calculation 78
5.1.7 Generation of Biweekly Integrated Time Series Data 78
5.1.8 Gap filling of fAPAR data 79
5.1.9 Special processing of test sites with data gaps due to snow 85
5.2 Extraction of Phenological and Productivity Parameters 86
5.2.1 Introduction 86
5.2.2 Derivation of the SoS 87
5.2.3 Calculation of the Baseline 88
5.2.4 Definition and derivation of all further phenological parameters and of productivity parameters 91
5.3 Aggregation of rainfall and soil moisture parameters 93
5.4 Background and Derivation of RUE and SMUE 94
6 Indicator Algorithms 99
6.1 Lakes Indicators 99
6.1.1 Fist Order Indicators: Status, Change and Trend Maps 99
6.1.2 Second Order Indicators 103
6.2 Dryland Indicators 103
6.2.1 First Order Indicators 104
6.2.2 Second Order Indicators 109
6.2.3 Phenology Indicators 117
7 Relationships between RS Indicators and Biodiversity 121
7.1 Inland Waters Biodiversity indicators 121
7.1.1 Water Temperature 121
7.1.2 Suspended Sediment 123
7.1.3 Chlorophyll 124
7.2 Relationships between Dryland Indicators and Biodiversity 125
7.2.1 Relation between Biodiversity and Primary Productivity 126
7.2.2 Relation between Land Use, Degradation and Biodiversity 131
7.2.3 Functional Biodiversity 134
9 References 145

List of Figures

Figure 1: Scheme for DIVERSITY II inland waters processing. The algorithms described in this document are coloured in white. Light grey marks intermediate products, dark grey marks input data, and blue marks final output products. 13

Figure 2: Scheme for DIVERSITY II drylands processing. Net Primary Productivity (NPP, green), Rain Use Efficiency (RUE, blue-green) and Water Indices (blue) are derived and collected in regional databases, and then further assembled to first and second order indicators. 13

Figure 3: AMORGOS directory structure 15

Figure 4: Global relative accuracy results (unit: meter); source: Bicheron et al., 2011 16

Figure 5: Principle of the sensor independent Pixel identification method 22

Figure 6: Processing chain for mixed pixel estimation: the pure pixel selection was made only once, and spectra of each pixel used as inputs in the SMA for all images 27

Figure 7: Full resolution land abundance map (in red) overlaid onto a reduced resolution land abundance image of the same area (left); RGB composition (right). 28

Figure 8: Variations of bottom reflectance when viewed through different depths of seawater. The grey bars show typical wavebands of HR multispectral imagers (from Robinson, 2010, after Mumby and Edwards, 2000). 29

Figure 9: Example pixel location and spectra, for optically shallow water (red), optically deep and clear water (blue), optically deep and turbid water (green) and an unknown water type (pink). 30

Figure 10: A comparison of an L3 optically shallow water indicator and a reference map, for the Northern basin of Lake Michigan. Left: May-October 2008 L3 mean aggregate of ratio_413. Right: MODIS shallow water classification by Shuchman et al. (http://www.mtri.org/cladophora.html); Light brown is sandy benthos, green is submerged vegetation. 31

Figure 11: Example lakes where the ratio_490 approach does not indicate any shallow water areas. From left to right: Lake Vanern (Sweden), Lake Baikal (Russia), Lake Peipus (Estonia/Russia). 32

Figure 12 Example lakes where ratio_490 is lowered by constantly high turbidity. From left to right: Lake Brienz (Switzerland), Lake Balaton (Hungary), Markermeer (The Netherlands). 32

Figure 13: Ratio_490 shallow water indicator (left), screenshot from Google Maps (centre) and bathymetry map from www.wldb.ilec.or.jp in 20 m intervals (right) for Lake Vattern, Sweden. 33

Figure 14: Ratio_490 shallow water indicator (left), screenshot from Google Maps (centre) and bathymetry map from www.lake-garda-revealed.com in 10+ m intervals (right) for Lake Garda, Italy. 33

Figure 15: Ratio_490 shallow water indicator (top left), screenshot from Google Maps (right) and bathymetry map from www.jsedres.sepmonline.org for Lake Issykkul, Kazakhstan. 34

Figure 16: Estimation of the relative error in reflectance retrieval caused by the assumption of a Lambertian surface (Rahman and Dedieu, 1994) after resampling to the GlobAlbedo AOD550 grid and the spectral response (Lopez et al., 2013). 36

Figure 17: MERIS band 13 (865 nm) radiance transects across Lake Constance, on 5 dates with variable atmospheric density. The solid, uncorrected transects reveal a significant increase in radiance towards the shoreline, while the dashed, ICOL corrected spectra correspond better to the homogenous water properties outside the emerging plume in red (from Odermatt et al. (2008)). 38

Figure 18: Comparison between reflectance spectra calculated by SCAPE-M and the BEAM lake processors. All the data were processed by ICOL and C2R processors in BEAM, except for Lake Albufera and Lake Rosarito, to which the eutrophic lakes processor was applied (from Guanter et al. (2010)). 40

Figure 19: Atmospheric correction scheme for the MERIS lakes processor (from Doerffer and Schiller (2008a)). 41

Figure 20: ICOL overview processing flow chart (from Santer and Zagolski (2009)). 42

Figure 21: Reflectance matchup comparisons for hypertrophic water in the Albufera Lagoon (Spain, 25 May 2005, left) and Lake Hartbeespoort (South Africa, 15 October 2010, right). The Idepix land flag is raised for the Albufera example. 45

Figure 22: Reflectance scatter plots for 3 measurements in Lake Hartbeespoort, using BRR (left) and Scape-M (right) atmospheric corrections. 45

Figure 23: Reflectance matchup comparisons for mesotrophic water for two different sites in Lake Balaton (Hungary, 22 August 2010). 46

Figure 24: Reflectance matchup comparisons for eutrophic water in Lake Peipsi (Estonia, left: 12 May 2011, right: 2 September 2011). 46

Figure 25: Reflectance matchup comparisons for CHL dominated eutrophic water for two different sites of the Almendra Reservoir (Spain, 10 July 2007, left). 46

Figure 26: Reflectance matchup comparisons for eutrophic water in the Rosarito Reservoir (Spain) on 15 June 2004 (left) and 1 July 2004 (right). 47

Figure 27: Reflectance scatter plots for 11 measurements in Lake Balaton, using Scape-M, CCL2R, C2R and FUB (left to right) atmospheric corrections. 47

Figure 28: Reflectance matchup comparisons for clear, oligotrophic water in the Loskop Reservoir (South Africa, 1 August 2011, left) and Lake Zurich (Switzerland, 15 August 2007, right). 48

Figure 29: Reflectance matchup comparisons for CDOM dominated oligotrophic water in Lake Paijanne (Finland, 7 August 2007, left) and Lake Pyhajarvi (Finland, 23 August 2007, right). 48

Figure 30: Scheme of the recommended applicability for the assessed algorithms. Entries in brackets indicate partial limitations, i.e. the 709 nm peak by CHL in eutrophic waters and the vanishing signal level in CDOM dominated oligotrophic water. 51

Figure 31: Data source of the final global TRMM data set 54

Figure 32: TRMM versus station precipitation at location no. 5 in the right hand map 54

Figure 33: Potential limits to vegetation net primary production based on fundamental physiological limits by solar radiation, water balance, and temperature (from Churkina & Running, 1998; Nemani et al., 2003; Running et al., 2004). Source: http://www.ntsg.umt.edu/project/mod17 55

Figure 34: Precipitation and temperature trends 1982-2012 in Central Asia, source: Zhou et al. 2015 56

Figure 35: Different spatial patterns of the "water" data sets in the Sahel test site of the first half of August 2004. (relative scaling was adjusted, a general N to S gradient of increasing moisture from orange to green / blue tones can be seen in all products. 57

Figure 36: Comparative time series of GIMMS NDVI, TRMM rainfall, CCI soil moisture, and MODIS evapotranspiration for two dryland test sites 57

Figure 37: Pearson correlation coefficient between one year time series of TRMM rainfall data and MODIS evapotranspiration data (missing areas are due to TRMM 3B42 data gaps) 58

Figure 38: Input data used for BETHY/DLR, overview provided by M. Tum, DLR 59

Figure 39: In situ and CC atmospherically corrected spectra and corresponding water types in Lakes Zurich, Paijanne, Loskop (upper left to right), Kasumigaura, Hartbeespoort and Peipsi (lower left to right). The floating point numbers in the legend indicate the calculated class membership. 60

Figure 40: Case 2 water classes for CHL (left column), TSM (center) and CDOM (right) concentrations, with high to low concentration classes from top to bottom, and the remaining two constituents varying in x- and y-directions of each box. Class names and concentration ranges are titled in each box. Algorithm validation ranges are indicated as boxes and labeled with corresponding retrieval methods or center wavelengths. Bold labels indicate validation experiments with >10 images, hatched areas indicate simultaneous retrieval of all constituents. Reading example: Binding et al.(2010a) validate the FLH and MCI algorithms for CHL in eutrophic waters with 0.85–19.60 g/m^3 TSM and 0.26-7.14 m^{-1} CDOM. From Odermatt et al. (2012) 62

Figure 41: Distribution of valid concentration cases after application of the FUB covariance constraints. 63

Figure 42: Algorithm performance for the MPH algorithm, for the 14 selected reference datasets. Bar height indicates R for the given algorithm (left y-axis), dotted bar tops indicate the highest R achieved by any of the 74 evaluated procedures. CHL median and n are given on top of each bar. 69

Figure 43: FUB CHL matchup scatter plots for Lake Geneva (Laboratoire data), using bulk reprocessed (left) or the previously available CoastColour MERIS FR input datasets. 69

Figure 44: All processing combinations (3 columns on the left) and their correlation (colour coded and in the 3 columns to the right) with the 14 reference datasets. The dominant OWT for each reference datasets is given in the second row. 70

Figure 45: Surface water temperatures in March in Lake Biwa. The spatially averaged ARC Lake LSWT are represented by bars and dashed lines, and contrasted with in situ temperature measurements of the Univ. Kyoto’s limnological survey program taken at 1 m depth and 35.2161° N, 135.9986 E (asterisks and solid lines; basemap from NASA SRTM). 71

Figure 46: Illustration of the water body mapping algorithm. Decision rules are represented by the black diagonal line and the two dashed lines. The water and the land regions in the feature space of TV and MB are marked accordingly in light blue and green, respectively (from Santoro and Wegmuller, 2014). 72

Figure 47: Time series (left) and scatter plot (right) comparison of water level in Lake Victoria from in situ gauges (green time series) and Jason-1 radar altimetry (from Crétaux et al., 2011)... 73

Figure 48: Seasonal variations of g2 MR and JRC MERIS fAPAR mean values over the main biomes existing in the Guadalquivir basin during the year 2003 (source: Geoland 2 BP-RP-BP022, 2011).. 77

Figure 49: MERIS fAPAR versus ground measured fAPAR in Senegal (black star in upper image indicates location) 78

Figure 50: Number of filled gaps in [%] for the period 2003-2011 (100% = 216 half-months). On the right, the yellow arrow points to the test area of the gap filling simulation, where it can be clearly seen that it contains the pattern of filled gaps from the area marked with the black square to the east. 80

Figure 51: Portions of simulated and filled additional gaps (left) versus changes of the resulting Median SoS (Start of the vegetation years 2003-2011) compared to the original SoS Median 81

Figure 52: Impact of the gap simulation on product 01: Vegetation year average fAPAR 2003-2010 82

Figure 53: Impact of the gap simulation on product 02: Mean Cyclic Vegetation fAPAR 2003-2010.................. 83

Figure 54: Impact of the gap simulation on product 33: Trends of vegetation year average fAPAR 2003-2010.. 84

Figure 55: Scheme of the extracted phenological descriptors and periods, and corresponding rainfall and soil moisture data. Location: South Africa, Y: -29.896337, X: 25.7373764 (same as figure 3) 87

Figure 56: Empirically fixed relation between amplitude and dry season MIN 89

Figure 57: Comparison of the Cyclic Fraction fAPAR sums derived by GeoVille (GMP) versus results of the Timesat phenology software (TMP) 90

Figure 58: RUE in several ecosystems of Tunisia. Source: Floret and Pontainer 1978, taken from Le Houérou 1984. 95

Figure 59: Contrasting MERIS fAPAR derived indicators with BETHY/DLR modelled NPP based indicators in test site 04, Northern Kazakhstan. The black line is the northern country border of Kazakhstan, the brown polygon represents the WWF ecoregion boundary of the actual study site. 98

Figure 60: First order rainfall, soil moisture, fAPAR, RUE and SMUE products of site 12, Southern Africa West107

Figure 61: fAPAR, RUE, SMUE and rainfall trends, rainfall and soil moisture epochal change products, site 20, Southern.. 108

Figure 62: P50 Functional classes in test site 17, Southern Central USA 111

Figure 63: P51 Functional differences in test site 17, Southern Central USA 112

Figure 64: P52 Seasonal Trend Relation, test site 17, Southern Central USA 113

Figure 65: Relation between seasonal vegetation productivity and rainfall, site 14, Patagonian 115

Figure 66: TRMM rainfall versus MERIS fAPAR dry season greenness trends 2003-2010, test site 02, Northern Australia 116

Figure 67: P56 Trend relations of GPCP rainfall and GIMMS NDVI data for vegetation years1982 – 2002........ 116

Figure 68: Trend relations of rainfall and NPP proxies (per vegetation year) for the two trend periods 1982-2002 and 2003-2010, respectively. Test site 21, Southern Africa East 117

Figure 69: P57 Median start of vegetation year 2003-2010, site 10, Southern Europe 118

Figure 70: P59 Mean start of vegetation season 2003-2010, site 10, Southern Europe 119

Figure 71: P58 Mean length of vegetation season 2003-2010, site 01, Northern – Central Mexico 120

Figure 72: P58 Mean length of vegetation season 2003-2010, site 05, Eastern Mongolia Western Manchuria 120

Figure 73: Schematic diagram showing the relationships between climate change and other major anthropogenic influences and their effects on biodiversity. The two major factors resulting directly from climate change and the four major anthropogenic factors have both individual and interactive effects on biodiversity in freshwater ecosystems (adapted from Kappelle et al. 1999; Heino et al. 2009). 122

Figure 74: Observed water temperatures in comparison to fish spawning envelopes. The solid line shows the temperature of the Murrumbidgee River at Wagga Wagga where cold water pollution occurs. The dotted line shows water temperature at Jugiong Creek at Jugiong where there is no cold water pollution (adapted from New South Wales, 2006). 123

Figure 75: Overview of climate change impacts on ecosystem and biota, and how they interact with contaminants, and their fate and effects (from Schiedek et al. 2007). 124

Figure 76: Association of the total density and zooplanctonic biomass with chlorophyll-a concentration in lakes during the dry (a and b) and rainy (c and d) seasons (adapted from Bonecker et al, 2012)............................. 125

Figure 77: Biodiversity highlights in Southern Africa: Succulent Karoo (shown in RUE map in blue ellipse on the left), Area south to the Etosha Pan (shown in soil moisture map in the blue ellipse on the right) 126

Figure 78: Number of Species of Flowering Plants in Selected Countries across the Aridity Gradient (per 1,000 sq. km). Each column represents a mean of two countries. Selected dryland countries are at least 95% dryland, either of one subtype, or two of roughly similar dimensions. Grey columns indicate non-dryland countries. Source: Millennium Assessment (http://www.millenniumassessment.org/documents/document.291.aspx.pdf), compiled from CIA (Central Intelligence Agency), 2004: The World Fact Book, https://www.cia.gov/redirects/ciaredirect.html, and from WRI (World Resources Institute), 2004: EarthTrends, the Environmental Information Portal [Online], Drylands, People, and Ecosystem Goods and Services: A Web-based Geospatial Analysis (pdf version), by R.P. White and J. Nackoney. 126

Figure 79: NPP and tree diversity relationship (source: Kale and Roy 2012). 127

Figure 80: Results from the survey of pond species diversity relative to *in situ* primary productivity at local and regional scales. Top panels: producers (vascular plants and macroalgae); bottom panels: benthic animals (e.g. insects, crustaceans, amphibians). a) Local species diversity within-ponds (N . 30). Both relationships are significantly unimodel (P, 0:05). The line represents the estimated quadratic function. b) Regional species diversity within-watershed. For both producers (regression: N. 10, R2. 0:74, P, 0:001) and benthic animals (regression: N . 10, R2 . 0:75, P , 0:001) regional species diversity was linearly related to primary productivity (source: Chase and Leibold 2002). 128

Figure 81: The relationship between log10 NPP and (a) square-root of human population density, (b) log10 total species richness (weighted index), (c) square-root bird species richness, (d) log10 butterfly species richness, (e) log10 mammal species richness, (f) log10 restricted species richness, and (g) log10 threatened species richness. Sample grain is 1 grid squares (n = 683) (from Luck 2007). 129

Figure 82: Relationship between NPP and the value of ecosystem services by biome (from Costanza et al. 1998). 130

Figure 83: Conceptualized pathways of greening. Point symbols represent different woody species; arrows indicate possible pathways of change towards "greener" conditions. Source: Herrmann et al. 2013.............. 131

Figure 84: Shannon-Wiener diversity index (H) and evenness (J) of plant and small mammals. Source: Mugatha et al., 2003, from Maitima 2009. 132

Figure 85: (a) Ecosystem Functional Types derived by Ivits et al. (2013) and (b) Diversity II Functional Units .. 135

List of Tables

Table 1: Smile correction parameters. 18

Table 2: Definition of values for classification features 22

Table 3: Feature definition. 23

Table 4: Confusion matrix for the Idepix validation using PixBox. The upper table is for pure pixel, the lower for pure and ambiguous pixel cases together (Ruescas et al., 2014). 25

Table 5: Idepix spectral mixture analysis parameters. 27

Table 6: Spectro-radiometric matchup measurements available for validation in the scope of Diversity II. Measurement techniques for the ASD FieldSpec and RAMSES are described in (Kallio et al., 2007). The minima and maxima of applicable constituents refer only to the 'n_valid' cases, i.e. those identified as cloud free and valid. 43

Table 7: Counts of ICOL test cases and number of rel. RMSE improvements propagated to atmospherically corrected spectra for CCl2R, C2R and FUB. All spectro-radiometric matchups with valid pixels in Table 6 are included, apart Vanern and the Spanish reservoirs. The percentage in brackets is the average decrease in relative spectral RMSEs for the improved cases. 50

Table 8: Relative RMSEs (ε, [%]) for the reflectance matchup comparisons using 'bulk' reprocessed MERIS FR as in Figure 21 and Figure 29, and for the CoastColour ('CC') MERIS FR data basis prior to reprocessing. 50

Table 9: Training ranges and IOP to concentration conversion equations for the C2R and FUB algorithm, updated from Odermatt et al. (2012). 63

Table 10: Evaluated arithmetic algorithms for CHL estimation in inland waters. 64

Table 11: Evaluated arithmetic algorithms for TSM estimation in inland waters. 64

Table 12: Evaluated arithmetic algorithms for Turbidity and Secchi depth estimation in inland waters. 64

Table 13: Water constituent data available for matchup analyses. The column "No." indicates the number of matchups prior to invalid pixel flagging, whereof multiple samples corresponding to one pixel are counted only once. 66

Table 14: Contingency matrix built on the comparison between a reference dataset of 1844 footprints and the LC-CCI WB product. 72

Table 15: Test sites with and without (or neglected) snow cover 85

Table 16: Major phenological and productivity parameters derived for each pixel (highlighted parameters are directly used for generating the Diversity II products) 92

Table 17: *Water quality parameters and EO source* 99

Table 18: Maps and indicators (L3 & L4) 100

Table 19: Concentration ranges for categorisation of different lake types 101

Table 20: Deliverable: Example of diversity and trend table. 101

Table 21: Maps and relative indicators (L3) 102

Table 22: Deliverable: Diversity status and trend table. 102

Table 23: Overview of the organisation of the first order indicators and the related product numbers 105

Table 24: Overview of the systematic of the second order indicators (colours reflect product types) 109

Table 25: Aggregations of input parameters for second order product P50: Functional classes 111

Table 26: Phenology products.. 117

Table 27: Total number of plant species, herbaceous (grasses and herbs) species and total plant biomass (gm-2) between grazed and un-grazed sites. * Means significantly different at (p < 0.05), t-test. Sample size was 245 plant species. Source: Kamau, 2004, from Maitima 2009. 132

Table 28: Overview on processing and algorithms 136

Change Records

Date	Version	Change Record	Author
05.12.2012	1.0	Final draft of ATBD Version 1.0	Diversity Team
25.01.2013	1.1	Inclusion of improved radiometric as additional pre-processing step (chapter 3.3), changing of orders in the pre-processing chapter	Stelzer
25.01.2013	1.1	Further input for Combined Indicators (Multi-annual Status and Trends) (chapter 6.2.2)	Gangkofner
25.01.2013	1.1	Update of overview table (table 19)	Stelzer
25.09.2013	2.0	Review of all chapters for preCDR	all
13.12.2013	2.2	Update according to product design at the end of the experimental phase/CDR	Odermatt
20.10.2015	2.4	Update to reflect all changes and to be coherent with the final set of products.	Odermatt, Gangkofner

Acronyms and Abbreviations

AC	Atmospheric Correction
AOT	Aerosol Optical Thickness
ATBD	Algorithm Theoretical Basis Document
BC	Brockmann Consult GmbH
BG	Brockmann Geomatics Sweden
BOA	Bottom-of-atmosphere
BRR	Bottom-of-Rayleigh
C2R	Case 2 Regional algorithm
CBD	Convention on Biological Diversity
CCI	Climate Change Initiative
CDOM	Coloured Dissolved Organic Matter

CHL	Chlorophyll Concentration
CIBIO	Research Centre in Biodiversity and Genetic Resources
CMAP	CPC Merged Analysis of Precipitation
CPC	Climate Prediction Centre
ECV	Essential Climate Variables
EO	Earth Observation
ET	Evapotranspiration
fAPAR	Fraction of Absorbed Photosynthetically Active Radiation
FLH	Fluorescence line height
FR	Full Resolution
FRS	Full Resolution Full Swath
FUB	Freie Universität Berlin
GIMMS	Global Inventory Modeling and Mapping Studies
GIS	Geographic Information System
GMAO	Global Modeling and Assimilation Office
GMFS	Global Monitoring for Food Security
GMSM	Global Monitoring of Soil Moisture
GV	GeoVille Information Systems GmbH
ICOL	Improve Contrast between Ocean & Land
IOP	Inherent optical properties
L1b	Level 1b
LAI	Leaf Area Index
LC CCI	Land Cover Climate Change Initiative
MCI	Maximum chlorophyll index
MERIS	Medium Resolution Imaging Spectrometer
NDVI	Normalized Difference Vegetation Index
NDWI	Normalized difference water index
NIR	Near Infrared
NN	Neural Network
NPP	Netto Primary Production
OC	Ocean Colour
OLCI	Ocean Land Colour Instrument
PSD	Product Specification Document
PVASR	Product Validation and Algorithm Selection Report

RB	Requirements Baseline Document
RR	Reduced Resolution
SCAPE-M	Self-Contained Atmospheric Parameters Estimation from MERIS
SEPA	Swedish Environment Protection Agency
SRR	System Requirements Review
SST CCI	Sea Surface Temperature Climate Change Initiative
SMA	Spectral mixture analysis
SM-MW	Microwave based soil moisture data
SMU	Soil Moisture Use
SMUE	Soil Moisture Use Efficiency
SWBD	SRTM Water Body data sets
TOA	Top-of-atmosphere
TOSA	Top of standard atmosphere
TRMM	Tropical Rainfall Measuring Mission
TSM	Total Suspended Matter
UNESCO	United Nations Educational, Scientific and Cultural Organization
WUE	Water use efficiency

Applicable documents

[SoW] ESA Directorate of Earth Observation Programmes. Diversity II, supporting the Convention on Biological Diversity – Statement of Work, v. 1, 2011.

[TS] Diversity II Technical Specifications. Brockmann Consult, v. 2.0, 2013-02-08.

[RB] Diversity II Requirements Baseline Document. Brockmann Geomatics, v. 3, 2013-05-06.

[PQR] Diversity II Product Quality Report, CIBIO, v. 1, 2013-06-19.

1 Scope of the Document

This document contains descriptions of the algorithms that are of relevance for the DIVERSITY II project, and an analysis of the relationship between remotely sensed indicators and their effect on biodiversity. It focuses on algorithms that were used in the final processing, but includes also other algorithms that were considered during the development phase.

The structure of the document corresponds to the data processing order, starting with pre-processing techniques, and followed by lake and dryland algorithms. The description of the algorithms used in each processing step varies. For standard approaches, only a short description, basic equations and literature references are given. Where different applicable approaches are available, an evaluation was performed during the experimental phase, and validation results are provided to justify the final selection. Figure 1 and Figure 2 provide overview schemes for inland waters and drylands, respectively.

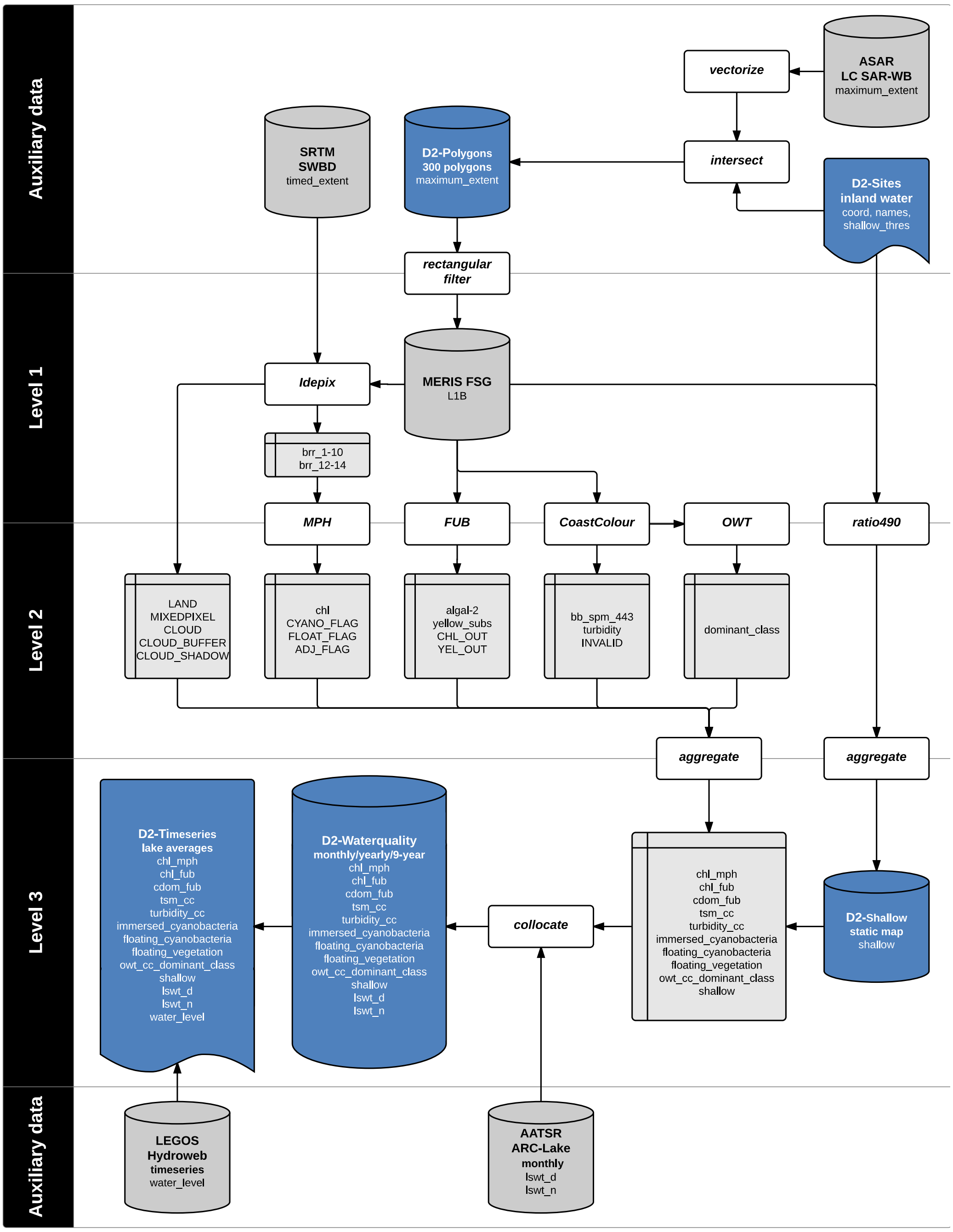

Figure 1: Scheme for DIVERSITY II inland waters processing. The algorithms described in this document are coloured in white. Light grey marks intermediate products, dark grey marks input data, and blue marks final output products.

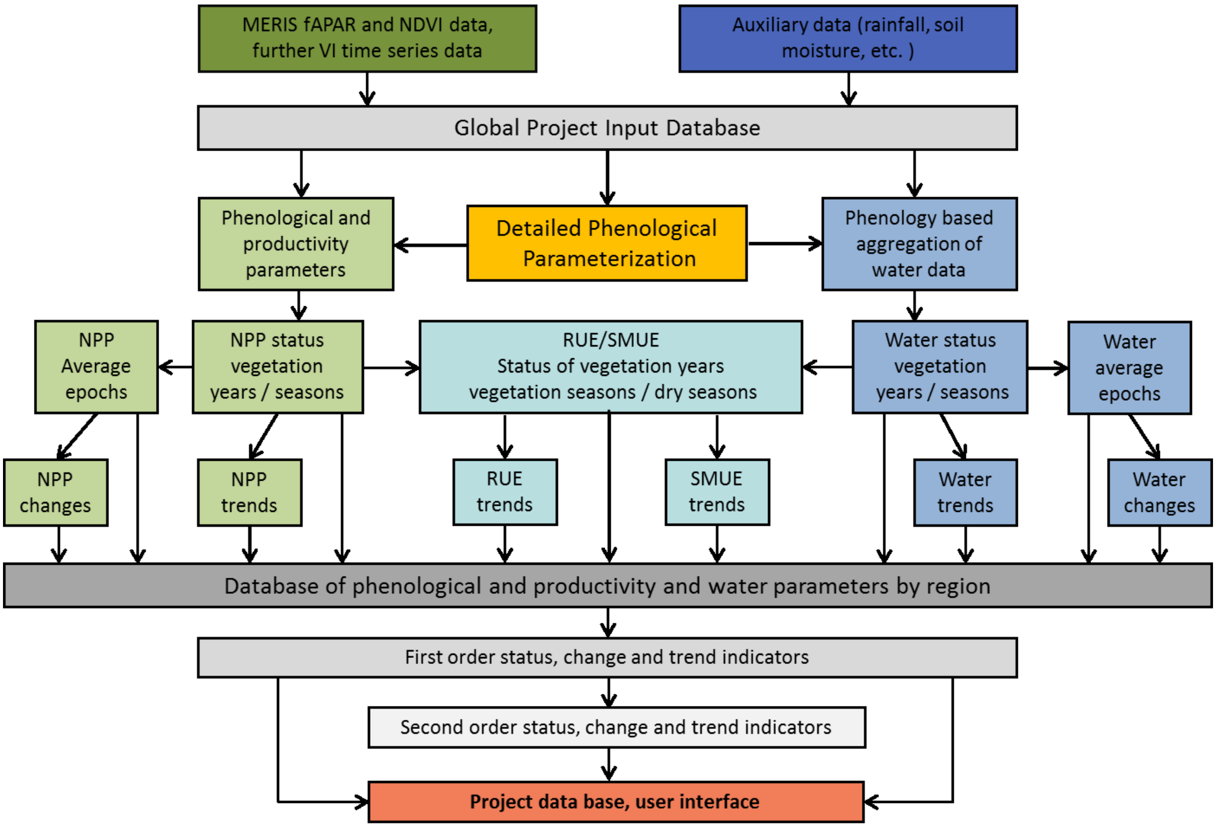

Figure 2: Scheme for DIVERSITY II drylands processing. Net Primary Productivity (NPP, green), Rain Use Efficiency (RUE, blue-green) and Water Indices (blue) are derived and collected in regional databases, and then further assembled to first and second order indicators.

2 Introduction

Deriving the basic water quantity and water quality parameters for inland waters is a challenge. In particular the identification of suitable atmospheric correction and water quality parameter retrieval algorithms for different lake types is an unresolved issue (Mark William Matthews, 2011; M. a. D. a. G. A. b. B. V. E. c. S. Odermatt, 2012). For Diversity II, previous experiences in this field are summarized and a comparison of various algorithms is performed, including our own adaptations of the Case2R and FUB algorithms to inland waters. The parameters under consideration are chlorophyll-a (CHL), total suspended matter (TSM), coloured dissolved organic matter (CDOM, also addressed as yellow substance or gelbstoff), turbidity/attenuation and Secchi depth. All these parameters except CDOM are assessed by means of in situ data from more than 37 lakes and reservoirs, and all available matchups in the 10-year MERIS FR database. This validation and intercomparison exercise exceeds any previously reported study regarding the number of different lakes considered.

EO based approaches to the assessment of dryland conditions and EO based findings with regard to biodiversity are primarily dependent of the geographic scale. Large area (> 0.5 Mio skm) assessments such as in this study, analyse time series data of above ground green biomass, which is estimated for fixed increments of time (most typically decades, months, years) using EO derived vegetation indices or bio-physical indices. Most commonly, the NDVI, the Normalised Difference Vegetation Index, is used as a proxy for NPP, where the NOAA GIMMS NDVI data constitute a prominent, very frequently used data set reaching back more than 30 years. Nevertheless, in Diversity II drylands, emphasis is laid on the usage of the MERIS based fAPAR as main vegetation indicator and biophysical variable. MERIS NDVI data are evaluated for two selected test sites for comparison with the fAPAR based results. The developed processing suite is also applied to the NOAA GIMMS NDVI data in order to provide longer term trends and for contrasting the results obtained with these widespread used data to the MERIS based outcomes. The generation of Rain Use Efficiency indicators was a further project requirement and was realised along with the derivation of an analogue indicator based on Soil Moisture data.

3 Pre-Processing

3.1 Improved Geolocation using Amorgos

Small islands and complex shorelines of coasts and lakes, as well as patchy structures in the water, cause a high spatial variability. A high accuracy of the geolocation in the order of sub-pixels is necessary for obtaining good spatial and temporal composites (Level 3 products). This high accuracy is a keystone when looking for matchups of in situ data for validation purposes.

The criteria, which lead to the choice of the final tool, are:

- geometric accuracy
- availability of the software
- usability in the context of the DIVERSITY processing chain
- completeness of the available software, e.g. with respect to auxiliary data
- processing performance

The initial accuracy specifications for MERIS absolute geolocation was 2000m (Sotis, Balducci, & Campbell, R., Goryl, 2011) with an operational goal of ±150m at nadir corresponding to about the half size of a ground pixel. Initial geo-location performance was significantly worse than required because of sensor attitude inaccuracies (Bicheron et al., 2011). With AMORGOS (Accurate MERIS Ortho Rectified Geo-location Operational Software), ESA has made available a tool that improves MERIS FR geolocation to an accuracy better than 70m RMS. This is sufficient for the application of DIVERSITY. AMORGOS has been developed by ACRI-ST. However, AMORGOS is known to be computationally intensive and having problems in high latitudes. Further, it should be pointed out that AMORGOS needed an update for working with the MERIS data acquired after the orbital change manoeuvre in November 2010. An updated version for Linux operating systems (version 3.0p1) is available, and provides compatibility also with the new ENVISAT Orbit. AMORGOS includes a precise orbit determination, instrument pointing and performs an ortho-rectification.

The documentation of the AMORGOS tool and installation is available on the ESA website. There are two documents that are relevant.

- *The AMORGOS MERIS CFI Software User Manual & Interface Control Document* describes the installation and operation of the AMORGOS Tool:
  http://earth.esa.int/services/amorgos/download/Amorgos_ICD-SUM_3.0a.pdf
- The *AMORGOS Software Transfer Document* describes the procedure which patches the AMORGOS software on one's system, starting from the set of deliverables pertaining to version 3.0patch1 and the local installation of version 3.0:
  http://earth.esa.int/services/amorgos/download/Amorgos_STD_i3r0p1.pdf

AMORGOS is run once for every MERIS_FRS_1P file and generates the corresponding MER_FSO_1P file. Re-build of the instrument projection is done using MER_FRS_1P internal data, the so-called MERIS detector index data set, and some additional MERIS Level 1b auxiliary data, the FR frame offset, extracted from appropriate MER_INS_AX file. For each MERIS pixel restored in instrument projection, an ortho-rectification algorithm computes the first intersection between the pixel's line of sight and the Earth surface, represented by interpolation of the Digital Elevation Model (DEM) cells elevations on top of the reference ellipsoid. Line of sight is determined using its pointing vector expressed relative to the satellite, the satellite location and attitude, which are in turn determined from Orbit and Attitude files using the appropriate CFI routines. Location of the intersection is expressed as longitude, geodetic latitude and geodetic altitude.

AMORGOS is producing a so-called FSG (Full Swath Geo-corrected) product. This is structurally identical with the FRS product but with 3 additional bands for the precise and corrected latitude, longitude and altitude. Tests have been performed on the performance of the AMORGOS Tool using different MERIS FRS products and different processing computers and network environments. The overall result of these tests is that AMORGOS processes 32000 pixel/sec on a 3GHz Xeon with Linux OS, 2GB RAM and data on local disks or accessible via a fast network.

AMORGOS is executable software, which takes a MERIS FRS product as input and generates an FSG product as output. AMORGOS performs an improved navigation and pointing calculation and ortho-rectifies the data using an external digital elevation model. An important issue is the limitation of frame numbers for the FSG product. Due to output product time limits, the number of lines of an FSG product cannot exceed the value of 10305. Because the input FRS product may consist of up to 12865 lines, the processing of such a product has to be performed in two steps. AMORGOS provides input switches in the configuration file to handle this constraint.

Since AMORGOS is a binary distribution for Linux, it runs only under this operating system. It expects a certain directory structure, as depicted in the following Figure 3, which is taken from the AMORGOS Software Transfer Document. The figure does not contain the DEM directory, where the tiles of the digital elevation model reside.

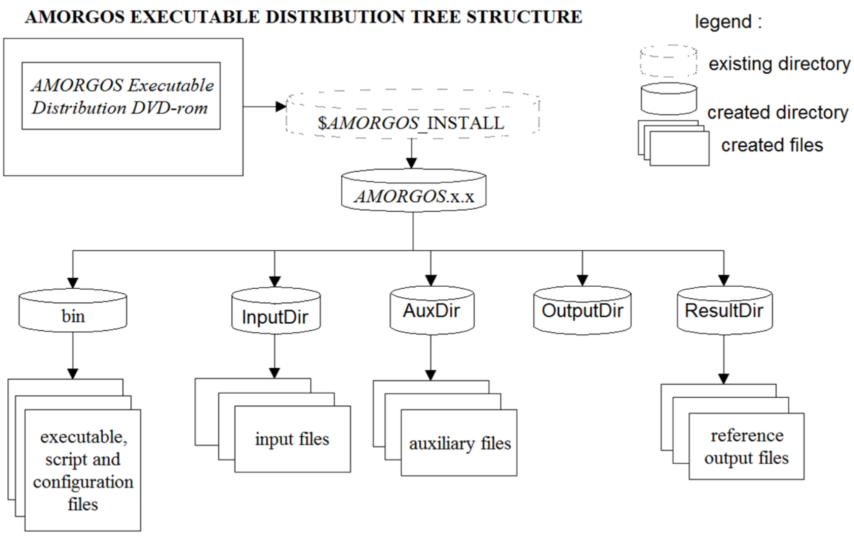

Figure 3: AMORGOS directory structure

The validation of the accuracy has been performed for the absolute accuracy as well as for the relative accuracy. In the latter one, pairs of MERIS FRG images have been collocated and the difference of randomly selected sample points have been calculated. Figure 4 represents the RMSE in longitude as a function of RMSE in latitude for the 146 pairs. Only 3 pairs are beyond a 150m threshold for the relative accuracy, which is half a MERIS FR pixel.

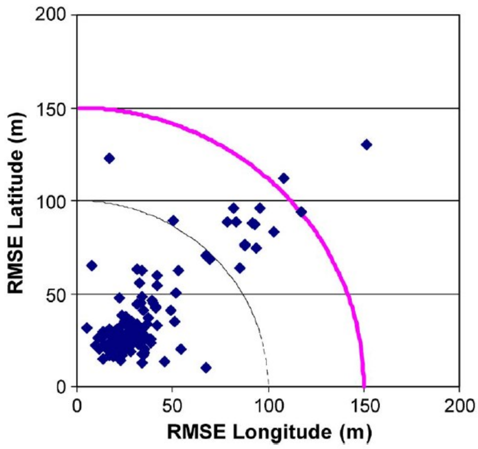

Figure 4: Global relative accuracy results (unit: meter); source: (Bicheron et al., 2011)

3.2 Radiometric Correction

MERIS Full Resolution data are provided as top-of-atmosphere (TOA) spectral radiances, i.e. with calibration applied to the raw data. However, the L1b archive that ESA is distributing consists of data processed at different dates, and with the calibration coefficients available at the time of processing. This leads to inconsistency in the dataset, and, more importantly, the quality of the sensor's degradation model has been improved throughout the years so that the latest model, available since 3rd reprocessing, ensures best quality. Further there are specific issues with the calibration that are not addressed in the standard calibration and which lead to residual errors visible as camera interface and vertical striping.

Hence the radiometric correction that will be applied to all MERIS FR scenes consists of three different processing steps. They have been investigated, validated and applied to the MERIS FRS archive within the CoastColour project. The three steps are the

- Improved calibration in order to rebuild 3rd reprocessing radiometric calibration, adjustment has been developed within the DUE II project CoastColour and LC-CCI
- Equalization to reduce coherent noise following (Bouvet & Ramino, 2010)
- Smile correction

3.2.1 Improved Calibration

Spectral and radiometric calibrations are key processes for all quantitative algorithms that exploit the spectral shape and magnitude. The spectral calibration of MERIS is performed by using measurements of a coloured diffuser and by a spectral matching technique using the measurements of the $O_{2\text{-}A}$ absorption band. The spectral calibration has been proved to be within 0.1nm accuracy. This is considered to be adequate for the generation of CCI-LC products. The radiometric accuracy is more critical. MERIS has two diffusers on-board, the first one being used regularly to monitor the radiometric response and the second one being exposed to sun light only 3 to 4 times per year in order to monitor the ageing of the first diffuser. With this technique it was possible to derive a new degradation model of the instrument, which is applied for the third reprocessing, which is taking place in Winter 2009/Spring 2010. This reprocessing quality is required for CCI-LC. The reprocessing, however, concerns only Reduced Resolution products. In spring 2011, also the IPF (the operational processor) will be upgraded with the new degradation model and from that point onwards, also FRS products will be processed with the improved calibration. But all archived FRS products will remain at old calibration status. Hence, an algorithm was developed to correct 2nd re-processing products to 3rd reprocessing radiometric quality.

The radiometric calibration as described below is a non-linear process including several steps. The radiometric gains are the second last step before the L1b are written. However, the last step is the stray light correction which is a non-linear process and not revertible from L1b product. The Improved Calibration is therefore only an approximation.

The valid MERIS samples are digital counts resulting from the detection and acquisition by MERIS of a bi-dimensional field of spectral radiance in front of the instrument. The objective of the radiometric processing, together with the stray light correction, is to estimate that spectral radiance. An inverse model of the MERIS processing is used for that purpose, using parameters stored in the Characterisation and Radiometric Calibration databases and the MERIS samples themselves. The MERIS acquisition model is described in Eq. 1.

$$X_{b,k,m,f} = \mathrm{NonLin}_{b,m}\left[g(T_f^{VEU}).\left[A_{b,k,m}\cdot\left(L_{b,k,m,f} + G_{b,k,m}(L_{*,*,*,f})\right) + Sm_{b,k,m,f}(L_{b,k,m,*})\right] + g_c(T_f^{CCD}).C^0_{b,k,m}\right] + \varepsilon \quad \text{Eq. 1}$$

Whereas:

- M is the camera (or module); b is the spectral band; k is the pixel column; f is a frame (processing unit of number of image lines)
- $X_{b,k,m,f}$ is the MERIS raw sample
- $\mathrm{NonLim}_{b,m}$ is a non-linear function, representing the non-linear transformations which take place in the CCD, amplifier and A/D converter; NonLin depends on band and gain settings
- T_f^{VEU} is the temperature of the MERIS amplifiers (VEUs) at the time of frame f
- T_f^{CCD} is the temperature of the MERIS detectors (CCDs) at the time of frame f
- g and g_c are (dimensionless) temperature correction functions
- $AL_{b,k,m}$ the "absolute radiometric gain" in counts/radiance unit; AL depends on band & gain settings
- $L_{b,k,m,f}$ the spectral radiance distribution in front of MERIS
- $Sm_{b,k,m,f}$ the smear signal, due to continuous sensing of light by MERIS
- $C^0_{b,k,m}$ the calibrated dark signal (possibly including an on-board compensation), dependent on band and gain settings
- $G_{b,k,m}$ a linear operator (weighted sum) representing the stray light contribution to the signal. For a given sample, some stray light is expected from all the other samples in the module, spread into the sample by specular (ghost image) or scattering processes
- ε is a random process representative of the noise and measurement errors

This model is inverted during processing: The inverse of the absolute instrument gain ALb,k,m is applied to the valid samples of all bands after dark and smear signal subtraction, with a compensation for the estimated temperature which is expressed as a function of time in Eq. 2.

$$R_{b,k,m,f} = \left(AL^{RR}_{b,k,m}\right)^{-1}\cdot\left\{\left(X'_{b,k,m,f} - S_{b,k,m,f}\right)\cdot\left[g_0 + g_1(t_f - t_{ref}) + g_2(t_f - t_{ref})^2\right] - C_{b,k,m,f}\right\} \quad \text{Eq. 2}$$

Where $R_{b,k,m,f}$ are the spectral radiances before the stray light correction. The Improved calibration is assuming the final stray light corrected radiances as equal to this $R_{b,k,m,f}$. The 2nd reprocessing radiometric gains (AL) are multiplied to R, and then the inverse of the 3rd reprocessing gains are multiplied to give an estimate of the 3rd reprocessing radiances.

3.2.2 Coherent Noise Equalisation

The MERIS equalization module performs a radiometric equalisation of the MERIS L1b products. It reduces detector-to-detector and camera-to-camera systematic radiometric differences and results into a diminution of the vertical stripping observed on MERIS L1b products. The MERIS swath is imaged by a CCD. The radiance at each pixel of a MERIS L1b products results from the measurements of 5 cameras spread across the swath, each one imaging a part of the swath with 740 so-called detectors in FR (corresponding to 185 mean detectors in RR). This results into 3700 detectors imaging the swath of MERIS FRS product (925 in RR). The response of each one of these detectors is calibrated during the routine operation of the instrument. Residual uncertainties in the calibration process result into detector-to-detector and camera-to-camera systematic radiometric differences. The equalisation corrects for these radiometric differences via a set of detector dependant coefficients correcting for the residual uncertainties in the calibration process. These coefficients are retrieved via a methodology described in Bouvet and Ramino, 2010, based on observations of the Antarctica plateau spread out throughout the MERIS mission lifetime.

The coefficients are different for MERIS Reduced and Full Resolution products. While the compilation of a full mission data set in reduced resolution, and subsequently the calculation of the noise equalisation coefficients, this process is not yet completed for full resolution data.

3.2.3 Smile Correction

MERIS is measuring the reflected sunlight using CCD technique. A CCD is measuring in one of its dimensions one image line, and in the other dimension the spectrally dispersed radiance for each pixel along the image line. I.e., the spectral measurements of each pixel along an image line are made by their own set of sensors of the CCD. This causes small variations of the spectral wavelength of each pixel along the image. This is called the "smile effect". The MERIS instrument is composed of 5 cameras; each equipped with it is own CCD sensor. The variation of the wavelength per pixel is in order of 1nm from one camera to another, while they are in the order of 0.1nm within one camera. Even though this variation is small compared to the spectral bandwidth of a band, which is typically 10nm, and can hardly be seen in an image, it can cause disturbances in processing algorithms that require very precise measurements, for example the retrieval of chlorophyll in the ocean. These disturbances can result in visual artefact ("camera borders") or reduced accuracy of the Level 2 products. Therefore, the MERIS Level 2 processor corrects the smile effect. The Level 1b product is not smile corrected, because this product shall provide the user exactly what the instrument is measuring, and that is in fact the radiance at the given wavelength of each pixel.

The smile correction consists actually of two parts: a radiance correction and a reflectance correction. The reflectance correction consists of an estimation of the reflectance spectral slope from the measurements in two neighbouring bands, and the interpolation of the reflectance along this slope from the actual pixel wavelength to the nominal wavelength of the considered band. It is defined in an external configuration data file, which bands will be corrected, and which bands are used for the slope estimation. The corrected reflectance is calculated according to Eq. 3 and Eq. 4. The required parameters are included in Table 1.

$$\rho_{slope} = \frac{\rho_{brr}(b_2) - \rho_{brr}(b_0)}{\lambda_{pix}(b_2, detector(j)) - \lambda_{pix}(b_0, detector(j))} \qquad \text{Eq. 3}$$

$$\rho_{sm-corr}(b_1) = \rho_{brr}(b_1) + \rho_{slope}(\lambda_{nom}(b_1) - \lambda_{pix}(b_1, detector(j))) \qquad \text{Eq. 4}$$

Table 1: Smile correction parameters.

Parameter	Description	Usage	Physical Unit
ρ_{brr}	Bottom-of-Rayleigh reflectances	input	none
λ_{pix}	wavelengths per pixel	input	nm
λ_{nom}	nominal wavelengths	input	nm
$detector(j)$	detector index at the pixel location of the spectra	input	none
b_1	the band index of reflectance to be corrected	input	none
b_2	upper band index for interpolating the slope	input	none

Parameter	Description	Usage	Physical Unit
b_0	lower band index for interpolating the slope	input	none
ρ_{slope}	slope of reflectance	input	none
$\rho_{sm-corr}$	smile corrected reflectance per band and pixel	output	none

3.3 Cloud Screening

3.3.1 Background

Clouds play an important role for optical satellite remote sensing and are treated in two opposite ways: Either cloud properties are retrieved, e.g. for weather forecast or climate studies (Liou, 1992; Rossow & Schiffer, 1999, 1999) or the focus of the interest is the Earth surface, land or water, which is concealed by clouds (Luo, Trishchenko, & Khlopenkov, 2008). In the latter case, the presence of the cloud needs to be identified, and the change of the surface reflectance due to the cloud has to be estimated.

An image pixel can be cloud free, totally cloudy, or partly cloudy:

- In the cloud free case there are no water droplets or ice crystals in the atmosphere which change the surface reflectance.
- In the totally cloudy case the optical thickness is so high that the portion of surface reflectance at the signal measured by the satellite is negligible.
- The partly cloudy case comprises all intermediate situations where the measured reflectance is a mixture of a significant portion of the surface reflectance, but modified due to the presence of a cloud. This can be either due to an optically thin cloud, or the cloud is covering only a fraction of a pixel in the field of view of the sensor (Preusker, Hünerbein, & Fischer, 2008).

Cloud free and totally cloudy pixels can be identified rather easily, and most of the tests used in earth observation processing systems for cloud identification today assign either of these two stages, and hence also partly cloudy cases have to be assigned to either of these two classes (EUMETSAT, 2006). Such a binary cloud flag is not appropriate if several different higher-level processing algorithms are applied, each of which having a different robustness to partial cloudy pixel. Some novel algorithms therefore deliver a graduated scale, as an indicator of the extent to which a signal is influenced by the presence of clouds (Gomez-Chova, Camps-Valls, Calpe-Maravilla, Guanter, & Moreno, 2007; C. Merchant, Llewellyn-Jones, Saunders, Rayner, & Kent, 2005; Schiller, H., Brockmann, C., Krasemann, H., & Schönfeld, 2008). Such an indicator can be related to cloud properties, e.g. apparent cloud optical thickness, the atmospheric transmission or cloud features.

Clouds have certain characteristics which can be used for their identification and characterisation (Luo et al., 2008):

- Brightness
- Whiteness
- Cold temperature
- High altitude

However, none of these characteristics is always given if a pixel is cloudy; and this is the main problem of cloud identification. For instance, thin lower clouds are difficult to differentiate from bright surfaces (like glint over water; snow or ice in land). Then methods based on other characteristics (features) than the ones given above must be used. In particular, the clouds can be also detected using the spatial and temporal variability of the reflected radiation. In addition, clouds screen the tropospheric gases. This leads to the increase in the reflection inside corresponding gaseous absorption bands (e.g., band 11 on MERIS (0.761 µm)), which is routinely used for the cloud top height monitoring (Richard Santer, Carrère, Dessailly, Dubuisson, & Roger, 1997).

One way to detect clouds would be to work directly with optical measurements. Further, derived cloud physical properties can be used to characterise clouds and assess their impact on the retrieved signal. This includes, amongst others, cloud fraction, cloud top temperature, cloud top pressure, cloud type, cloud phase, cloud optical depths and cloud effective particle size. Such properties can be studied using the radiative transfer modelling. (Jürgen Fischer, Schüller, & Preusker, 1999) have done extensive work in this respect over the past years (see also (Brenguier et al., 2000; Pawlowska et al., 2000; Rathke & Fischer, 2002). They have developed the MERIS algorithms for cloud top pressure, cloud optical thickness, cloud albedo and cloud type retrieval and have translated this knowledge into a probability based cloud detection algorithm (Preusker et al., 2008).

Cloud detection became important with the systematic processing of the NOAA AVHRR instrument in the 1980s. Statistical histogram analysis methods were developed by (Phulpin, Derrien, & Brard, 1983). Most common used were threshold algorithms, e.g. Saunders and Kriebel (1988). Large scale textures were identified using pattern recognition techniques as proposed by Garand and Weinman (1986).These methods worked quite well over the ocean but exposed problems in Polar Regions (separation of clouds from ice and snow) and in the tropics (low level, warm clouds). A good overview of the cloud screening techniques at the late 80s is given by Goodman and Henderson-Sellers (1988). Improved methods are proposed for the AVHRR (Simpson & Gobat, 1996) and later for ATSR (Simpson, Schmidt, & Harris, 1998).

The cloud screening algorithms for the ATSR 1 and 2 in the 1990s were mainly based on previous work for AVHRR and use spectral threshold tests (Costanzo, Hawkey, & Kelsey, 2012).The thermal band at 12µm is used as main tool to identify the cold cloud surface by a threshold, supported by other thresholds on band differences and on the histogram of the radiance distribution in the image. The unique feature of two views under different angles of the same pixel and the spatial coherence of the radiance are also exploited. The cloud screening of the AATSR is basically the same with refined and additional tests due to additional bands. Recently, tests on vegetation and snow indices have been introduced (Costanzo et al., 2012). However, application oriented projects are not satisfied with the standard cloud screening, and are proposing alternative methods, for example for the GlobCarbon processing (Plummer, 2008) and for the LC-CCI processing (Kirches, Krueger, et al., 2012).

The MERIS Level 2 cloud screening is a combination of 8 different tests (Richard Santer et al., 1997). Three of those are classical threshold tests on spectral radiances or differences, and five are connected with the pressure estimates derived from the differential oxygen A-band absorption measurements. The potential of the O2A feature has been addressed in ESA funded projects “Exploitation of the oxygen absorption band” and “MERIS AATSR Synergy”. The result of these activities led to an upgrade of the operational MERIS pixel classification in the third reprocessing. Major improvement is due to including dedicated pressure algorithms for detection of the height of the scattering surface over land and ocean.

A big problem is the distinction between clouds and snow/ice, in particular for instruments, which do not have spectral bands in the NIR and SWIR. An extensive study including the cloud screening over snow and ice has been undertaken by Stamnes et al. (2007), Hori et al. (2007) and Aoki et al. (2007) for the purpose of snow property retrieval. Snow and ice are less reflective in the NIR spectral region, and the so-called normalized differentiation ice index (NDII) and the corresponding snow index (NDSI) are good tools to differentiate clouds from snow and ice. These indices are defined in Eq. 5 and Eq. 6, respectively. The reflectance for ice decreases with the wavelength much faster as compared to snow. Therefore, large values of NDII signify the bare ice case.

$$NDII = \frac{R(0.545\,\mu m) - R(1.05\,\mu m)}{R(0.545\,\mu m) + R(1.05\,\mu m)} \quad \text{Eq. 5}$$

$$NDSI = \frac{R(0.545\,\mu m) - R(1.64\,\mu m)}{R(0.545\,\mu m) + R(1.64\,\mu m)} \quad \text{Eq. 6}$$

Also measurements of trace gas vertical columns (e.g., SCIAMACHY onboard ENVISAT) are disturbed by cloud presence because corresponding instruments have large fields of view to enhance the sensitivity to small gaseous concentrations. Cloud clearing algorithms are described in Cervino et al. (2000) for GOME, and Kokhanovsky (2008) described the use of MERIS to support the cloud screening for SCIAMACHY.

Another cloud detection scheme based on Bayesian methods for deriving a per-pixel probability of cloud-free conditions is proposed by Merchant et al. (2005) and is continually developed by Mackie et al. (2010; 2010). The Bayesian Statistics can be regarded as a general theory for inversion problems and provides a theoretical basis for look-up tables for the observed values. In the approach presented by Mackie et al. (2010; 2010) satellite observations have been compared with simulated clear and cloudy sky radiances using information from both spectral and textural features. The Bayesian Statistics pays attention to the knowledge about the considered object and uncertainties in the measured values. Clear-sky brightness temperatures and reflectances are simulated from numerical weather prediction data using forward radiative transfer models and cloudy radiance look-up tables are defined empirically. Application specific cloud masks can be retrieved through the knowledge of the posteriori probability of clouds by varying the severity of cloud mask. Furthermore the Bayesian methodology can be used with other satellite instruments where forward modelling is used for simulating the observed conditions or corresponding data sets exist.

3.3.2 Categorisation of Cloud Detection Methods

Cloud detection methods used here can be categorized in the following classes:

- Spectral threshold methods: spectral characteristics, such as temperature, brightness, whiteness or height of the scatterer are tested against a threshold value. The threshold can be parameterized by viewing geometry, location or time. Most cloud screening algorithms given in the reference list include such tests.
- Feature extraction and classification: the spectral data space, if transformed into a feature space, can be statically or dynamically (i.e. scene dependent) separated into cloud or clear classes. This group of algorithms also includes spatial structure based algorithms. Examples are given by Gomez-Chova et al. (2007).
- Learning algorithms: the Bayesian probability approach and general data mining techniques are employed. Cloud probability or cloudiness index values are generated after training the algorithm with simulated or measured data. Examples are given in Merchant et al., (2005); Mackie et al. (2010; 2010); Gomez-Chova et al. (2007) for AATSR and in Schiller et al. (2008) for MERIS. A generic approach of a learning algorithm has been developed by Colapicchioni (2004).
- Multitemporal analysis*:* pixels are not always cloud covered and a time series of data is used to separate cloudy from clear cases. For example, such kind of method is applied in the Cyclopes processing (Baret et al., 2007).
- Multi sensor approach*:* in cases, where multiple sensors are on the same platform and perform simultaneous measurements, the synergetic algorithms can be used to better identify clouds. This was considered, for example, in the case of MERIS and SCIAMACHY (Kokhanovsky et al., 2008) and MISR and MODIS (Shi, Clothiaux, Yu, Braverman, & Groff, 2007).

As it follows from the discussion given above, the screening procedures are of great importance for successful retrievals of snow properties from space.

3.3.3 Theoretical description

Current standard MERIS cloud screening uses spectral thresholds on shortwave bands, complemented by spectral slope tests in order to recover bright land surface and snow (Richard Santer et al., 1997). In the third reprocessing of MERIS these cloud and snow tests are significantly changed and improved (Brockmann, Ruescas, & Stelzer, 2011) by adding tests on the height of the scattering surface (based on the oxygen absorption measurements in MERIS band 11), and new tests for snow and ice detection using the MERIS Differential Snow Index (MDSI), based on the ratio of bands 13 (865nm) and 14 (885nm).

A new approach is making use of the knowledge gained during the development of the MERIS 3rd reprocessing cloud screening. The tests are translated into features and integrated into a probabilistic arithmetic approach.

In a first step of the feature based probabilistic arithmetic approach, the sensor measurements are transformed into features ranging from [0…1], where 0 has a very low cloud probability and 1 indicating a high probability respectively. A value of 0.5 is the uncertainty value – no further indication if it is a cloud or not.

Afterwards the standardized features will be combined in a logical order of a sequence of threshold tests. The combination will be done by arithmetic operations, addition and multiplication. This extends the Boolean logic into a probabilistic space. The results range again between [0…1]. If tests result in the extreme 0 and 1, the probabilistic calculations are identical to the Boolean expressions.

3.3.4 Practical considerations

3.3.4.1 *Sensor independent approach*

The feature based probabilistic arithmetic approach enables decoupling the sensor specific measurements from the physically based features and the logical combination. After the feature values have been derived from a sensor measurement, all subsequent calculations do not depend on the sensor anymore. Thus the pixel identification developed here is mainly sensor independent and can be considered as unique for any optical sensor.

The uniqueness consists of a certain set of features, which are calculated for each instrument and probabilistic combination of these features in order to calculate a set of pixel classification attributes. The implementation how the features are calculated is instrument specific (Figure 5).

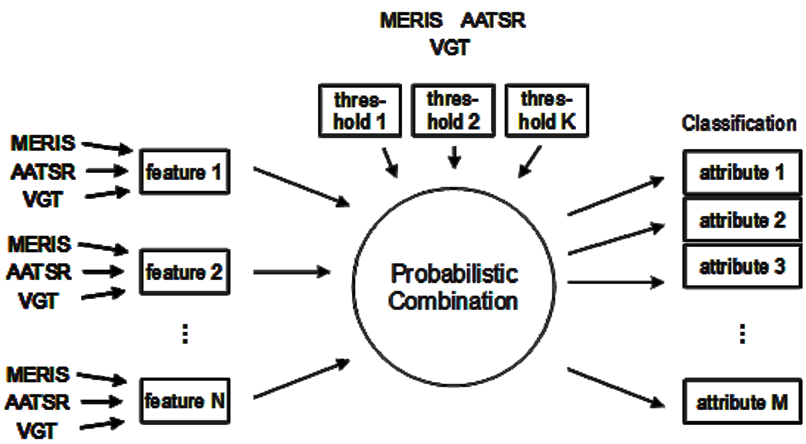

Figure 5: Principle of the sensor independent Pixel identification method

3.3.4.2 *Probabilistic Arithmetic*

A feature is a probabilistic quantity with a value between 0 and 1, with the following meaning (Table 2):

Table 2: Definition of values for classification features

Value	Meaning
0	The feature is definitely FALSE
0.5	The status of the feature is not known
1	The feature is definitely TRUE

Features are combined by simple arithmetic averaging. We can assume, as an example, two features, f1 and f2, which do have no dependency from each other, and both being an indication that a third feature, f3, is true. Then, f3 is the average of f1 and f2. The introduction of the probability scale [0 … 1] has further the advantage that it enables decoupling of feature values from the instruments. It does not matter how a physical quantity is derived because it will be mapped to the interval [0 … 1]. For example, the brightness feature will be calculated from top of atmosphere radiances in the case of MERIS, whereas it will be calculated from reflectances in the case of VGT. These are different physical quantities, but they are both scaled to [0 … 1].

The scaling from a physical quantity, such as radiance or temperature, to a probability value may include a non-linear mapping. This can express the (un-)certainty that we have in value ranges in the physical data space. For example, very low temperatures have a very high probability to be a cloud, whereas above a certain temperature value the probability decreases exponentially.

Not every feature can be calculated for every instrument. In such cases the feature value is constant equal to 0.5. This convention allows formulating the logical combination of features even if a feature is not available for a certain instrument, and hence the logical combination can be formulated instrument independently.

3.3.4.3 Single Image Features

The following table (Table 3) lists the features, which are used in the probabilistic combination, and how they are calculated for each instrument.

Table 3: Feature definition.

Feature	**Explanation**
Pressure	Indicating a high altitude from where the photons are scattered. Can be derived from measurements in gaseous absorption bands, e.g. O2A or water vapour
NDVI	If calculated for a pixel that is potentially a cloud, a high vegetation index is an indication of a (semi-) transparent atmosphere
NDSI	The NDSI is a meaningful quantity only above bright surfaces. Then it can be used to separate snow/ice from clouds
White	A bright and spectrally flat signal; can be a cloud or snow/ice
Spectral Flatness	A spectrally flat signal; The colour can be anything from black over grey to white.
Temperature	Temperature of the emitting surface; clouds can be very cold.
Bright	Brightness of the scattering surface
Glint Risk	The glint risk can be calculated from the observation geometry and wind speed, assuming a certain wave distribution (e.g. Cox and Munk). Glint and clouds are hardly separable and hence it is useful to identify glint risk in addition to the cloud/water classification.
Radiometric Land Value	A classification of the surface type as land, provided that the pixel is clear and the measurement can be used to assess the surface type.
Radiometric Water Value	A classification of the surface type as water, provided that the pixel is clear and the measurement can be used to assess the surface type.
A priori Land Value	Classification of the pixel using a static background map and the geolocation of the pixel.
A priori Water	Classification of the pixel using a static background map and the geolocation of the

Value	pixel.

3.3.4.4 Spectral Features

The following new spectral features have been considered, investigated und applied within the LC-CCI project (Kirches, Krueger, et al., 2012):

- Blue band feature;
- Cloud value feature;
- Clear land feature.

The blue band feature based on the Blue Band Cloud Screening of the GlobCover Project and the entire description may be found in the GlobCover Design Justification File. A simple blue band test has been adopted for MERIS by using the 412 nm channel. The developed cloud screening method is applied to reflectances. A first threshold for band 1 reflectances is used to detect the most brilliant dense clouds. The clear pixels are tested by a filter, which performs the reflectance ratio of band11 and band10 related to the altitude of the scattering surface. An optimised threshold permits identifying thin clouds which are not detected by the first blue band test. Three states are supposed: 0=Out of Orbit, 1=Clear and 2=Cloud. The optimised cloud mask is globally coherent with the bright flag of standard MERIS products. However, a higher performance of the cloud screening over semi-transparent clouds can be observed. Large areas are not detected by the bright flag or probability algorithms. The analysis shows that the blue band algorithm is more able to detect semi transparent clouds.

The cloud value feature is predicted by two neuronal network models or to put it more succinctly, they are back-propagation neuronal networks (NN) with one input and one output layer. The NNs have been trained with a back-propagation learning algorithm by using the PixBox data (see section 3.5.6) whereas the training dataset was splitted w.r.t. the surface properties land and water and these two datasets have been used separately for the training. Therefore we get a so-called LandNN and a WaterNN for the prediction of the cloud value. The PixBox data are described in the LC-CCI PVR (Kirches, Brockmann, et al., 2012). The decision which NN will be used is only depending on the classified surface type through IdePix. Afterwards the cloud value is calculated through the NN by using the MERIS FSG respectively and RRG TOA reflectance spectrum as input. The cloud value has a range from 0 through 2. The user defined thresholds - 1.25 for the LandNN and 1.35 for the WaterNN are used for the verification of the current pixel status as clear land or clear water. If the cloud value is greater than the particular threshold then the pixel status is set to cloud.

3.3.5 Cloud shadow and cloud edge detection

A more comprehensive representation of clouds is provided by two additional pixel properties, ‘cloud edge’ and ‘cloud shadow’ (Kirches, Krueger, et al., 2012). These two properties are also kept in the pixel identification flag and can be considered as a kind of “postprocessing” in the cloud detection. To detect dark cloud shadow pixels - whose spectra are polluted by the shadow - the position of the shadow will be determined by projecting the ‘cloud pixels’ onto the ground using the sun position, the pixel’s altitude on Earth, and the cloud height estimated from cloud top pressure.

Cloud edge pixels are in principle regarded as neighbour pixels of a ‘cloud’ as identified before in the pixel classification. The width of this edge (in number of pixels) can be set by the user. In brief, the algorithm to identify cloud edge pixels works as follows:

- Use a 2x2 square with reference pixel in upper left.
- Move this square row-by-row over the given tile.
- If reference pixel was not cloud, do not do anything.
- If reference pixel is cloudy:
    - if 2x2 square only has cloud pixels, then set cloud buffer of two pixels in both x and y direction of reference pixel;
    - if 2x2 square also has non-cloudy pixels, do the same but with cloud buffer of only 1.

3.3.6 Validation of the cloud screening using PixBox

PixBox is a dedicated software tool that facilitates the efficient collection of reference pixels for the validation of Idepix. Using a large dataset of globally distributed imagery, individual pixels are manually selected as validation sample points and characterized by a visual inspection of its spectral and image content related properties. In order to achieve a balanced distribution of sampled properties (e.g. atmospheric conditions, surface type, climate zone, season, observation angles), adequate numbers of pixels for each class are collected. All identified pixels are then processed using Idepix, and the agreement is quantified in terms of confusion matrices.

A large set of 17k MERIS FR pixels was collected in the scope of the CoastColour project, and detailed validation results are provided in the corresponding report (Ruescas, Brockmann, Stelzer, Tilstone, & Beltran, 2014). We recapitulate two confusion matrices here, for pure land/water/cloud/ice, and for mixed pixels that are affected by semi-transparent clouds or spatially mixed (Table 4). The land cases (in-situ database) are almost completely identified by the Idepix classification (3624 from 3942 = 92%) for pure and also for pure and ambiguous pixel cases. However, a significant portion of the cloudy pixels have been misclassified as land (3008 from 12839 = 23%) for pure and ambiguous pixel case. In contrast the portion the misclassified cloudy pixel is insignificant (201 from 5552 = 4%) for the pure pixel cases. A main conclusion of the two resultant confusion matrixes is that some of the cloud pixels are added to the clear land class, probably semi-transparent clouds. In addition, the more detailed analysis of the result of the Africa region shows that bright surfaces are classified as clouds.

Table 4: Confusion matrix for the Idepix validation using PixBox. The upper table is for pure pixel, the lower for pure and ambiguous pixel cases together (Ruescas et al., 2014).

		Database				Users Accuracy
		CLOUD	LAND	WATER	SNOW/ICE	
IdePix	CLOUD	5343/N_{all}	271/N_{all}	18/N_{all}	589/N_{all}	0.86
	LAND	201N_{all}	3624/N_{all}	8/N_{all}	8/N_{all}	0.94
	WATER	6/N_{all}	46/N_{all}	57/N_{all}	0/N_{all}	0.52
	SNOW/ICE	2/N_{all}	1/N_{all}	24/N_{all}	179/N_{all}	0.87
Producers Accuracy		0.96	0.92	0.53	0.23	Overall Accuracy 0.89 N_{all}=10377

		Database				Users Accuracy
		CLOUD	LAND	WATER	SNOW/ICE	
IdePix	CLOUD	9762/N_{all}	271/N_{all}	18/N_{all}	611/N_{all}	0.92
	LAND	3008N_{all}	3624/N_{all}	8/N_{all}	8/N_{all}	0.55
	WATER	22/N_{all}	46/N_{all}	57/N_{all}	0/N_{all}	0.46
	SNOW/ICE	47/N_{all}	1/N_{all}	24/N_{all}	182/N_{all}	0.72
Producers Accuracy		0.76	0.92	0.53	0.23	Overall Accuracy 0.77 N_{all}=17689

3.4 Land and Water Separation

For the identification of lakes and precise delineation of the shorelines, a good method is needed to separate between land and water surfaces. The current separation in standard MERIS products uses a static background map that holds the information of land or water for each pixel position. Especially for lakes with scale structures in the shoreline and small islands inside of lakes, the accuracy of this background information is not sufficient. In addition, the extent of a lake is not always static and due to water level changes, the shoreline of a lake can change over time. The information about these changes is an important element to be covered within DIVERSITY. Therefore, a good static map and a subsequent radiometric test are necessary for our applications.

Idepix identifies several problematic pixel classes that prevent appropriate characterization of the water composition. It uses the SRTM Water Body data sets (SWBD) as a basis map (see Diversity II TS for a data description), but combines these preliminary outlines with a mixed pixel test. Especially in medium resolution satellite data, the pixels are often a mixture of different surface types. Thus, along coastlines or the shoreline of a lake, the single pixels cover land as well as water areas. The land portion within a pixel is influencing the spectral signal significantly and thus the water retrieval will fail. Floating algal blooms, caused by e.g. cyanobacteria blooms, will also be recognized as mixed pixels. This floating vegetation is also influencing the signal measured at the satellite sensor and therefore has to be recognised in the images.

When speaking about a mixed pixel, this is referring to the mixed spectrum, which is the sum of the pure spectra of each component within the Pixel, weighted by the spatial proportion of each material. When scattered photons interact with multiple components, the mixture has the potential of becoming nonlinear. This happens more often over land with low-resolution sensors.

So far, these mixed pixels are classified as land, water or cloud -within one unique category - when they can really contain a portion of each. There is a need of a better screening of pixels in sub-pixel level and identification and flagging as mixed pixel. For doing this, it is assumed a linear relationship within the different components of the spectrum's pixel, and an analysis based on their mixture is done by means of a spectral mixture analysis (SMA). The SMA technique is a spectral unmixing approach that assumes that pixel values are linear combinations of reflectance from a limited set of constituent's elements or end members (Adams, J.B., Smith, M.O., & Gillespie, A.R., 1989). The essential assumptions for SMA are that landscapes are composed of a limited number of fundamental components, and that the remotely sensed signal of a pixel is linearly related to fractions of the end member used. In the SMA, the spectral properties of a pixel are modelled as a linear combination of end member spectra weighted by the percent ground coverage of each end member according to Eq. 7, and the parameters described in Table 5.

$$P_{i\lambda} = \sum_{k=1}^{N} f_{ki} * P_{k\lambda} + \varepsilon_{i\lambda} \qquad \text{Eq. 7}$$

Table 5: Idepix spectral mixture analysis parameters.

Parameter	Description	Usage	Physical Unit
$P_{i\lambda}$	Measured mixed spectrum from pixel *i*	input	none
N	Number of endmembers	input	none
$P_{k\lambda}$	*k*-th endmember spectrum	input	none
$\varepsilon_{i\lambda}$	Residual term in pixel *i*	output	none
f_{ki}	Fraction of endmember *k* in pixel *i*	output	none

Retrieving the best fit with the measured mixed spectrum in Eq. 7 provides for the fraction of endmembers. The model fit is assessed by either an error in the fraction (negative fractions or fractions exceeding 100%), the residual term at each wavelength or as a root mean square error across all bands. The inversion can be done by least squares estimation, single value decomposition or Gram-Schmidt orthogonalization. A flowchart of the Idepix algorithm is provided in Figure 6. Further documentation is available from Aquamar and CoastColour project documentation by Brockmann Consult.

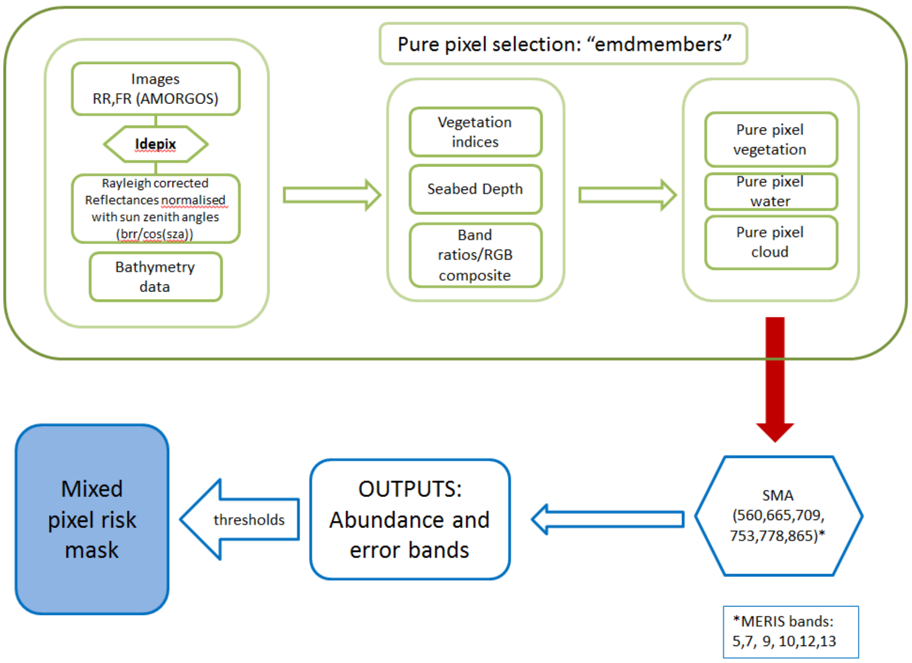

Figure 6: Processing chain for mixed pixel estimation: the pure pixel selection was made only once, and spectra of each pixel used as inputs in the SMA for all images

MERIS FR and corresponding RR images are used to validate the Idepix processor. Each RR pixel is a mixture of 16 FR pixels. The FR land-water mask is thus a reference for the retrieval of pixel mixtures from the MERIS RR image.

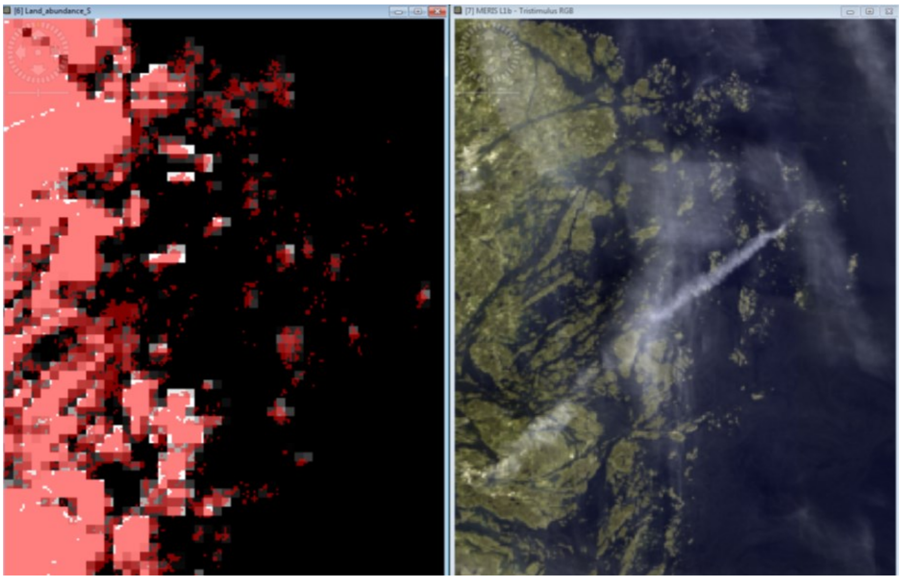

Figure 7: Full resolution land abundance map (in red) overlaid onto a reduced resolution land abundance image of the same area (left); RGB composition (right).

3.5 Identification of optically shallow Water

3.5.1 Bottom reflected Radiance

Water bodies in which a significant portion of the water leaving radiance ($L_w(\lambda)$ is reflected by the bottom substrate are referred to as *optically shallow*. Water quality retrieval in optically shallow waters is complicated by a number of additional parameters that affect the remotely sensed signal, namely:

- Bottom depth, including tidal effects
- Bottom albedo (i.e. substrate types)
- Water column transparency and its vertical variability
- Illumination conditions
- Air-water interface effects including whitecaps and sun glint

Most research on remote sensing of optically shallow waters is focused on clear, oligotrophic marine coastal waters with a euphotic depth of up to 30 m, including tropical lagoons and coral reefs. Preferred instruments are ground, airborne or high-resolution spaceborne sensors, which provide signals that allow for the retrieval of water column and bottom optical properties in such waters (Maritorena, Morel, & Gentili, 1994). In these cases, the effect of the water column through which sunlight must pass twice is significant. The differential attenuation increase with wavelength from blue to green causes the signature of a seabed type to vary with depth, as depicted in Figure 8. A large number of scientific approaches to treat the signal contributions from bottom reflectance is discussed in version 1 of this ATBD, including forward models by Lyzenga (1981; 1978), Maritorena et al. (1994), and Lee et al. (1998, 1999), bathymetry estimation by Bierwirth et al. (1993) and Dierssen et al. (2003), the correction of benthic reflectance for water constituent retrieval (Cannizzaro & Carder, 2006; Giardino et al., 2012), or the classification of seabed habitats (Kenny et al., 2003; Louchard et al., 2003).

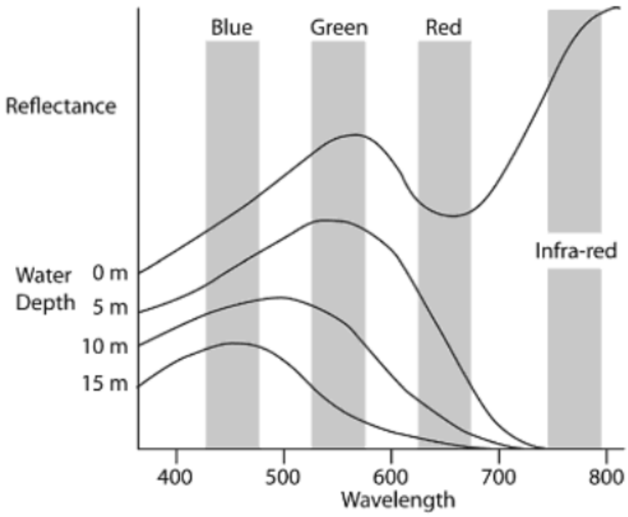

Figure 8: Variations of bottom reflectance when viewed through different depths of seawater. The grey bars show typical wavebands of HR multispectral imagers (from Robinson, 2010, after Mumby and Edwards, 2000).

In turbid water, where scattering is relatively high across the whole spectrum, the attenuation coefficients are large and few photons can penetrate more than 1m (Robinson, 2004), making bottom reflectance negligible. However, depending on the vertical stratification, turbid water layers can mimic the water-leaving reflectance of shallow waters, introducing considerable ambiguity in the separation of optically deep and shallow waters. As a matter of fact, the requirements in the scope of Diversity II, to identify optically shallow pixels of a medium resolution sensor, without a priori information of water optical properties or bathymetry, for all lake water types and without manual intervention, go beyond all currently known approaches.

3.5.2 Shallow Water Identification Algorithm Development

The objective within Diversity II is to identify and flag pixels for which bottom reflection significantly affects the retrieval of water quality parameters. A new approach was developed, which is remotely based on the band arithmetic bottom reflectance indicator suggested by Cannizzaro and Carder (2006). Their study however differs significantly from our requirements. First, they applied their algorithm only to in situ reflectance measurements, and most of the MERIS atmospheric corrections under consideration for Diversity II are not applicable to shallow waters. Second, a significantly larger variability of water optical properties is expected for the 300 Diversity II lakes, than represented by their experimental data.

In consequence, we evaluate similar spectral band ratios as in Cannizzaro and Carder (2006), but for use with TOA radiances and bottom-of-Rayleigh reflectances (BRR, see Diversity II TS). Figure 9 shows exemplary the bottom signal effect in TOA radiances, enhancing especially the signal in MERIS band 5, while enhancement at shorter and longer wavelengths is almost absent. In contrast, the signal enhancement by turbid water affects more or less the whole spectrum.

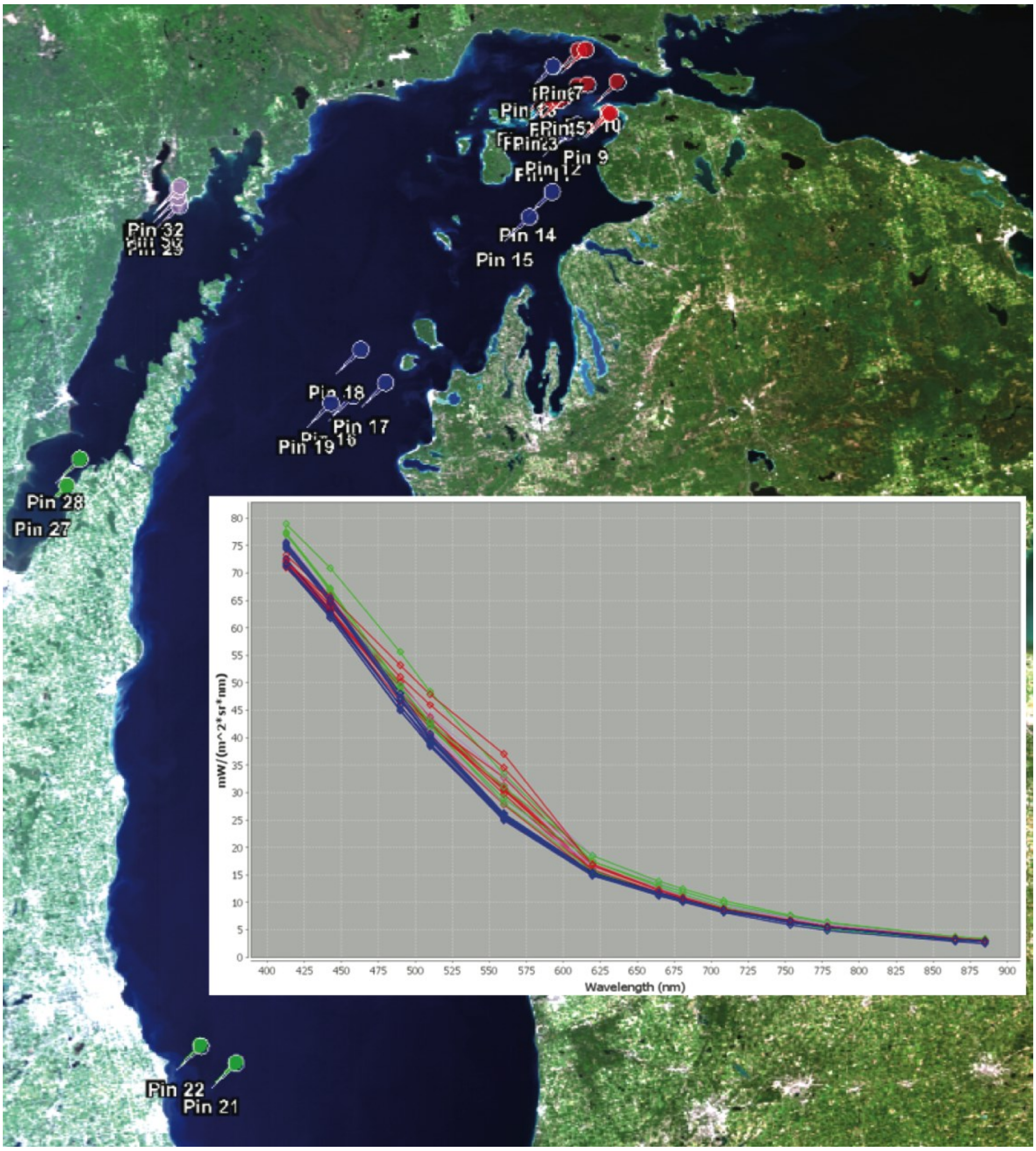

Figure 9: Example pixel location and spectra, for optically shallow water (red), optically deep and clear water (blue), optically deep and turbid water (green) and an unknown water type (pink).

The expressions in Eq. 8 and Eq. 9 are evaluated with MERIS imagery, using radiance and BRR data as input. When applied to individual images, the image-to-image variability of the indicators does not allow setting a fix threshold. A considerable ambiguity with turbid estuaries occurs, as expected especially for stratified waters. The temporal persistence of shallow water specific signals can help to prevent such cases. Consequently, Eq. 8 and Eq. 9 are applied in temporal aggregation expressions for several months of available MERIS data (e.g. the Mai-October for seasonally freezing high latitude lakes). Minima, 10-percentiles and averages are compared for both expressions using BRR and radiance, resulting in a total of 16 static indicator maps.

$$IF \quad ratio\_413 = \frac{L_{s,band1} \cdot L_{s,band7}}{(L_{s,band5})^2} < Thres, \; shallow = TRUE \qquad \text{Eq. 8}$$

$$IF \quad ratio\_490 = \frac{L_{s,band3} \cdot L_{s,band7}}{(L_{s,band5})^2} < Thres, \; shallow = TRUE \qquad \text{Eq. 9}$$

These simplistic approaches to identify areas with permanently elevated signals in band 5 correspond well to a more extensively derived MODIS shallow water map created for Lake Michigan (see Figure 10). Among the 8 perennial prototype lakes (Balaton, Michigan, Nicaragua, Peijanne, Peipsi, Tahoe, Vanern, Victoria), significant shallow areas in the 300 m resolution data are expected only for the clearest ones, i.e. Michigan and Tahoe. Mean aggregates of Eq. 9 (ratio_490) are identified as the most coherent indicators in this scope, based on the qualitative assessment of the indicator's spatial distribution, histograms and comparisons with bathymetry data.

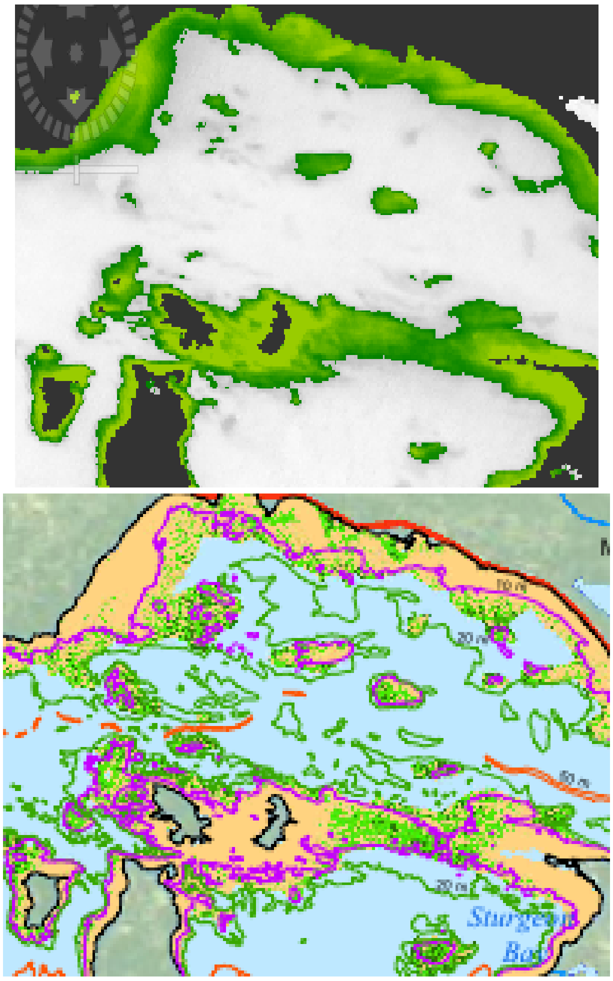

Figure 10: A comparison of an L3 optically shallow water indicator and a reference map, for the Northern basin of Lake Michigan. Left: May-October 2008 L3 mean aggregate of ratio_413. Right: MODIS shallow water classification by Shuchman et al. (http://www.mtri.org/cladophora.html); Light brown is sandy benthos, green is submerged vegetation.

Taking into account the complete lack of shallow water identification methods for inland or turbid coastal waters, setting the thresholds of the ad hoc shallow water identification described here is subject to significant trade-offs. They are chosen such that relatively small, near-shore areas are identified, while the false identification in permanently turbid estuary areas (e.g. the Detroit river estuary in Lake Erie, or the Rhone estuary in Lake Geneva are minimized. In this regard, a threshold of ratio_490 < 0.65 is found to extract reasonable shallow water extents along the shorelines in Lakes Michigan and Tahoe, while masking only very few pixels along the shoreline for other lakes with smaller shallow areas. However, an exception occurs in the most turbid prototype lake, Balaton, where many false-positive shallow pixels are identified, and a reduced threshold of ratio_490 < 0.5 is required. The ratio_490 indicator thresholds for all 350 Diversity II lakes are documented in the lake list appended to the Diversity II Technical Specifications document.

3.5.3 Assessment and validation of the shallow water indicator

The visual assessment of the temporally aggregated ratio_490 revealed that the vast majority of the 350 lakes considered in Diversity II falls into three categories:

- **Ratio_490 > 0.7 for the entire lake area**. This is the largest category making up for roughly half of all assessed cases, and consists among others of lakes located at high latitudes, where particle concentrations are too low to cause a sufficiently high peak in L_s at 550 nm, or CDOM absorption is so high that it effectively masks it. Examples for this case are shown in Figure 11 and Figure 12.
- **Ratio_490 < 0.6 for most of the lake area.** This second category includes about 30 % of all cases, including a lot of knowingly sediment-rich lakes and reservoirs, where consistently high turbidity causes high peaks at 550 nm. Examples for this case are shown in Figure 12.
- **Intermediate ratio_490 gradients.** This final category includes about 20% of all cases. These are the cases where an extended assessment was carried out in order to verify the indicated shallow water areas, shown for the examples in Figure 13 to Figure 15.

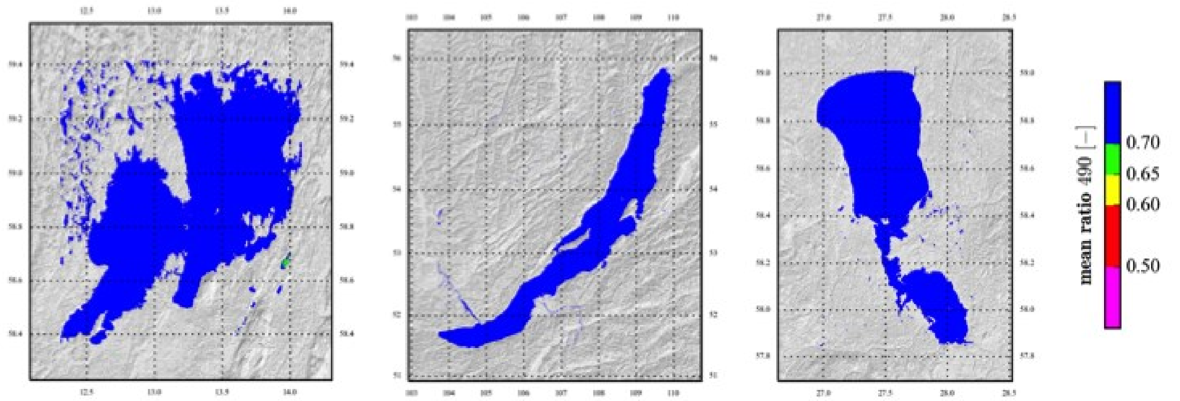

Figure 11: Example lakes where the ratio_490 approach does not indicate any shallow water areas. From left to right: Lake Vanern (Sweden), Lake Baikal (Russia), Lake Peipus (Estonia/Russia).

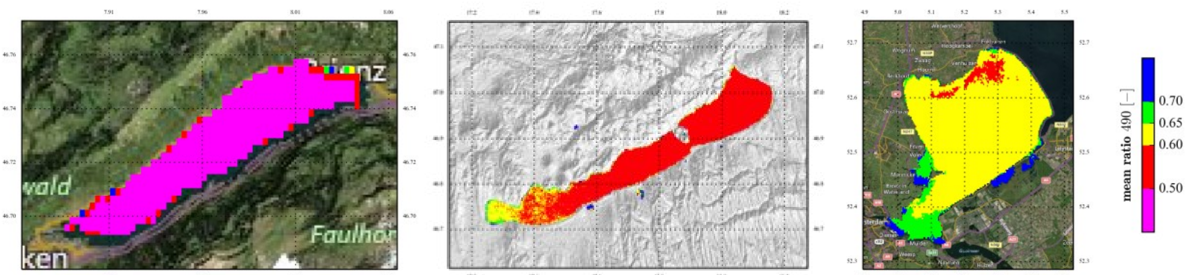

Figure 12 Example lakes where ratio_490 is lowered by constantly high turbidity. From left to right: Lake Brienz (Switzerland), Lake Balaton (Hungary), Markermeer (The Netherlands).

Category 1 was processed with the default threshold of 0.65 without further evaluation, because these lakes do not exhibit the spectral feature that was identified to indicate shallow water areas. Accordingly, it is not possible to quantify the likeliness of type II errors (false negatives). Category 2 comprises of type I errors (false positives) that are relatively easy to identify, because ratio_490 does not follow the expected gradient of shallowness, from littoral to pelagic areas within the lake. The high turbidity that is typical for the lakes of Category 2 make bottom reflectance generally unlikely, even more so in MERIS' 300 m pixels. Furthermore, the degree of ambiguity between backscattering from suspended sediments and sandy substrates is very high, making a separation impossible with the available approach. Consequently, category 2 was processed with reduced thresholds that prevented the masking of significant areas of the lake, reducing the number of type I errors to almost zero.

For the lakes in category 3, verification of the indicator was done on a case-by-case basis with high-resolution RGB satellite images (Google Maps, other sources) and bathymetry maps as reference. High-resolution RGB satellite images were highly useful to identify spatial patterns of benthic vegetation, sand banks, eroded channels and even aqua farms. Bathymetry maps were not found for all lakes, and had often a relatively low depth resolution, but were often useful as a reference for the shoreline slope in identified areas. Examples for successfully identified shallow waters are given in Figure 13 to Figure 15. The default threshold of 0.65 worked reliably in the depicted examples, but was adjusted occasionally when the reference data did not provide evidence for the presence of shallow waters. In this way, the risk to commit type I errors was minimized also for this category.

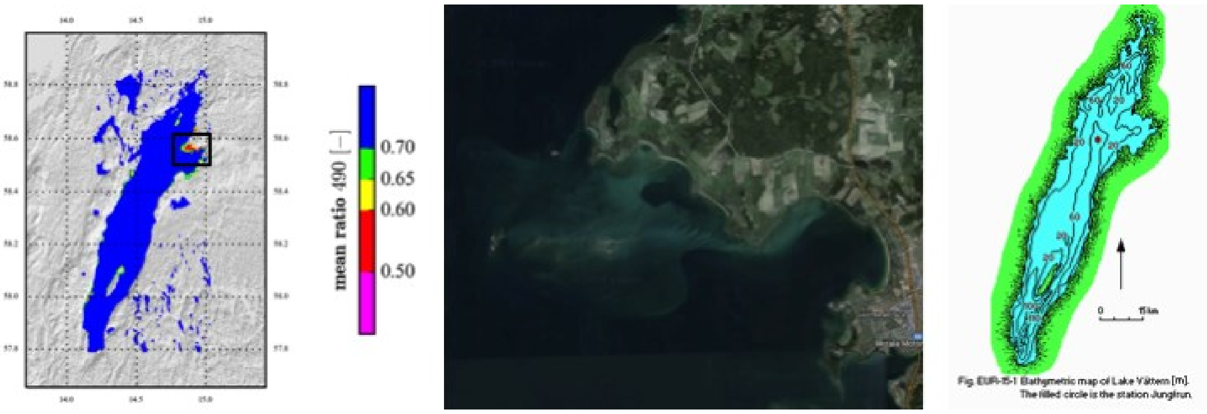

Figure 13: Ratio_490 shallow water indicator (left), screenshot from Google Maps (centre) and bathymetry map from www.wldb.ilec.or.jp in 20 m intervals (right) for Lake Vattern, Sweden.

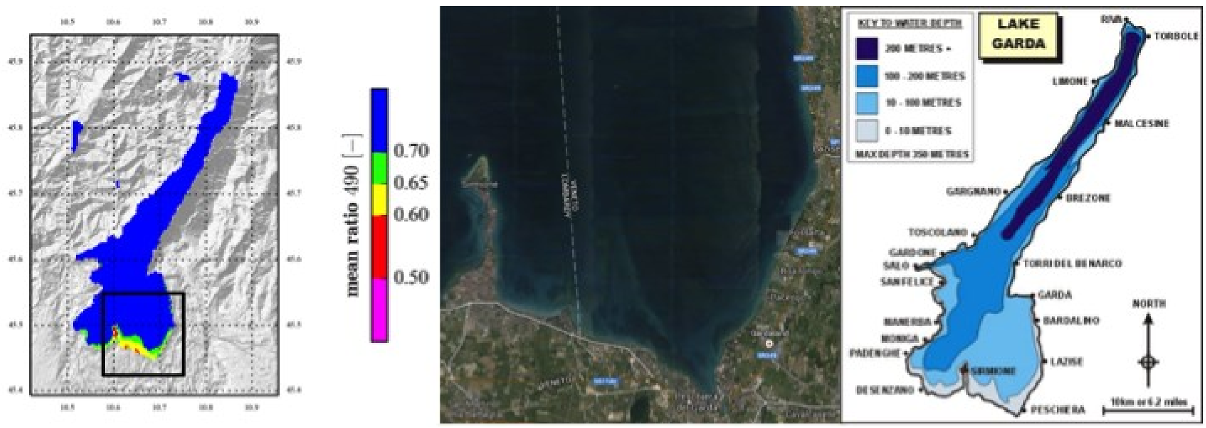

Figure 14: Ratio_490 shallow water indicator (left), screenshot from Google Maps (centre) and bathymetry map from www.lake-garda-revealed.com in 10+ m intervals (right) for Lake Garda, Italy.

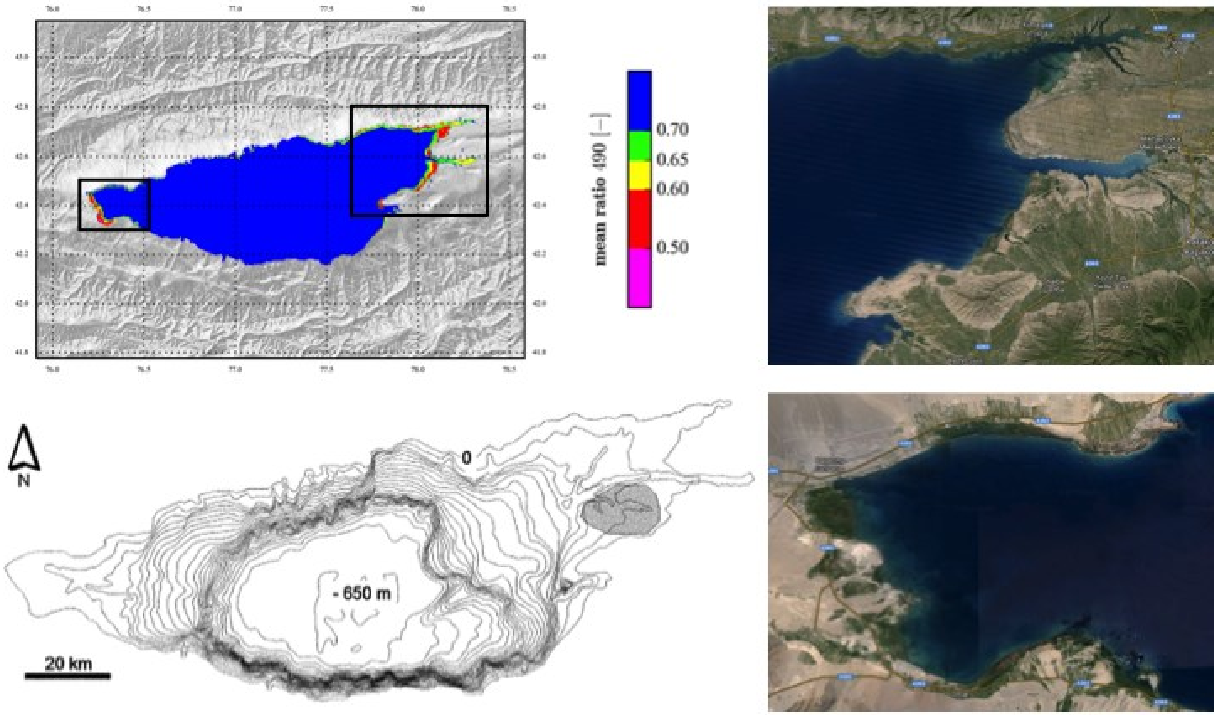

Figure 15: Ratio_490 shallow water indicator (top left), screenshot from Google Maps (right) and bathymetry map from www.jsedres.sepmonline.org for Lake Issykkul, Kazakhstan.

In summary, the application of the ratio_490 application enabled for the identification for about 40 cases of verified shallow water areas in relatively clear lakes, at a minimal risk of false positives. Given that such shallow water mapping was done for the first time, the resulting masks are a valuable output of the project that could among other uses serve as training data for further development of corresponding algorithms. Accordingly, the shallow water mask is included in all Diversity II products. The assessment however also revealed that the indicator does not work in turbid waters, where false positives were removed manually.

3.6 Atmospheric Correction

Optical satellite measurements are subject to atmospheric scattering and absorption. Most methods to retrieve geophysical parameters from such measurements require a correction for these atmospheric effects, i.e. to derive surface directional reflectances (SDR), also called bottom of atmosphere (BOA) reflectance, from top of atmosphere (TOA), at-sensor radiances. A variety of methods exist to do this correction, corresponding to different requirements for different ground targets and atmospheric conditions. An overview of the basic theory and relevant methods for Diversity II is given, introducing specific approaches for land and inland water targets, and the adaptation of the former approaches for the latter kind of targets. Validation analyses performed with different candidate algorithms are summarized thereafter.

3.6.1 Theoretical Background

The atmospheric correction is of critical importance since the effects of the temporally and spatially variable atmosphere can significantly affect the efficiency of any subsequent algorithm which aims at the determination of land or water surface characteristics (e.g. Synergy-Aerosol and land surface ATBD, 2009, or Antoine and Morel 1999). The atmospheric correction is normally performed in two stages. Firstly, the atmospheric properties are determined at the time of satellite overpass. In the second step, the transfer of radiation in the atmosphere is inverted to estimate the surface reflectance, accounting for the absorbing and scattering effects of atmospheric gases, in particular ozone, oxygen and water vapour, of the scattering of air molecules (Rayleigh scattering) and for the correction of absorption and scattering due to aerosol particles. Various techniques exist to perform this inversion, e.g. by simplification to single scattering and analytical solution, or by approximating the multiple scattering case with polynomials (Steinmetz, Deschamps, & Ramon, 2011) or neural networks. Very often pre-calculated look-up tables (LUT) (Grey, North, & Los, 2006; Rahman & Dedieu, 1994) are used. Of these two stages, the estimation of atmospheric properties is the most challenging and greater source of error (Vermote & Kotchenova, 2008). All components except aerosols can be rather easily corrected. Ozone can be taken from other satellites, available from met services, and oxygen and water vapour can be taken from MERIS measurements thanks to dedicated spectral bands. However, aerosols are spatially and temporally highly variable and do not have a distinct spectral absorption features. MERIS has been designed to provide measurements that allow the determination of aerosols, however, this is difficult and still subject to ongoing research and algorithm development. The aerosol correction typically consists of two parts: the calculation of these aerosol properties and secondly the actual correction of the reflectance (after Rayleigh and gas absorption correction). This can be a sequential process where the reflectance correction takes an aerosol optical depth and its spectral dependency as input, or a one-step approach where aerosol properties and reflectance corrections are one implicit step.

Currently, atmospheric radiative transfer (RT) codes allow retrieval of surface reflectance with a high degree of precision for a known atmospheric profile, with theoretical error typically <0.01 in surface reflectance (Juergen Fischer & Grassl, 1984; Kotchenova, Vermote, Matarrese, & Klemm, 2006). This enables both forward simulation of satellite radiances, and inversion of such models to estimate surface reflectance given a set of top-of atmosphere (TOA) radiances. Over land, the key problem in correction of surface reflectance for aerosol effects lies in simultaneous estimation of aerosol at the time of acquisition.

3.6.1.1 Definitions

The apparent spectral directional reflectance R* λ in the waveband λ of the coupled surface-atmosphere system is related to the radiance L_λ measured by a satellite at the TOA by:

$$R_\lambda^* = \frac{\pi\, L_\lambda(\Omega_s,\Omega_v)}{\mu_s\, E_{s,\lambda}} \qquad \text{Eq. 10}$$

Where $E_{s,\lambda}$ is the extraterrestrial irradiance at the time of the measurement. The view and solar vectors are denoted by Ω_s and Ω_v respectively, while μ_s and μ_v denotes cosines of solar and view zenith.

Over land, often a uniform, Lambertian surface is assumed as a basis for the modelling of the atmosphere-surface radiative transfer for operational atmospheric correction algorithms of single-view instruments. Under that assumption, the relationship between top of atmosphere reflectance R* and the surface directional reflectance R_λ can be approximated by Eq. 11:

$$R_\lambda^* = R_{atm,\lambda}(\Omega_v,\Omega_s) - \gamma_\lambda(-\mu_s)\,\gamma_\lambda(\mu_v)\frac{R_\lambda}{1-\overline{\rho_\lambda}\,R_\lambda} \qquad \text{Eq. 11}$$

Where R_{atm} means the atmospheric scattering term (TOA reflectance for zero surface reflectance), γ_λ denotes atmospheric transmission for either sensor to ground or ground to sensor for waveband λ, and s denotes atmospheric bi-hemispherical albedo with respect to the surface. The view and solar vectors are denoted by Ω_s and Ω_v respectively, while μ_s and μ_v denotes cosines of solar and view zenith. Spectral directional reflectance R is derived from TOA reflectance by means of the analytical inversion

$$R_\lambda^* = R_{atm,\lambda}(\Omega_v,\Omega_s) - \gamma_\lambda(-\mu_s)\,\gamma_\lambda(\mu_v)\frac{R_\lambda}{1-\overline{\rho_\lambda}\,R_\lambda} \qquad \text{Eq. 11}$$

and the corresponding equation is:

$$R_\lambda(\Omega_v,\Omega_s) = \frac{R^*_\lambda(\Omega_v,\Omega_s) - R_{atm,\lambda}(\Omega_v,\Omega_s)}{\gamma_\lambda(-\mu_s)\,\gamma_\lambda(\mu_v) + \overline{\rho_\lambda}\,[R^*_\lambda(\Omega_v,\Omega_s) - R_{atm,\lambda}(\Omega_v,\Omega_s)]} \qquad \text{Eq. 12}$$

As discussed in GlobAlbedo ATBD, 2010, the Lambertian equivalent reflectance R_λ, which is taken as SDR in the GlobAlbedo processing chain, represents a smoothed version of the surface BRDF, with errors up to 15% for turbid atmospheres (Hu, Lucht, & Strahler, 1999).

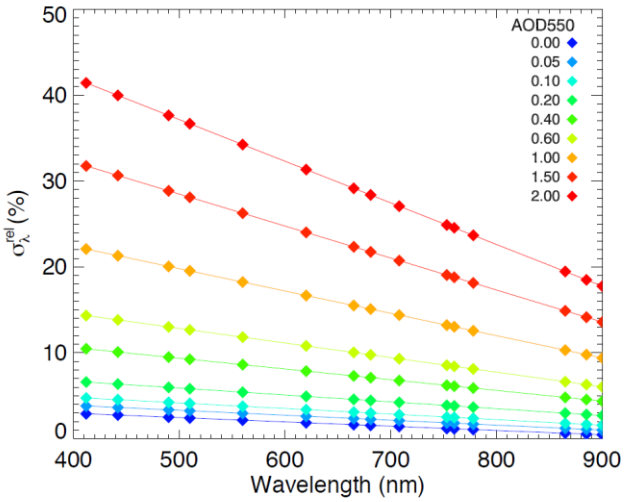

Figure 16: Estimation of the relative error in reflectance retrieval caused by the assumption of a Lambertian surface (Rahman & Dedieu, 1994) after resampling to the GlobAlbedo AOD550 grid and the spectral response (Lopez et al., 2013).

3.6.1.2 Aerosol retrieval approaches

The parameters required to model aerosol radiative effects are aerosol optical depth (AOD) for a given reference wavelength, its spectral dependence, which may be defined by the Angstrom coefficient, single scattering albedo, and phase function. These properties are closely related to aerosol amount, composition and size distribution. Aerosol retrieval methods can be categorized in the following classes:

- single-view methods
- multi-temporal methods
- multiple view-angle (MVA) methods

Single-view methods: These algorithms are based on different assumptions, depending on available spectral sampling. MERIS is an imager providing mainly spectral information in 13 different channels (2 of its 15 bands are dedicated to measure oxygen and water vapour absorption) measured from a single viewing geometry. Thus the retrievals have to explore the wavelength dependence in order to provide information on the aerosol. The separation of the surface contribution is always based on a priori knowledge about the spectral properties of the surface. This is rather easy in the case of open ocean water, but challenging for turbid coastal water and land surfaces. A number of approaches have proven successful:

- Identification of dark targets: Where it is possible to identify targets of dark dense vegetation (land) or clear water, with known spectral properties, this may be used to derive aerosol path radiance over these targets (Kaufman & Sendra, 1988). Operational algorithms have been developed for MERIS (Richard Santer, Carrère, Bubuisson, & Roger, 1999; R. Santer, Ramon, Vidot, & Dilligeard, 2007) on this basis, but the areas where the surface is dark enough are sparse and spatial-temporal interpolation is necessary. Also, these derived aerosols optical properties are connected with a substantial error.
- Spectral mixing: This method is used to retrieve aerosol optical properties over land. The algorithm described by Guanter et al. (2007) uses mainly the assumption that aerosol is spatially more

homogeneous than surface reflectance. Therefore the algorithm searches locally for pixels with the most and the least dense vegetation cover (darkest and brightest pixels) and assumes the atmospheric information to be constant. This allows the determination of the aerosol content. Once the aerosol properties over land are known, they can be interpolated to provide the necessary parameterization of atmospheric correction over water (see section 3.6.2.2).

- Coupled aerosol retrieval: Coupled inversion algorithms allow for the simultaneous retrieval of aerosol optical parameters and background reflectance. Such methods are computationally more expensive, since the number of unknown parameters in the inversion is significantly increased. However, dark but optically complex water bodies make this expensive strategy necessary due to the low ratio of water-leaving to TOA radiance. C2R-type neural networks perform an explicit atmospheric correction step where a reduced set of background reflectances is applied to retrieve aerosol optical properties (Doerffer & Schiller, 2007). In contrast, the FUB neural network algorithm (Schroeder, Behnert, Schaale, Fischer, & Doerffer, 2007a) achieves a coupling by training water constituent concentrations directly for corresponding TOA radiances, performing no explicit atmospheric correction. More recent approaches of this kind (Brajard, Santer, Crépon, & Thiria, 2012; Steinmetz et al., 2011) have not yet been evaluated for Diversity II, but potential stands for further improvement, especially if the troublesome sun glint effect is adequately accounted for.

Multi-temporal methods: Related to single view retrieval methods are those which allow retrieval from time series, assuming greater stability of land surface reflectance compared to aerosol (Lyapustin & Wang, 2009) The time series allows use of recent reflectance retrievals as a prior in inversion, but such techniques are particularly relevant where high temporal sampling is available, such as from geostationary instruments

Multiple view-angle (MVA) methods: While spectral methods may produce very good results in regions where the assumptions are fulfilled, global aerosol retrievals show a number of uncertainties due to the large variability in spectral surface properties. The principal advantage of an MVA approach is that no a priori information of the surface spectrum is required and aerosol properties can be retrieved over all surface types, including bright deserts. Limitations of the angular approach are that the algorithms require accurate co-registration of the images acquired from multiple view angles.

3.6.1.3 Adjacency effects

We refer to adjacency effects as signal contributions from surfaces adjacent to a pixel's instantaneous field-of-view, which enter the field of view as a consequence of atmospheric path scattering. The effect is spectrally dependent and occurs along the border of strongly contrasting surfaces, e.g. near-zero NIR reflectance of clear or absorbing water, and high NIR reflectance of dense vegetation. It mainly depends on atmospheric turbidity and the observation and illumination geometry. An assessment of adjacency effects over surface waters was carried out by Santer and Schmechtig (2000), and several methods to correct for them have been developed (Bulgarelli, Kiselev, & Zibordi, 2014; Richard Santer & Zagolski, 2009; Sterckx, Knaeps, Kratzer, & Ruddick, 2014). It was described by Odermatt et al. (2008) that the publicly available ICOL adjacency correction module (Richard Santer & Zagolski, 2009) facilitates effective removal of adjacency related spatial radiance gradients over lakes of low reflectance (Figure 17). However, the consistent improvement in terms of radiative accuracy does not consistently propagate to the accuracy of retrieved water constituents (Daniel Odermatt, Giardino, & Heege, 2010), and validation for other lake and environment types are lacking. Therefore, further evaluation of the ICOL algorithm is necessary.

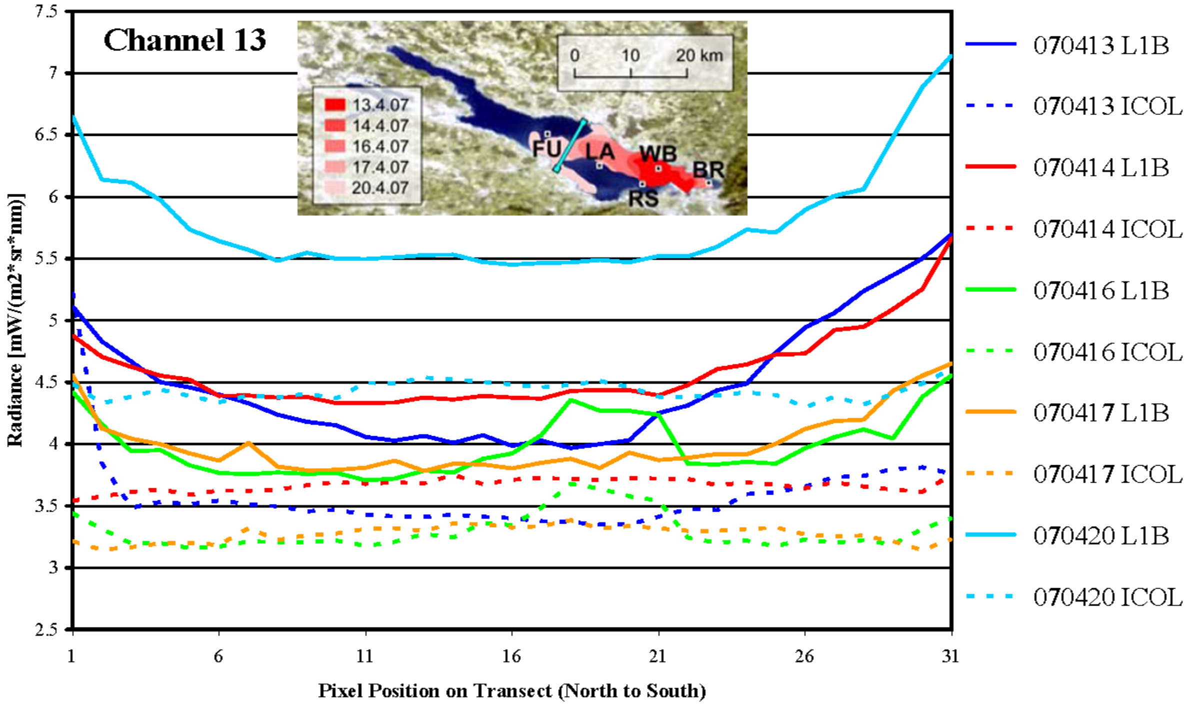

Figure 17: MERIS band 13 (865 nm) radiance transects across Lake Constance, on 5 dates with variable atmospheric density. The solid, uncorrected transects reveal a significant increase in radiance towards the shoreline, while the dashed, ICOL corrected spectra correspond better to the homogenous water properties outside the emerging plume in red (from D Odermatt et al., 2008).

3.6.2 Candidate algorithms for atmospheric correction over water

3.6.2.1 Bottom-of-Rayleigh processor

In a very simplistic model the atmosphere consists of three distinct layers: a top layer composed of the absorbing gases (ozone, oxygen), a middle layer composed of air molecules (Rayleigh scattering) and a bottom layer where all aerosols are included. The geometric depth of the Rayleigh layer extends to the ground, i.e. the aerosol layer is geometrically infinite small, or all aerosols are on the ground.

The concentrations of the gases are known from external sources (i.e. it is included in the MERIS tie-points from ECMWF forecast or re-analysis) or, in case of oxygen and water vapour, can be derived from dedicated MERIS spectral bands. The transmission can then easily be calculated and the radiance at the bottom of the gas layer can be calculated by diving by the gaseous transmission.

The optical effect of the second layer, the air molecules, can be calculated from Rayleigh's theory. The Rayleigh scattering depends on the angles of the incoming light (= sun zenith and azimuth) and the scattering direction (= sensor zenith and azimuth). The Rayleigh phase function is analytically described. The intensity of the scattered light then depends on the air mass, which is a function of the surface air pressure and the geometric length of the line of sight. I.e. all components of the scattering within the Rayleigh layer can be computed from geometry and air pressure, which is known from external sources (in the case of MERIS it is contained in the tie-point data within the Level 1 product).

The Rayleigh scattering is quantitatively the largest contribution in the atmosphere in the blue and green wavelengths. If only gaseous absorption and Rayleigh scattering are corrected (but not the aerosol) a rough estimate of the surface reflectance is already obtained. This approximation of the surface reflectance was found useful in highly turbid waters, where aerosol retrieval is very challenging due to the high backscattering even in the red and NIR parts of the spectrum (Mark William Matthews, Bernard, & Robertson, 2012). In contrast, water-leaving signals in low turbidity waters are often smaller than aerosol scattering, making the BRR processor an insufficient approach for such targets.

3.6.2.2 SCAPE-M

The Self-Contained Atmospheric Parameters Estimation for MERIS data (SCAPE-M) algorithm (Guanter et al., 2008) has been designed for SDR retrieval from MERIS TOA data over land and inland waters and has been successfully validated against ground-based measurements and other processing approaches. The algorithm intercomparison performed within Diversity II has revealed that it is a good choice for highly scattering inland waters, yet suffers certain operationalization limitations.

SCAPE-M applies a sequential approach to retrieve aerosol loading and water reflectance (L. Guanter et al., 2007; Luis Guanter, Gómez-Chova, & Moreno, 2008). It performs automatic cloud screening, aerosol and water vapour retrieval according to Figure 18, making use of LUTs compiled with the MODTRAN radiative transfer model. The atmospheric optical properties retrieved over land are thereby spatially interpolated from small to medium lakes, avoiding several potential error sources of AOT retrieval over water, e.g. assumptions of background reflectance or corresponding iterations of a bio-optical model, and adjacency effects. It is on the other hand vulnerable to spatially heterogeneous atmospheric conditions, and only applicable to lakes of a limited size.

Aerosol optical thickness and water vapour are retrieved for 30x30 km tiles. Within each tile, dark pixels (including inland waters) are used as a maximum threshold for AOT at 550 nm to prevent negative reflectances. The sensor radiance of 5 land pixels within the tiles is inverted to estimate AOT at 550 nm using the MODTRAN based LUTs. Surface reflectance is assumed to be a linear mixture of vegetation and soil. The abundance of these two endmembers and AOT at 550 nm are retrieved concurrently, using a simple rural aerosol model. In order to finalize the correction, AOT estimates are spatially interpolated to tiles where the retrieval was unsuccessful, and a resulting continuous AOT (550 nm) map is smoothed by means of cubic convolution.

Because aerosols can spatially quite variable, the interpolation of AOT should be limited in space. Guanter et al. (2010) set the limit to lakes of less than 1600 km^2 area, and inland water pixels within 20 km of the shore. Technically we have removed this constraint within the SCAPE-M processor in order to be able to process every pixel. The error or uncertainty associated with the atmospheric correction should be increased with increasing extrapolation distance.

With the continuous AOT map obtained in this way, a cloud mask, digital elevation model (DEM), observation angles and columnar water vapour, a pixel by pixel correction for Lambertian ground reflectance is performed, including inland waters (Luis Guanter et al., 2010). The strengths and weaknesses of this approach have been demonstrated in a comparison with in situ measured and C2R retrieved reflectances where the retrieval of red-NIR reflectance by eutrophic waters works significantly better than with C2R, while the latter works more accurately for oligotrophic waters (Figure 18).

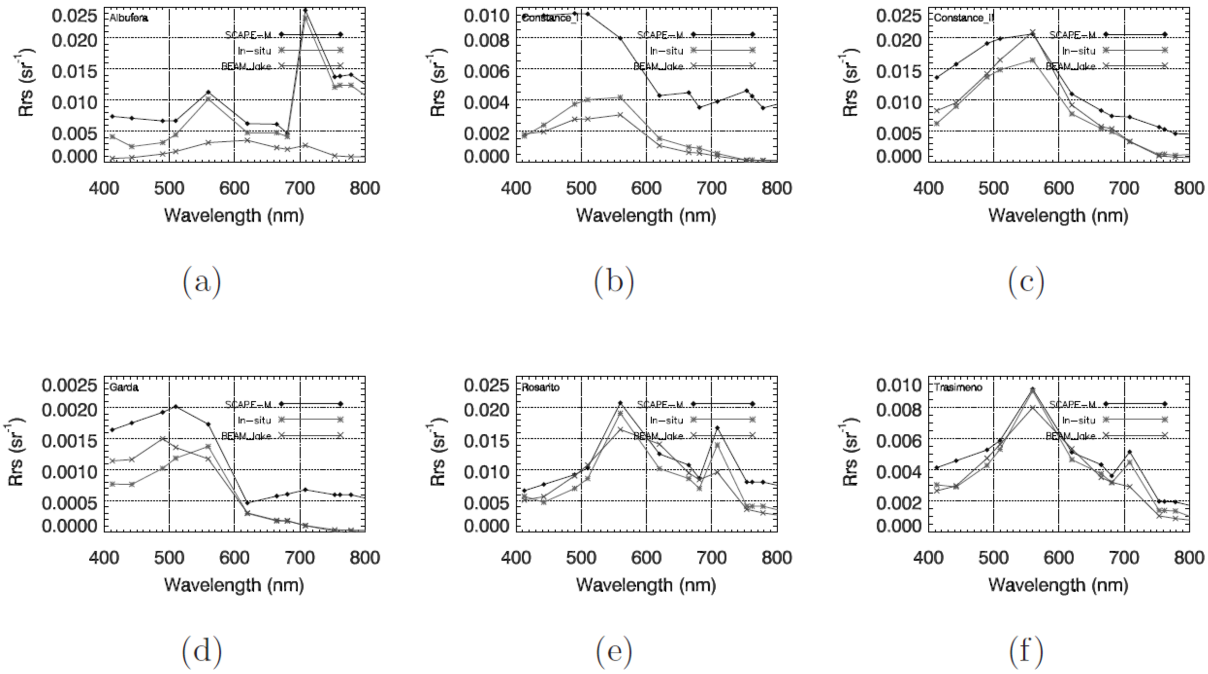

Figure 18: Comparison between reflectance spectra calculated by SCAPE-M and the BEAM lake processors. All the data were processed by ICOL and C2R processors in BEAM, except for Lake Albufera and Lake Rosarito, to which the eutrophic lakes processor was applied (from Guanter et al. (2010)).

3.6.2.3 C2R and CoastColour Neural Networks

The Case 2 Regional (C2R) processor has been developed for the MERIS instrument for water bodies where the assumption of a black ocean in the NIR is not valid due to scattering from particles in case of high concentrations of TSM and phytoplankton, or where high scattering in the visible part exists due to yellow substance. In all those cases the standard ocean atmospheric correction algorithms no not work. The neural network approach of (Doerffer & Schiller, 2007) is based on an inversion of the full spectrum, using all wavelengths. The TOA full spectrum results from the water leaving spectral radiance transmitted through the atmosphere; hence the TOA radiance carries all information of the water leaving spectrum as well as the atmospheric contribution. A numerical radiative transfer model is used to simulate a large number of TOA radiance spectra, where both the water leaving spectrum as well as the atmospheric parameters are varied. The radiative transfer is a non-linear process, and hence a non-linear inversion method is required for correcting for the atmospheric effect and retrieving the water-leaving signal. This non-linear inversion is performed mathematically by a neural network.

The modelled atmosphere consists of three parts, according to Doerffer and Schiller (2008b):

[1] A module to compute the water leaving radiance reflectance $RL_w(\lambda)$ (elsewhere R_w) at BOA

[2] A standard atmosphere, which includes 50 layers with variable concentrations of different aerosols, cirrus cloud particles and a rough, wind dependent water surface with specular reflectance, but with a constant air pressure- and ozone profile up to the top of standard atmosphere (TOSA)

[3] A layer on top of TOSA, which contains only the difference between the standard and real atmosphere concerning air molecules and ozone, completing to TOA

The determination of spectral water leaving radiance reflectance $RL_w(\lambda)$ from the TOA radiance reflectance $RL_{TOA}(\lambda)$ starts by adjusting air pressure and Ozone concentration to a standard atmosphere of 1013.2 hPa and 350 DU, respectively, using metadata provided with MERIS L1 imagery (1-4 in Figure 19). In this way, the number of variables of the subsequent inversion step could be reduced.

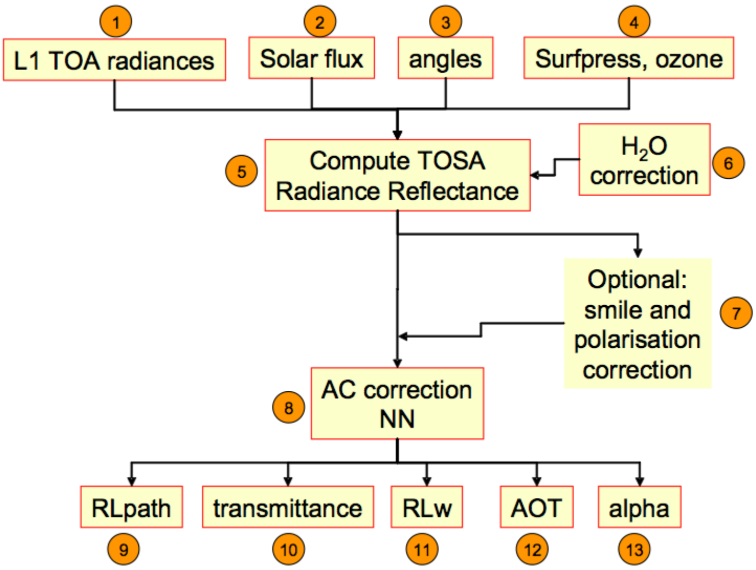

Figure 19: Atmospheric correction scheme for the MERIS lakes processor (from Doerffer and Schiller (2008b)).

The atmospheric correction neural network (NN, step 8) has a structure of several hidden layers with a large number of fully connected neurons. The NN uses TOSA radiance reflectance in 12 MERIS bands (412, 443, 490, 520, 560, 620, 665, 681, 708, 756, 778, 865 nm), and illumination and viewing geometry as input. It thereof retrieves the water leaving reflectance (RL_w) in all bands, along with atmospheric optical thickness in 4 bands and the corresponding Angstrom coefficient (alpha), and path radiance and transmittance. Absorption, scattering and surface reflection by the water body are also retrieved, but not written to the output product.

The Monte Carlo model used for modelling the optical properties of the atmosphere is based on publications by Gordon (1997), Mobley (1994), Morel and Gentili (1991). A special emphasis is put in the parameterization of aerosol optical properties. Continental, maritime, urban and stratospheric aerosols are included. In order to cover the full variability encountered in AERONET measurements, a custom, logarithmic aerosol size distribution was applied. The contribution by small aerosols was increased in this way, having a significant effect on Angstrom coefficients. During simulations, specific vertical profiles for each aerosol type are randomly weighted. In order to create a uniformly distributed variable space for AOT, a random value within the occurring total attenuation is chosen. The attenuation is then randomly assigned to each aerosol type.

The background water leaving reflectance is provided a forward NN that is trained with Hydrolight simulations (Mobley, 1994), since water is too high in optical thickness to efficiently run the Monte Carlo model. In the case of coastal waters (i.e. the C2R module), the computed ranges are:

- Scattering coefficient for all particles, range b(442 nm) 0.01 – 59.5 m^{-1}
- Absorption of phytoplankton pigments, range a(442 nm) 0.001 – 2.0 m^{-1}
- The absorption of yellow substance and bleached particles, range a(442 nm) 0.0029 – 9.2 m^{-1}

Validation of the MERIS lakes/C2R atmospheric correction is available in (S Koponen et al., 2008).

In the framework of the ESA DUE CoastColour project the C2R approach was modified in order to cope with extreme waters, where the TSM concentration goes up to 1000mg/l and the chlorophyll concentration can go up to 100mg/l. The bio-optical model was modified to allow for flexible spectral dependencies of yellow substance absorption and scattering of suspended sediments. The atmospheric model was extended to include other aerosol types, representative for coastal areas. These extensions make the CoastColour atmospheric correction much more flexible for different water types and atmospheric conditions as compared to the C2R atmospheric correction.

3.6.2.4 Improve Contrast between Ocean & Land

The Improve Contrast between Ocean & Land (ICOL) is a BEAM plugin processor that removes adjacency effects in MERIS L1B imagery and produces L1C images for further processing (Richard Santer & Zagolski, 2009). The procedure towards estimation and correction of adjacency effects requires the application several modules that account for Rayleigh and aerosol effects, the water pixel's distance from the shore along the solar principal plane, and the illumination and observation geometries (Figure 20). The separate treatment of these steps prior to the actual atmospheric correction and water constituent retrieval leads to relatively high processing costs, but introduces also additional uncertainties. For example, the application of a dark water assumption for ICOLs AOT estimation corresponds to a relatively rough approximation prevented by state-of-the-art atmospheric correction algorithms. Nonetheless, the application of ICOL often lead to radiometrically improved reflectance, even when those improvements did not necessarily propagate to the accuracy of retrieved constituents (Kratzer & Vinterhav, 2010; Daniel Odermatt et al., 2010). These findings were generally confirmed in the Diversity II algorithm selection, therefore ICOL was experimentally assessed but not applied to derive the final Diversity II products.

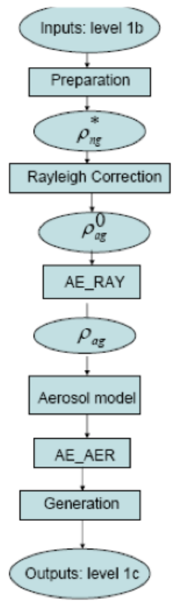

Inputs are level-1b images. Bands at 761 nm and 900 nm remain unchanged.

The "preparation" module transforms TOA radiance into TOA reflectance after correction of the gaseous transmittance.

The "Rayleigh" module corrects all the pixels from the Rayleigh scattering.

The "AE_RAY" module corrects the pixels in the vicinity of land (d>30 km) from the AE + FLM Rayleigh.

The "aerosol" module determines the aerosol model over these pixels.

The "AE_AER" module corrects from the AE+ FLM aerosol.

The "generation" module transforms, in 13 MERIS bands, the level 1c reflectance into radiance. For pixels not corrected from the AE and for 761 nm and 900 nm, level 1C is equal to level 1B.

Figure 20: ICOL overview processing flow chart (from Santer and Zagolski (2009)).

3.6.3 Validation of atmospheric correction over water

According to the MERIS Lakes Validation Protocol (Kari Kallio et al., 2007), validation of atmospheric correction is done using above or below water surface reflectance measurements. In the scope of Diversity II, a large number of such data was collected from supportive scientists, but no preference regarding the measurement method was made in order to cover as many different lakes as possible.

3.6.3.1 In situ spectro-radiometric measurements

Data of altogether 20 lakes is used, and matching MERIS acquisitions are available for 18 of them (Table 6). All data is converted to water-leaving reflectance following the MERIS Lakes Validation Protocol for comparison. Matchup extraction was done using a Calvalus instance that searches the MERIS FR archive and processes only relevant pixels and subsets as required by the algorithms (Scape-M, ICOL). All matchups are supplied with Idepix cloud screening (Section 3.3) and land/water separation flags (Section 3.4). No shallow water tests were applied, assuming that all field samples represent optically deep water.

For Lake Vanern, a total of 171 matchups from the Palgrunden AERONET Ocean Colour station are found, whereof 74 are valid. For the other 17 lakes, 140 measurements from field campaigns are available, whereas certain closely located field measurements may correspond to the same MERIS pixel. 46 out of those 140 measurements correspond to valid pixels. The main reason for this significant difference is that the dataset for Spanish lakes and reservoirs consists of numerous cases where manual identification of suitable matchup pixels is necessary due to the narrowness of the basins. Using only coordinate metadata in our automated matchup extraction, the extracted pixels represent often adjacent land. Cases representing invalid cases are still considered, but quoted separately.

Another limitation of the available reference data is that relatively little simultaneously sampled water constituent concentrations are available, in particular almost no CDOM measurements. Locally expected variability ranges and visual estimation of the water composition from reflectance spectra will therefore be discussed for further interpretation.

Table 6: Spectro-radiometric matchup measurements available for validation in the scope of Diversity II. Measurement techniques for the ASD FieldSpec and RAMSES are described in (Kari Kallio et al., 2007). The minima and maxima of applicable constituents refer only to the 'n_valid' cases, i.e. those identified as cloud free and valid.

Lake name	Provider Institution	Quantity Device	n_total n_valid	chl Range [mg/m^3]	tsm Range [g/m^3]	cdom Range [m^{-1}]
Albufera	Antonio Ruiz-Verdú Univ. Valencia	R_{rs}^+ ASD FieldSpec	14 9	327.1-489.6	-	-
Alcantara	Antonio Ruiz-Verdú Univ. Valencia	R_{rs}^+ ASD FieldSpec	3 0	-	-	-
Almendra	Antonio Ruiz-Verdú Univ. Valencia	R_{rs}^+ ASD FieldSpec	10 5	42.1-59.5	-	-
Balaton	Peter Hunter Univ. Stirling	R_{rs}^+ Satlantic HyperSAS	18 8	6.6-26.5	9.5-14.0	-
CuerdaDelPozo	Antonio Ruiz-Verdú Univ. Valencia	R_{rs}^+ ASD FieldSpec	7 0	-	-	-
Geneva	Daniel Odermatt Univ. Zurich	R^- Trios RAMSES	3 3	-	-	-
Hartbeespoort	Mark Matthews Univ. Cape Town	R_{rs}^- Satlantic HyperTSRB	4 0	-	-	-
Iznajar	Antonio Ruiz-Verdú Univ. Valencia	R_{rs}^+ ASD FieldSpec	10 0	-	-	-
Kasumigaura	Bunkei Matsushita Univ. Tsukuba	R_{rs}^+ ASD FieldSpec	10 7	75-95	32-48	-
Loskop	Mark Matthews Univ. Cape Town	R_{rs}^- Satlantic HyperTSRB)	8 2	1.0	0.5-1.7	-
Paeijanne	Sampsa Koponen SYKE	R_{rs}^+ ASD FieldSpec, WISP	3 3	1.9-2.1	0.7-1.1	2.5-2.8
Peipsi	Tiit Kutser Univ. Tartu	R_{rs}^- (Trios RAMSES)	6 4	9.0-26.8	2.2-6.9	4.7-11.0
Pyhajarvi	Sampsa Koponen SYKE	R_{rs}^+ ASD FieldSpec	3 3	5.3-7.2	2.0	1.5-1.6

Lake name	Provider Institution	Quantity Device	n_total n_valid	chl Range [mg/m^3]	tsm Range [g/m^3]	cdom Range [m^{-1}]
Rosarito	Antonio Ruiz-Verdú Univ. Valencia	R_{rs}^+ ASD FieldSpec	37 2	54.6-58.3		
Tremp	Antonio Ruiz-Verdú Univ. Valencia	R_{rs}^+ ASD FieldSpec	4 0	-	-	-
Vanern	Susanne Kratzer Univ. Stockholm	$R_{w,n}$ AERONET OC	171 74	-	-	-
Vesijarvi	Sampsa Koponen SYKE	R_{rs}^+ ASD FieldSpec	4 4	1.7-4.6	1.2-2.6	0.9-1.8
Zurich	Daniel Odermatt Univ. Zurich	R^- Trios RAMSES	3 3	-	-	-

3.6.3.2 Matchup results

Radiometric validation was performed for reflectance outputs of the BRR, C2R, CoastColour, FUB and Scape-M algorithms. C2R, CoastColour, FUB are used with and without ICOL adjacency effect correction, resulting in a total of 8 estimated reflectances in each matchup. The different algorithms have different applicability constraints; therefore not all 8 estimates are available for each matchup. In addition, FUB estimates occasionally negative reflectances, which are not visible in plot canvas. The matchups were calculated with MERIS FR bulk reprocessed input products, a comparison with the previously available CoastColour data is provided in the end of the Section.

In hypertrophic waters of more than 100 mg/m^3 CHL, the variability of optical properties is highly complex, since small changes in phytoplankton pigment composition have a large impact on the shape of the spectral reflectance. This favours the application of BRR and Scape-M, which do not require any previous knowledge of the water's apparent optical properties, while the NN algorithms are challenged not only in terms of training range, but also with regard to the predefined phytoplankton absorption properties they are trained for. This effect is evident in matchups of the Albufera Lagoon and Lake Hartbeespoort (Figure 21). The mixed_pixel flag is raised in both cases, but the agreement of BRR and Scape-M in situ spectra at > 800 nm indicate that there is perhaps little and no significant land signal in the Albufera and Hartbeespoort matchup pixel, respectively. The shape of the Scape-M and BRR retrieved spectra are equally adequate, including the 709 nm reflectance peak at the edge of the secondary CHL absorption feature. However BRR strongly overestimates the in situ reflectance in the Albufera case, where Scape-M retrieves almost double (τ = 0.24) the AOT as for Hartbeespoort (τ = 0.16), which leaves a much larger aerosol effect being neglected by BRR. A somewhat larger scatter similarly indicates the effect of aerosol scattering for BRR when comparing all 3 cloud-free Hartbeespoort measurements at once (Figure 22).

An assessment of superimposed TSM and CDOM variability ranges cannot be taken into account for hypertrophic waters due to a lack of data.

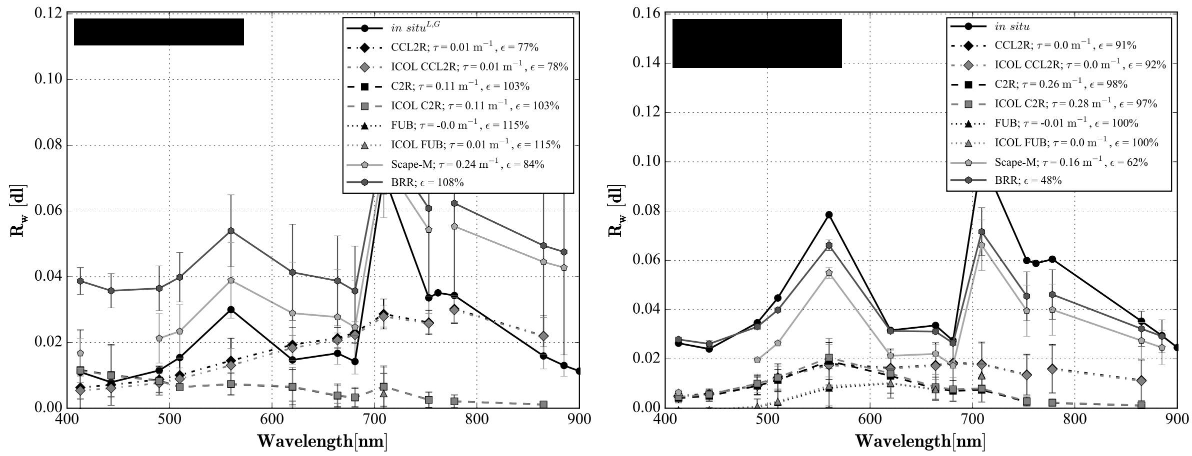

Figure 21: Reflectance matchup comparisons for hypertrophic water in the Albufera Lagoon (Spain, 25 May 2005, left) and Lake Hartbeespoort (South Africa, 15 October 2010, right). The Idepix land flag is raised for the Albufera example.

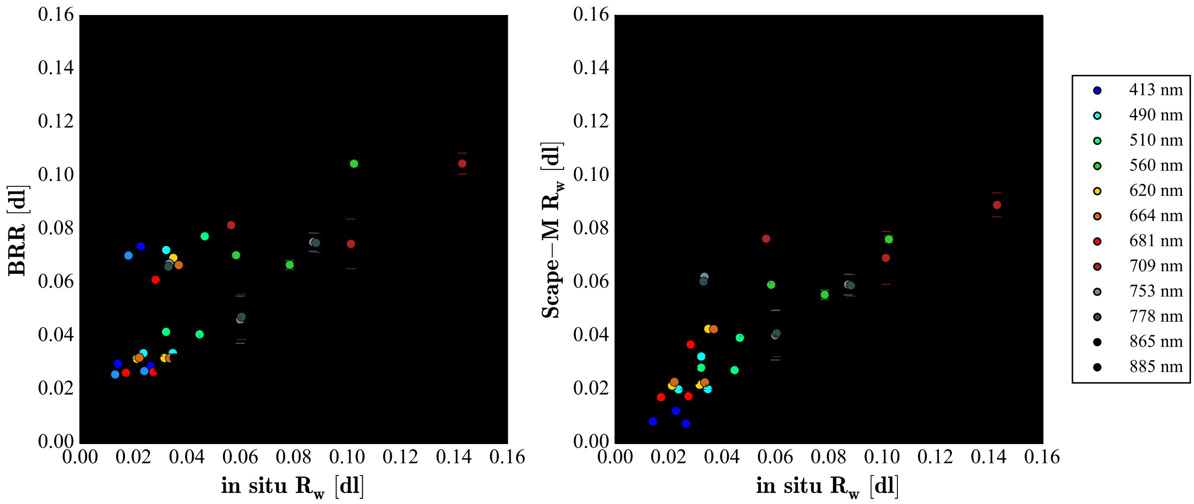

Figure 22: Reflectance scatter plots for 3 measurements in Lake Hartbeespoort, using BRR (left) and Scape-M (right) atmospheric corrections.

In meso- and eutrophic waters of 10-100 mg/m^3 CHL, a larger variety of different optical cases is available, although the missing TSM and CDOM in situ data make careful interpretation necessary. [1] In Lake Balaton, the reflectance levels are higher than for any other site, at only intermediate CHL levels. This indicates significant scattering by inorganic particles (Figure 23), as expected from permanent re-suspension in the shallow lake. [3] In Lake Peipsi, CHL concentration is at similar levels as in Balaton, however, TSM is significantly lower, and CDOM clearly dominant according to the extraordinary concentrations measured (Figure 24). [3] In the Almendra and the Rosarito Reservoirs, CHL is about twice that in Balaton and Peipsi, and the spectral reflectance features indicate that CHL is dominant over allochthonous TSM and CDOM. The reflectance in the first two MERIS bands, where scattering, CDOM and CHL absorption coincide, remains at intermediate levels unlike the drop caused by CDOM in Peipsi. At the other end of the spectrum, NIR reflectance of approximately R_w = 0.005 to 0.01 at 753 and 780 nm remains clearly lower than in Balaton, indicating lower TSM scattering in spite of the higher CHL and thus phytoplankton abundance.

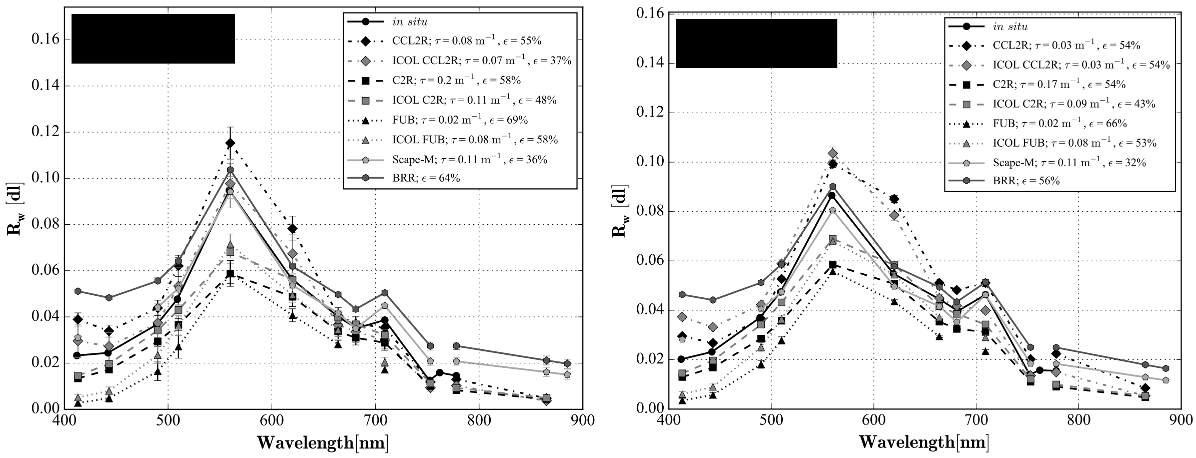

Figure 23: Reflectance matchup comparisons for mesotrophic water for two different sites in Lake Balaton (Hungary, 22 August 2010).

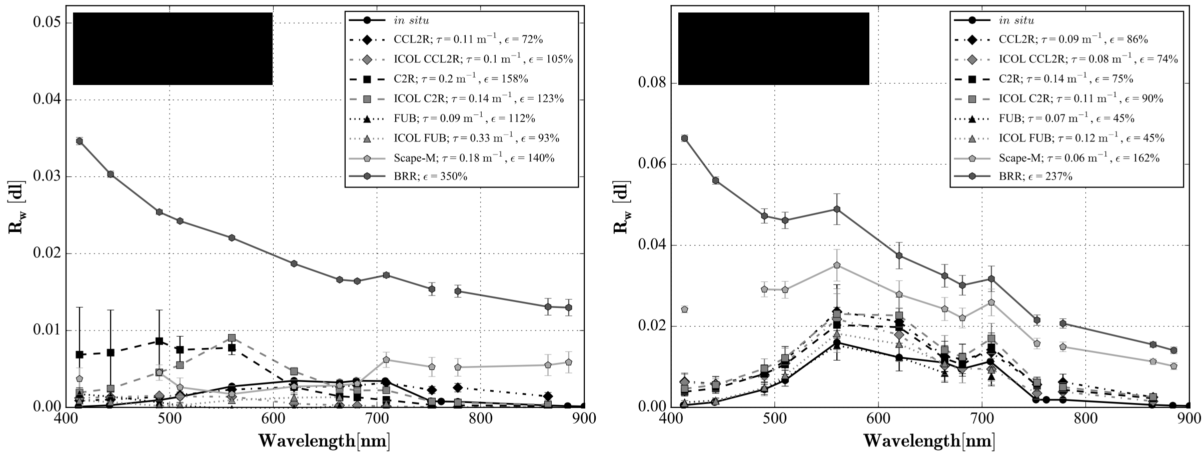

Figure 24: Reflectance matchup comparisons for eutrophic water in Lake Peipsi (Estonia, left: 12 May 2011, right: 2 September 2011).

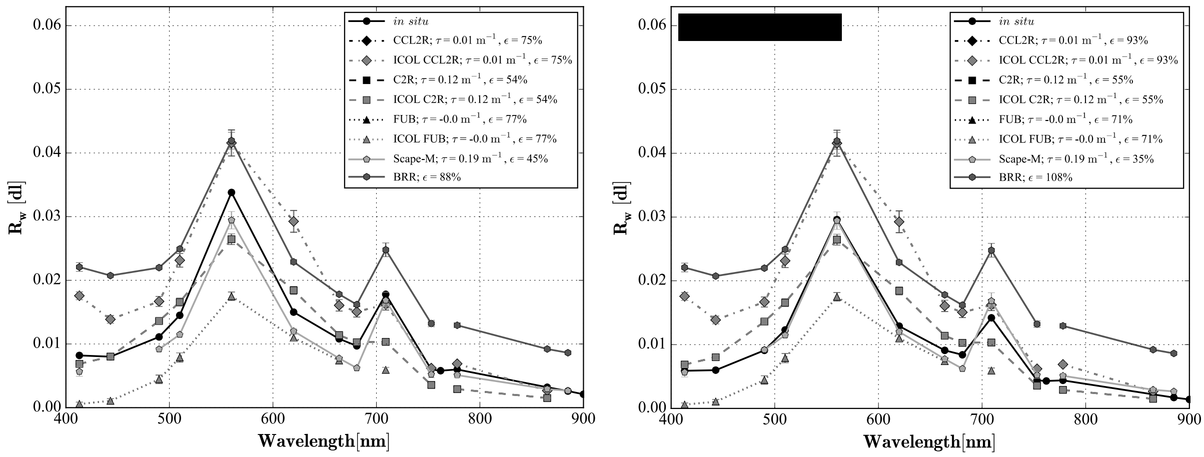

Figure 25: Reflectance matchup comparisons for CHL dominated eutrophic water for two different sites of the Almendra Reservoir (Spain, 10 July 2007, left).

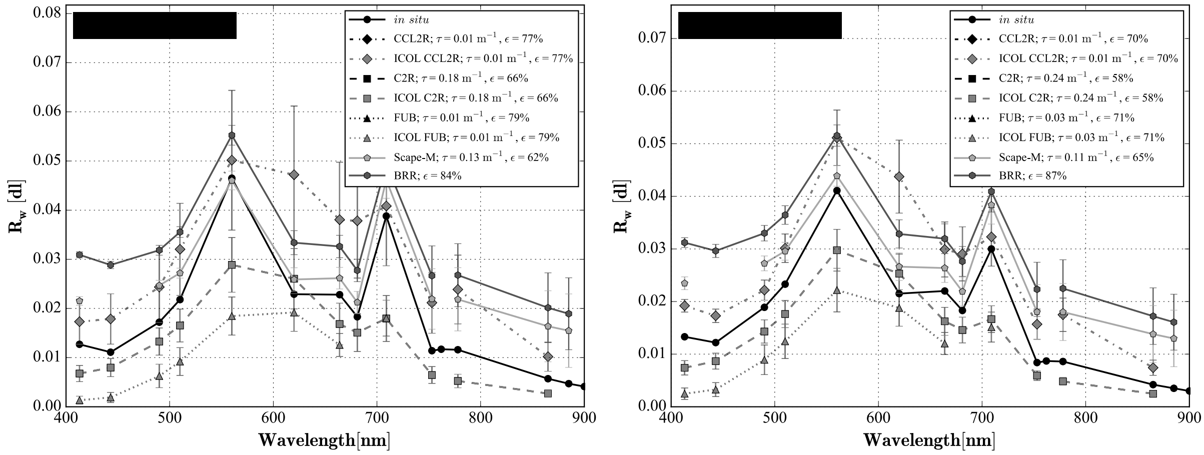

Figure 26: Reflectance matchup comparisons for eutrophic water in the Rosarito Reservoir (Spain) on 15 June 2004 (left) and 1 July 2004 (right).

As far as spectral features are concerned, the reflectance peak at 709 nm remains a preferred means to retrieve CHL in meso- and eutrophic waters with MERIS (Binding, Greenberg, Bukata, Smith, & Twiss, 2012; Mark William Matthews et al., 2012; Moses, Gitelson, Berdnikov, & Povazhnyy, 2009). It can be seen from the examples above that this feature is very prominent in the third case, persists in the TSM influenced Balaton conditions, but diminishes completely in the case of Peipsi. As previously shown for hypertrophic conditions, this exact retrieval of the 709 nm peak favours again the use of BRR and Scape-M. But unlike for the hypertrophic cases, the bio-optical variability in meso- and eutrophic waters is mostly within the NN algorithms' training range, making them a reasonable alternative. The CoastColour atmospheric correction (CCL2R) has a larger training range, which is generally an asset, but only really visible in the Lake Peipsi matchups. On the downside, the AOT is frequently underestimated at $\tau = 0.01$, raising doubts about its overall optical closure. Reflectances estimated by C2R have somewhat lower relative RMSEs (ε) than CCL2R for Lake Balaton and the Almendra and Rosarito Reservoirs, but primarily for their magnitudes, while the shape is usually worse, which is visible as an uneven scatter in Figure 27. FUB significantly underestimates reflectance in most cases, and provides only visible bands and the one at 709 nm. The low relative RMSEs by FUB is not comparable to CCL2R and C2R, as relative errors in the absent bands are relatively high for the latter two due to the low signal level.

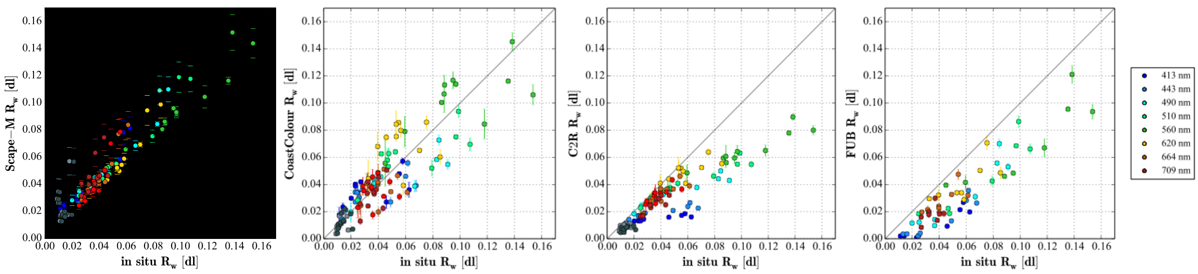

Figure 27: Reflectance scatter plots for 11 measurements in Lake Balaton, using Scape-M, CCL2R, C2R and FUB (left to right) atmospheric corrections.

As far as oligo- to mesotrophic waters of less than 10 mg/m^3 are concerned, the available data represents clear and CDOM dominated waters, but lacks TSM dominated waters (e.g. high alpine reservoirs). In both water types, reflectance levels are significantly lower than for the previous trophic levels, due to a lack of particulate scattering. Under these circumstances, the ratio of water-leaving to path scattered radiance at sensor level decreases to levels below 10%. Consequently, the line-of-sight type NN atmospheric corrections perform significantly better (Figure 28) than when AOT is interpolated (Scape-M) or if aerosol scattering is entirely neglected (BRR). When low scattering is combined with allochthonous CDOM as in boreal regions, reflectances can drop even further towards sensor noise level, making all atmospheric correction challenging and error prone as e.g. negative reflectances from FUB indicate (Figure 29).

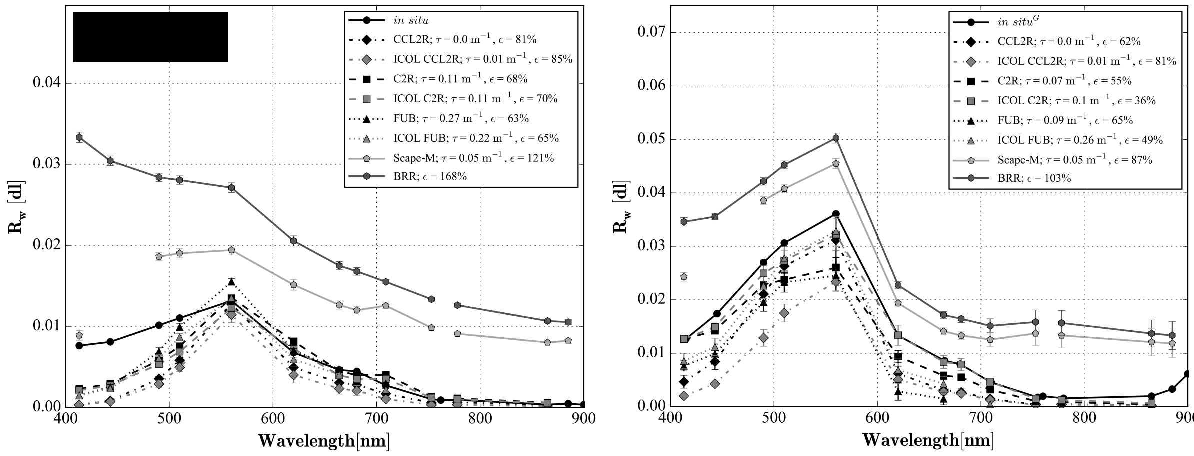

Figure 28: Reflectance matchup comparisons for clear, oligotrophic water in the Loskop Reservoir (South Africa, 1 August 2011, left) and Lake Zurich (Switzerland, 15 August 2007, right).

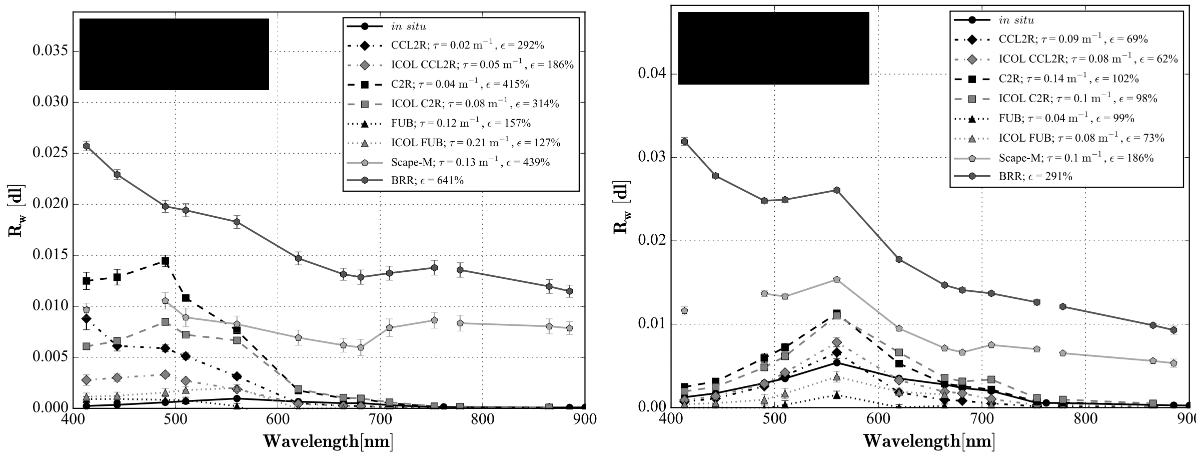

Figure 29: Reflectance matchup comparisons for CDOM dominated oligotrophic water in Lake Paijanne (Finland, 7 August 2007, left) and Lake Pyhajarvi (Finland, 23 August 2007, right).

As far as the performance of ICOL is concerned, a total of 37 of valid matchup pixels are available for evaluation. The relative spectral RMSE (Daniel Odermatt et al., 2010) shown in the spectral plots above is a suitable means to evaluate the reflectance magnitude adjustment by ICOL, while it does not allow an assessment of the retrieved shape and thus overall accuracy.

Table 7 summarizes the counted improvements in terms of relative RMSE for each measured spectrum and algorithm. This analysis was done with the CoastColour processed MERIS FR L1B data, before the bulk reprocessed archive was available. The Spanish reservoirs are not included. The outcome indicates a significant improvement by ICOL in the cases of C2R and FUB, while for CCL2R, less than half of all measurements are improved, while the relative RMSEs increase for a larger number of measurements (counts not shown). The counted improvements are quite randomly distributed across the lakes, while it seems that the most significant improvements in terms of reduction in rel. RMSE occur for CDOM-rich Finnish lakes.

Table 7: Counts of ICOL test cases and number of rel. RMSE improvements propagated to atmospherically corrected spectra for CCl2R, C2R and FUB. All spectro-radiometric matchups with valid pixels in Table 6 are included, apart Vanern and the Spanish reservoirs. The percentage in brackets is the average decrease in relative spectral RMSEs for the improved cases.

Lake name	ICOL test cases	CCL2R improved	C2R improved	FUB improved
Balaton	8	5 (5%)	8 (8%)	8 (11%)
Geneva	3	0 (-)	3 (26%)	3 (16%)
Kasumigaura	7	4 (5%)	6 (2%)	4 (2%)
Loskop	2	0 (-)	1 (2%)	1 (1%)
Paeijanne	3	3 (43%)	3 (74%)	3 (20%)
Peipsi	4	0 (-)	3 (15%)	3 (16%)
Pyhajarvi	3	2 (11%)	2 (2%)	3 (28%)
Vesijarvi	4	0 (-)	2 (17%)	0 (-)
Zurich	3	0 (-)	3 (17%)	3 (14%)
Sum	***37***	***14***	***31***	***28***

The effect of the MERIS FR bulk reprocessing on retrieved reflectances is generally small, and barely visible in spectral plots. Table 8 contrasts relative RMSEs for both input data types and the two extreme examples depicted above, namely the most eutrophic (Albufera, Hartbeespoort: Figure 21) and CDOM dominated ones (Paijanne, Pyhajarvi: Figure 29). The example of lake Paijanne is the only one where significant differences are observed, but the causes for this difference are not further investigated.

Table 8: Relative RMSEs (ε, [%]) for the reflectance matchup comparisons using 'bulk' reprocessed MERIS FR as in Figure 21 and Figure 29, and for the CoastColour ('CC') MERIS FR data basis prior to reprocessing.

	Albufera (Figure 21)		Hartbeespoort (Figure 21)		Paijanne (Figure 29)		Pyhajarvi (Figure 29)	
	bulk	**CC**	**bulk**	**CC**	**bulk**	**CC**	**bulk**	**CC**
CCL2R	77	n.a.	91	91	292	263	69	69
ICOL-CCL2R	78	n.a.	92	91	186	179	62	62
C2R	103	103	98	98	415	410	102	100
ICOL-C2R	103	103	97	97	314	315	98	98
FUB	115	114	100	100	157	158	99	99
ICOL-FUB	115	114	100	100	127	141	73	73
Scape-M	84	83	62	61	439	435	186	189
BRR	108	108	48	n.a.	641	627	291	291

3.6.3.3 Algorithm selection and usage

A qualitative summary of the assessed atmospheric correction algorithms' suitability is provided in Figure 30. The results are in line with the findings in previous studies (Luis Guanter et al., 2010; Daniel Odermatt et al., 2010; Ruiz-Verdu et al., 2008). However, the analysis of matchup measurements cannot account for all relevant selection criteria, which includes further algorithm-specific limitations:

- Smooth spatial gradients (Scape-M)
- Dependence on distance from shoreline (Scape-M)
- The availability of bands (Scape-M, FUB)
- The propagation of small modifications (ICOL)
- Limited training ranges (FUB, C2R, CCL2R)

In addition, although an unparalleled amount of data was available for Diversity II, reference data remain limiting. Regular measurements are only available from the Lake Vanern AERONET station. Those in situ measurements are derived using an anisotropy assumption based normalizing procedure, which is quite reliable for ocean colour measurements, but less so in inland water remote sensing.

Therefore, no final selection decisions are derived from the radiometric matchup validation. Instead, corresponding observations will be applied to interpret the outcome of the constituent matchup validation, which will be used as the main algorithm selection benchmark.

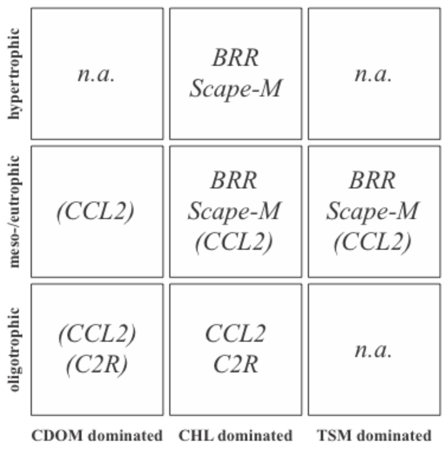

Figure 30: Scheme of the recommended applicability for the assessed algorithms. Entries in brackets indicate partial limitations, i.e. the 709 nm peak by CHL in eutrophic waters and the vanishing signal level in CDOM dominated oligotrophic water.

3.7 Drylands Auxiliary Data pre-processing

In this project, the spatial differentiation of vegetation greenness and trends thereof will be related to various kinds of space-based data that represent water availability for plants. In general, the relation between vegetation biomass and water availability as measured by these data sets has major drawbacks imposing limitations on their direct confrontation. One major factor is the coarse spatial resolution of these "water" data sets that does not match the 300 m pixel width of the MERIS FR data. Thus, the temporal /spatial variability of rainfall or soil moisture present at the MERIS pixel level and influencing vegetation growth cannot be reproduced with these datasets. In addition, rainfall feeds only partially into vegetation growth; substantial parts of it evaporate or run of. The latter makes soil moisture data that relate directly to water in the root zone in general better suited for such comparisons, but they would also be required at a much better spatial resolution. First high-resolution soil moisture data sets are being produced and tested by various research groups, however no data sets consistently available for the study sites during the MERIS period do yet exist for ready usage in this project. High-resolution sensor data are often scarce (e.g. ENVISAT ASAR) and thus their availability hinders the production of coherent time series.

3.7.1 Soil Moisture Data

3.7.1.1 Rational and objective

Reasons to include Soil Moisture (SM) data in the analyses are that they are part of the ECVs (Essential Climate Variables), and that space based SM data are available on a global scale for the last 30 years. Within Diversity II – Drylands they are of scientific interest as soil moisture is more directly related to the actual water availability for plants than rainfall, as it constitutes – roughly – the water that remains in the soil or root zone after surface runoff and evapotranspiration. The SM data have been used as variable per se and for the derivation of SMUE – Soil Moisture Use Efficiency, an analogue product to Rain Use Efficiency. SM and SMUE status and trends as well as epochal difference indicators have been generated and can becompared with corresponding products derived from rainfall data. .

3.7.1.2 Soil moisture data

The global soil moisture data set has been generated in the ESA funded WACMOS project (http://wacmos.itc.nl/) by merging active and passive microwave spaceborne sensor data as described by Liu et al. 2012. The SM-MW (microwave based soil moisture data) has a spatial resolution of 0.25 x 0.25°, a daily coverage and represents the upper few ~ 2 cm of the soil (Dorigo et al., 2012). Even though the data go back as far as to 1978, trend analyses should only be performed from 1988, as the underlying SMMR sensor (1978 – 1987) “*has only a very short overlap with the successive SSM/I sensor, making a trend-preserving match with later datasets impossible*” (Dorigo et al., 2012). The selected SM-MW data fulfil the (SOW) criteria that they originate from space borne EO measurements and are globally available. Currently this data is being used for comparative trend analyses (Dorigo et al., 2012), is being cross-validated with soil moisture data from other sources, and will be further improved in the ESA CCI project (http://www.esa-soilmoisture-cci.org/).

In Diversity II, CCI SM v2.0 were used.

3.7.1.3 Pre-processing of the CCI SM data

The SM data were integrated to half-monthly data by summing up the daily values. A half-monthly value was accepted if at least one valid daily measurement was available during the respective half-month. The SM data, like the rainfall data, were resampled (nearest neighbour) to a grid spacing of ≈ 0.07273° (8 km at the equator), and geographic coordinates (WGS84) to match the GIMMS NDVI data.

Prior to their further usage the SM data were low-pass filtered (averaged) with a kernel size of 3*3 (0.07273°) pixels in order to generate smooth transitions between the sub-sampled pixels. Note that the filter kernel is about as large as one pixel of the original data, thus the filtering constitutes an interpolation and slight smoothing with the objective to avoid artificially strong differences between the pixels and to obtain later on an overall smooth appearance of the derived indicator maps.

For their actual usage in the dryland sites, the data were temporally integrated in phenological periods, which have been derived with the MERIS fAPAR data. Spatial sub-sampling (bilinear) to fit the MERIS data resolution was an integrated part of the ERDAS models that were developed for their analysis.

3.7.2 Hydro-Meteorological Data and Pre-processing

3.7.2.1 Rational and objective

The usage of hydro-meteorological data has the broad objective to relate vegetation growth and its variability to the major driving factors, i.e. water and energy. Water as the main constraint of vegetation growth in drylands is, besides the SM data, was represented by TRMM and GPCP rainfall data. The GPCP data were used to supplement the TRMM data that cover only latitudes between 50° N and S. Further on, air temperature data (CPC) were available as well as actual evapotranspiration data (MOD16 ET) on a global scale. The latter two parameters and their relation to NPP trends are of special interest for drylands in moderate climates, where besides water also energy is a significant constraint for vegetation growth. Whereas such analyses were done globally on a systematic base by Fensholt et al. (2012), for this project it was planned to perform only limited and exemplary tests in selected sites, concentrating on evapotranspiration. When comparing the ET data to rainfall data, globally quite inconsistent results were obtained as described in section 3.7.2.6. For this reason, the ET data were not further used in the project. Moreover, due to the large number of indicator products that were derived based on fAPAR, rainfall and SM data alone, we refrained from the application of the air temperature data. It would without any doubt be of interest to contrast ET and air temperature data to vegetation productivity, and we refer to the literature where such analyses have been reported (Diversity II Product User Handbook, drylands).

3.7.2.2 GPCP rainfall data

GPCP rainfall data are a blended gage-satellite product by NOAA (http://precip.gsfc.nasa.gov/). They reach back to 1979, are gridded with a resolution of 2.5 x 2.5° and produced for monthly intervals. For that reason they are not the first choice in the project because half-monthly time intervals have been chosen for the vegetation time series data. However, they have been used in numerous investigations and constitute therefore a common reference to many studies (Fensholt et al., 2012). As noted above, they were only used to supplement the TRMM rainfall data beyond 50° N and S, and pre-processed analogue to the SM data. Further on, for usage along with half-monthly data, these monthly data were broken down to halfmonthly values by halving the monthly figures.

3.7.2.3 TRMM Rainfall data

The Tropical Rainfall Measuring Mission, a joint venture of NASA and the Japanese space agency JAXA, provides EO based rainfall data with a ground resolution of 0.25 x 0.25° beginning in 1997. The gage corrected TRMM 3B42 v6 data with a temporal resolution of three hours were summed to halfmonthly values and the small number of remaining gaps was filled with TRMM 3B43 data, applying the below described procedure. Resampling to the GIMMS NDVI grid (≈ 0.07273°) and 3*3 low pass filtering after the resampling were applied such as to the SM and GPCP rainfall data.

Beyond 50° N and S, GPCP v2 data were mosaicked with the TRMM data after breaking down these monthly data to halfmonthly values, as noted above. Thus in the test sites crossing the northern and respectively southern latitude of 50°mixed rainfall data were used, as it was preferred to exploit the TRMM data with their significantly better resolution to the maximum extent.

Filling gaps of the TRMM 3B43 data

On a global scale, the half-monthly aggregated TRMM 3B42 precipitation estimates are quite complete with only a few regions containing a pronounced amount of data gaps. To retrieve a data set with no remaining gaps globally, TRMM 3B43 (monthly data) data were used and the 3B42 data were recalculated as follows:

- Recalculation of bi-weekly sums to hourly average sums
- Where one out of two data points within one month is missing the following procedure is applied: $b_{42} = 2x_{43} - a_{42}$ $b_{42} = 2x_{43} - a_{42}$, where b represents the missing value, a and x the available values, and the indices represent the data source, i.e., 42 for TRMM 3B42 and 43 for TRMM 3B43.
- For cases where both half-monthly 3B42 data points are not available within one month, both are replaced with 3B43 values assuming that the hourly precipitation is equally distributed over one month.
- $b_{42} = 02x_{43} < a_{42}$For cases in which one 3B42 is missing and $2x_{43} < a_{42}$,it is assumed that $b_{42} = 0$, since the monthly mean precipitation is significantly below the precipitation for the known part of the month.
- In a final step bi-weekly sum precipitation is calculated from the hourly sums assuming that two weeks comprise 15.21 days.

Figure 31 depicts the amounts of pixel being affected by the processing described above for global coverage. Annual values are totals for the contained 24 bi-weekly layers.

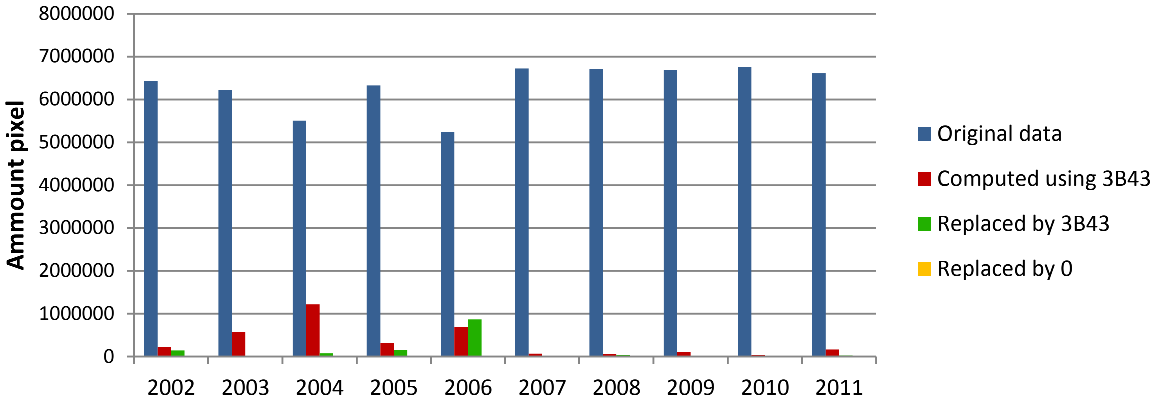

Figure 31: Data source of the final global TRMM data set

The TRMM rainfall data have been compared to data of several ground stations in Australia. In spite of the difficulty of spatially and temporarily matching EO based rainfall data with ground station and thus point data, the validation delivered mainly good correlation results between TRMM rainfall and the station data, where only two out of 10 sample points show a low (point 4) or very low correlation (point 5), as reported in PQR. The Pearson correlation coefficients are listed in Figure 32. As a general tendency, a small positive bias in the precipitation estimates was observed. In Figure 32 the monthly rainfall sums for the sample point 5, the one with the lowest correlation are plotted for the TRMM and the station data. Despite of the low correlation at this location, the temporal courses of the two time series are well comparable and show that the low correlation is mainly due to a shift of one month between most of the values in this case. Promising validation and evaluation results for TRMM rainfall data were also obtained by Nair et al. 2009, or by Liechti et al. 2012.

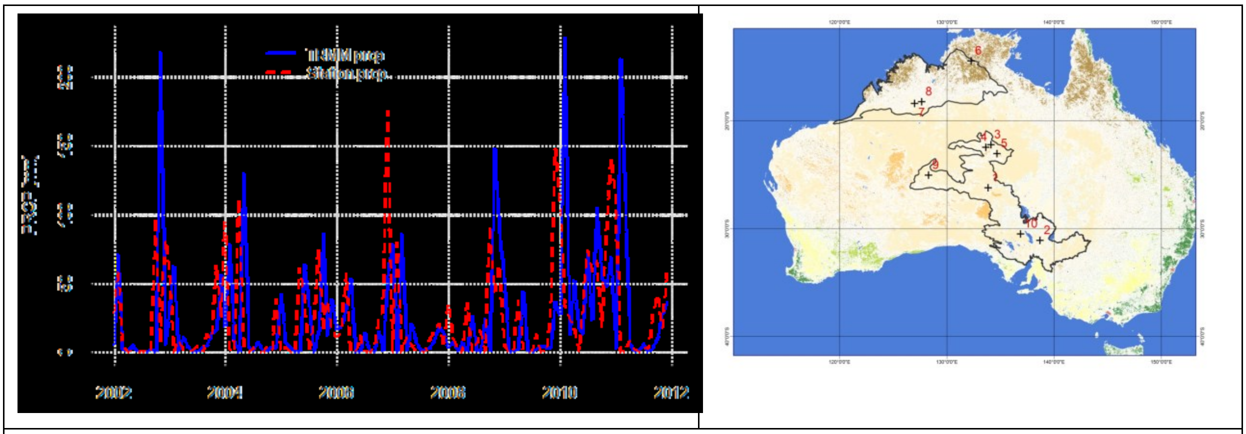

Pearson r between monthly TRMM and station rainfall amounts 2002 – 2012 at the sample points:

1: 0.90, 2: 0.85, 3: 0.43, 4: 0.74, **5: 0.10,** 6: 0.95, 7: 0.91, 8: 0.92, 9: 0.9, 10: 0.87

Figure 32: TRMM versus station precipitation at location no. 5 in the right hand map

3.7.2.4 CMORPH Rainfall data

In addition to the TRMM rainfall data, CMORPH data of the NOAA Climate Prediction Center (http://www.cpc.ncep.noaa.gov/products/janowiak/cmorph.shtml) have been pre-processed by BC and used for comparison with the TRMM 3B42 data. CMORPH rainfall data are available from 2002, have a nominal ground resolution of 8*8 km² and rely solely on EO data. Due to their higher spatial resolution they might better capture small-scale rain events, however their quality in relation to other products is controversially judged in the literature. For example, according to Liechti et al. (2012) CMORPH is overestimating the rainfall by nearly 50 %. Tian et al. (2007) state: "*The analyses show that at annual or seasonal time scales, TRMM 3B42 has much lower biases and RMS errors than CMORPH. CMORPH shows season-dependent biases, with overestimation in summer and underestimation in winter. This leads to 50% higher RMS errors in CMORPH's area-averaged daily precipitation than TRMM 3B42*". Significant higher rainfall amounts were also found with the CMORPH data in this project compared to the TRMM data, also spatial and temporal inconsistencies of their correlations. Based on these and the literature findings, and as the CMORPH data are only based on EO data versus the gage corrected TRMM 3B42 data, we decided to use the TRMM 3B42 precipitation data as major source for rainfall estimates, supplemented with the GPCP data beyond 50° N and S.

3.7.2.5 CPC Air Temperature data

The selected CPC global surface air temperature data originates from interpolation of climate station data, and is available since 1948 as monthly data in a ground resolution of 0.5 x 0.5° (http://iridl.ldeo.columbia.edu/SOURCES/.NOAA/.NCEP/.CPC/.GHCN_CAMS/.gridded/.dataset_documentation.html). However, as mentioned above, the air temperature data have not been used for product generation because we concentrated on contrasting the NPP proxies with water parameters only in the derived indicator products. Precipitation is the most important limiting factor to vegetation growth in drylands, and has as such been used as sole factor to contrast vegetation productivity against, without establishing a relation to the other major climate factors of vegetation productivity, i.e., temperature and solar radiation. Figure 33 shows the weight of these fundamental growth limiting factors at the global scale. Especially in the test sites located in temperate climate zones, temperature and to a lesser degree solar radiation constitute potential constraints to primary production. However, in the regional context the weight of these factors depends on further variables including topography, vegetation types, soil nutrients and other soil properties etc., factors which could not be taken into account in this global project, even though at the spatial resolution of the MERIS data these factors are important. As this study does not model NPP we have related the derived NPP proxies only to precipitation and soil moisture, which can be regarded as the major growth constraining factors in the analysed test sites.

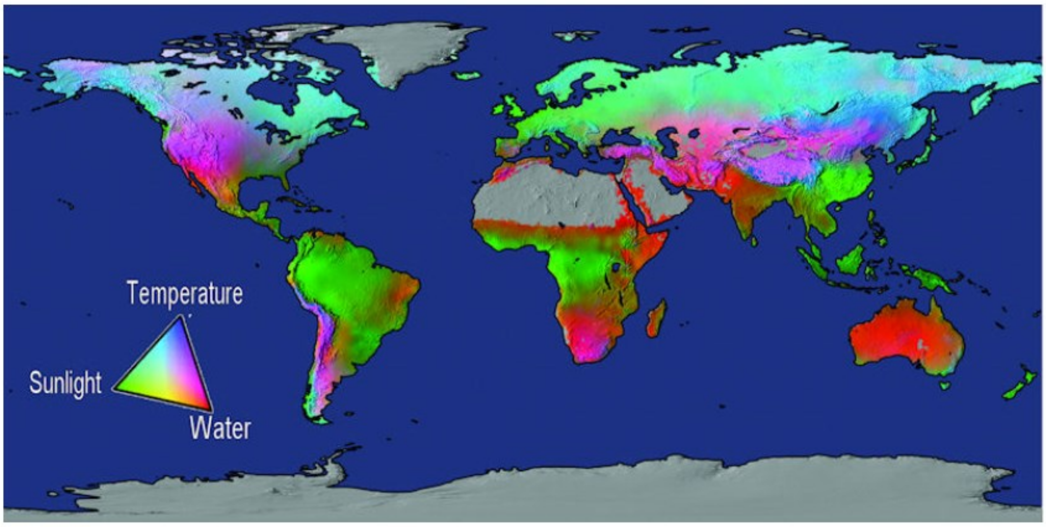

Figure 33: Potential limits to vegetation net primary production based on fundamental physiological limits by solar radiation, water balance, and temperature (from Churkina & Running, 1998; Nemani et al., 2003; Running et al., 2004). Source: http://www.ntsg.umt.edu/project/mod17

Nevertheless, temperature trends during the past decades have been found to influence vegetation activity, for instance in a recent study by Zhou et al. (2015). They detected a significant warming trend with an increasing rate of 0.052 °C/year in the years 1982-2012 covering over 90% of the vegetated areas in Central Asia (Figure 34), and correlated the temperature trends with vegetation activity trends by means of partial correlation and thus excluding the influence of rainfall trends. They concluded: "*The increasing temperature prompted* *vegetation greening before 1991 for most areas. However, in 1992–2011, this warming trend resulted in desiccation, suppressing the greening trend by increasing evapotranspiration and fire occurrences. The precipitation-controlled area expanded in 1992–2011, compared to 1982–1991*" (Zhou et al. 2015).

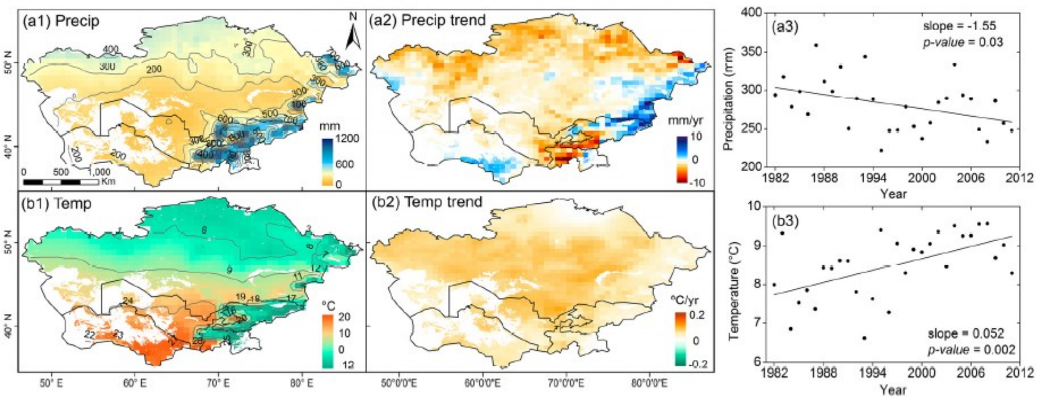

Figure 34: Precipitation and temperature trends 1982-2012 in Central Asia, source: Zhou et al. 2015

Also Sensoy et al. (2013) state, based on temperature trend analyses in Turkey: "*The most interesting feature in this time series is the relatively strong change in air temperature since 1994, which corresponds well to similar trends in many parts of the world* " (Houghton et al. 2001, cited by Sensoy et al. 2013).

3.7.2.6 MOD16 ET Evapotranspiration data

This ET data set is computed globally daily at 1km, using MODIS land cover and MODIS fAPAR/LAI data and global surface meteorology from the GMAO (Global Modeling and Assimilation Office) (http://www.ntsg.umt.edu/project/mod16#data-product, where also a brief description of the data is found). MOD16 ET data had been considered to be used for WUE - water use efficiency analyses in selected test sites. Such studies have for instance been performed for the conterminous United States by Lu and Zhuang (2010).

The different spatial patterns of water availability (first half of August 2004) are shown in Figure 35. While a general N – S gradient is common to all products; spatial detail and patterns deviate considerably. It can be easily envisaged that RUE, SMUE and WUE indicators derived with these different "water products" will vary significantly in spatial regards. Another presentation of differences between these data sets is given in Figure 36, where time series of GIMMS NDVI, TRMM rainfall, CCI soil moisture and MODIS evapotransporation are contrasted. While in the upper example (Caatinga, Brazil) a clear seasonal relation between all data sets exists, in the Namibian site, which is much dryer, the MODIS evaporation data do not show a seasonal behaviour analogue to the other data sets. The vegetation and water highs are not matched in the evapotranspiration data there. The same missing (or weak) temporal correlation between MODIS evapotranspiration data sets and other time series reflecting moisture conditions can be seen at other sites (not shown here). Thus the question arises especially with regard to the MODIS evapotranspiration data whether and/or where their usage can be expected to deliver meaningful Water Use Efficiency results. Figure 37 shows the pearson correlation coefficient between the timeseries data (one calendar year) of TRMM 3B42 rainfall and MODIS evapotranspiration, respectively. Pearson r varies significantly between climate zones, which can be expected, but it also varies substantially within and between the dryland sites, analogue to what has been stated above for the time series diagrams. Thus in regions with low correlations between the two, very different results for RUE and WUE can be expected. Due to these expected strong inconsistencies, we refrained from the usage of the ET data for the calculation of WUE indicators.

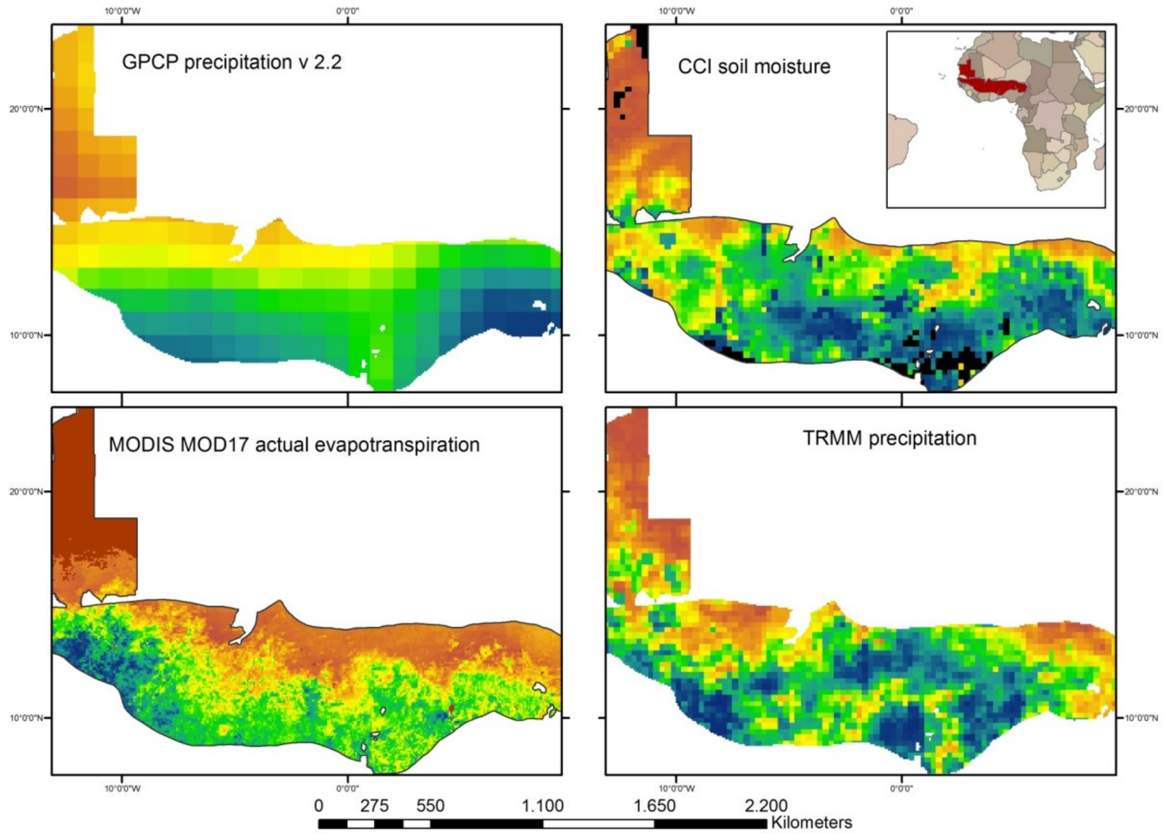

Figure 35: Different spatial patterns of the "water" data sets in the Sahel test site of the first half of August 2004. (relative scaling was adjusted, a general N to S gradient of increasing moisture from orange to green / blue tones can be seen in all products.

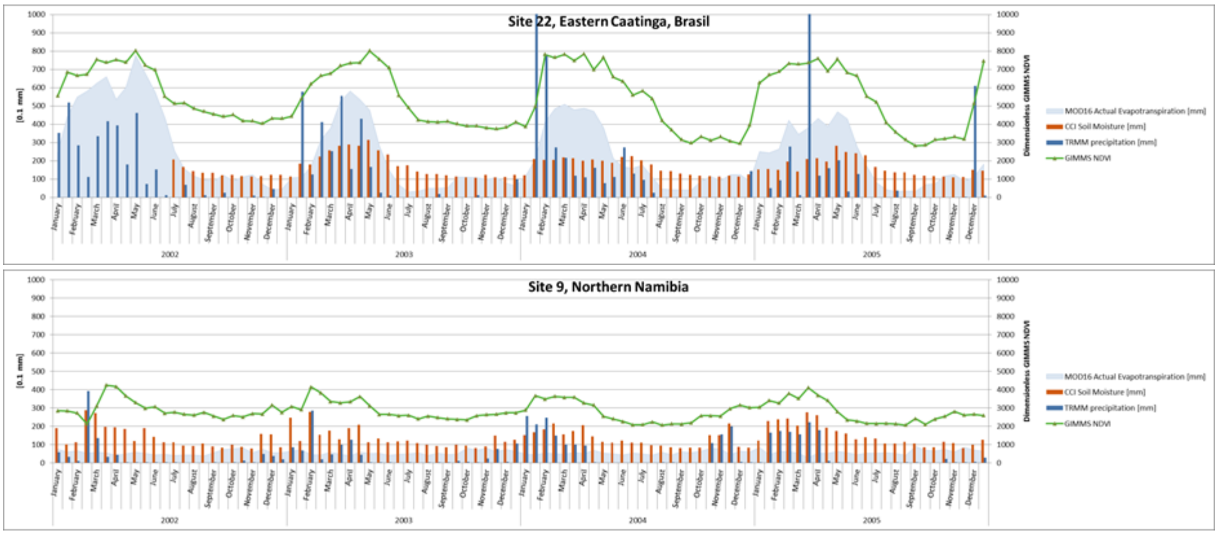

Figure 36: Comparative time series of GIMMS NDVI, TRMM rainfall, CCI soil moisture, and MODIS evapotranspiration for two dryland test sites

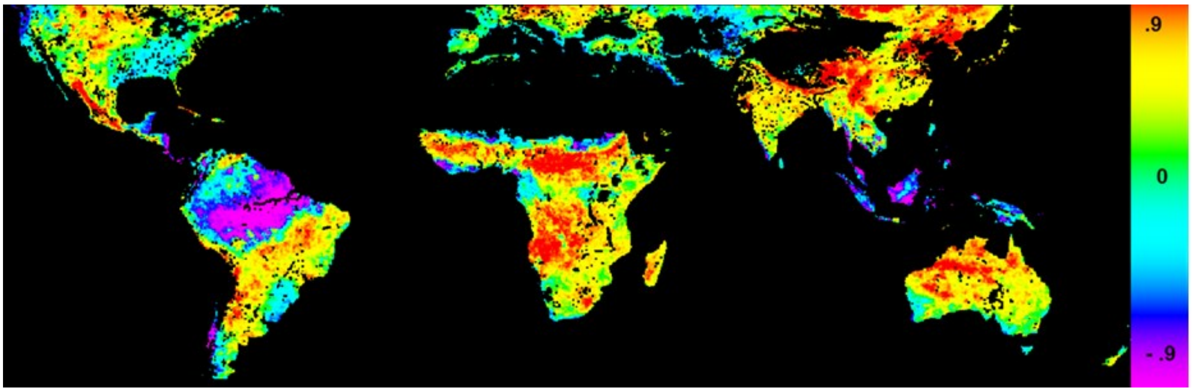

Figure 37: Pearson correlation coefficient between one year time series of TRMM rainfall data and MODIS evapotranspiration data (missing areas are due to TRMM 3B42 data gaps)

3.7.3 AVHRR NDVI

3.7.3.1 Rational and objective

The NOAA AVHRR GIMMS NDVI time series (http://glcf.umd.edu/data/gimms/) reaches back to 1981 and provides thus a means to tie the relatively short MERIS time series into a longer observation of NPP. This way, the MERIS NPP status and trends can be better assessed, e.g. whether these MERIS years constitute part of an ongoing trend, or show the start of a new trend or vice versa. In the Diversity II project, NOAA GIMMS NDVI 3g data were quite extensively used for the following reasons and purposes:

- This data has been investigated in a large number of studies, which provide useful reference information to this project
- Vegetation trends of NOAA GIMMS derived in Diversity II have been compared to the MERIS fAPAR based trends (see PUH section 3.5.10) to check the consistency of the applied methods. In addition, various further GIMMS based applications of the Diversity II methodology are demonstrated in the PUH.
- For demonstrating past trends prior to the period with MERIS data and comparison of the developments within the MERIS periods to the preceding 20 years: based on the GIMMS NDVI data and GPCP rainfall data, the vegetation trends versus rainfall trends were expressed in a second order product.

3.7.3.2 GIMMS3g NDVI

NOAA AVHRR GIMMS3g NDVI data cover the period from 1981 to 2011 and constitute the latest release of this unique long-term NDVI time series of the GIMMS research group (Fe). The data is available in 0.07 x 0.07° ground resolution and half-monthly time intervals (Tucker et al. 2004).

No pre-processing is necessary for the GIMMS NDVI data (phenological analysis not being regarded as pre-processing). Instead, the other auxiliary datasets were geometrically adapted to the GIMMS data as described earlier.

3.7.4 Modelled NPP data based on BETHY/DLR

For test sites 04 Northern Kazakhstan and 12, Southern Africa West modelled NPP time series data have been processed and compared to the MERIS based indicators. The NPP data were derived with the most recent version (spring 2015) of BETHY/DLR (Biosphere Energy Transfer Hydrology Model, DLR), and provided by M. Tum and K. Günther (DLR).

BETHY/DLR is a soil-vegetation-atmosphere-transfer (SVAT) model that was modified to the usage with meteorological and EO based vegetation time series data (Wißkirchen et al. 2013, Tum 2012). BETHY/DLR has been tested for several regions in the world. It is used at DLR to estimate sustainable bioenergy potentials. It employs remote sensing products (Albedo, LAI, Landcover, CO_2 concentration, elevation), meteorological parameters (Wind speed, Temperature, Precipitation, PAR), climatic zones, and static data, i.e., soil types. Figure 38 provides an overview of the input data used. BETHY/DLR is currently assessed at continental to country scales.

The BETHY NPP data were generated as monthly NPP sums in grams C/m² and 1km² pixel size (at the equator). For comparisons to the MERIS fAPAR derived NPP proxies, they were converted into half-monthly values and 300m*300m pixel size, and then aggregated into sum values per vegetation year, starting from 2003 and ending 2010, exactly like the MERIS fAPAR based NPP proxies.

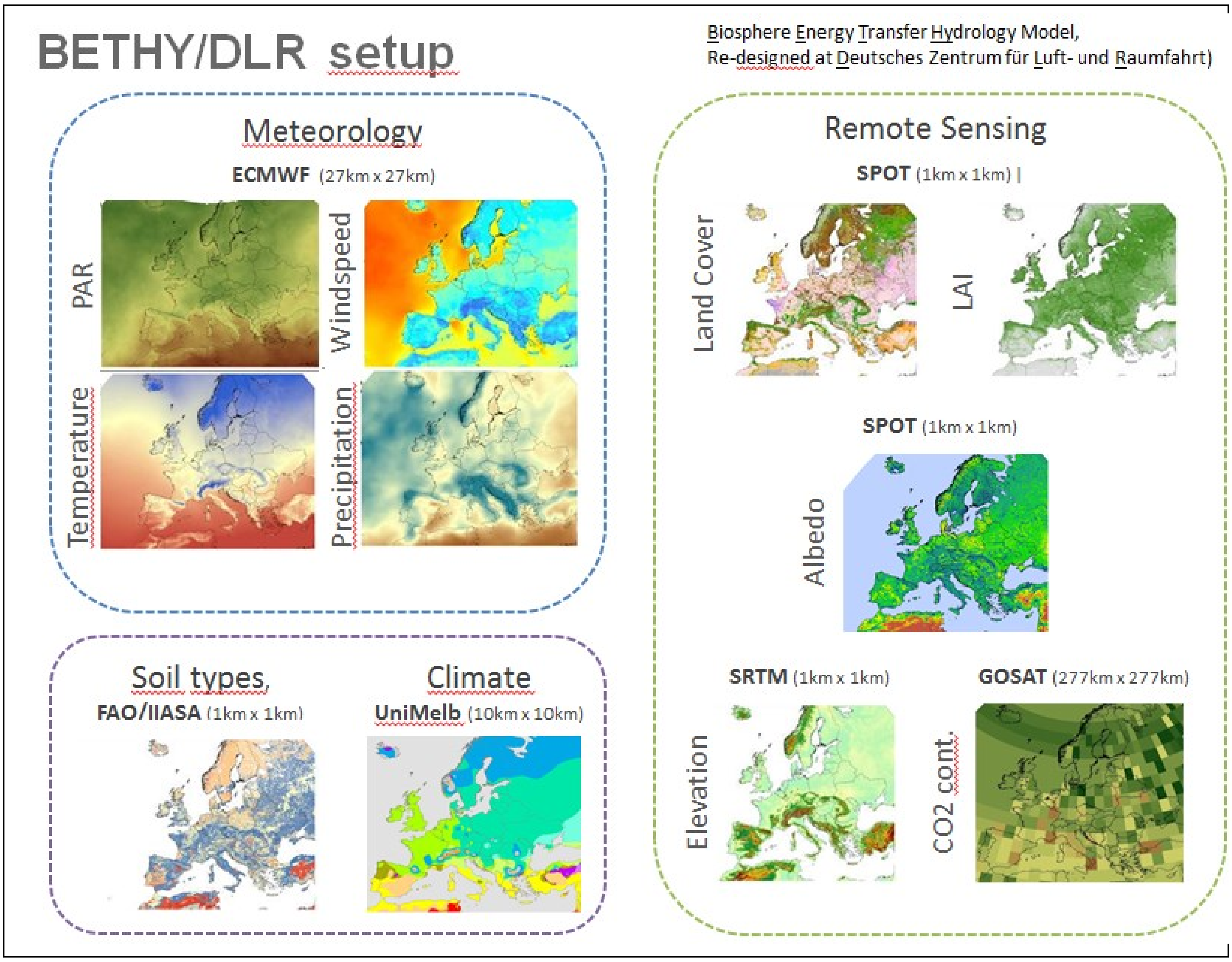

Figure 38: Input data used for BETHY/DLR, overview provided by M. Tum, DLR

The BETHY/DLR derived NPP data were provided as monthly time series data for the entire MERIS period (2002-2012). For adaptation to the half-monthly data used in Diversity II, the monthly data were split into two half-monthly data sets with half of the NPP amount of the respective monthly value each. The resulting half-monthly time series data were then smoothed with a gliding mean over three half-monthly values, i.e. each data value was replaced by the mean of the value itself, the preceding value and the following value.

The resulting half-monthly time series data were processed with the Diversity II tools in order to derive the most essential first order products and to compare these to the corresponding fAPAR based products. The comparison results are reported in the PUH, section 3.5.3 and in the PQR,

While we are dealing with NPP data in this context as opposed to “only” NPP proxies generated in Diversity II, we must be aware that the data are originating from models, underlying assumptions and input data with their own uncertainties. Thus the performed comparisons will also depend on the uncertainties associated with the BETHY/DLR NPP data. These depend for instance on the underlying SPOT Vegetation based LAI data or the GLC land cover data and their parametrisation in the model, where the alignment with GLC land cover boundaries for example is quite obvious in the BETHY/DLR NPP data. Nevertheless, such comparisons help building confidence in both products, if they show the expected commonalities. For this reason the comparison results were deliberately published in the PUH. Discrepancies on the other hand, which were partially also observed, should serve as valuable incentive to further study and improve the data sets and models.

4 Algorithms Lakes Processing

4.1 Water Quality Retrieval

Water quality is estimated from MERIS data (optically relevant constituents) and AATSR data (lake surface temperature emission). The former will be processed by means of several different algorithms, while the latter have already been processed to higher-level products and is described in Section 4.1.5.

4.1.1 Optical Water Types Identification

The Optical Water Type algorithm (OWT) separates input water-leaving reflectance spectra in seven classes, according to their fuzzy membership in classes that were clustered from in situ reflectance measurements (Moore, Dowell, Bradt, & Ruiz Verdu, 2014). Types 1-3 represent clear to absorption-dominated waters, class 4-5 represent highly productive waters, and class 6-7 are for high levels of turbidity. These seven endmember spectra are depicted in Figure 39. A mode-aggregated L3 product layer representing the dominant OWT per time interval for each pixel is provided with the Diversity II inland water products.

The applicability of OWT was assessed using CoastColour (CC) atmospheric corrected MERIS and in situ water-leaving reflectance spectra (see Section 3.6.3.1 for a description of the in situ data). 42 matchup comparisons in 10 lakes are available.

- In 21 cases, the same class is assigned to the CC and the corresponding in situ spectrum
- In 14 cases, the classes are adjacent
- In 7 cases, the classes are farther apart. 5 out of these 7 cases are combinations of OWT 1 and OWT 3, which are of relatively high optical similarity (examples in Figure 39).

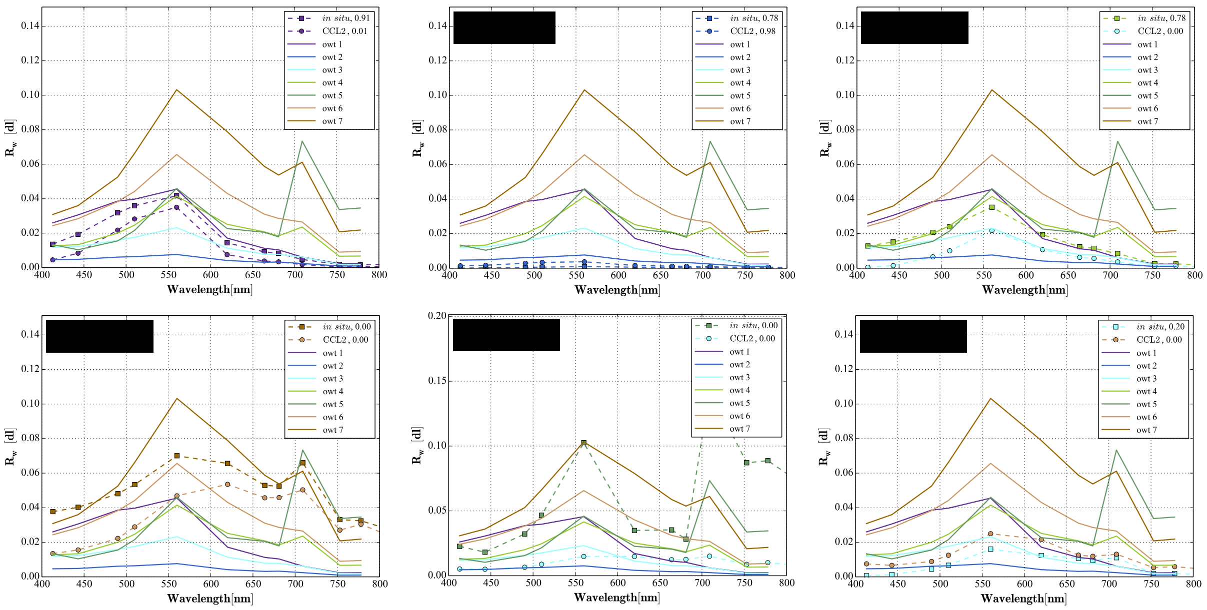

Figure 39: In situ and CC atmospherically corrected spectra and corresponding water types in Lakes Zurich, Paijanne, Loskop (upper left to right), Kasumigaura, Hartbeespoort and Peipsi (lower left to right). The floating point numbers in the legend indicate the calculated class membership.

In summary, the evaluated OWT results allow for a quite robust separation of classes 1-3 from classes 4-7, although the uncertainties of the CoastColour atmospheric correction have a significant impact on the retrieved OWT within these two groups. This result is sufficient to provide a decision criterion for the selection of the FUB CHL product (classes 1-3) or the MPH CHL product (classes 4-7) as described in Section 4.1.3.

4.1.2 Theoretical background of Water Constituent Retrieval

Water constituent retrieval means to calculate inherent optical properties (IOPs) or concentrations for individual or multiple water constituents from an apparent optical property (AOP), usually water-leaving reflectance (R_w) or irradiance reflectance (R^-) (IOCCG & Lee, 2006). Definitions of relevant constituents vary, but include most commonly Chlorophyll-*a* (CHL), Total Suspended Matter (TSM) and Coloured Dissolved Organic Matter (CDOM), The corresponding IOPs are pigment absorption (a_{CHL}), particle scattering (b_{TSM}) and occasionally detritus absorption (a_{DET}), and CDOM absorption (a_{CDOM}), respectively.

Several different approaches were demonstrated to achieve this task, and there are several different ways to classify these approaches. An extensive review of validated approaches published between 2006-2011 is provided in Odermatt et al. (2012). They describe separately spectral inversion algorithms and band arithmetic algorithms. Neural networks are the most prevailing representatives of the former, due to the limited availability and challenges in parameterization of non-linear optimization algorithms. Based on simulated reflectance training data and predefined, accustomed IOPs, neural networks achieve good closure with satellite retrieved reflectance at relatively low constituent concentrations. The increasing optical variety in very turbid waters is usually represented less accurately, either because of limitations in the concentration training ranges, or because of the limited appropriateness of the training IOPs. Band arithmetic algorithms on the other hand work most accurately with simple spectral features that can be related to an individual constituent, typically the (differential) reflectance peak at 700 nm for CHL, or the reflectance magnitude at NIR and SWIR bands for TSM. However, such features are increasingly masked at lower concentrations, either by the other constituents or atmosphere related error sources. A special case in this regard are the Ocean Colour algorithms, which work even at very low CHL concentrations, but only in case the abundances of TSM and CDOM are strictly proportional to the CHL level, as in the open ocean.

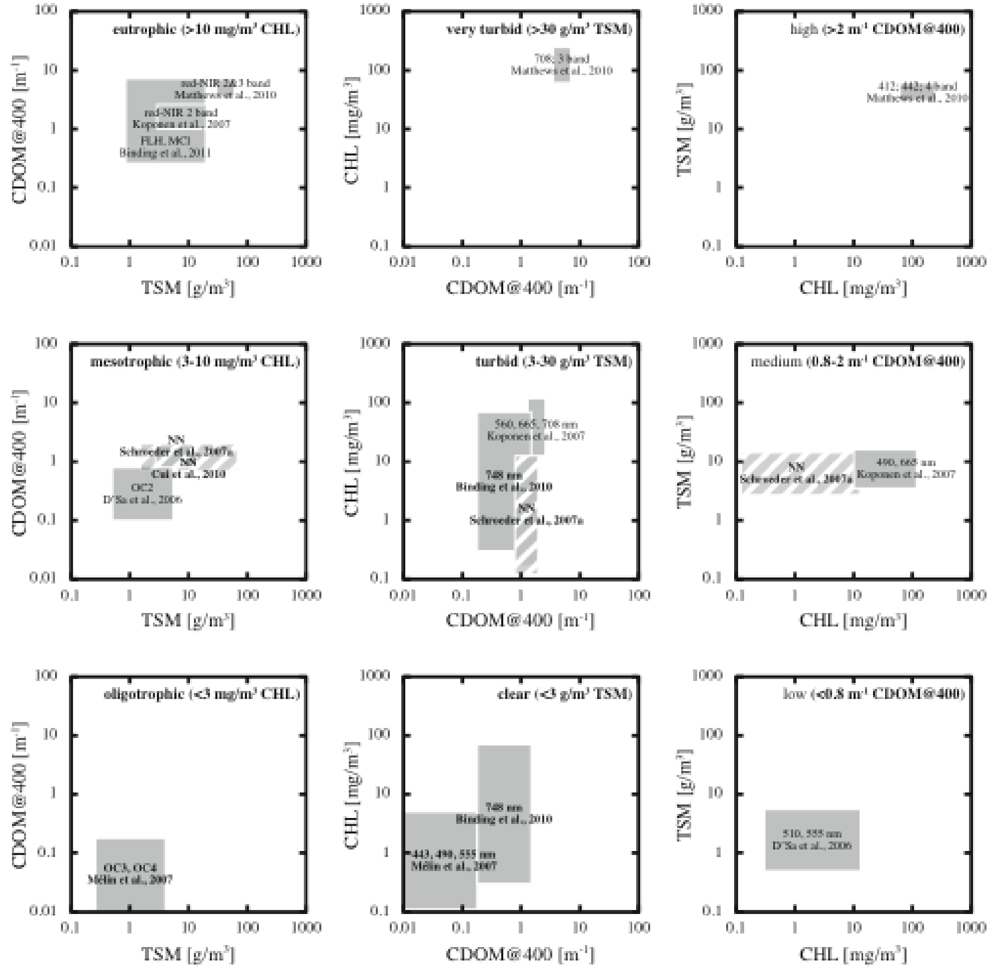

Figure 40: Case 2 water classes for CHL (left column), TSM (center) and CDOM (right) concentrations, with high to low concentration classes from top to bottom, and the remaining two constituents varying in x- and y-directions of each box. Class names and concentration ranges are titled in each box. Algorithm validation ranges are indicated as boxes and labeled with corresponding retrieval methods or center wavelengths. Bold labels indicate validation experiments with >10 images, hatched areas indicate simultaneous retrieval of all constituents. Reading example: Binding et al.(2010a) validate the FLH and MCI algorithms for CHL in eutrophic waters with 0.85–19.60 g/m3 TSM and 0.26-7.14 m– 1 CDOM. From Odermatt et al. (2012)

4.1.3 Candidate Algorithms for Water Constituent Retrieval

4.1.3.1 Case 2 Regional and CoastColour

The C2R algorithm (Doerffer & Schiller, 2007, 2008a) and CoastColour algorithms (Doerffer, Brockmann, Röttgers, Moore, & Dowell, 2012) are based on the simulated relationship between IOPs (i.e. absorption and scattering of components, such as CHL, CDOM and TSM) and water leaving reflectances. The multi-variate non-linear relationship between IOPs and reflectance is inverted using a neural network (NN), which relates the bidirectional water leaving radiance reflectances with corresponding IOPs. Simple conversion factors are finally used to translate the components' IOPs into the respective concentrations.

Regionalization of C2R is achieved through the training of separate networks, which consist of site-specific IOPs, constituent concentration training ranges and distributions, and IOP to concentration conversion factors. C2R is based on a bio-optical model constructed from measurements in European coastal waters, and the frequency distribution for the training simulations was randomized for bulk absorption and scattering rather than individual IOPs, in order not to bias the solution space. An overview of the C2R (and FUB) training ranges and conversion equations is given in Table 9. The CoastColour algorithm is a newer version of C2R that is trained with an extended range of concentrations and a revised IOP model.

Table 9: Training ranges and IOP to concentration conversion equations for the C2R and FUB algorithm, updated from Odermatt et al. (2012). The concentration ranges for the CoastColour (C2R heritage) algorithm are 0.03-1000 g/m^3 TSM and 0.03-500 mg/m^3 CHL.

	C2R		FUB	
a_{pig} range [1/m]	0.001	2	0.008	0.62
CHL-*a* range [mg/m^3]	0.016	43.181	0.05	50
Eq.	a_{pig} = 0.054 CHL-$a^{0.96}$		a_{pig} = 0.052 CHL-$a^{0.635}$	
b_{whit} range [1/m]	-	-	-	-
b_{part} range [1/m]	0.005	30	0.025	25
TSM range [g/m^3]	0.009	51.9	0.05	50
Eq.	b_{part} = 0.578 TSM		b_{part} = 0.5 TSM	
a_g range [1/m]	0.005	5	0.005	1
a_d range [1/m]	-	-		

4.1.3.2 FUB

The FUB algorithm (Schroeder et al. 2007a, 2007b) is applied to MERIS level 1b data and is based on four separate artificial NN which were trained with extensive radiative transfer simulations with the MOMO code (Fell & Fischer, 2001; Juergen Fischer & Grassl, 1984). One of the four NN conducts atmospheric correction to retrieve aerosol optical thickness (AOT) and bottom of atmosphere reflectances, while the other three retrieve water constituents directly from top of atmosphere reflectance. It makes use of MERIS level 1B TOA of bands 1-7, 9-10 and 12-14 as inputs and retrieves CHL and TSM concentrations, CDOM absorption, aerosol optical depth and reflectances in bands 1-7 and 9. The algorithm was trained with literature collected IOPs. A certain degree of covariance among the water constituents is assumed in order to prevent a bias towards unrealistic single component solutions. Figure 41 displays the distribution of applicable constituent combinations corresponding to the following covariance boundaries:

$$TSM(CHL)_{\min} = 0,12\,CHL^{0,77} \quad , \quad TSM(CHL)_{\max} = 5,89\,CHL^{0,77}$$
$$YEL(CHL)_{\min} = 0,079\,CHL^{0,75} \quad , \quad YEL(CHL)_{\max} = 0,25\,CHL^{0,75}$$
$$YEL(TSM)_{\min} = 0,0063\,TSM^{0,9} \quad , \quad YEL(TSM)_{\max} = 0,44\,TSM^{0,9}$$

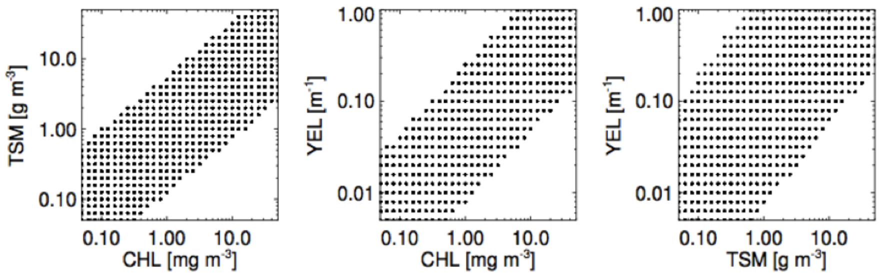

Figure 41: Distribution of valid concentration cases after application of the FUB covariance constraints.

4.1.3.3 Constituent retrieval by feature specific band arithmetic

Band arithmetic algorithms are derived by empirical regression or semi-analytical inversion of measurements or simulations. A comprehensive summary of proposed algorithms is given in Matthews (2011). Most of them consist of ratios or normalized differences, and become therefore less sensitive to atmospheric effects. In consequence, these algorithms can be tuned for various TOA, BRR or reflectance signals. For Diversity II, a selection of band arithmetic algorithms for CHL (9 different ones, see Table 10), TSM (4 different ones, Table 11) and Secchi depth/Turbidity retrieval (2 different ones, Table 12) are evaluated in accordance to regional studies by Matthews et al. (2010) and S. Palmer (pers. Comm.) for South African Lakes and Lake Balaton, respectively.

Table 10: Evaluated arithmetic algorithms for CHL estimation in inland waters.

Name	Input	Bands	Algorithm	Reference
2-band red-NIR v.1	All (index)	B8: 681 B9: 708	$B9*B8^{-1}$	(K Kallio et al., 2001)
2-band red-NIR v.2	All (index)	B7: 665 B9: 708	$B9*B7^{-1}$	(Ammenberg, Flink, Lindell, Pierson, & Strombeck, 2002; Gons, 2004; K Kallio et al., 2001; Moses et al., 2009)
2-band red-NIR v.3	All (index)	B7: 665 B9: 708	$(B9-B7)* (B9-B7)^{-1}$	(Gómez, Alonso, & García, 2011)
3-band red-NIR	All (index)	B7: 665 B9: 708 B10: 753	$B7^{-1}*B9^{-1}*B10$	(Gitelson et al., 1993; Moses et al., 2009)
Fluorescence Line Height (FLH)	All (index)	B7: 665 B8: 681 B9: 708	B8-B7-(B9-B7)*0.372	(Binding, Greenberg, Jerome, Bukata, & Letourneau, 2010b)
Maximum Chl. Index (MCI)	All (index)	B8: 681 B9: 708 B10: 753	B9-B8-(B10-B8)*0.375	(Binding et al., 2012)
OC2v4	R_w	B3: 490 B5: 560	R=log10(B3/B5) $chl=10^{(0.319-2.336R+0.879R^2-0.135R^3-0.071)}$	oceancolor.gsfc.nasa.gov
OC4v4	R_w	B2: 443 B3: 490 B4: 510 B5: 560	R=log10(max(B2:B4)/B5) $chl=10^{(0.366-3.067R+1.930R^2+0.649R^3-1.532R^4)}$	oceancolor.gsfc.nasa.gov
MPH	R_{BR}	B6: 620 B7: 665 B8: 681 B9: 708 B10: 753 B14: 885	See ref.	(Mark William Matthews et al., 2012; Mark William Matthews & Odermatt, 2015)

Table 11: Evaluated arithmetic algorithms for TSM estimation in inland waters.

Name	Input	Bands	Algorithm	Reference
2-band NIR	All (index)	B9: 708 B10: 753	B9-B8	(Härmä et al., 2001)
3-band vis-NIR	All (index)	B5: 560 B7: 665 B9: 708	$B9*(B5+B7)^{-1}$	(Sampsa Koponen et al., 2007)
band 7 relation	All (index)	B7: 665	B7	-
band 12 relation	All (index)	B12: 778	B12	-

Table 12: Evaluated arithmetic algorithms for Turbidity and Secchi depth estimation in inland waters.

Name	Input	Bands	Algorithm	Reference

OCK490	R_w	B3: 490 B5: 560	$0.1565*(B3/B5)^{-1.540}$	oceancolor.gsfc.nasa.gov
3-band Secchi	All (index)	B3: 490 B6: 620 B10: 753	$(B3-B10)*(B6-B10)^{-1}$	

4.1.4 Validation of Water Constituent Retrieval Algorithms

4.1.4.1 In situ data

Water constituent concentrations from 7 out of the 10 originally selected prototype lakes, and for 42 lakes in total are gathered, including both water quality monitoring measurements as well as remote sensing validation campaign measurements. The latter is in most cases related to the spectro-radiometric measurements described in Section 3.6.3.1 and accordingly of limited spatio-temporal representativeness. The variety in measurements techniques is equally wide as for spectro-radiometric measurements, especially in the case of monitoring data. This includes different sampling techniques, lab analysis methods or probe deployment. Their suitability for comparison with remote sensing depends on many factors and can only partly be estimated from data provider declarations and metadata. It is thus assessed retrospectively, i.e. datasets where none of the applied EO algorithm procedures leads to a sufficient agreement are considered to either represent lakes of extraordinary bio-optical conditions, or be inapplicable for validation due to the specific acquisition technique. The following paragraphs document individual modifications applied for some of the datasets. An overview of all available datasets is given in Table 13.

In the Lake Balaton dataset by Matyas Presing, a measurement taken on 19 Sept 2011 (46.48 mg/m3 CHL, 160.91 g/m3 TSM) was removed from the analysis in order to prevent a distorted regression. This sample was taken just after a storm and represents an exceptionally high TSM value, with the range of all other matchups being between 0-50 g/m3.

In Lake Champlain, Chlorophyll-a and TSS samples are collected using a vertically-integrated hose-sampler beginning at the lake surface to a depth representing twice the Secchi depth (VTDEC,2006). Measurements taken at more than 10 m depth (corresponding to 5 m Secchi depth) are removed from the analysis in order to reduce known inaccuracies occurring in such composite samples (Odermatt et al., 2010).

The Lake Geneva data by INRA-CARRTEL consists of 50 Secchi disk measurements. They were taken aside 195 measurements with a different contrasting INRA panel. The 50 combined measurements were used in a linear regression, whereas zsecchi = 0.83 zINRA + 0.25 ($R2=0.96$). All 195 INRA panel measurements are converted according to this relationship and used for further analysis.

In the Lake Hartbeespoort monitoring dataset, a measurement taken at the very surface on 7 May 2008 (4357.75 mg/m3 CHL) was removed from the analysis in order to prevent a distorted regression, with all other (valid) matchup data points being at < 500 mg/m3.

In Lake Michigan similarly, all data measured at depths larger than 5 m are removed, and only the topmost measurement usually at 2 or 5 m was used where vertically resolved observations are available. 207 measurements are commented as erroneous or not quality checked and thus also excluded.

For Lake Vanern, the CDOM measurements are measured as absorbance of filtered samples at 420 nm, and then divided by 0.028726 to get CDOM absorption at 440 nm. Only 3 TSM measurements for Vanern are available and thus omitted, as well as all 3 CHL measurements with the value “<1 mg/m3”.

The Lake Victoria measurements were collected by several different investigators in different years. The datasets from each campaign are processed separately since consistent quality among the datasets is rather unlikely. All data that can not be assigned to a specific investigators is tagged as ‘various’.

Table 13: Water constituent data available for matchup analyses. The column "No." indicates the number of matchups prior to invalid pixel flagging, whereof multiple samples corresponding to one pixel are counted only once.

Lake name	Data source	Parameters	No.
Albert Falls -29.436/30.388	Mark Matthews mttmar017@myuct.ac.za	CHL [mg/m^3]	199
Balaton A 46.80/17.70	Matyas Presing presing.matyas@okologia.mta.hu	CHL [mg/m^3] TSM [g/m^3]	252 259
Balaton B 46.80/17.70	KdtVI[1] www.kdtvizig.hu	CHL [mg/m^3] TSM [g/m^3]	816 179
Bronkhorstspruit -25.887/28.721	Mark Matthews mttmar017@myuct.ac.za	CHL [mg/m^3]	277
Champlain 43.715/-73.383	- www.vtwaterquality.org	CHL [mg/m^3] TSM [g/m^3] Secchi [m]	2053 557 2528
Erie A 42.200/-81.200	Environment Canada caren.binding@ec.gc.ca	CHL [mg/m^3] Secchi [m]	2196 5139
Erie B 42.200/-81.200	EPA sn.greb@wi.gov	CHL [mg/m^3] Turbidity [ntu]	743 500
Eyre -28.30/137.30	-	-	-
Geneva 46.389/6.421	Ghislaine Monet ghislaine.monet@thonon.inra.fr	CHL [mg/m^3] (Fluorescence probe) CHL [mg/m^3] (Laboratory) Turbidity [ftu] Secchi [m]	187 190 169 195
Hartbeespoort -25.726/-27.849	Mark Matthews mttmar017@myuct.ac.za	CHL [mg/m^3] PHYCO [mg/m^3] TSM [g/m^3] CDOM [m^{-1}@442nm] a_{pig} [m^{-1}@442nm] Secchi [m]	4 4 4 4 4 4
Huron 44.800/-82.400	Environment Canada caren.binding@ec.gc.ca	CHL [mg/m^3] Secchi [m]	117 1143
H. Georgian Bay 45.500/-81.000	Environment Canada caren.binding@ec.gc.ca	CHL [mg/m^3] Secchi [m]	90 225
Kasumigaura 36.065/140.233	CEBES cebes.data@nies.go.jp	CHL [mg/m^3] PHYCO [mg/m^3] TSM [g/m^3] Secchi [m]	1110 360 1110 1110

[1] Central Transdanubian (Regional) Inspectorate for Environmental Protection, Nature Conservation and Water Management

Lake name	Data source	Parameters	No.
Klipvoor -25.134/27.812	Mark Matthews mttmar017@myuct.ac.za	CHL [mg/m^3]	277
Loskop -25.418/29.360	Mark Matthews mttmar017@myuct.ac.za	CHL [mg/m^3] TSM [g/m^3] CDOM [m^{-1}@442nm] a_{pig} [m^{-1}@442nm] Secchi [m]	8 8 8 8 8
Michigan A 44.00/-87.00	Chris Strait cstrait@upstatefreshwater.org	CHL [mg/m^3] TSM [g/m^3] CDOM [m^{-1}@400nm] a_{pig} [m^{-1}@440nm]	15 12 15 15
Michigan B 44.00/-87.00	EPA (Mar/Apr, Aug cruises) Steven.Greb@wisconsin.gov	CHL [mg/m^3] Turbidity [ntu] c_{tot} [m^{-1}@660nm] T_{horiz} [%]	438 381 417 418
Midmar -29.501/30.2	Mark Matthews mttmar017@myuct.ac.za	CHL [mg/m^3]	201
Natron -2.40/36.00	Emma Tebbs ejt15@le.ac.uk	TSM [g/m^3] CDOM [m^{-1}@440nm] ISS [g/m^3]	4 (3 repetitions) 4 (3 repetitions) 4 (3 repetitions)
Neagh 54.618/-6.395	Peter Hunter p.d.hunter@stir.ac.uk	CHL [mg/m^3]	256
Nicaragua 11.60/-85.40	Steve Greb sn.greb@wi.gov	CHL [mg/m^3] TSM [g/m^3] CDOM [m^{-1}@400nm] a_{pig} [m^{-1}@440nm] Secchi [m] Turbidity [ntu]	17 17 17 17 17 17
Of the Woods 49.249/-94.750	Environment Canada caren.binding@ec.gc.ca	CHL [mg/m^3] Secchi [m]	253 242
Ontario 43.700/-77.900	Environment Canada caren.binding@ec.gc.ca	CHL [mg/m^3] Secchi [m]	2088 1989
Paeijaenne 61.50/25.30	Sampsa Koponen sampsa.koponen@ymparisto.fi	CHL [mg/m^3] TSM [g/m^3] CDOM [m^{-1}@400nm] Secchi [m]	234 11 9 11
Peipsi 58.70/27.50	Tiit Kutser tiit.kutser@sea.ee	CHL [mg/m^3] TSM [g/m^3] CDOM [m^{-1}@400nm] Secchi [m]	364 9 9 289
Simcoe 44.436/-79.339	Environment Canada caren.binding@ec.gc.ca	CHL [mg/m^3] Secchi [m]	63 108
Spanish Lakes	Antonio Ruiz-Verdú	CHL [mg/m^3]	204

Lake name	Data source	Parameters	No.
40.417/-3.704	alandar@gmail.com	PHAEO [mg/m^3] k_d [m^{-1}] CDOM [m^{-1}@400nm] Secchi [m]	158 92 28 219
St. Clair 42.467/-82.667	Environment Canada caren.binding@ec.gc.ca	CHL [mg/m^3] Secchi [m]	40 238
Sterkfontein -28.448/29.022	Mark Matthews mttmar017@myuct.ac.za	CHL [mg/m^3]	79
Superior 47.700/-87.500	Environment Canada caren.binding@ec.gc.ca	Secchi [m]	354
Tahoe 39.10/-120.05	-	-	-
Vaal -26.883/28.117	Mark Matthews mttmar017@myuct.ac.za	CHL [mg/m^3]	179
Vaalkop -25.309/27.475	Mark Matthews mttmar017@myuct.ac.za	CHL [mg/m^3]	117
Vaenern 55.80/13.00	Petra Philipson petra.philipson@brockmann-geomatics.se	CHL [mg/m^3] CDOM [m^{-1}@440nm] Turbidity [fnu] Secchi [m]	505 454 55 1207
Victoria -1.50/33.00	Kai Sorensen kai.sorensen@niva.no	CHL [mg/m^3] TSM [g/m^3] Turbidity [ntu] Secchi [m]	350 47 179 318
Zug 47.099/8.492	Ct. of Zug Environmental Agency peter.keller@bd.zg.ch	CHL [mg/m^3] Secchi [m] Turbidity [ntu]	107 110 107
Zurich 47.344/8.560	Water supply city of Zurich oliver.koester@zuerich.ch	CHL [mg/m^3]	234

4.1.4.2 Matchup Results and Algorithm Selection

All matchup data listed in Table 13 were compared with in total 74 different combinations of adjacency effect corrections (ICOL or none), atmospheric corrections (C2R, CCL2, FUB, BRR, Scape-M, none) and water constituent retrieval algorithms (as listed in 4.1.3). Several combinations are missing e.g. because an atmospheric correction algorithm does not output a band required by a retrieval algorithm, or because a retrieval algorithm explicitly needs a specific reflectance input type (e.g. BRR for MPH). Reference datasets with at least one processor combination achieving a correlation $R \geq 0.8$ with $n \geq 8$ are considered valid references and retained for the algorithm performance assessment. The linear regression results for MPH and the 14 reference datasets selected in such manner are depicted in Figure 42. MPH achieves in average R=0.71 across all datasets. When concerning a subgroup composed only of the 7 reference datasets with prevailing OWT 4-7, average R is even 0.82. However, for OWT 1-3 dominated datasets, average R is only 0.60. The FUB algorithm performs best in this subgroup, with R=0.64. If ICOL is applied in combination with FUB, R decreases to 0.53 for the OWT 1-3 reference data subgroup. All other matchup results are depicted in Figure 43.

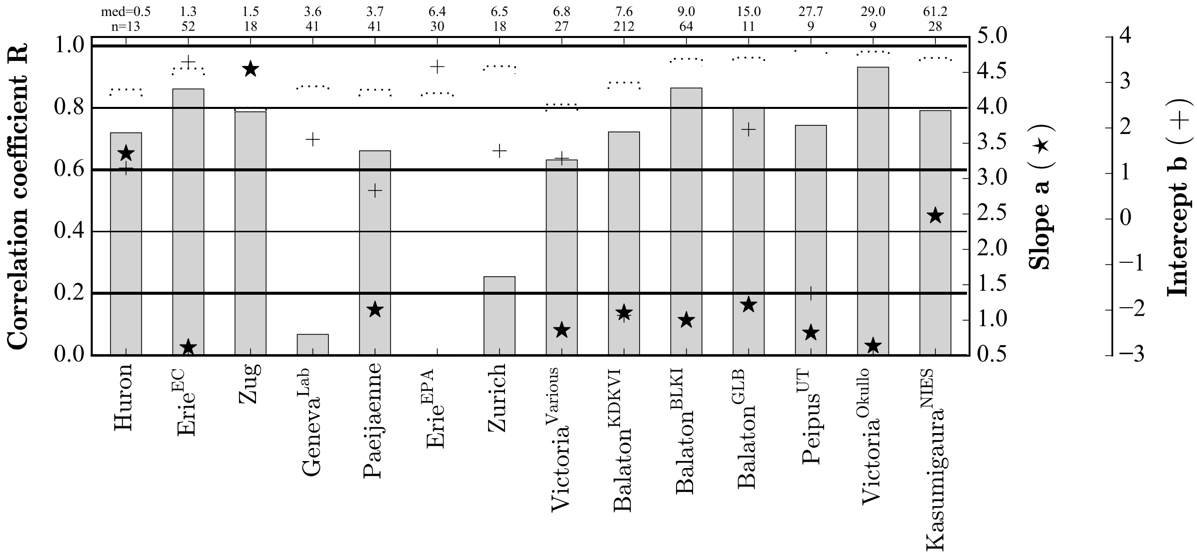

Figure 42: Algorithm performance for the MPH algorithm, for the 14 selected reference datasets. Bar height indicates R for the given algorithm (left y-axis), dotted bar tops indicate the highest R achieved by any of the 74 evaluated procedures. CHL median and n are given on top of each bar.

It is no surprise that MPH does not work equally well in oligotrophic OWTs 1-3, given that the spectral feature it is based on is hardly noticeable even in in situ spectroradiometric measurements for such waters (see examples in Section 3.6.3.2). Accordingly, a second CHL product from the FUB algorithm is provided for usage with lakes that are dominated by OWT 1-3. The difference between MERIS bulk reprocessed and previously available CoastColour MERIS FR input data is visible in the matchup data, but no significant and consistent improvement (nor such worsening) are visible in the constituent valiation data (see e.g. Figure 43).

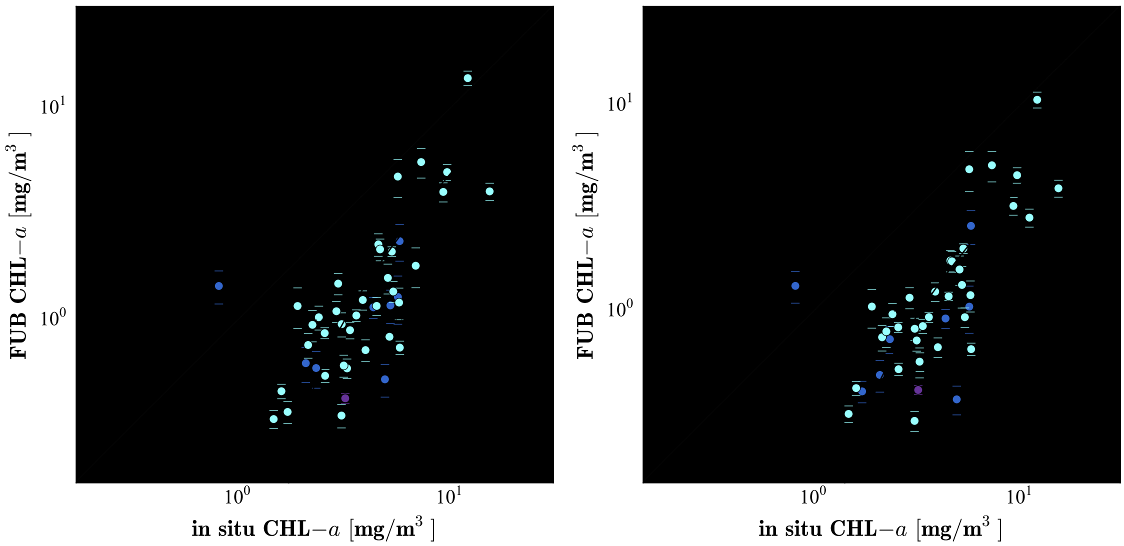

Figure 43: FUB CHL matchup scatter plots for Lake Geneva (Laboratoire data), using bulk reprocessed (left) or the previously available CoastColour MERIS FR input datasets.

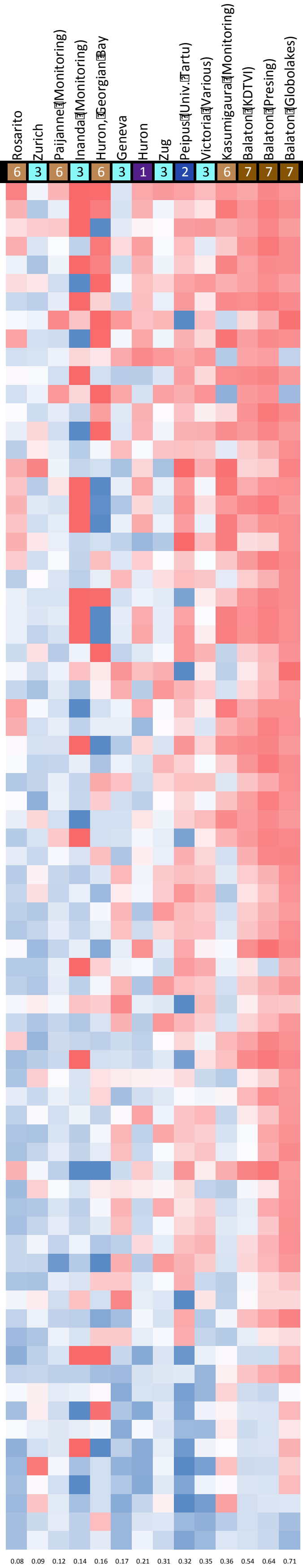

ADJ	AC	WC	Average R, OWT 1-7	Average R, OWT 1-3	Average R, OWT 4-7
-	CCL2	-			
-	BRR	MPH	**0.71**	0.60	**0.82**
-	BRR	3BAND	0.57	0.39	0.75
-	BRR	MCI	0.51	0.57	0.45
-	CCL2	3BAND	0.53	0.32	0.73
-	BRR	2BANDv2	0.52	0.37	0.67
-	SCAPE	MCI	0.49	0.35	0.64
-	BRR	2BANDv1	0.49	0.40	0.58
-	FUB	OC4v6	0.48	0.35	0.60
-	-	3BAND	0.47	0.21	0.73
-	FUB	FUB	0.44	**0.64**	0.25
ICOL	-	FLH	0.42	0.32	0.53
ICOL	FUB	FUB	0.44	0.53	0.35
-	CCL2	2BANDv1	0.45	0.29	0.62
-	-	MCI	0.45	0.27	0.64
-	C2R	2BANDv1	0.39	0.42	0.35
-	FUB	2BANDv2	0.44	0.32	0.55
-	-	2BANDv2	0.45	0.42	0.48
-	BRR	FLH	0.41	0.38	0.44
ICOL	-	2BANDv2	0.43	0.44	0.43
ICOL	FUB	2BANDv2	0.34	0.16	0.52
-	CCL2	2BANDv2	0.45	0.25	0.66
-	C2R	3BAND	0.35	0.38	0.32
-	SCAPE	3BAND	0.39	0.16	0.62
ICOL	-	2BANDv1	0.43	0.45	0.40
-	-	2BANDv1	0.41	0.44	0.38
ICOL	C2R	FLH	0.36	0.35	0.37
-	FUB	OC2v4	0.35	0.30	0.40
ICOL	C2R	2BANDv2	0.31	0.27	0.34
ICOL	-	3BAND	0.40	0.22	0.57
ICOL	CCL2	3BAND	0.33	0.07	0.60
-	-	FLH	0.39	0.38	0.39
ICOL	CCL2	CCL2	0.34	0.25	0.43
-	C2R	C2R	0.35	0.30	0.41
ICOL	CCL2	2BANDv1	0.32	0.04	0.60
ICOL	-	MCI	0.35	0.20	0.49
-	SCAPE	2BANDv2	0.34	0.18	0.50
-	CCL2	MCI	0.35	0.21	0.50
-	C2R	2BANDv2	0.34	0.41	0.28
ICOL	C2R	MCI	0.31	0.48	0.13
ICOL	C2R	C2R	0.30	0.27	0.32
-	C2R	C2R	0.32	0.30	0.33
-	CCL2	CCL2	0.32	0.28	0.36
-	SCAPE	OC2v4	0.32	0.39	0.25
ICOL	C2R	C2R	0.30	0.27	0.33
ICOL	FUB	OC4v6	0.31	0.25	0.38
ICOL	C2R	2BANDv1	0.27	0.27	0.27
ICOL	CCL2	2BANDv2	0.27	0.04	0.49
-	SCAPE	2BANDv1	0.24	0.08	0.40
-	CCL2	OC4v6	0.30	0.32	0.28
ICOL	CCL2	MCI	0.27	0.04	0.50
-	C2R	MCI	0.33	0.45	0.21
ICOL	C2R	OC4v6	0.27	0.26	0.28
-	C2R	OC4v6	0.27	0.25	0.29
-	SCAPE	FLH	0.28	0.16	0.40
-	CCL2	OC2v4	0.27	0.31	0.23
ICOL	C2R	OC2v4	0.25	0.26	0.24
-	C2R	OC2v4	0.24	0.25	0.23
-	C2R	FLH	0.27	0.32	0.22
ICOL	C2R	3BAND	0.16	0.30	0.01
ICOL	CCL2	OC4v6	0.21	0.19	0.23
ICOL	FUB	OC2v4	0.22	0.23	0.20
-	CCL2	FLH	0.14	0.06	0.23
ICOL	CCL2	OC2v4	0.18	0.19	0.17
-	SCAPE	2BANDv3	0.07	-0.07	0.20
ICOL	CCL2	FLH	0.06	-0.14	0.25
ICOL	C2R	2BANDv3	0.03	-0.16	0.22
-	-	2BANDv3	-0.01	-0.26	0.24
-	C2R	2BANDv3	0.06	-0.11	0.22
-	BRR	2BANDv3	-0.04	-0.03	-0.05
-	FUB	2BANDv3	-0.08	-0.29	0.13
ICOL	-	2BANDv3	-0.08	-0.27	0.10
ICOL	FUB	2BANDv3	-0.09	-0.27	0.09
ICOL	CCL2	2BANDv3	-0.13	-0.22	-0.04
-	CCL2	2BANDv3	-0.15	-0.20	-0.11

1
0.8
0.6
0.4
0.2
R=0
-0.2
-0.4
-0.6
-0.8
-1

Figure 44: All processing combinations (3 columns on the left) and their correlation (colour coded and in the 3 columns to the right) with the 14 reference datasets. The dominant OWT for each reference datasets is given in the second row.

4.1.5 Lakes Water Temperature

The Lake Surface Temperature (LWST) product layers were adopted from the ARC-Lake project (http://www.geos.ed.ac.uk/arclake). The initial phase of the ARC-Lake project focused on only large lakes, with surface areas > 500 km² as defined in (Lehner & Döll, 2004) and (Herdendorf, 1982). These 263 lakes included in the version 1 and version 2 databases were however supplemented in the version 3 database, where a total of 1628 lakes are included. 300 of these lakes coincide with the 345 selected Diversity II targets, which means only 13% of the final Diversity II products are without applicable LWST layer. The version 3 database also includes lakes of variable surface extent, which was enabled by a water detection algorithm (for day-time observations) and an annual minimum area for night-time observations. All processing steps are described in the Arc Lake ATBD (MacCallum & Merchant, 2013).

ARC Lake Products are available in various different aggregation formats, as described in the Diversity II Technical Specifications (TS, Daniel Odermatt et al., 2015). Examples for the DINEOF monthly aggregated 0.05° resolved spatial products are shown in Figure 45. Aggregates of night time acquisitions are provided together with aggregates of day time acquisitions, because different limitations apply, and depending on the application one or the other dataset may be favoured. The ARC Lake Validation Report for the v.1 products (MacCallum & Merchant, 2010) indicates an overall bias of 0.3 and -0.36 °K for the day and night time acquisitions, respectively (calculated as satellite minus in situ), and a relative standard deviation of 0.49 and 0.56 °K, respectively.

Due to the projects extensive own documentation, the ARC Lake LSWT products were not again systematically validated for Diversity II. Only one comparison with minimum winter LSWT for Lake Biwa was carried out for the Lake Biwa Biodiversity Story, using temperature data at 1 m depth provided by the Center for Ecological Research of the Kyoto University. The agreement is very good for the first five years but less so in 2008, 2010 and later years (2009 reference data missing, Figure 45). This divergence is however also owed to the 1 m depth at which the topmost Lake Biwa water temperature measurements are taken; as opposed to LSWT buoy measurements used in the ARC Lake validation.

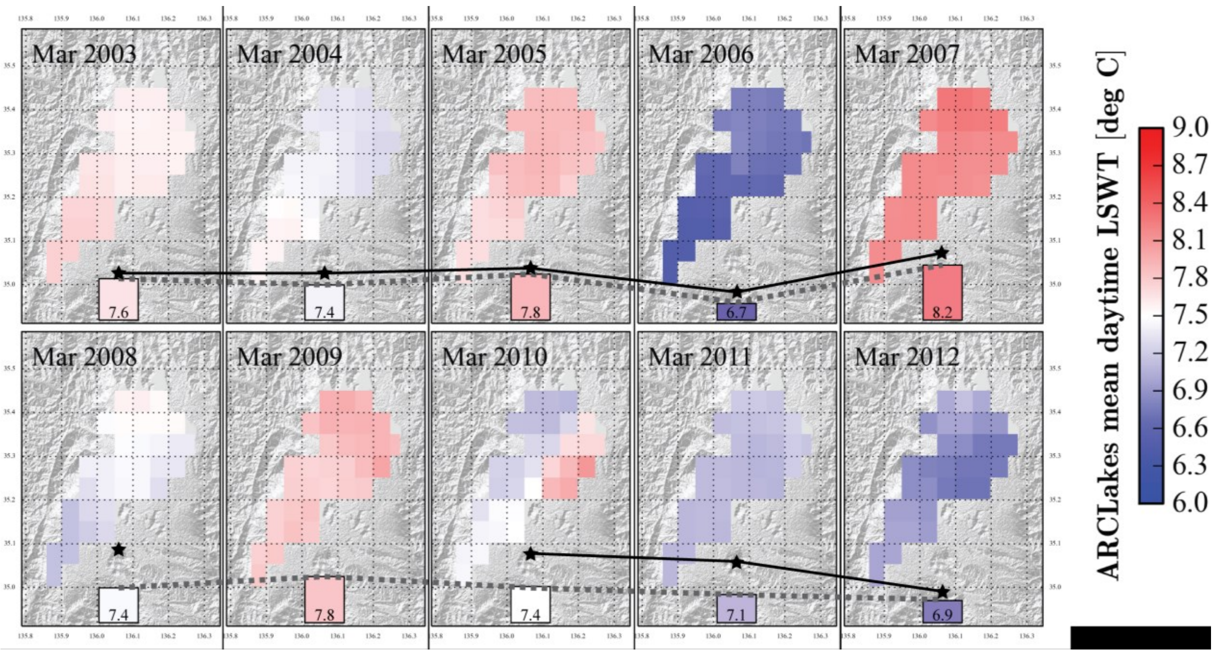

Figure 45: Surface water temperatures in March in Lake Biwa. The spatially averaged ARC Lake LSWT are represented by bars and dashed lines, and contrasted with in situ temperature measurements of the Univ. Kyoto's limnological survey program taken at 1 m depth and 35.2161° N, 135.9986 E (asterisks and solid lines; basemap from NASA SRTM).

4.2 Water Quantity Auxiliary Data and Algorithms

Remotely sensed estimates of lake water quantity can either be retrieved as water extent from SAR or optical imagery, or as water level from Radar Altimeter measurements. The following sections describe corresponding approaches used for existing datasets that were used for final Diversity II production. In addition, a dynamic extent estimation for ephemeral lakes was evaluated during the first phase of the project but not applied in the final production. Details on the lake extent algorithm are documented in Version 1 of the Diversity II ATBD.

4.2.1 Landcover CCI Water Bodies

The 300 m Landcover CCI Water Bodies (LC-CCI WB) map was vectorized and used for the initial selection and delineation of individual inland water bodies for Diversity II. LC-CCI WB is a static map of the maximum water extent of global surface waters in 2005-2010, locally up to 2012, (Kirches et al., 2014). It is based on an algorithm that uses the high Temporal Variability (TV) and low Minimum Value (MV) in a time series of Envisat ASAR Wide Swath Mode backscatter measurements for the separation of open water bodies from other land cover types (Santoro & Wegmuller, 2014). Figure 46 shows schematically how the two measures are applied. Ambiguous cases occur in mixed pixels, in steep terrain of >10° slope angle, and when less than 10 backscatter observations are used. In addition to the ASAR data, the Shuttle Radar Topotraphy Mission Water Body data (SWBD) and MERIS data were used for the creation of the LC-CCI WB map. The final map can be downloaded from the LC-CCI homepage (http://www.esa-landcover-cci.org). According to the contingency matrix in Table 14, the overall accuracy of the product is 96%.

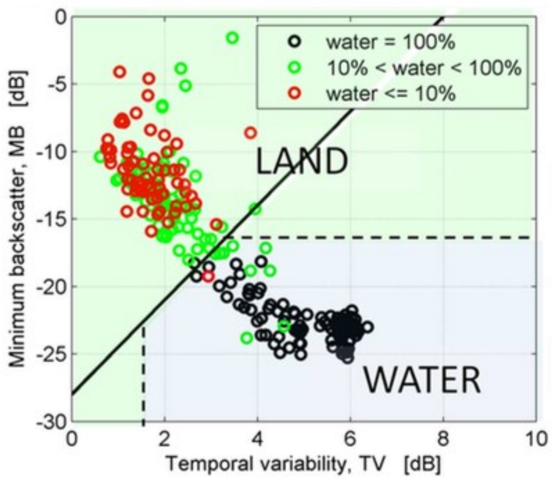

Figure 46: Illustration of the water body mapping algorithm. Decision rules are represented by the black diagonal line and the two dashed lines. The water and the land regions in the feature space of TV and MB are marked accordingly in light blue and green, respectively (from Santoro & Wegmuller, 2014).

Table 14: Contingency matrix built on the comparison between a reference dataset of 1844 footprints and the LC-CCI WB product.

		REFERENCE DATASET			
		NO WATER	WATER	SUM	USER ACCURACY
CCI-LC WB PRODUCT	NO WATER	1089	66	1155	94%
	WATER	12	677	689	98%
	SUM	1101	743	1844	
	PRODUCER ACCURACY	99%	91 %		96 %

4.2.2 SRTM Water Body Dataset

The SRTM Water Body data set (SWBD) is a high-resolution worldwide coastline and lakes outline dataset in vector format, divided into 12229 files, each covering a tile of 1° x 1°. The data represents the instantaneous water extent during the SRTM acquisition campaign in February 2000. Per definition, lakes greater than 600m minimum length and 183m minimum width are included. The data is available between -56°S and 60° N. Within that range, it is used for improved land/water identification by the Idepix algorithm. Outside that range, the original MERIS L1B flags are used. The SWBD is distributed by USGS and available from their EarthExplorer portal (https://lta.cr.usgs.gov/srtm_water_body_dataset).

4.2.3 LEGOS Hydroweb Lake Water Level

Lake water levels from Hydroweb (http://www.legos.obs-mip.fr/soa/hydrologie/hydroweb/) are provided for 103 or the 350 Diversity II lakes, with the kind permission by LEGOS. The Hydroweb products are based on data from Topex/Poseidon, Jason-1 and 2, ENVISAT RA-2 and GFO. These instruments emit a series of microwave pulses at dual frequencies in nadir direction. The two-way time delay between pulse emission and echo reception allows for the determination of lake surface height. For large lakes, the geoid slope is corrected using the EGM2008 geoid model and averages from several altimetry measurements along the observation track, the estimate is accordingly referred to as 'mean lake level'. The accuracy of the final water level estimates for large lakes are within 5 cm root-mean-square for large lakes like Lake Victoria, Lake Superior or other American Great Lakes (Crétaux et al., 2011).

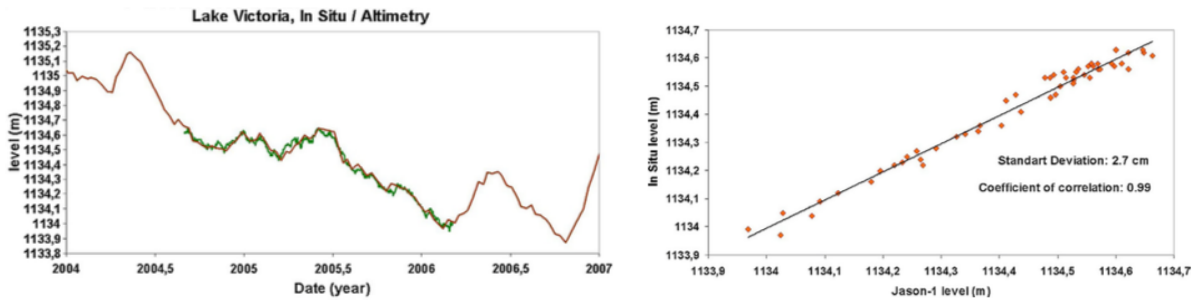

Figure 47: Time series (left) and scatter plot (right) comparison of water level in Lake Victoria from in situ gauges (green time series) and Jason-1 radar altimetry (from Crétaux et al., 2011).

Several other lake altimetry databases are available, including the ESA River & Lake database (http://tethys.eaprs.cse.dmu.ac.uk/RiverLake/shared/main) or the USDA's Crop Explorer database (http://www.pecad.fas.usda.gov/cropexplorer/global_reservoir/). Hydroweb was selected because it provided a significantly better coverage of the lakes selected for Diversity II than the River & Lake database. The ESA funded CRUCIAL project by Newcastle University and other future activities may however close this gap in the near future.

5 Algorithms Drylands Processing

According to the CBD, dry and sub-humid lands, including arid and semi-arid regions, grasslands, savannahs, and Mediterranean landscapes, encompass approximately 47% of the Earth's terrestrial area. Their biological diversity provides critical ecosystem services to support two billion people, 90% of whom live in developing countries (cited from http://www.cbd.int/drylands/what.shtml). Given this high significance of drylands and their extreme sensitivity to external influences like direct (land use) or indirect human pressure (climate change), new outcomes of current status and trend observations of patterns and temporal variability of NPP and RUE to be generated by Diversity II will be a welcome piece of knowledge about these regions, which contain valuable biodiversity resources. However, it must be scientifically sound and relevant.

The algorithms and processing procedures applied for this purpose must therefore undergo a thorough screening in several directions: Valid input data and pre-processing must be used, the processing algorithms used must hold strong within the currently available alternatives, and the defined products must be relevant for the user requirements and valid and relevant in a scientific context as well.

The below presented state of these considerations reflects a part of our literature studies, own experiences, and consultancy within the project through Rasmus Fensholt and Kurt Günther.

5.1 Vegetation Indices for NPP

The NPP is one of the most important indicators to understand the ecosystem functioning, providing a basis to understand the associated carbon sequestration patterns, ecosystem services and its response to climate change (Lobell et al., 2002; Kale and Roy, 2012). The rate of NPP is determined by the conversion of solar energy to plant matter via photosynthesis and represents an ecosystem's maximum potential carbon storage, allowing the estimation of vegetation dry matter per unit of time and space (Luck, 2007; Kale and Roy, 2012).

One of the big strengths of Earth Observation is that satellite data provide global means to map and monitor NPP, more correctly ANPP (Above Ground Net Primary Production) using repeatedly recorded multispectral information. From these, vegetation indices can be derived that may be defined as "*optical measures of vegetation canopy "greenness", a composite property of leaf chlorophyll, leaf area, canopy cover, and canopy architecture*" (Jiang et al., 2008, p. 3833). VIs for NPP estimations based on optical EO data may be subdivided into band-ratio and/or band-difference based vegetation indices on the one hand, and biophysical indices based on physical modelling approaches on the other hand.

5.1.1 Ratio-based Vegetation Indices

The Normalised Difference Vegetation Index (NDVI), the Soil-Adjusted Vegetation Index (SAVI) (Huete, 1988) or respectively the modified SAVI (MSAVI and MSAVI2) (Qi et al., 1994) and the Enhanced Vegetation Index (EVI) (Jiang et al., 2008) are examples of EO techniques for estimating vegetation greenness, i.e. the photosynthetic activity via multispectral band-differences/ratio approaches. These vegetation indexes are based on the combination of different bands for enhancing vegetation greenness by contrasting the reflectance of different wavelengths and removing a large portion of noise components in distinct wavelength regions. The NDVI (Tucker, 1979) is the most commonly used vegetation index and is based on the premise that photosynthetically active vegetation is capable of absorbing most of the incident red light, reflecting at the same time much of the near infrared light. The basic formula for the NDVI calculation is: NDVI = (NIR – RED) / (NIR + RED), i.e. the difference between the NIR and the Red band is divided (i.e., normalised) by the sum of the two bands.

The SAVI and MSAVI a soil adjusted vegetation index that addresses some of the limitation of NDVI when applied to areas with a high degree of exposed soil surface, like deserts and drylands (Qi et al. 1994, Gao et al. 2000). The formulas of SAVI or MSAVI have been repeatedly modified or adapted to various sensors and their original versions can be found in the cited papers. Despite the advantages associated with SAVI or MSAVI, there are also some limitations that should be taken into account. The most significant for MSAVI is that it sacrifices overall sensitivities to changes in vegetation cover in order to obtain a reliable correction for the soil surface brightness (Qi et al. 1994). This leads to a worse sensibility for detecting changes and trends of vegetation communities. Additionally, MSAVI is more sensitive to differences in atmospheric conditions between areas and times. For these reasons, MSAVI could be used for obtaining status maps for dryland areas, but not for evaluating trends in these regions.

The enhanced vegetation index (EVI) is one of the proposed MODIS VI products and includes a soil adjustment factor as well as atmosphere resistance term, using the blue band (Liu and Huete, 1995; Huete et al., 1997, cited in Gao et al., 2000, where also the formula can be found). Jiang et al. (2008) present a version of EVI without a blue band, which is thus also applicable to NOAA AVHRR data and other sensors without a blue band.

5.1.2 Physical Modelling Approaches

The physical models use principles of how light energy is absorbed or reflected from different surfaces to estimate physical characteristics of vegetation. Biophysical models incorporate parameters related to how light interacts with processes like photosynthesis, evapotranspiration and stress. These methodologies use theoretical models of radiative transfer theory to estimate the absorbed photosynthetically active radiation and have been successful in predicting biomass across wide scales and different climatic regimes. The Fraction of Absorbed Photosynthetically Active Radiation (fAPAR) and the Leaf Area Index (LAI) represent two examples of physical models for measuring biomass production. Gao et al. (2000, p. 609) based on work of several further authors state that "*fAPAR is an important variable in studies of the energy budget and hydrology of the vegetated land surface, while LAI is closely related to a variety of canopy processes, such as interception, evapotranspiration, photosynthesis, respiration, and leaf litterfall*".

5.1.3 Choice of Vegetation Indices

According to Gao et al. (2000, p. 610), the *"choice and suitability of a VI is generally determined by its sensitivity to the characteristics of interest, and/or its sensitivity to disturbing factors. Many efforts have been made to optimize vegetation indices and render them insensitive to variations in sun-surface-sensor geometries, atmosphere, calibration, and canopy background. Solar zenith, sensor view angle, and atmospheric influences are increasingly being handled with improvements in atmospheric correction algorithms and bidirectional reflectance distribution function (BRDF) models".* In the dryland part of Diversity II, the vegetation productivity of arid, semiarid and sub-humid regions are to be monitored in a consistent way over a period of several years, with predominantly strong interferences of the vegetation signals with those of the soil background. A biophysical VI index was preferred over NDVI-type indices, which is physically related to primary production and biomass.

Among the vegetation indices for NPP or NPP proxies, fAPAR – fraction of photosynthetically active radiation absorbed by the vegetation is a key variable e.g. in many climate models, as it directly expresses a canopy's energy absorption capacity (Fensholt, Sandholt, & Rasmussen, 2004). *"fAPAR is a primary variable controlling the photosynthetic activity of plants, and therefore constitutes an indicator of the presence and productivity of live vegetation, as well as of the intensity of the terrestrial carbon sink"* (Nadine Gobron & Verstraete, 2009). According to Gobron and Verstraete (2009, p V), the systematic observation of fAPAR "*is suitable to reliably monitor the seasonal cycle and inter-annual variability of vegetation photosynthetic activity over terrestrial surfaces*". Further on, fAPAR is the index most directly related to loss of plant productive capacity and it is the core variable used in models of primary production in terrestrial ecosystems (GEO BON, 2011). According to Gobron et al. (Nadine Gobron, 2011) the "*fAPAR has been also recognized as one of the fundamental Essential Climate Variable (ECV) by Global Terrestrial Observing System (GTOS) and Global Climate Observing System (GCOS) (Nadine Gobron & Verstraete, 2009)*".

For these reasons, **fAPAR is THE NPP proxy** that was selected as number one NPP index for the Drylands studies.

In addition to fAPAR, it was decided to also include the NDVI in the studies, as this approach provides for the maximum continuity between the AVHRR GIMMS NDVI time series that are used for longer term NPP analyses, and the MERIS based trends of this study. There are numerous NDVI based trend studies, many of them at global scale and/or restricted to (specific) drylands (e.g., (Fensholt & Proud, 2012; Julien et al., 2011; Prince, Becker-Reshef, & Rishmawi, 2009; Wessels, van den Bergh, & Scholes, 2012). Fensholt (consultant to this project) and his group are among the leading authors during the last 10 years, and their research covers specifically NPP and RUE indices and trends, including NDVI and fAPAR based approaches.

While the soil colour and brightness dependence of the NDVI is a well-known limitation or uncertainty of the NDVI (e.g., (Carlson & Ripley, 1997), (Fensholt, Sandholt, Rasmussen, Stisen, & Diouf, 2006)) (Sebego, Arnberg, & Ringrose, 2002) point to another limitation: *"However there is still some uncertainty as to what the NDVI means on the ground in terms of woody cover species types and in terms of the tree: grass ratio. In work intended to help overcome this uncertainty, Ringrose et al. (1989), Ringrose and Matheson (1991) and Matheson and Ringrose (1994), determined that the NDVI was predominantly useful in semi-arid areas after the rains by indicating the extent of woody vegetation re-growth and (green) grass cover. In terms of the normal dry season and frequent drought conditions the NDVI has limited value over Botswana because it can imply a bare soil condition (low NDVI) when sparse to dense, microphyllous leafed woody plants are prevalent on the ground (Ringrose et al., 1998). The kinds of vegetation that lead to a lower than anticipated NDVI are referred to as darkening species (Otterman, 1974; Ringrose et al., 1989; Chavez and MacKinnon, 1994; Ringrose et al., 1998; Moleele, 1999)".* (the authors referred to in this citation are not listed in this report, but the Sebego et al. paper is easily accessible at http://www.isprs.org/proceedings/XXXIV/6-W6/papers/sebego.pdf). While the latter is an effect that is most likely found in areas other than Botswana as well and would be an interesting object for further studies, the implication of the first statement is important for this study in the context of calculating RUE or similar efficiency indices.

On the other hand, Prince et al. (2009) like many other authors take the NDVI as a surrogate for NPP. According to Fensholt et al. (2006) there is a near-linear relationship between NPP and ΣNDVI in tropical grassland, cropland and sparse woodland and light use efficiency has been shown not to improve accuracy.

5.1.4 fAPAR Calculation

fAPAR is difficult to measure directly, but is inferred from models describing the transfer of solar radiation in plant canopies, using remote sensing observations as constraints (Nadine Gobron & Verstraete, 2009). The basic form of these models is:

NPP = ε * fAPAR * PAR, where NPP is net primary productivity, PAR is incoming irradiance in the photosynthetically active region (i.e. 400-700 nm) during a time period (i.e. day, month) and ε is defined as light use efficiency, or the efficiency to convert solar radiation into plant biomass" (Vina, 2004).

There are several approaches of satellite data based fAPAR modelling. For MERIS data, two major approaches are reported in the literature: First, the approach developed by (Nadine Gobron, 2011) at the JRC, second the Geoland 2 fAPAR, which is part of the biophysical products from MERIS FR data and derived with the Overland software developed by SISA (Geoland 2 BP-RP-BP022, 2011). The ATBD of the Geoland 2 fAPAR product is contained in the report g2-BP-RP-BP038 - ATBD of MERIS FR products.

The validation report of the Geoland 2 (BP-RP-BP022) biophysical products compares the Geoland 2 fAPAR with the JRC fAPAR. Figure 48 shows the seasonal course of g2 and JRC MERIS fAPAR mean values over the main biomes existing in the Guadalquivir basin (Spain) during the year 2003.

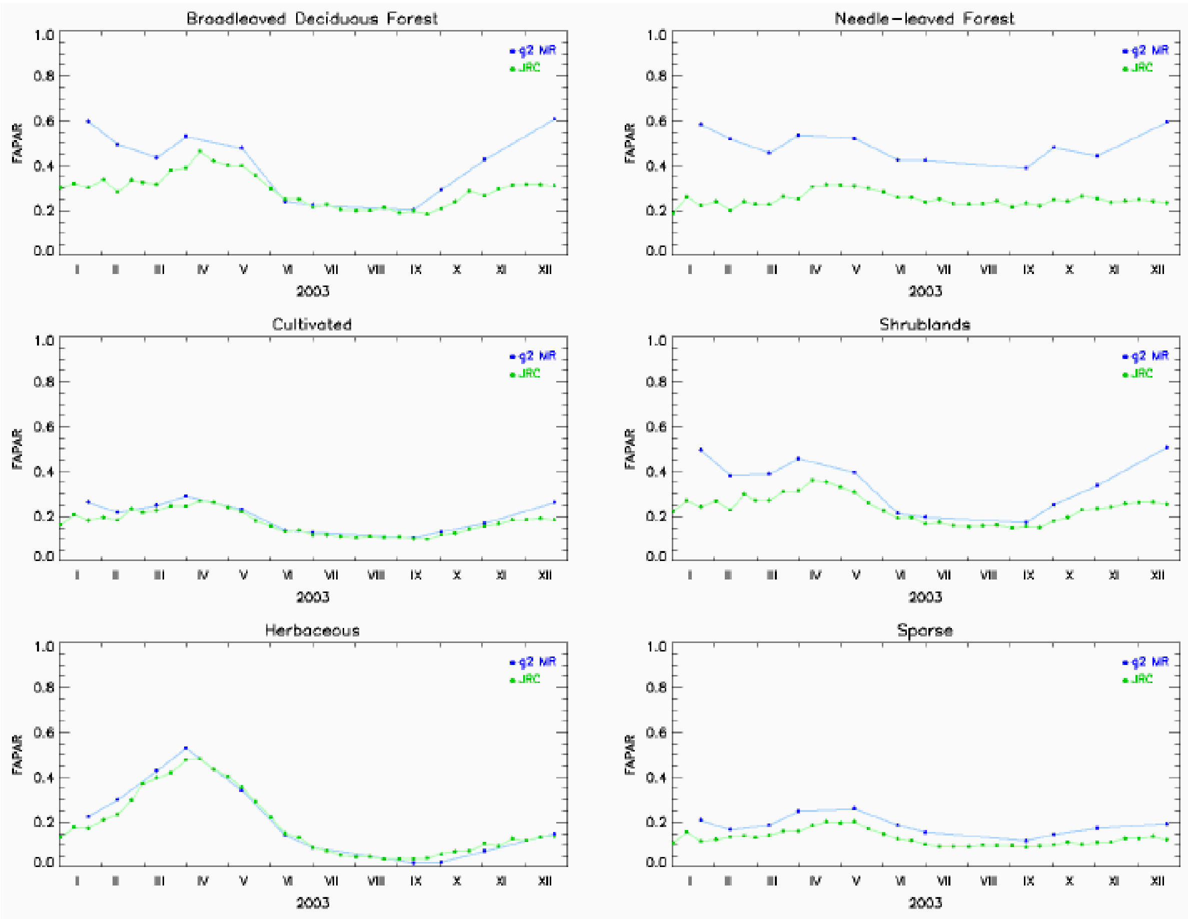

Figure 48: Seasonal variations of g2 MR and JRC MERIS fAPAR mean values over the main biomes existing in the Guadalquivir basin during the year 2003 (source: Geoland 2 BP-RP-BP022, 2011)

The g2 validation report states (p. 56): "*A good consistency is found for agriculture and herbaceous areas, with overall uncertainties better than 0.1 and no systematic deviations. However, the performance is very low in forest and shrublands, with overall errors higher than 0.15. The spatial distribution of the difference between g2 and JRC product shows clearly that these differences are associated to the impact of the CSF parameter in g2 MR retrievals*". The CSF parameter is the Canopy Shadow Factor, which is derived and used to compensate for the mutual shading effects of vegetation canopies in the Geoland 2 biophysical products. This leads to considerably higher g2 fAPAR values over forests and shrubland compared to the JRC fAPAR, which is known to deliver in general lower values than other fAPAR algorithms according to the g2 validation report (BP-RP-BP022). The JRC fAPAR is based on a homogeneous canopy vegetation model assuming a horizontally homogeneous canopy. The much lower JRC fAPAR over needle-leaved forest in Figure 48 is partly or mainly a consequence of this difference between the two approaches. While the CSF parameter is an important factor to consider over canopies, its consideration may on the other hand lead to overcompensations under certain conditions, and in general to higher inconsistencies of the results. This effect is also mentioned in the g2 validation report. The high wintertime g2 fAPAR values for broadleaved deciduous forest and shrubland in Figure 55 may be an expression of such inconsistencies. The JRC fAPAR in Figure 48 shows more of what may be expected as seasonal vegetation behaviour at these locations, with a maximum in spring time and a second maximum in fall after onset of the rainy season.

We conclude from this comparison that the MERIS fAPAR algorithm developed by Gobron (2011) appears as the more consistent approach, even though it can be seen to lead to underestimations of fAPAR.

For this reason we prefer to use the JRC algorithm, which is also routinely applied by the ESA ground segment. The computation is implemented in a highly operational software system: ESA BEAM, which was used as a platform for processor development and improvement. Brockmann Consult maintains BEAM. The algorithm is called the MERIS Global Vegetation Index (MGVI). In addition, such a fAPAR algorithm is also proposed for the future Ocean Land Colour Instrument (OLCI) (Nadine Gobron, 2011) on board Sentinel-3 considering the continuity for having a long time series of observation requested for any global change applications.

The algorithm delivers in addition to the fAPAR product "rectified reflectance" bands of the NIR and RED bands, which will be input to the NDVI calculation.

5.1.5 Validation of the JRC MERIS fAPAR

Uncertainty estimates and validation of the MERIS fAPAR have been performed in extenso, e.g. by (N Gobron et al., 2008) and (Pinty, Lavergne, Kaminski, Gobron, & Taberner, 2008). Nevertheless, ground station based fAPAR measurements are rare, but In Diversity II, validation with ground measured fAPAR data and biomass data could be performed. Rasmus Fensholt maintains a ground measurement station in Senegal in a herbaceous area and provided time series data from this station to the project. In addition, in situ derived biomass data from various location in Senegal were provided by project users from the Centre de Suivi Ecologique in Dakar. Figure 49 shows two scattergrams and corresponding pearson r between MERIS fAPAR and ground station based fAPAR. Here especially the left hand scattergram, even though only five values were available, contains results with high significance for the project. It shows that differences between yearly integrated (more precisely: integration over the increasing part of the growing season) fAPAR values on the ground are very well captured by the MERIS fAPAR data. This supports the main assumption of the project, i.e. that annual NPP developments (differences and trends) can be reliably mapped with our MERIS fAPAR product.

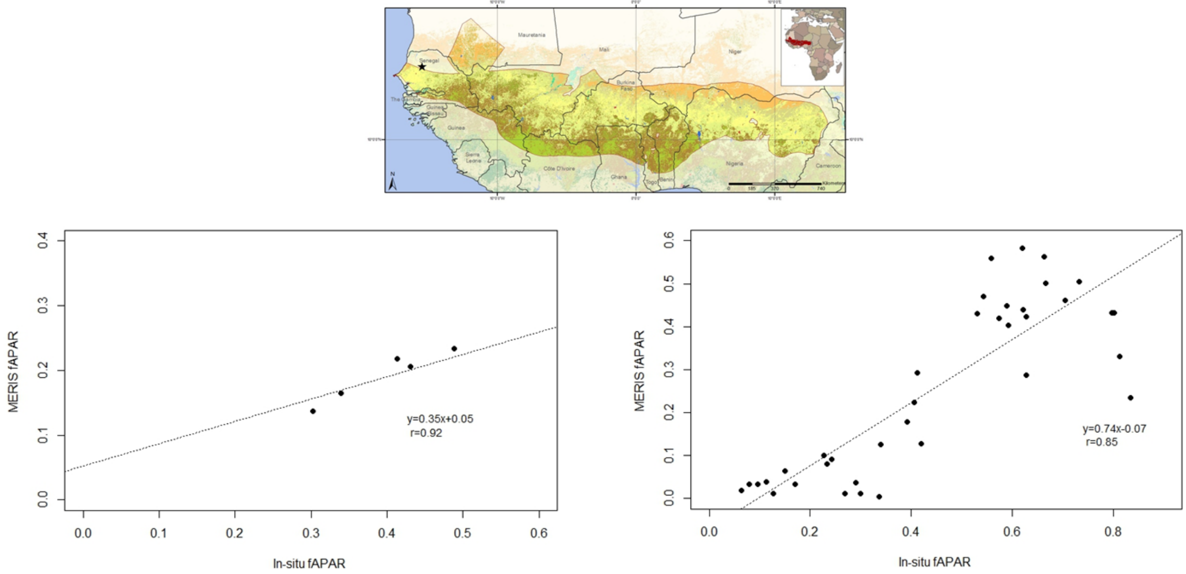

fAPAR integrated over growing season June-November, 2005-2009, 2011

Increasing fAPAR values in the growing season, 2005-2011

Figure 49: MERIS fAPAR versus ground measured fAPAR in Senegal (black star in upper image indicates location)

Further validation approaches have been applied using modelled NPP data from the DLR, which have been derived with the model BETHY/DLR. These data have been presented in section 3.7.4. The validation performed and the results are reported in the PUH, section 3.5.3 and in the Diversity II Products Quality Report (PQR, Brito et al., 2015).

5.1.6 NDVI calculation

The NDVI formula is straight forward: (NIR – RED) / NIR + RED). However, comparability of the NDVI derived with a specific sensor with that of other sensors depends on the spectral input bands, which must be identical or close to each other. As the MERIS NDVI will be computed to compare it with the longer time series of the AVHRR GIMMS NDVI, a thorough band selection of the MERIS bands has to be performed for NDVI calculation. For this purpose, we followed an approach described in an ATBD by Günther (consultant to this project) and Maier (Günther & Maier, 1999), who simulate the AVHRR channels with MERIS channels and derive a "continuity" NDVI from these simulated bands. The simulation is done by deriving weighted sums of the MERIS bands that correspond to the red and NIR bands of the AVHRR.

As the MERIS fAPAR data were used as the main source for the Diversity II products, the MERIS NDVI data were only processed for two exemplary sites. These were site 04 Northern Kazakhstan and site 12, Southern Africa West. The results were compared to the fAPAR based results. Evaluation results are shown in the PUH, section 3.6.3.

5.1.7 Generation of Biweekly Integrated Time Series Data

Time series data have been computed for the two MERIS NPP proxies fAPAR and NDVI, as well as for the ancillary data sets described in section 3.7. The temporal integration period was determined to be half-monthly (= bi-weekly). Half-monthly values have the advantage that they provide a better characterisation of the seasonality of regions than monthly values, especially in very dry regions, where the growing seasons may not be longer than two or three months or even shorter. Monthly values, on the other hand, are more robust, especially with regard to cloud contamination of the MERIS data, and may thus lead to higher quality data (e.g. by maximum compositing approaches). Smaller computational efforts and storage requirements would be further advantages of monthly time series data, however it was felt that the higher temporal resolution of half-monthly values outweighs these advantages.

The half-monthly fAPAR data were rescaled to a range from 0 to 1000 (originally they range from 0 to 1) by multiplication with 1000 and subsequent rounding to integer values. This way the input data and many intermediate files could be handled as 16 bit data, which takes much less storage capacity and computation time than float formats. The NDVI data have been treated in the same way. Negative NDVI values (which do not occur in the fAPAR data), i.e. pixels free of vegetation in the respective time interval (or permanently), were recoded to zero.

5.1.8 Gap filling of fAPAR data

After the initial filling of MERIS FR fAPAR with MERIS RR fAPAR data, remaining data gaps were filled using a two-sided weighted linear trend extrapolation approach. This means, the gradients on both sides of data gaps (> one halfmonth) were extrapolated toward the outer values of the gap. On both sides, i.e., before and after a gap, the two adjacent gradients were used and differently weighted in order to derive weighted mean gradients. Two iterations were applied (filling the first and the last gap of a longer gap series each). Prior to, in between and after these two iterations, gaps of single halfmonths were filled by linear interpolation. This way, gaps of up to five halfmonths have been filled (with ERDAS, i.e. without the necessity to transform the data in order to use other gap filling tools), which was sufficient for all but one test site, i.e. site 15, Caatinga in Brazil. In this test site, data gaps were especially frequent and could not be sufficiently filled with the described approach.

Timesat software, a freeware of the University of Lund developed by Eklundh and Jönsson (2012), was tested and applied in this site for filling remaining gaps with the Savitzky–Golay filter after application of the above procedure. When directly applying the Savitzky–Golay filter to the data, the data gaps were too large and frequent in this particular test site to be properly filled with the Savitzky–Golay filter. As the resulting portion of filled gaps was quite large in this test site, we decided to perform a sensitivity analysis by estimating the influence of the gap-filling on the project outcomes. The results are reported in section 5.1.8.1.

Pixels that had remaining data gaps after the gap filling procedure were discarded from the results and labelled as no data values in the indicator maps.

The metadata provide exact information for each single fAPAR (and MERIS NDVI) data value, whether it is an original (FR or RR) value, or has been gap filled.

5.1.8.1 Gap filling simulation and evaluation of the results in Caatinga

As mentioned earlier, the Caatinga test site in Brazil has an especially large number of MERIS data gaps, which have been filled with two different approaches: First, with the above described procedure, which was implemented in an ERDAS model, and second with the Timesat software (Eklundh & Jönsson, 2012). In order to obtain an estimation of how the large number of filled, often elongated gaps stretching over two to three months, may impact the final results, we conducted a test with a gap simulation, comparing results obtained with the filled gaps to those derived with the original data. Figure 50 illustrates the location of the Caatinga test site, and within the site the position of the gap filling simulation area. A yellow arrow points to this area in the right hand map, and an empty square in the left hand map at the corresponding location. The MERIS data gaps naturally occurring in the area bounded with the eastern black square in the right hand map were extracted, their geographical coordinates were changed to those of the test area to the west, and then the gaps were "cut" into the time series fAPAR data (the version where the original gaps had been filled). Originally, this area only contains a limited amount of gaps, which can be seen in the left hand map. It shows that within the gap filling test area, the original amount of gaps is overall below 20% (of totally 216 = 9*24 half-monthly fAPAR values made up by the data from 2003-2011), and partly below 10%. After transferring the gaps to the test site, the additional portion of gaps amounts up to 40% in large parts, with extreme areas reaching 50% additional gaps. These gaps were filled in the above described way. The entire processing chain was then applied, and the most essential NPP proxy status and trend results were compared.

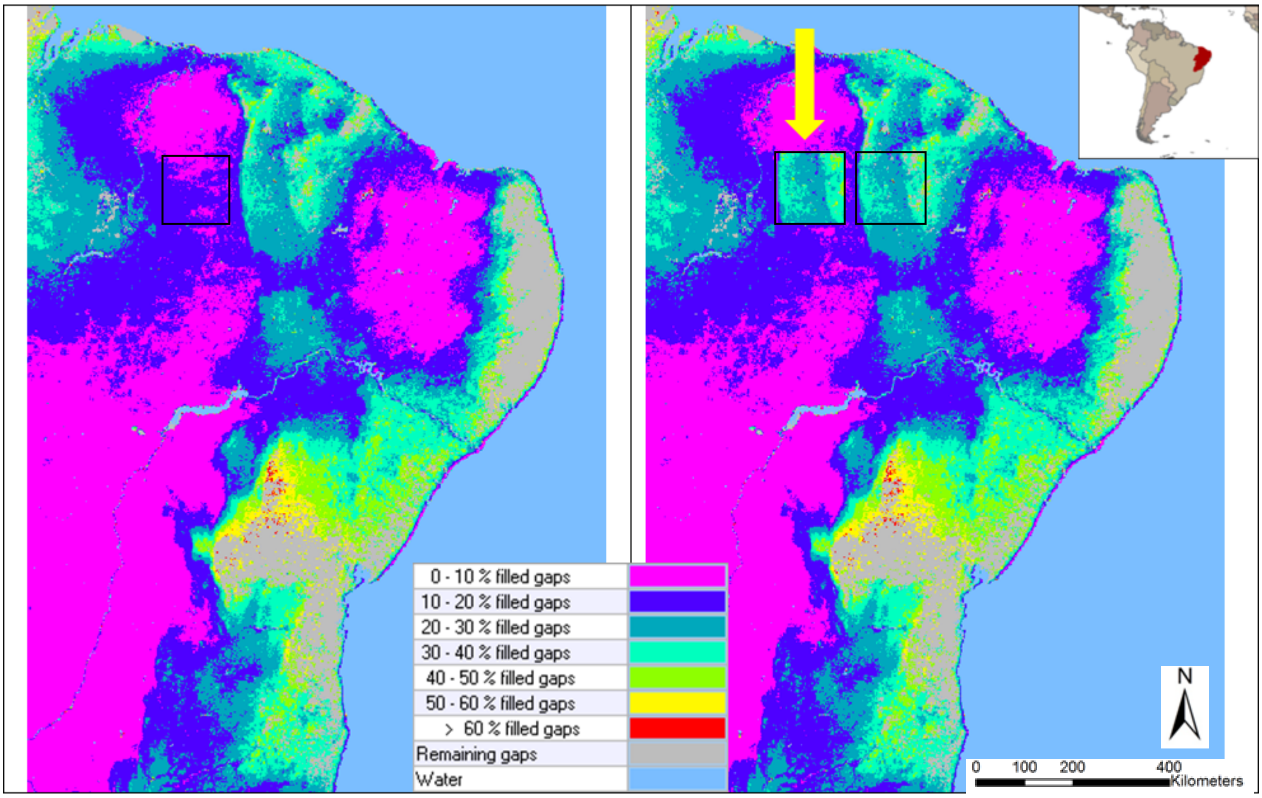

Figure 50: Number of filled gaps in [%] for the period 2003-2011 (100% = 216 half-months). On the right, the yellow arrow points to the test area of the gap filling simulation, where it can be clearly seen that it contains the pattern of filled gaps from the area marked with the black square to the east.

Figure 51 shows the portions of the simulated and filled gaps versus the resulting change of the Median SoS (2003-2011), expressed in half months change of the simulated gap based SoS relative versus the original SoS. Quite obviously, the larger SoS shifts occur in areas with larger portions of simulated gaps, especially in the eastern and north-western part. Nevertheless, the total impact on the SoS timing is relatively small compared to the large areas with considerable amounts of simulated gap. More than 85% of the area exhibits no Median SoS change, and further >10% deviate by one HM only, mainly towards a delayed SoS. Only in 0.5% of the area changes are larger than 3 HM, even though the part of the area with e.g. 30-40% simulated gaps amounts to >40%. Thus, the sensitivity of the SoS timing to the gap filling is low and mainly dependent on the lengths of the gaps. The latter has not been quantified, but the comparison shows that the combined impact of gap length and gap filling is relatively low with regard to the SoS, a key parameter for the NPP proxies.

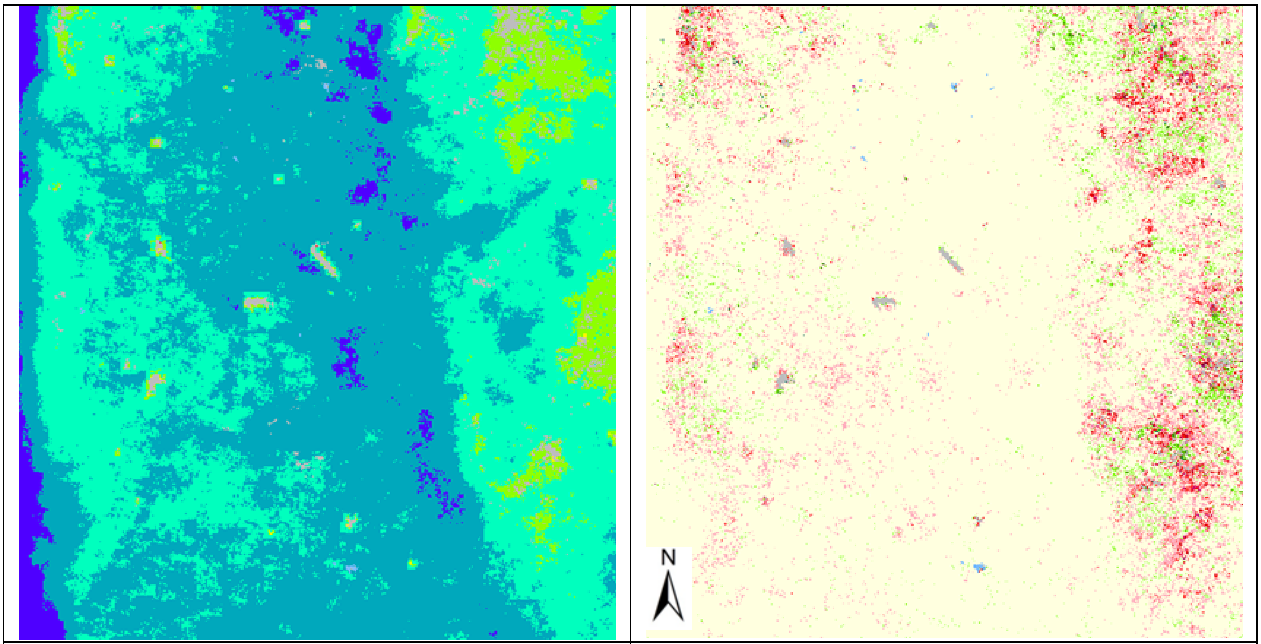

Number of simulated and filled gaps

10 - 20 % filled gaps		3.25
20 - 30 % filled gaps		50.81
30 - 40 % filled gaps		40.42
40 - 50 % filled gaps		4.52
50 - 60 % filled gaps		0.04
> 60 % filled gaps		0.00
Remaining gaps		1.50
Water		0.04

The values in the right column show the range percentages of the portions of the simulated gaps.

Difference of SoS to the original SoS in HM

simul.gap fAPAR SoS > 6 HM later		0.04
simul.gap fAPAR SoS 5 HM later		0.10
simul.gap fAPAR SoS 4 HM later		0.26
simul.gap fAPAR SoS 3 HM later		0.63
simul.gap fAPAR SoS 2 HM later		1.72
simul.gap fAPAR SoS 1 HM later		7.06
simul.gap fAPAR SoS 1 HM earlier		3.63
simul.gap fAPAR SoS 2 HM earlier		0.76
simul.gap fAPAR SoS 3 HM earlier		0.19
simul.gap fAPAR SoS 4 HM earlier		0.05
simul.gap fAPAR SoS 5 HM earlier		0.01
simul.gap fAPAR SoS 6 HM earlier		0.02
simul.gap fAPAR SoS same as original SoS		85.53

Where: HM = half months
The values in th right column are percentages

Figure 51: Portions of simulated and filled additional gaps (left) versus changes of the resulting Median SoS (Start of the vegetation years 2003-2011) compared to the original SoS Median

Further on, the impact of the filled simulated gaps on the essential NPP proxy parameters has been examined. Figure 52 shows the impact of the gap simulation on Diversity II product 01: vegetation year average fAPAR 2003-2010. Again, the major differences are found in the areas with the largest portion of simulated gaps, but overall the impact is very small on the vegetation year averages, and amounts in over 95% of the area only to 0 to 5%, with a bias towards slight increases.

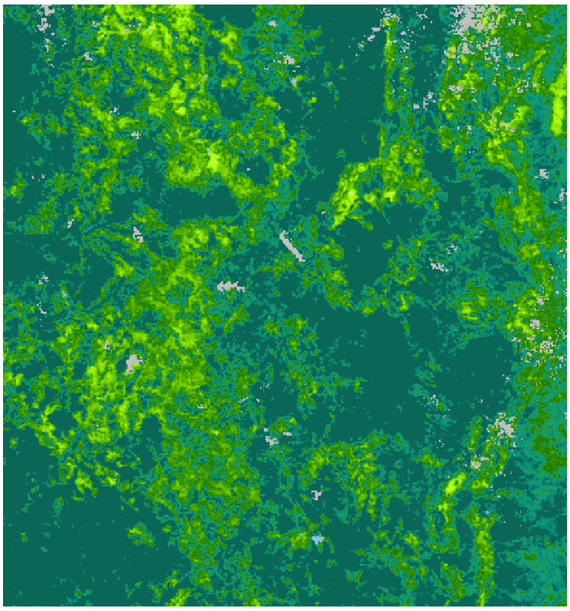

(a) Original product 01: Vegetation Year average fAPAR

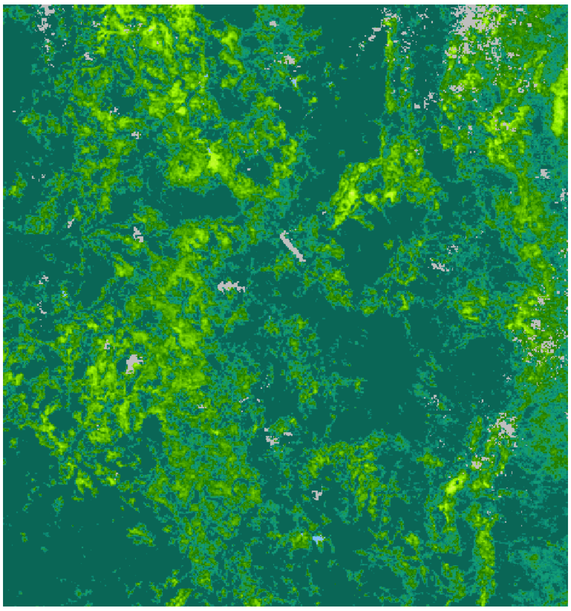

(b) Product 01 (simul. gaps): Vegetation Year average fAPAR

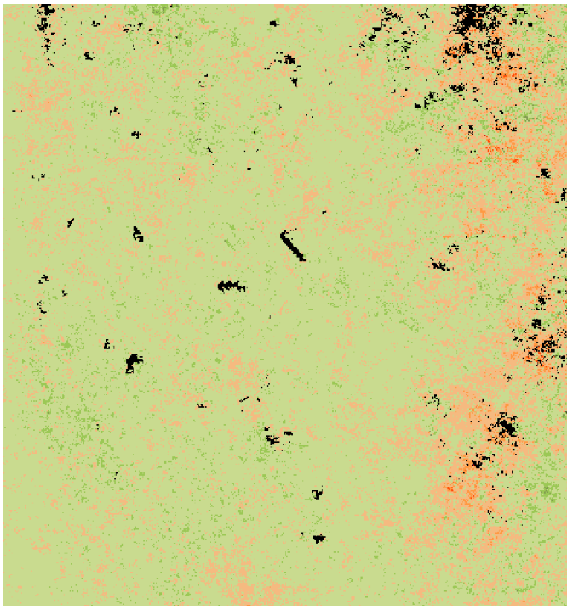

(c) Percentages of the NPP proxy values derived with the simulated gaps of the NPP proxy values derived with the original data (Vegetation year averges of the 8 vegetation years 2003-2010)

CLASS_NAME	Color	Percent orig	Percent simul. gaps
Area outside of WR		0.00	0.00
< 17		0.00	0.00
17 - 34		0.00	0.00
34 - 51		0.00	0.00
51 - 68		0.00	0.00
68 - 85		0.00	0.00
85 - 102		0.00	0.00
102 - 119		0.00	0.00
119 - 136		0.00	0.00
136 - 153		0.00	0.00
153 - 170		0.01	0.01
170 - 187		0.03	0.03
187 - 204		0.06	0.06
204 - 221		0.13	0.11
221 - 238		0.27	0.24
238 - 255		0.57	0.48
255 - 272		1.03	0.88
272 - 289		1.70	1.48
289 - 306		2.55	2.34
306 - 323		3.56	3.28
323 - 340		4.72	4.36
340 - 357		6.12	5.75
357 - 374		7.64	7.10
374 - 391		8.86	8.40
391 - 408		9.53	9.16
408 - 425		9.98	9.72
> 425		43.26	46.62
Data gaps, bare		0.00	0.00
Water (Globcover 2009)		0.00	0.00

Legend of average vegetation year fAPAR 2003-2010 (fAPAR * 1000) with class percentages for (a) and (b)

remaining data gap		0.00
< 80 %		0.00
80 - 85 %		0.00
85 - 90 %		0.07
90 - 95 %		1.03
95 - 100 %		17.75
100 - 105 %		77.74
105 - 110 %		3.36
110 - 115 %		0.05
115 - 120 %		0.00

Legend of map (c) with the right column expressing the percentages of the change intervals. > 95% of the area show only changes of +/- 0 to 5% as impact of the gap simulation

Figure 52: Impact of the gap simulation on product 01: Vegetation year average fAPAR 2003-2010

Figure 53 shows the same comparison for the second dryland indicator product: Mean Cyclic Vegetation fAPAR 2003-2010. In this case the impact of the gap filling is slightly stronger than for the vegetation year averages, as the gaps concentrate on the rainy season and hence on the cyclic vegetation period. Thus the possible distortions through the gap filling can be expected to have the heaviest influence on the cyclic vegetation. Map (c) in Figure 53 highlights this stronger impact most obviously, while the map products themselves (map (a) and (b)) hardly show any outstanding differences. Again, a bias towards NPP proxy increases can be seen as a consequence of the gap-filling exercise.

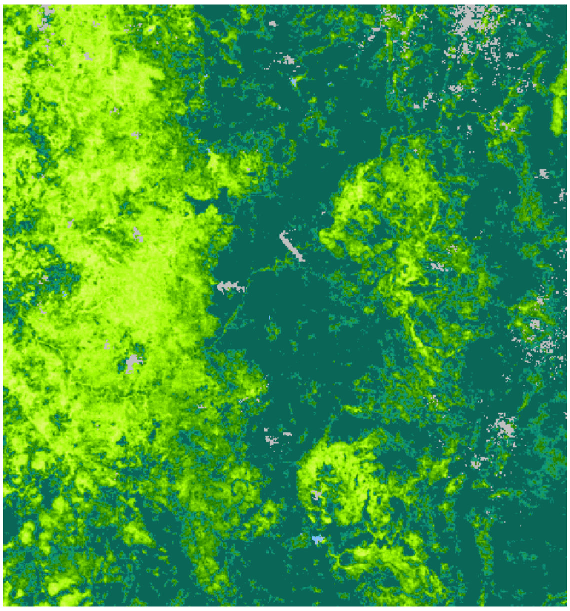

(a) Original product 02: Mean Cyclic Vegetation fAPAR

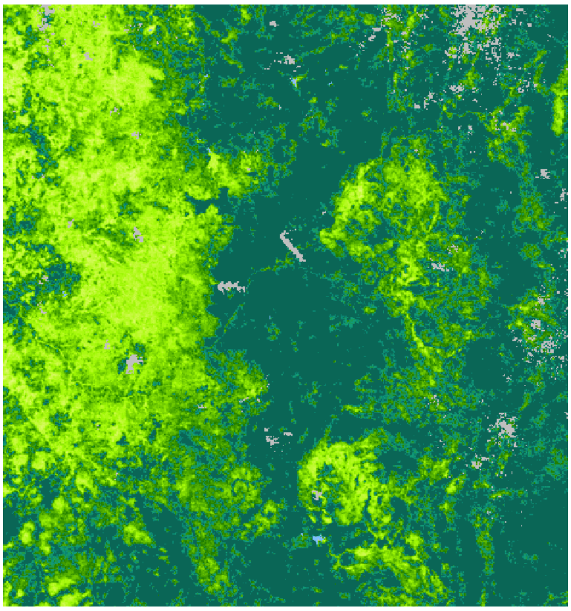

(b) Product 02 (simul. gaps): Mean Cyclic Vegetation fAPAR

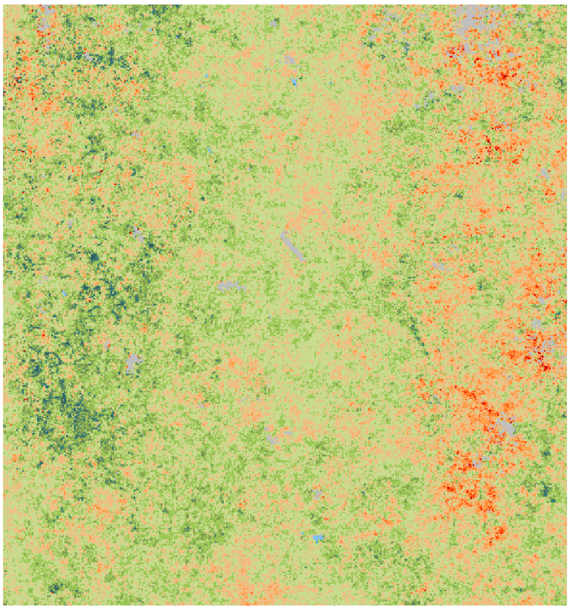

(c) Percentages of the NPP proxy values derived with the simulated gaps of the NPP proxy values derived with the original data (mean cyclic fraction fAPAR of the 8 vegetation years 2003-2010)

CLASS_NAME	Color	Percent orig	Percent simul. gaps
Area outside of WR		0.00	0.00
< 175		0.00	0.00
175 - 350		0.00	0.00
350 - 525		0.00	0.00
525 - 700		0.00	0.00
700 - 875		0.00	0.00
875 - 1050		0.02	0.01
1050 - 1225		0.09	0.05
1225 - 1400		0.26	0.16
1400 - 1575		0.64	0.43
1575 - 1750		1.26	0.89
1750 - 1925		1.98	1.60
1925 - 2100		2.63	2.20
2100 - 2275		3.08	2.85
2275 - 2450		3.42	3.24
2450 - 2625		3.82	3.60
2625 - 2800		4.03	3.88
2800 - 2975		4.06	4.07
2975 - 3150		4.08	4.10
3150 - 3325		4.14	4.17
3325 - 3500		4.23	4.28
3500 - 3675		4.37	4.38
3675 - 3850		4.55	4.68
3850 - 4025		4.83	4.82
4025 - 4200		5.20	5.24
4200 - 4375		5.51	5.51
> 4375		37.81	39.84
Data gaps, bare		0.00	0.00
Water (Globcover 2009)		0.00	0.00

Legend of mean cyclic vegetation fAPAR 2003-2010 (fAPAR * 1000) with class percentages for (a) and (b)

remaining data gap		0.00
< 80 %		0.01
80 - 85 %		0.09
85 - 90 %		0.67
90 - 95 %		4.03
95 - 100 %		21.89
100 - 105 %		45.84
105 - 110 %		21.49
110 - 115 %		4.64
115 - 120 %		0.99
> 120 %		0.34

Legend of map (c) with the right column expressing the percentages of the change intervals. > 93% of the area show only changes of +/- 0-10% as impact of the gap simulation

Figure 53: Impact of the gap simulation on product 02: Mean Cyclic Vegetation fAPAR 2003-2010

As last example the gap-simulation impact on the trend of the vegetation year average is shown in Figure 54. The trend maps (a) and (b) are quite similar and the bigger pattern is very stable, though some differences are visible. In comparison to the status products, where the averaging over eight years levels out many single year effects, the trends react more sensible to the gap filling procedures as can be seen especially Figure 54 (c). The share of relatively stable trend slopes (< 20% change) is not higher than ≈65%, and extreme deviations occur in 23.5%. However relative to the width of the trend slope classes, the differences appear less dramatic: e.g., the trend slope difference between two adjacent lower slope classes can amount to 300%, such as the trend slope of 3 versus 9 !

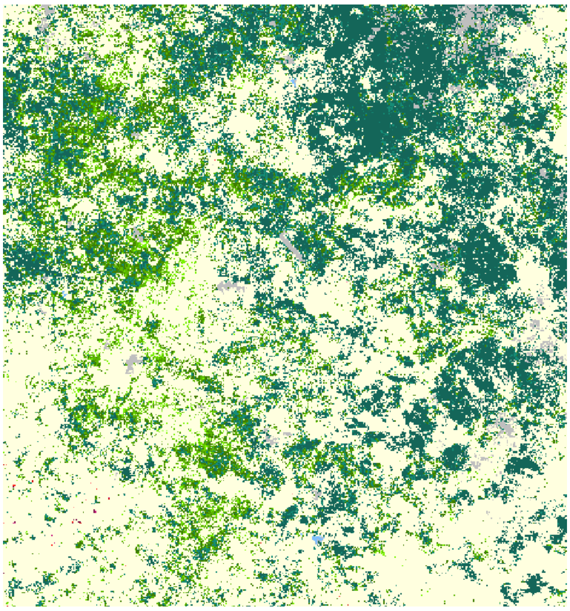

(a) Original product 33: Trend slope of Vegetation Year average fAPAR 2003-2010

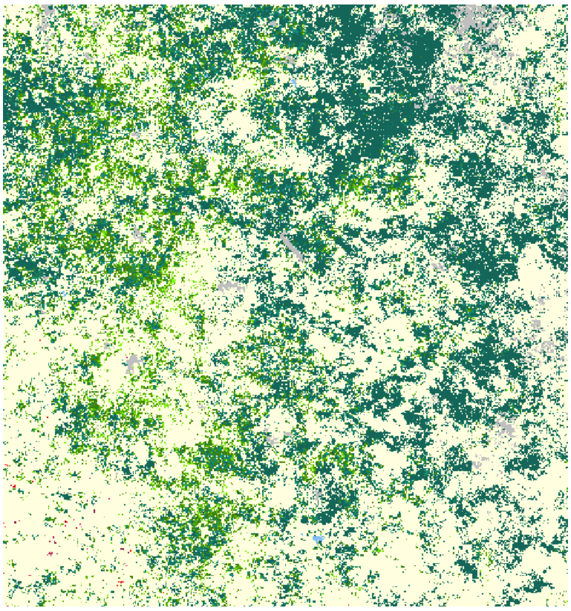

(b) Product 33 (simul. gaps): Trend slope of Vegetation Year average fAPAR 2003-2010

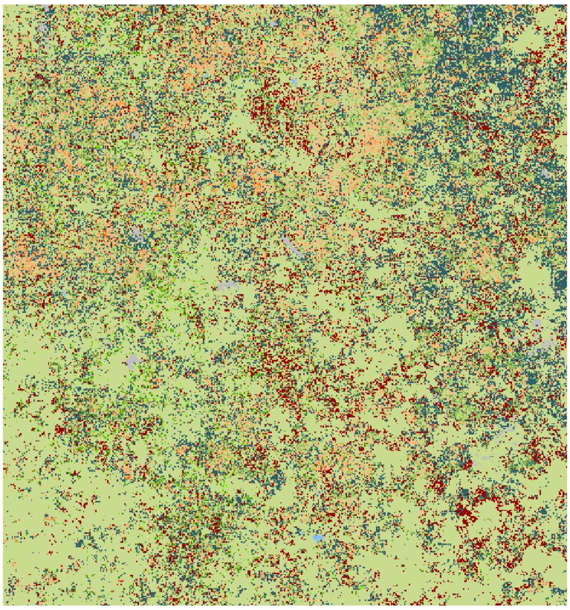

(c) Percentages of the fAPAR vegetation year trends derived with the simulated gaps of the fAPAR vegetation year trends derived with the original data (trends of the 8 vegetation years 2003-2010)

CLASS_NAME	Color	Percent orig	Percent simul. gaps
Area outside of WR		0.00	0.00
yearly decrease > 15		0.00	0.01
yearly decrease 12 - 15		0.00	0.01
yearly decrease 9 - 12		0.00	0.01
yearly decrease 6 - 9		0.00	0.01
yearly decrease 3 - 6		0.00	0.01
yearly decrease < 3		0.00	0.00
yearly increase < 3		0.04	0.03
yearly increase 3 - 6		0.94	0.74
yearly increase 6 - 9		4.73	3.53
yearly increase 9 - 12		8.69	6.64
yearly increase 12 - 15		9.14	7.57
yearly increase > 15		18.96	21.12
Insignificant or no trend		57.50	60.33
Data gaps, bare		0.00	0.00
Water (Globcover 2009)		0.00	0.00

Legend of the trend slopes of fAPAR vegetation year trends 2003-2010 (fAPAR * 1000) with class percentages for (a) and (b)

data gaps		0.00
< 20 %		8.23
20 - 40 %		0.02
40 - 60 %		0.28
60 - 80 %		2.20
80 - 100 %		7.43
100 - 120 %		57.76
120 - 140 %		5.60
140 - 160 %		2.30
160 - 180 %		0.93
> 180 %		15.26

Legend of map (c) with the right column expressing the percentages of the change intervals. > 65% of the area show changes of +/- 0-20% as impact of the gap simulation

Figure 54: Impact of the gap simulation on product 33: Trends of vegetation year average fAPAR 2003-2010

It can be summarized that the gap filling simulation leads overall to quite small changes of major project outputs, even though the portion of additional gaps that has been filled amounts to over 40% of the time series data in many cases. The impact patterns are clearly related to the number of simulated gaps. As these simulated gaps, which were transferred to the test area from a nearby area with real gaps, are concentrated in the rainy season, the cyclic vegetation is more effected than the vegetation year average fAPAR. Trend react more sensible to the gap filling and hence exhibit more and stronger changes than the status product. Still, even in the trend product, the overall patterns are well maintained after the gap filling.

It must be added, that the simulated gaps may partly not fit the phenology of the pixels, where they have been spatially transferred to. This may lead to worse gap filling results than if the gaps occur during the increase of the vegetation peak.

In summary we conclude that in Caatinga the partially heavy reliance on gap filling measures due to the somewhat meagre MERIS coverages in South America does quite likely not significantly distort the results at a large scale. Where this is the case, it can be expected that only smaller areas are affected, and mostly only to minute or moderate degrees, while the overall patterns should be quite trustable in spite of many filled gaps.

5.1.9 Special processing of test sites with data gaps due to snow

Snow cover or other winter conditions without measured fAPAR was observed and specially treated in 13 out of 22 test sites during the local winter time (see Table 15).

Table 15: Test sites with and without (or neglected) snow cover

Test sites with snow cover	Test sites without snow cover
03 South West Iran	01: Northern - Central Mexico
04 Northern Kazakhstan	02: Northern Australia
05 E Mongolia W Manchuria	07 Southern India
06 Central Tibetan Plateau	11 Eastern Africa
08 Pontic Steppe	12 Southern Africa West
09 Northern Africa	13 Western Sahel
10 Southern Europe	15 Caatinga, Brazil
14 Southern Argentina	20 Southern Australia
16 Western South America	21 Southern Africa East
17 Southern Central USA	
18 Northern USA Southern Canada	
19 South West USA	
22 Eastern Mediterranean Countries	

When generating the fAPAR data, snow and clouds resulted in undifferentiated no-data values, i.e. data gaps. While the data gaps related to clouds and rainfall during the growing season could be closed with the above described procedure for the most parts, it was neither appropriate nor possible to close the data gaps related to snow cover or other winter related conditions without plant growth. In parts of the regions with snow cover in the winter time the snowy periods (including winter clouds and frozen soils) caused data gaps extending through several months. These data gaps had to be identified as “winter gaps” in order to treat them properly and to use the remaining valid data and not discard these pixels due to extensive data gaps.

fAPAR data gaps with potential snow cover and/or clouds (during the winter season) were derived by labelling respective data gaps as snow based on the following assumptions:

- Continuous data gaps starting at the begin of the calendar years on the northern hemisphere, or starting in July on the southern hemisphere, were classified as snow
- Any data gaps occurring during the first seven and last five halfmonths, i.e. on the northern hemisphere from January to mid April, and from mid October to end of December (in the South shifted by half a year), were classified as snow respectively “winter gaps”.

These temporal limits were derived by checking the data gaps in the respective test sites and studying meteorological information about the test sites. Prior to the next step, i.e. the derivation of the Start of Season, the data gaps classified as snow were set to zeroes. For the later calculation of the vegetation productivity, the snow values were assigned the estimated dry (cold) season mean values of the respective vegetation years, in order to not overestimate the fAPAR averages of the vegetation years (relative to pixels not concerned by snow cover) by calculating the means only for the valid values during the vegetation season, or to underestimate the averages by counting the snow gaps as zero values.

5.2 Extraction of Phenological and Productivity Parameters

5.2.1 Introduction

For the extraction of phenological and productivity parameters from NPP proxy time series data, several approaches exist. They differ in underlying definitions of phenological points in time and seasons and consequently in the productivity parameters, computational complexity, geographic applicability (regional versus global), etc. White et al. (2009) for instance demonstrated comparison results for various approaches of SoS derivation including the below discussed Timesat approach for Northern America.

Among the developed approaches and respectively tools is the Timesat software, developed by Eklundh and Jönnson (2012, software manual), which appears to be the most wide spread software (download free of charge). Timesat not only performs a phenological time series analysis, but also smoothing and gap-filling of the time series data by using local polynomial least-squares functions that are fit to the upper-envelope of observed values with an adaptive Savitzky-Golay filter. The upper envelope is the level of values that do not constitute low outliers, which to Huete et al. (1999) can be regarded as negatively biased noise in NDVI time series (cloud contamination and haze lowers NDVI values).

While it seems to be widespread applied, the Timesat software is not used for analysis in the project due to several reasons: First, GeoVille had already developed some phenology tools, which proved to be successful in e.g. the GMFS project, second, Timesat requires some pre-processing and data transformations that could be avoided by staying within the ERDAS environment; also, Timesat does not readily allow for the extraction of NPP proxies for the entire vegetation year and the dry season, but puts a strong focus on the extraction of the cyclic vegetation of the growing season and differentiated parameters thereof. Further on, the usage of Timesat would have required a great deal of individual, test site (and possibly sub-site) specific parameter tuning for the extraction of the SoS especially in regions with multiple or partly weak SoS, whereas the developed SoS tool and processing chain is universally applicable without further adaptations.

Another approach for calculating phenological and productivity parameters is described by Ivits et al. (2013), who developed the “Phenolo” software at the EC Joint Research Centre. Phenolo derives a full range of phenology and productivity parameters and is globally applicable without regional adaptations. The basic principle of the SoS derivation of Phenolo is a time lagged moving average filter and the extraction of the intersection points of the filtered time series with the actual time series, which mark the turning points (start and end of season) of the seasonal trends. The length of the required filter window is spatially and temporally variable (even within years) and is automatically determined on a yearly basis by Phenolo (Ivits et al. 2013). Consequently, the adaptive length of the moving window is the key factor of this approach: “*While Reed et al. (1994) determined a general lag based on a priori knowledge about the average phenology of the study area, Phenolo is data driven using for each individual pixel its time series dynamism to determine the lag. The lag (i.e. the size of the moving average window) is the estimated length of the non-growing season defined for each pixel separately” (Ivits et al., 2013).* Phenolo uses smoothed time series data (Savitzky–Golay filter with 4th polynomial degrees) and interpolates the data to daily values.

Phenolo extracts a wealth of phenological and productivity parameters covering the entire vegetation cycles including the off-season periods, e.g., the amount of senescent vegetation outside of the growing season (Ivits et al., 2013). Beyond this approach, the method of phenological/productivity parameter extraction in Diversity II considers explicitly what was called the “***vegetation year”*** (a new feature in this domain, see section 5.2.4) and a row of further parameters. The vegetation year is closely linked to what was named the ***“dominant SoS***”, which was defined on the basis of a multi-year analysis of the SoS, as in many cases there are several or fluctuating SoS within a year, which cannot directly be taken as start of the vegetation year without selecting one of them as the dominant SoS. The methodology for this approach is described in section 5.2.2.

Figure 55 provides an overview of the derived phenological and productivity parameters, whose derivation and meaning will be explained in the below subsections.

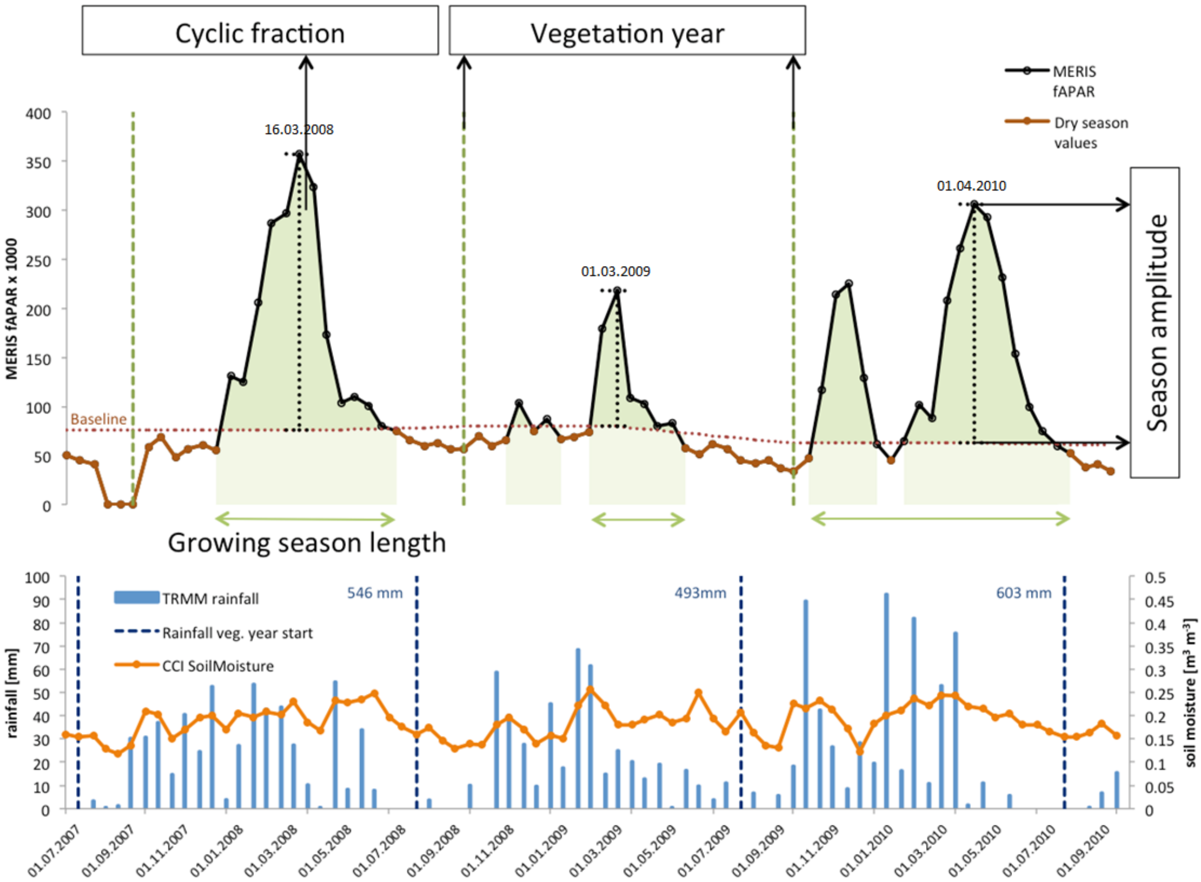

Figure 55: Scheme of the extracted phenological descriptors and periods, and corresponding rainfall and soil moisture data. Location: South Africa, Y: -29.896337, X: 25.7373764 (same as figure 3)

5.2.2 Derivation of the SoS

The Start of the Season (SoS) is the key phenological parameter, which provides access to many further phenological properties and data of a location. Yet it is differently defined and calculated by different authors with consequently deviating results, as demonstrated by White et al. (2009) for various approaches.

Within the Diversity II test sites, a large variety of phenological conditions was met both in spatial and temporal respects. Hence, the method for deriving the start of the vegetation season had to cope with a wide range of SoS conditions, including sharp to weak increases of the vegetation signal, big to very small and hardly recognisable vegetation peaks, unimodal vegetation curves and multiple SoS per year, and all combinations of the above.

In Diversity II, half-monthly, unsmoothed time series data were used and processed with specifically developed ERDAS IMAGINE models. Only for the derivation of the SoS, a slight smoothing was applied by linearly interpolating low outliers (values lower than their neighbours by more than 5% of the amplitude of the underlying fAPAR values within the time period considered, i.e. three years). In order to automatically cope with all global conditions, we developed a method that is very sensitive to any increases in the vegetation curve in order to minimise the number of missed SoS. At the same time, vegetation peaks considered too small or of too short duration could be discarded by respective fine-tuning of the method. Basically, a three-step procedure was applied:

1. Derivation of individual SoS

First, for each year, the timing of all potential SoS was derived based on the cumulative gradients of the fAPAR or NDVI time series. The moving sum values of six consecutive increments were derived, which create peaks around the start of growing seasons, whose height and length depend on the intensity of the increase of fAPAR values in relation to the preceding gradient. These peaks are thresholded with regard to negative values (discarded), and the remaining lengths and height of the peaks. By means of further fine-tuning, the SoS was defined to occur right at the start of the respective vegetation increase period. This procedure led to a 24 layer raster file per calendar (one layer per halfmonth) year indicating for every halfmonthly value if there was a SoS or not. It was derived for the years from 2003 to 2011, for which full MERIS coverages were available.

2. Derivation of dominant SoS

In the second step, the temporal ranges of the most frequent SoS accumulations per year during these nine years were determined. The starts of season within these ranges were taken as the “dominant” SoS group, which constitutes the local start of the vegetation year. In cases where no SoS had been derived for a given year or several years within the defined range, the mean SoS of the other years was used for substitution. This way, singular SoS (not occurring in temporal clusters) could be discarded, and missing SoS in extremely dry years substituted. In regions with two (or more) growing seasons per year, in many cases not all of their SoS were detected in all years. Consequently, within one of the resulting temporal SoS ranges, the number of SoS derived was higher than in the other(s). This SoS group constituted the dominating SoS group. If two SoS groups were detected in the same number of years, the first within the calendar year was taken as the dominant SoS.

3. Smoothing the dominant SoS

In the third step, the series of single year SoS were smoothed in the following way: the mean of the SoS of the previous and following years was derived for each SoS, and the SoS of a particular year was replaced by the mean of its “neighbours” if the mean was earlier than the actually determined SoS. This way, an overly varying length of the vegetation years from year to year could be avoided. This is relevant for the calculation of the average fAPAR (NDVI) per vegetation year. Without the smoothing, the average greenness of vegetation years with a late SoS followed by a vegetation year with an early SoS (this fluctuation was found to be typical) would be overestimated, as it would include a much shorter dry season.

5.2.3 Calculation of the Baseline

Besides the SoS, the “baseline” is a crucial parameter in the presented concept of vegetation phenology and productivity, as it separates dry (or cold) season values from the cyclic vegetation and determines the amount of the “cyclic vegetation”, as well as the size of the “amplitude”.

A commonly applied and very straight forward approach for deriving the baseline is implemented in the Timesat software package (Eklundh & Jönsson, 2012). It defines the baseline as (user adjustable) threshold in percent of the amplitude given by the minimum level and the vegetation peak maximum, e.g., typically using 20% or 25% of the amplitude as threshold. I.e. once the vegetation index time curve reaches this level, the growing season would start. The cyclic vegetation is calculated as integral of the time series curve above this baseline (called “small integral” in the Timesat software). We have first taken a similar approach, and compared the outputs to Timesat derived outputs (for the cyclic vegetation alias “small integral”), resulting in pearson $r^2 > 0.9$ in most cases (see section 5.2.3.1).

However it turned out that the resulting baseline may vary quite strongly from year to year and did sometimes not well reflect the upper dry season boundary, which we felt would represent the baseline. Thus, for using the dry season average values as explicit parameter (the Timesat concept does not explicitly consider the dry season level as a parameter), some other determination of the baseline appeared more appropriate.

Conceptually, we figured that the baseline should represent the approximate upper boundary of the low season values with smooth transitions from one vegetation year to the next. Further on, based on studying numerous examples of fAPAR / NDVI curves, it seemed that the baseline should not only be determined using the amplitude directly, but be also be based on the ratio of the amplitude to the dry season level. The larger this ratio, the stronger appeared the (relative) fluctuations of the dry season values, and consequently the higher the required threshold to be surpassed between the defined dry season and the growing season.

To obtain such a baseline, we developed an approach based on an estimation of the mean amplitude of every two consecutive vegetation years and its relation to the average of the smallest values in between these maxima. The procedure consists of the following steps (explained for the example of the two vegetation years 2003 and 2004):

1. The average of the four lowest (fAPAR, NVDI) values between the two consecutive vegetation peaks of (in this example) vegetation year 2003 and 2004 is derived and the average maximum value is calculated.
2. An empirically derived regression formula is used to derive the upper threshold of dry season values that are used (along with this threshold as value) to determine the basevalue. This will vary with the quotient of the amplitude (average MAX minus average MIN from step 1) and the average MIN: The larger the quotient, the larger the resulting factor will be that is used to multiply the average MIN. The product of this factor and average MIN will constitute the searched upper threshold for the dry season values. The factor varies mostly between 1.05 (very small ratios between amplitudes and mean low values, e.g. for a ratio of 0.15 the factor will be 1.05) and 1.5 (for a ratio of 4). The regression equation is shown in Figure 56.

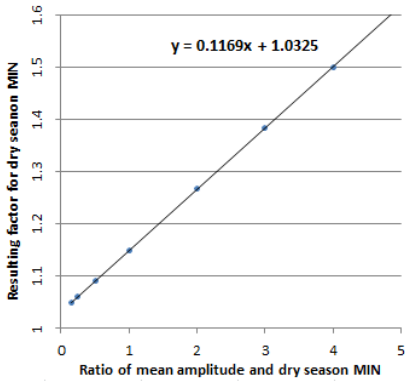

Figure 56: Empirically fixed relation between amplitude and dry season MIN

3. All values below this threshold plus the threshold value itself (to account for cases where all or most dry season values are 0) are averaged, and their standard deviation (SD) is determined.
4. The average plus SD * 1.5 will constitute the base value (average and SD derived in step 3)
5. If the MAX value of vegetation year 2003 is more than double of the 2004 MAX or less than half, the basevalue for the values after the 2003 peak vegetation is being calculated separately, based on the amplitude built by the MAX 2003 only.
6. If step 5 is realised, the baseline of 2003 will end at the end of the vegyear 2003, and the new baseline for the beginning of vegyear 2004 will start then.
7. Most frequently, the basevalue derived in step 4 constitutes the common basevalue of the dry season between 2003 and 2004 cyclic fractions.
8. The same procedure is applied to all further low seasons between consecutive vegetation year peaks
9. The baseline is being derived in the following way: In the described case the calculated basevalue will be applied from the start of the vegetation year 2004 until (and including) the MAX of 2004, and will then linearly grade into the next basevalue (derived for the low season between the peaks of 2004 and respectively 2005), reaching this value at the end of the vegetation year 2004.

This procedure was applied to the MERIS fAPAR data, the MERIS NDVI data (where these were tested, i.e. in site 4 and 12) and to the GIMMS NDVI data. Figure 55 shows the baseline for three consecutive vegetation years for a location in South Africa.

5.2.3.1 Comparison of the Cyclic Fraction fAPAR with TIMESAT derived results

The project took also the opportunity to compare one of the NPP proxies derived with the GeoVille phenology tools to that derived with the Timesat software. The fAPAR sums of the cyclic vegetation were compared for several areas composed of 400 pixels and located in areas of different vegetation density. These tests were conducted before the above described procedure for the baseline calculation had been developed. The first approach, as described above, was analogue to the Timesat method. Some results are illustrated in time series and scatterplots in Figure 57.

Generally there is a high linear correlation between the variables derived with the two different tools, with pearson r in the order 0.95. The Timesat (TMP) cyclic vegetation fAPAR sums are consistently higher than the project derived results: this difference can be related to the data smoothing of Timesat, where the upper envelope level of the data is used as base level, or/and a systematic shift of the period of the cyclic vegetation towards an earlier start and a later end. More likely is the first interpretation, as in both cases a 10% threshold to the amplitude was applied for delineating the cyclic vegetation period. Further contributing to the difference may also the fact that Timesat applies a definition of the phenological periods by doy (day of the year), whereas we include only the halfmonthly fAPAR values that are above the thresholds. Given these differences in the derivation of fAPAR sum values for the cyclic fraction vegetation, we feel that the results are very similar especially in their internal variation to each other.

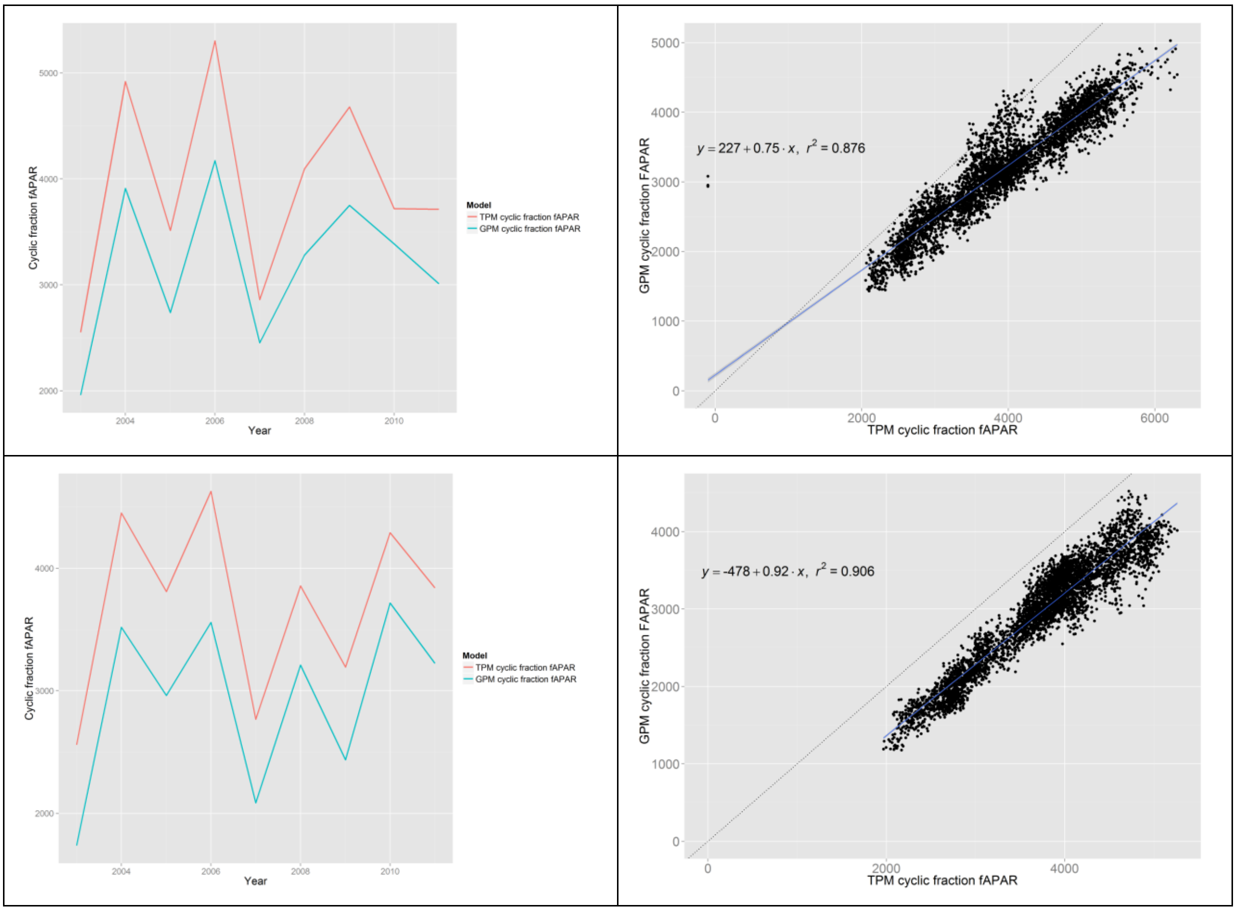

Figure 57: Comparison of the Cyclic Fraction fAPAR sums derived by GeoVille (GMP) versus results of the Timesat phenology software (TMP)

5.2.4 Definition and derivation of all further phenological parameters and of productivity parameters

As mentioned earlier, the vegetation year was introduced as a new feature, which was not explicitly addressed in other work or in a similar way to our knowledge. Le Houérou (1984, p. 216) basically calls for exactly this when he writes in the context of contrasting yearly vegetation productivity and rainfall: *"In connection with the above it should also be mentioned that annual data on both variables should not concern the 'calendar year' but the 'biological year' or the 'agricultural year', i.e. from the beginning of the rainy (growing) season to the end of the dry (dormancy) season; for instance from September to August under the Mediterranean climates of the northern hemisphere, from May/June to April/May in tropical West Africa, etc. The correlations are thus evidently much better than using calendar-year rainfall data…".* In comparison to these fixed "biological years", Diversity II goes a step further and determines the local vegetation year, which depends on the local, pixel-based seasonal cycles.

The concept is illustrated in Figure 55, showing three consecutive vegetation years, which start and end at the dominant yearly SoS. The selected point is located in South Africa in a grass land area according to CCI Land Cover. In the shown example, the variability between the three vegetation years is very high, both with regard to the absolute fAPAR values and to the seasonality, ranging from one distinct green peak in the vegetation year 2007 to two peaks in vegetation year 2009, and a year with low values, and a weak first peak in vegetation year 2008. The timing of the highest peaks is quite close and varies only by one month.

The vegetation year constitutes a statistical SoS based time frame, used for temporally referencing all further phenological parameters derived from the vegetation times series data. The vertical green dashed lines in Figure 55 mark the starts of the vegetation year in the shown example. As the SoS depends on the local (i.e. pixel) vegetation/land cover/land use, the vegetation years may vary accordingly on a small scale.

Like the SoS and the baseline, the parameters were derived with specifically developed ERDAS models. For the phenological and productivity parameters, the SoS and the basevalues served as inputs, along with the fAPAR data. The extraction methodology is straight forward and evolves directly from the definition of the parameters (see Table 16), with the exception of the SoS and the baseline, for which the definition and methodology have already been described in Section 5.2.2. The resulting phenological and productivity parameters are raster image data, where the phenological parameters express the timing of the phenological events as number of the respective halfmonth within the vegetation year, and the productivity parameters (NPP proxies) are made up by sums, averages, or single values (e.g., in case of the maxima or amplitudes) of the underlying vegetation index values. These parameters were calculated for the eight vegetation years starting in 2003 to 2010, and ending in 2004 to 2011, and consequently constitute time series with (vegetation-)yearly values for eight years. These time series data were the input for the Diversity II NPP status and trend indicators. The definition and calculation of the dryland indicators is described in section 6.2.

A wealth of phenological and productivity parameters was extracted, which all relate to the temporal frame of the local (pixel based) vegetation years. However, only the highlighted parameters have been actually used for generating the Diversity II products, as they were regarded as the most important parameters, and in order to avoid an overload of products. However, all these results are available and could be activated for further applications.

The phenology and productivity parameters were derived for:

- MERIS based fAPAR data for the 22 globally distributed Diversity II test sites covering the period from 2002/June to 2012/April
- MERIS based NDVI data for Diversity II test sites 04 Northern Kazakhstan and site 12, Southern Africa West covering the period from 2002/June to 2012/April
- NPP data provided by DLR, using the BETHY/DLR model 2003-2010, test site 04 Northern Kazakhstan and site 12, Southern Africa West, and
- NOAA GIMMS NDVI data (globally, 1982-2011)

Table 16: Major phenological and productivity parameters derived for each pixel (highlighted parameters are directly used for generating the Diversity II products)

No.	Phenological and productivity parameters	Description
1	Start of Season (SoS)	Turning points at the start of vegetation peaks
2	Dominant start of vegetation year	The average timing of the most frequently occurring SoS group, derived from (1)
3	Yearly start of the vegetation year	The specific SoS of single years within the dominant SoS group. If in a particular year no SoS was derived during the time period of the dominant SoS group, the average (2) is taken (see section 5.2.2)
4	Vegetation year average greenness	Average yearly fAPAR (NDVI): proxy for the annual vegetation productivity within the period between two yearly SoS (3). This parameter interferes with biomass estimation to an unknown degree, depending on the structure of the vegetation canopy and the activity throughout the year. In test sites with fAPAR (NDVI) data gaps due to winter conditions (snow, frozen ground, clouds), the estimated average cold season level of the fAPAR values were filled in the gaps in order to make the yearly averages of those pixels better comparable to pixels where no winter-gaps were present. Otherwise the average greenness of the vegetation year may be underestimated (if the "winter gaps" are included in the average), or overestimated, if they are not included.
5	Baseline	Threshold line separating the growing season from the dry or cold season base values. It is defined based on the amplitude and the average dry (cold) season values (see Figure 55) and delineates approximately the upper limit of the dry (cold) season values.
6	Start of growing season	Time when the baseline is surpassed on the way from the dry (cold) season to the (first if more than one) peak
7	End of growing season	Time when the curve falls the last time within the vegetation year under the baseline
8	Overall cyclic vegetation	Sum of all values above the baseline; from every value the baseline is subtracted
9	Length of overall cyclic vegetation	Number of half-months from the first value above the baseline to the last value above the baseline
10	Start of growing season excluding very small and short peaks	Time when the baseline is surpassed on the way from the dry (cold) season to the (first if more than one) peak, not considering very small and short peaks (see (14) for definition of "small" and "short" peaks)
11	End of growing season excluding very small and short peaks	Time when the curve falls the last time within the vegetation year under the baseline not considering very small and short peaks (see (14) for definition of "small" and "short" peaks)
12	Cyclic vegetation from start of growing season to maximum	Sum of all values above the baseline prior and including the maximum value; from every value the baseline is subtracted
13	Cyclic vegetation from maximum to and of growing season	Sum of all values above the baseline after the maximum value; from every value the baseline is subtracted
14	Cyclic vegetation without very small and	Sum of all values above the baseline excluding very small and short

	short peaks	peaks; from every value the baseline is subtracted. Small is defined as peaks including not more than five percent of the overall cyclic fraction sum; short is defined as peaks no longer than 2 half-months.
15	Length of cyclic vegetation without very small and short peaks	Same as (9) minus the number of half-months with very small or short peaks.
16	Dry season average	Average of all values after the end of the growing season
17	Dry season average including very small and short peaks	Same as (16) including values of very small or short peaks (see (14) for definition of "small" and "short" peaks)
18	Time of Maximum	Number of half-month with the highest value within the vegetation year relative to the start of the vegetation year
19	Maximum value	Highest value of the vegetation year; if there are two or more equal maximum values, the earliest is taken
20	Amplitude	Difference between maximum and baseline value at the time of maximum
21	Number of peaks	Number of peaks within the vegetation year; a peak is defined as a maximum within 11 halfmonths that is larger than (or equals) the minimum value of the vegetation year plus 25% of the amplitude
22	Time of peaks	The numbers of half-months with defined peaks (19) relative to the start of the vegetation year
23	Percent of cyclic vegetation sum of vegetation year sum values	This percentage reflects the share of annual vegetation of the overall greenness of the vegetation years and has, along with (4) been used for the derivation of second order indicator P50: Functional Classes

5.3 Aggregation of rainfall and soil moisture parameters

The rainfall and the soil moisture data were aggregated, i.e. summed and respectively averaged for the vegetation year and the cyclic vegetation in order to be used for the derivation of the RUE and SMUE indicators. Thus, like the phenology and productivity parameters, one rainfall and one soil moisture value were derived per vegetation year and cyclic vegetation, totalling also to time series data with eight values each.

The rainfall and soil moisture data were aggregated based on the phenology of the vegetation index time series data they were used for. Thus for relating rainfall and soil moisture to the MERIS fAPAR based NPP proxies, the MERIS fAPAR derived parameters were used, whereas for MERIS NDVI the phenological parameters generated with the MERIS NDVI were used, and for the GIMMS NDVI data the GIMMS based phenology parameters, respectively. Only for the modelled NPP data the phenology parameters of the vegetation time series data the NPP data were contrasted with were used for aggregating the rainfall and soil moisture data, in order to cover the same periods for the comparison.

As mentioned above, rainfall and soil moisture data were aggregated into two periods:

Firstly, the vegetation year, where sum values for the rainfall data were derived, and average values for soil moisture. The time for the aggregation of the rainfall data was shifted back by two month prior to the start of the vegetation year, the period for the soil moisture data was shifted back by one month. Both temporal shifts were defined based on visual comparisons of the time series data and on various experiences with such time lags (see Figure 55).

The second aggregation period starts at the same time as that of the vegetation year, but ends at the end of the growing season. The rainfall sums and soil moisture averages of this period were compared to the cyclic vegetation.

The yearly rainfall sums and those for the growing season were slightly smoothed prior to the indicator calculation: every yearly value was replaced by a weighted average of the prior value (*0.5) and the current (*1) value. This was done in order to account to some degree for the known "memory effect" of ecosystems, i.e. to react on rainfall amounts of the previous year(s) in addition to the rainfall of the current year. This memory effect was studied for instance by Zhou (2013) or Martiny at al. (2005).

5.4 Background and Derivation of RUE and SMUE

In addition to the NPP proxies, Rain Use Efficiency (RUE) and Soil Moisture Use Efficiency (SMUE) indicators were derived. Le Houérou (1984) defined RUE as quotient of annual primary production by annual rainfall. RUE thus indicates the amount of biomass growing per unit rainfall water per year, where the NPP is typically expressed in kilogram above ground dry matter phytomass per hectare and year [kg DM/ha/year] (ANPP – above ground net primary production), and for rainfall the average yearly precipitation in [mm] is taken.

While RUE is based on a widely applied, tested, discussed, and partly modified (with regard to the temporal integration periods) approach of Le Houérou (1984), SMUE is an analogue concept based on soil moisture data instead of rainfall as water availability parameter. Theoretically, soil moisture is more directly related to plant water availability than rainfall, so SMUE is offered as a potentially useful additional indicator in Diversity II.

5.4.1.1 Theoretical Background of RUE

Spatial analysis of RUE

Le Houérou (1984) analysed numerous RUE values worldwide and established relations between RUE and average annual rainfall for a large variety of environments: in different plant communities, under different vegetation conditions, soil conditions or under different photosynthetic conditions. While Le Houérou did not find a significant overall correlation between precipitation and worldwide collected RUE figures, he states (p. 232) that "*considering a given type and intensity (or level) of management, there seems to exist a consensus among investigators that RUE does increase with rainfall up to a certain point where nutrients or water logging may become a limiting factor*". Some examples are illustrated in Figure 58, contrasting RUE values for a range of rainfall conditions from 100 to 500 mm/year for different soil conditions and plant communities in different conditions.

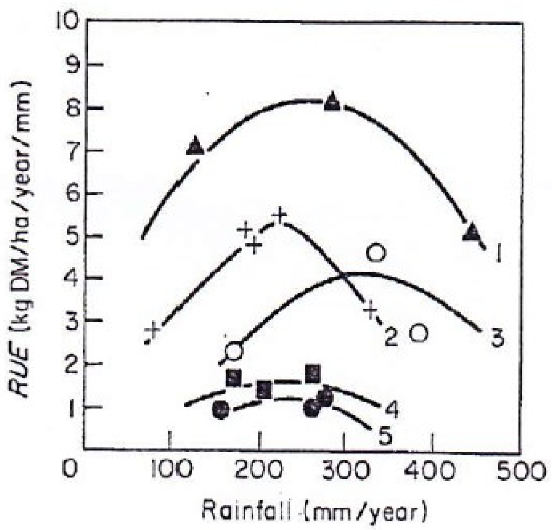

1 —— ▲—— Open nanophanerophytic scrub of *Ziziphus lotus–Atriplex halimus–Cynodon dactylon*. Silty (SL/LS) alluvial depression with run-in and deep water table.
2 —— + —— Chamaephytic steppe of *Rhantherium suaveolens* and *Stipa lagascae*. Loose sand on sandy loam.
3 ——O—— Depleted *Artemisia herba alba* steppe with sparse *Hammada scoparia* and periodical cultivation. Deep silty loam and sandy clay alluvia.
4 ——■—— Depleted chamaephytic steppe of *Rhantherium suaveolens* and *Atractylis serratuloides*. On sandy silt over sandy loam.
5 ——●—— Chamaephytic steppe of *Anarrhinum brevifolium* and *Zygophyllum album*. Loose sand veil on thick gypsum crust.

Figure 58: RUE in several ecosystems of Tunisia. Source: Floret and Pontainer 1978, taken from Le Houérou 1984.

All different RUE curves exhibit a hump shape, but show different absolute RUE values and different rainfall amounts at their peaks. Le Houérou (1984, p. 236) demonstrates for instance that in "*conditions of non-fertilization, optimum productivity of sandy soil, either for olive trees or rangeland, is reached with precipitations of 225-250 mm while on silty soil the higher level is only reached around 350 mm and above"*. Le Houérou further concludes (also based on numerous other figures) that RUE on sandy soils is limited due to a shortage of nutrient above 250 – 300 mm of rainfall. Or with other words, rainfall cannot be turned into higher production above this rainfall threshold as sandy soils are lacking the necessary nutrients. Silty or loamy soils on the other hand, according to Le Houérou will start their productivity only from a higher rainfall threshold on, and reach their peak production efficiency at higher rainfall amounts than sandy soils, before their RUE also drops at still higher rainfalls.

This means vice versa, that in the spatial domain RUE values cannot be directly compared and interpreted in terms of vegetation condition, without knowing these soil/plant community/vegetation condition and management–specific relationships of RUE and rainfall.

Further on according to Le Houérou, only heavily degraded plant communities and ecosystems show RUE values in the order of 0.5 – 1 independent of rainfall amounts, while reasonably healthy vegetation, no matter which precipitation level, usually exhibits RUE values larger than 2: "*it would seem that, whatever the rainfall, RUE should not go much below a score of 2.0, even on shallow soils, whenever vegetation is in reasonably good dynamic condition*" (Le Houérou, 1984, p. 234). This would mean that RUE values smaller that approximately 2 would indeed point to (severe) vegetation degradation. Le Houérou (1984) reports such low values especially but not exclusively for North Africa and the Near East.

Zhongmin et al. (2010) report about a study of RUE based on in situ NPP data from 580 sites along a 4500 km long grassland transect in China. The summary of the results with regard to PUE (Precipitation Use Efficiency = RUE) is cited here (p. 842): *"PUE decreased with decreasing mean annual precipitation (MAP), except for a slight rise toward the dry end of the gradient. The maximum PUE showed large site-to-site variation along the transect. Vegetation cover significantly affected the spatial variations in PUE, and this probably accounts for the positive relationship between PUE and MAP".* Thus the positive relation between RUE and MAP in the spatial analysis stated by Le Houérou is also found in the study of Zhongmin et al. (2010).

Consequence for the application of RUE in spatial concepts of land degradation mapping

Based on these findings RUE values above approximately 2 seem to be harder to interpret without available additional information on soil and vegetation types (biome type), management, etc. Under the same rainfall amounts or aridity conditions, RUE values at different locations can differ substantially without pointing to any degradation, as can be seen in Figure 58. Vice versa, (moderately) degraded and intact plant communities may have overlapping RUE ranges without any clues to their vegetation condition. Following Le Houérou, spatial comparisons of RUE levels greater than approximately 2 intended to lead to the assessment of vegetation conditions can only (if at all) be made, if all other vegetation, management and environmental factors besides the degradation status are known and equal/comparable within the assessed areas. Such conditions are hardly if ever met. Also Ruppert et al. (2012, p. 24) state: "*Meta-analyses revealed that ANPP and RUE response to* *land use and precipitation were strongly modulated by biome and soil type*"…. and further they suggest (p. 24): "*For example, the diverging magnitude of precipitation effects across biomes (and soils) strongly suggests to use RUE as a biome-specific indicator. We propose to establish reference values of maximum and mean RUE for different biomes and if possible further stratified for soil types. This would considerably increase the usability of RUE as an ecological indicator for ecosystem state, productivity and degradation*".

Approaches such as "2dRUE", developed by Del Barrio et al. (2010) and applied to the Iberian Peninsula take into account the influence of aridity on RUE and hence normalise RUE for aridity. Still, RUE status (average condition) values, even if normalised for aridity, cannot directly be interpreted in terms of existing soil degradation or exposure to degradation or richness/poverty of biodiversity without knowledge about growth factors other than rainfall, especially soil and terrain types, hydrology, plant communities, land management, etc.

A further limiting factor of such spatial RUE assessments is the fact that the spatial distribution of the rainfall during a given observation period will certainly influence the measured average RUE condition of an area: Regions that received a larger amount of rainfall (than longer term average) during a given observation period may appear "greener" and more productive or efficient in rain use than other regions that may be in a better ecological condition, but received comparably little rainfall. For these reasons the spatial comparison of local or regional average RUE conditions is not straight forward and cannot be properly accomplished in detail without information on the local or regional response of vegetation in a (relatively) good condition to the entire spectrum of rainfall variability.

While vegetation productivity and RUE obviously follow the rainfall gradients at the large scale (not considering temperature and radiation differences) of respective maps, the smaller scale differentiations exhibit the presence of further influences on vegetation growth at more local scales. These local and regional factors are especially land use, soil properties and topography and include also the protection status of areas. For instance many linear features with (mostly) higher NPP proxy and RUE values than their surroundings can be related to river valleys (often with only seasonal or ephemeral surface water).

Hence we do not try to establish direct and generalised links between spatial gradients of RUE (status, or average condition) and the ecological condition of the land, as for instance exercised by del Barrio et al. (2010).

Temporal RUE analysis and usage for the monitoring of vegetation degradation

Based on the assumption that yearly vegetation productivity at a given location varies linearly with- and is even proportional to yearly rainfall, RUE has been introduced as a concept to retrieve areas with a loss of vegetation productivity independently from rainfall or soil moisture variability and thus to diagnose potential man-made soil degradation. A prerequisite for applying RUE as a monitoring tool for land degradation is that the linear relation between rainfall and (above ground) net primary production is stable through time in the area studied during unchanged biophysical conditions, as long only rainfall varies. Changes in RUE would then signal either potential land degradation or improvement. In the above cited study of Zhongmin et al. (2010) the autors state (p. 842): "*However, there was no significant relationship between inter-annual variations in precipitation or vegetation cover and PUE within given ecosystems along the transect".* This may confirm the assumption for using RUE as degradation measure, as RUE seems to be independent of rainfall and vegetation cover within given ecosystems of the grassland transect.

However, in various studies it turned out that there are constraints to using RUE as indicator for vegetation degradation, in particular its variable correlation with precipitation – for which it is supposed to normalize vegetation productivity. As Fensholt and Rasmussen (n.d.) point out, there is not a simple relation between vegetation greenness and rainfall amounts, and these authors demonstrate the very limited relevance of the original RUE concept for the assessment of potential degradation or biophysical "improvement" in dryland areas at the example of the Sahel zone. Fensholt and Rasmussen point among other objections to the offset of the NDVI – based RUE, i.e. the fact that the NDVI has to surpass a certain, soil dependent value, until the NDVI signal starts to react to vegetation. This results in an offset of NDVI plotted against rainfall, which decreases in its relative size with increasing NDVI/Rainfal and thus leads to a decreasing RUE with increasing rainfall, if this pixel-specific offset is not corrected. Using fAPAR instead of NDVI, this sort of bias is expected to be less since theoretically zero fAPAR is obtained for zero NPP.

Further on, Fensholt and Rasmussen (2011, p. 445) state that "*the correlation of annual RUE and RFE rainfall (1996–2007) for the Sahelian belt was characterized by strong negative r* [pearson correlation coefficient, added by authors] *values (average of −0.86) meaning that RUE is not able to normalize the NDVI for variations in rainfall in those regions. The high negative correlation between RUE and annual rainfall implies that this simple RUE approach does not succeed in producing a ratio that is independent on the effects of annual rainfall change, which was the original intention when introduced (Le Houerou, H.N. 1989)*".

A way to overcome the above described problems with RUE calculation when using NDVI was demonstrated in another publication of Fensholt et al. (2013), whose findings were used for the project. Essentially the authors suggest that instead of the annual sums of NDVI (often being used as a proxy for NPP) and rainfall, the sum of the increments of NPP (NDVI or fAPAR) during the growing season may be taken, with accordingly integrated rainfall data to improve the usefulness of RUE. However, it turned out that also for this vegetation proxy, called "cyclic vegetation" (see section 5.2.4) RUE was found to be frequently correlated both positively and negatively, with rainfall.

In summary, the temporal relation between NPP and rainfall depends on factors such as

- the amount and temporal distribution of rainfall within an observed period,
- other climatic conditions, especially temperature and evapotranspiration,
- changes of these variables and climatic systems through time, or
- the current conditions of the ecosystems with regard to environmental changes (e.g. , time elapsed since the last drought, see Miehe et al. 2010 or Ratzmann 2014),
- regional and local characteristics, such as soil properties, hydrology, land cover & land use, etc. and their changes through time.

RUE as a lumped indicator is not revealing whether negative RUE trends for instance are related to increasing rainfall and/or to decreasing vegetation productivity. In addition, RUE depends on the type of NPP (or proxy) data used, as can be seen for instance in Figure 59, where NPP (modelled by BETHY/DLR) based and MERIS fAPAR based RUE average maps are contrasted.

Due to these influences many areas do not fulfill the basic assumption of RUE, i.e. a linear or even proportional relation between rainfall and NPP through time (see for instance Fensholt et al. 2013 and Ratzmann 2014).

Against this background and the short observation period, we stress again that the derived RUE indicators should only serve as qualitative indicators of potentially worsening or improving areas, and not as strict measures of the presence and degree of vegetation degradation. The same applies to the RUE status maps, which however do provide qualitative indications of functional vegetation properties and differences between the biomes.

The RESTREND method is an alternative way to study degradation trends, by determining the trends of residuals of linear regression analysis between NPP (proxies) and rainfall, assuming a linear relationship between NPP and rainfall during the observation period. A decreasing trend of the regression residuals would point to a potential degradation. Based on a comprehensive study of the RESTREND method including simulations of trend input variables in South Africa, Wessels et al. (2012, p. 20) came to the conclusion that "*Unless a confirmed non-degraded reference period is available to establish the expected ΣNDVI–rainfall relationship for an area, the RESTREND method will suffer from this inherent limitation. Correcting for rainfall trends and variability therefore remains one of the biggest challenges when monitoring land degradation*".

The generation of RUE based on moderate resolution EO data in this project certainly bears a larger potential than the more commonly used of low resolution input data (e.g. GIMMS NDVI) on the one hand, but in the absence of in situ reference data, interpretability remains limited.

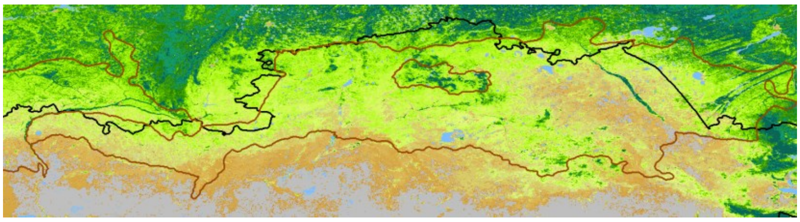

(h) Rain Use Efficiency from mean BETHY/DLR vegetation year sum NPP and mean TRMM rainfall 2003-2010 [kg C/ha/mm P/year]

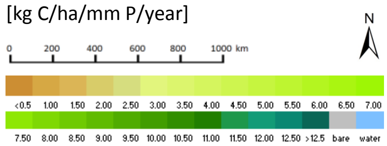

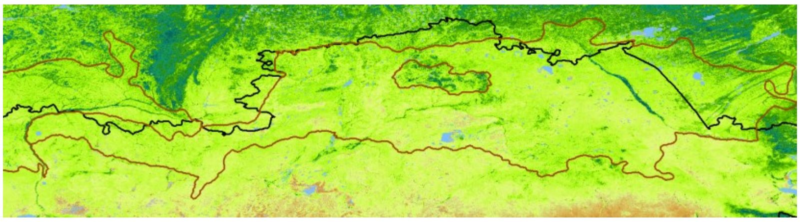

(i) Rain Use Efficiency based on MERIS vegetation year fAPAR (*1000) and TRMM rainfall 2003-2010

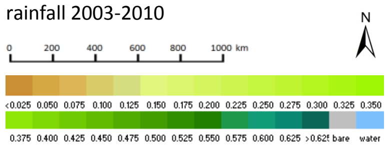

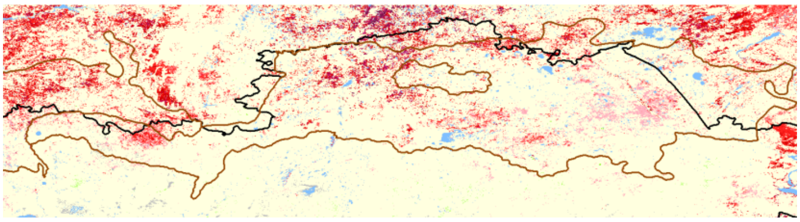

(j) Trend (Theil-Sen, 9 0.1) of Rain Use Efficiency based on BETHY/DLR vegetation year sum NPP and TRMM rainfall 2003-2010

[g C/m²/mm P/year]

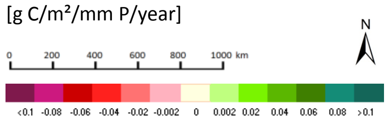

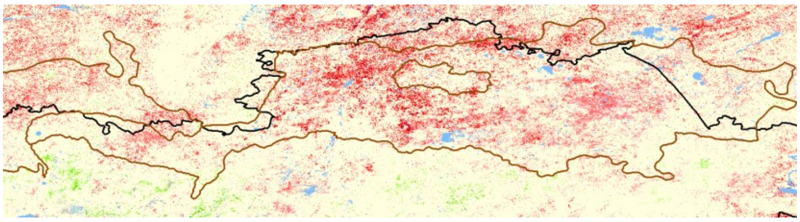

(k) Trend (Theil-Sen, 9 0.1) of Rain Use Efficiency based on MERIS vegetation year fAPAR and TRMM rainfall 2003-2010

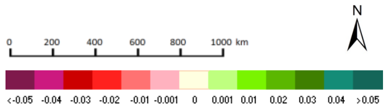

Figure 59: Contrasting MERIS fAPAR derived indicators with BETHY/DLR modelled NPP based indicators in test site 04, Northern Kazakhstan. The black line is the northern country border of Kazakhstan, the brown polygon represents the WWF ecoregion boundary of the actual study site.

5.4.1.2 RUE and SMUE calculation

For later usage in trend and variability analyses, RUE and SMUE were calculated on a yearly basis for the three major phenological period differentiated in the project, i.e., the vegetation years, the cyclic vegetation, and the dry season. The calculation is straight forward: the aggregated yearly means and respectively fAPAR (NDVI) sums for these integration periods (see Table 16) were divided by the corresponding aggregated rainfall and soil moisture data, resulting in 8(vegetation years) * 3(phenological periods) = 24 RUE and respectively SMUE values for each test site.

For derivation of the status indicators of RUE and respectively SMUE, more precisely for the 8-vegetation year averages, and correspondingly the cyclic vegetation and dry season RUE/SMUE, RUE and SMUE were directly derived as based on the underlying status parameters, i.e. the 8-year averages of fAPAR (NDVI) and rainfall as well as soil moisture.

6 Indicator Algorithms

6.1 Lakes Indicators

6.1.1 Fist Order Indicators: Status, Change and Trend Maps

Lake biodiversity threats could be classified in four main categories: physical intervention, pollution, invasive species and exploitation of populations (Sandlund, O.T & Viken, A., 1997). Of these four threats, it is primarily for the first two that there are clear practical and theoretical links to the diversity of lake habitats. Physical interventions, both in the form of water regulations and drainage will both generate changes in the habitat distribution and diversity. Emissions of pollutants in the form of nutrients, particles or organic matter that directly or indirectly reduces the light penetrating the water column will also affect the areal propagation and number if species in the lake habitats. Emission of acidifying substances is supposed to lead to clearer water and if this is true, the acidification will actually generate an expansion of the submerged vegetation habitat (Blomqvist,P., Kautsky, L., Pihl, L., & Wennhage, H., 2003). Remote sensing technique can provide reliable and quantitative measures of chlorophyll a, suspended sediments, yellow matter and turbidity. For example, high levels of Chlorophyll *a* concentrations serves as an index for high phytoplankton biomass, which often indicate poor water quality, and in a second step poor aquatic biodiversity. Status maps corresponding to the three primary constituents in lake waters are produced for the investigated lakes and can serve, without any further combination or aggregations, as a first order indicator of biodiversity status. Additionally, maps showing the turbidity/transparency and the inversely related Secchi Depth status are available. These two are mainly determined by the concentrations of TSM and/or yellow substance, and are often used as indicators for water quality, as well as, abundance and diversity of shallow underwater habitats. Finally, LSWT products from ARC Lake and LEGOS Hydroweb water level time series are available. In most cases, high/increasing temperatures will have negative effect on diversity. From these initial status maps temporal and spatial aggregations and combinations can be produced by the user in order to generate higher order status and trend indicators.

Table 17: Water quality parameters and EO source

Parameter	Indicator for	Sensor
Chla	Eutrophication	MERIS FRS L2 products
TSM	Physical disturbance	MERIS FRS L2 products
Yellow Substance	Contamination	MERIS FRS L2 products
Turbidity	Physical disturbance and/or contamination	MERIS FRS L2 products
Secchi Depth	Physical disturbance and/or contamination	MERIS FRS L2 products
Temperature	Eutrophication	CFI (AATSR producs)

In order to provide absolute indicators, i.e. calculated from accurately estimated optically active substances (OAS), one would have a lake specific parameterization of the algorithm.

It was considered to provide the following status and trend indicators for all 300 lakes and reservoirs:

- Annual status maps (S2002-S2011) for Chla, TSM, yellow substance, turbidity and Secchi Depth, as an average of 3-5 MERIS FRS images registered during one or two predefined months, e.g. July-August, for each lake or reservoir, including statistics for inter-annual variability.
- A lake average product as a status maps for temperature based on arithmetic means of CFI data available through the ARC-Lake project.
- Periodical status maps for each lake or reservoir, as an average of the annual products from three consecutive years. Three epochs in all. Aggregates of temperature products will be produces in a similar manner with respect to availability.

- Classification of each lake and reservoir into *Oligotrophic, Mesotrophic and Eutrophic* status based on the periodical status maps (AbsLakeStatus).

Calculation of periodical change for each lake and reservoir based on the periodical status maps (AbsLakeTrend).

Table 18: Maps and indicators (L3 & L4)

Map/Indicator	Derived from	Classification
L3.AP1	Mean(S2003-S2005)	Absolute concentrations/transp.
L3.AP2	Mean(S2006-S2008)	Absolute concentrations/transp.
L3.P3	Mean(S209-S2011)	Absolute concentrations/transp..
L3.AbsLakeStatus	Classification(P1-P3)*	Oligotrophic, Mesotrophic and Eutrophic status
L3.AT1	Mean(S2003-S2005)/Mean(S2006-S2008)	0-0.8 = negative diversity trend (NegDiv) 0.8-1.2 = No change (NoChange) 1.2+ = positive diversity trend (PosDiv)
L3.AT2	Mean (S2006-S2008)/ Mean (S209-S2011)	0-0.8 = negative diversity trend (NegDiv) 0.8-1.2 = No change (NoChange) 1.2+ = positive diversity trend (PosDiv)
L3.AT3	Mean (S2003-S2005)/ Mean (S209-S2011)	0-0.8 = negative diversity trend (NegDiv) 0.8-1.2 = No change (NoChange) 1.2+ = positive diversity trend (PosDiv)
L3.AbsLakeTrend	(T1 and T2)	POS, NEG, STABLE, UNCERTAIN
L4.P1	Lake average product	Low, moderate, high temperature
L4.P2	Lake average product	Low, moderate, high temperature
L4.P3	Lake average product	Low, moderate, high temperature
L4.LakeTempStatus	Classification(P1-P3)	Low, moderate, high impact on eutrophication.
L4.T1	TBD**	0-0.8 = negative diversity trend (NegDiv) 0.8-1.2 = No change (NoChange) 1.2+ = positive diversity trend (PosDiv)
L4.T2	TBD**	0-0.8 = negative diversity trend (NegDiv) 0.8-1.2 = No change (NoChange) 1.2+ = positive diversity trend (PosDiv)
L4.T3	TBD**	0-0.8 = negative diversity trend (NegDiv) 0.8-1.2 = No change (NoChange) 1.2+ = positive diversity trend (PosDiv)
L4.LakeTempTrend	TBD**	POS, NEG, STABLE, UNCERTAIN
L2.1ClimEu	AbsLakeStatus and LakeTempTrend	Possible climate change induced eutrophication (Yes) or (No)

** E.g. based on the lake type as defined in Ch. 3.2.1.*
*** Trend indicators will be produced if more than one temperature product is available.*

For all parameters in Table 18, except for Secchi depth, low concentrations indicate better status. This means that the Secchi depth trend maps is classified inversely to the description above, i.e. 0-0.8 indicates a positive diversity trend.

The concentration ranges of the water constituents in a lake are often used to determine the lake type. There are a number of trophic classifications schemes. The values for the three parameters CHL, TSM and CDOM are listed in Table 19.

Table 19: Concentration ranges for categorisation of different lake types

Parameter			
CHL	**Oligotroph**	**mesotroph**	**eutroph**
	<3mg/m3	3 - 10mg/m3	>10mg/m3
TSM	**Clear**	**turbid**	**very turbid**
	<3mg/m3	3 - 30mg/m3	>30mg/m3
CDOM	**Low**	**medium**	**high**
	<0.8m-1	0.8 - 2m-1	>2m-1

Such classification schemes could be used to produce indicators for absolute lake status (L3.AbsLakeStatus) for the investigated lakes. This indicator, as well as contents of tables and design of maps, might be modified based on the end user requirements.

Table 20: Deliverable: Example of diversity and trend table.

Lake	LakeStatus
Name	OL
Name	OL
Name	MESO
Name	MESO
Name	EU

If appropriate algorithms for retrieval of water constituents cannot be defined for all lakes/lake types, we propose to use lake algorithms that are developed on a generalised level, i.e. optical classification of lakes into major classes and parameterised with generic models. For these lakes and reservoirs we suggest a set of indicators based on relative estimations of the OAS and production of indicators that reflect unchanged, positive or negative trends in each lake:

- Annual status maps (S2002-S2011) for Chla, TSM, yellow substance, turbidity and Secchi Depth, as an average of 3-5 MERIS FRS images registered during one or two predefined months, e.g. July-August, for each lake or reservoir, including statistics for inter-annual variability.
- Periodical status maps for each lake or reservoir, as an average of the annual products from three consecutive years. Three epochs in all.
- Classification of each lake and reservoir into *Poor, Moderate or High* status based on the periodical status maps (LakeStatus).
- Calculation of periodical change for each lake and reservoir based on the periodical status maps (LakeTrend).

Table 21: Maps and relative indicators (L3)

Map/Indicator	Derived from	Classification
L3.P1	Mean(S2003-S2005)	Low, moderate, high parameter concentrations/transp.
L3.P2	Mean(S2006-S2008)	Low, moderate, high parameter concentrations/transp.
L3.P3	Mean(S2009-S2011)	Low, moderate, high parameter concentrations/transp.
L3.LakeStatus	Classification(P1-P3)*	Poor, moderate, high status
L3.T1	Mean(S2003-S2005)/Mean(S2006-S2008)	0-0.8 = negative diversity trend (NegDiv) 0.8-1.2 = No change (NoChange) 1.2+ = positive diversity trend (PosDiv)
L3.T2	Mean (S2006-S2008)/ Mean (S2009-S2011)	0-0.8 = negative diversity trend (NegDiv) 0.8-1.2 = No change (NoChange) 1.2+ = positive diversity trend (PosDiv)
L3.T3	Mean (S2003-S2005)/ Mean (S2009-S2011)	0-0.8 = negative diversity trend (NegDiv) 0.8-1.2 = No change (NoChange) 1.2+ = positive diversity trend (PosDiv)
L3.LakeTrend	(T1 and T2)**	POS, NEG, STABLE, UNCERTAIN

**15 status indicators will be available, three for each parameter. The selection of parameters that will serve as basis for the final status and trend classifications will be determined during the preparatory phase with respect to user requirement and needs. An initial suggestion is given below.*

As described above, higher Secchi depth, indicates better status. Again, this means that the Secchi Depth trend maps will be classified inversely to the description above, i.e. 0-0.8 indicates a positive diversity trend.

Secchi Depth is a measure of water transparency and widely used as an indicator for water quality. Secchi depth, together with chlorophyll a, is often used to classify lakes into trophic classes. We propose an initial *relative* lake status indicator (L3.LakeStatus), based on a combination of Chla and Secchi depth from the three defined epochs, with the aim of producing similar results for the relative and absolute indicators. Lake status going from "high$_{Chla}$-high$_{SD}$" to "poor$_{Chla}$-poor$_{SD}$" and all seven combinations in between will be defined and delivered together with information on the trend. An example of how the result can be displayed is given in Table 22 below, where green, yellow and red colors correspond to high, moderate and low status respectively. Additionally, the direction and angle of the arrow indicates the direction and size of the change. This indicator, as well as contents of tables and design of maps, might be modified based on the end user requirements.

Table 22: Deliverable: Diversity status and trend table.

Lake	Chla Status	Secchi Depth Status
Name	Chla	SD
Name	Chla	SD
Name	Chla	SD
Name	Chla	SD

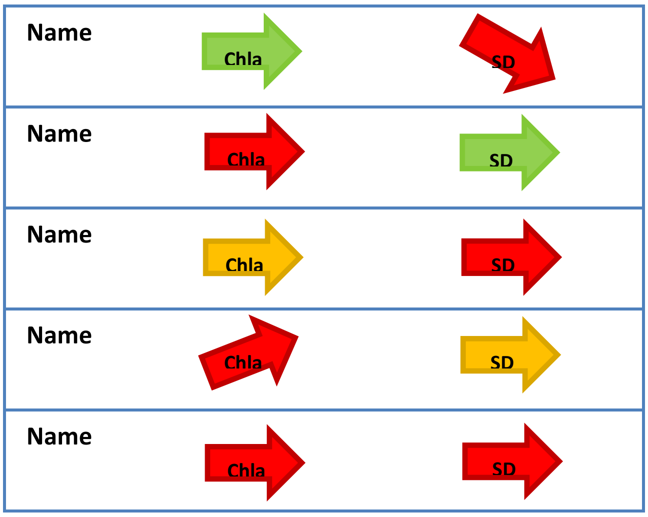

6.1.2 Second Order Indicators

The second order indicators should be based on the first order indicator and combine the available information. Combinations of water quality and water quantity, Lake Surface Temperature and most probably the bathymetry were foreseen as basis for second order indicators, possibly complemented with shoreline and shallow water indication. A highly structured shoreline indicates higher habitat heterogeneity for littoral communities and therefore has a higher potential for their development. This in turn indicates the intensity biological productivity of a lake. As an example, the investigation of cumulative effect of lake shore development on spatial distribution of fishes show, those lakes with a high perimeter–surface-area ratio and a relatively shallow littoral zone had much higher levels of fish aggregation (Scheuerell & Mahaffee, 2004).

However, user requirements indicated that the creation of universally applicable second order indicators for lakes is inappropriate. Instead, post-processing tools were provided that allow for further, case-specific processing of the inland water products by the users.

6.2 Dryland Indicators

This section describes the generation of the dryland indicators and provides an overview about the indicators products derived. Input to all final indicators are the phenological and productivity parameters derived from the MERIS fAPAR (and NDVI for test site 04 and 12) data, plus the phenologically aggregated rainfall and soil moisture data. The generation of these underlying parameters is described in the sections 5.2, 5.3, and 5.4.

Three groups of indicators were produced:

1. First order status and trend/change indicators (of vegetation productivity, Rain Use efficiency, Soil Moisture Use efficiency, rainfall and soil moisture)
2. Second order status and trend/change indicators (combinations of first order products)
3. Phenology maps (average conditions)

As the MERIS data period covers somewhat less than 10 years (June 2002 until March 2012), it is – depending on the local phenology - not everywhere possible to cover 9 full vegetation years with this time series. E.g. vegetation years starting in May can be covered with the MERIS data of 2003 at earliest, and the vegetation year starting in May 2011 is not entirely covered by the time series. Consequently some areas, especially those with season starts in part of the Northern hemisphere spring time, cannot only be covered for 8 full vegetation years. A uniform global solution was preferred with the first vegetation year starting (nominally) in 2003 (or late in 2002 earliest), and the eighth year ending sometime in 2011 (or 2012 latest). Hence, the period covered by the MERIS data comprises globally 8 vegetation years, considering the global variability of phenology. For these 8 vegetation years status, change and trend maps of the NPP proxies have been generated for the 22 test sites.

In addition, the 8 years have been subdivided into 2 epochs covering 4 vegetation years each. Originally, the partition into 3 epochs à 3 years was planned, but this was based on the availability of 9 vegetation years. Eight vegetation years can be meaningfully subdivided in only 2 epochs, which is however only an arithmetic epoch and not related to any true epoch-building developments of the biophysical variables.

Epochal changes were calculated for the rainfall and soil moisture data only. They are included as products in addition to the trend products, as they exhibit differences that are very often clearly related to the observed trends of vegetation productivity, although no significant rainfall trends may be present (because the rainfall-vegetation relationship goes beyond single vegetation years). For all other products, except some second order indicators, we preferred to only derive trend, but no epochal change products. Epochal NPP or RUE changes (if unfiltered) would only reflect quite arbitrary "change situations" exhibiting changes more or less everywhere due to the high temporal variability of the driving factors, i.e. rainfall and soil moisture. Trends, on the other hand, reflect significant steady developments. One NPP change product has been developed nevertheless as second order product, and its generation is described in 6.2.2

In summary, the Diversity II first order indicators reflect the condition, variability, trends and changes of the dryland vegetation, of rainfall and soil moisture, and of RUE and SMUE during the MERIS period for three major phenological aggregation periods (see Table 23: Overview of the organisation of the first order indicators and the related product numbers, first and second column). Second order indicators were derived from selected combined first order indicators (see section 6.2.2) and establish relationships between seasonal NPP proxies as well as between seasonal NPP trends and rainfall trends. In addition, a selection of three indicators represent some basic phenological properties (see 6.2.3).

All indicators have been generated as raster files in GeoTIFF format. Detailed information on these products is found in the Products User Handbook for the drylands. The products were generated using discrete classes, using uniform class intervals and colours for all test sites. This way, the products are directly comparable all over the globe. In rare cases, this may lead to sub-optimal local colour schemes, but users can change the colours as they like. In addition, the continuous data sets are provided on user request, so that users can aggregate the data as it fits their requirements.

Like the underlying phenological and productivity parameters, all final products have been generated with specifically developed ERDAS IMAGINE (version 2013, 2014, 2015) models.

6.2.1 First Order Indicators

Table 23: Overview of the organisation of the first order indicators and the related product numbers presents an overview of the first order dryland products. The left column indicates the basic observed parameters for which the products were derived. These basic parameters, represented by the MERIS fAPAR and NDVI time series data, plus the auxiliary time series data, have been aggregated into the phenological periods listed in column 2 of Table 23, as described in detail in section 5.2.4. The respective phenological and productivity parameters are listed in Table 16. Thus the final first order products described in this section were compiled from

a) the phenological and productivity parameters listed in Table 16 specifically from the ones that are highlighted in orange, and

b) from the aggregated rainfall and soil moisture data as described in section 5.3.

Table 23: Overview of the organisation of the first order indicators and the related product numbers

Observed parameter	Phenological integration period	Status parameters	Prod. No.	Trend/Change parameter Prod. No.	Prod.No.
MERIS fAPAR	Vegetation year*	- Average 2003-2010 - Coefficient of variation [%] of the yearly averages	1 4	- Theil-Sen trend slope	33
	Cyclic Vegetation period**	- Average of the sums of the cyclic fractions 2003-2010 - Coefficient of variation [%] of the yearly averages	2 5	- Theil-Sen trend slope	34
	Dry season ***	- Average 2003-2010 - Coefficient of variation [%] of the yearly averages	3 6	- Theil-Sen trend slope	35
RUE (Rain Use Efficiency) Based on MERIS fAPAR and TRMM rainfall	Vegetation year*	- Overall vegetation year RUE 2003-2010 - Coefficient of variation [%] of the yearly RUE	8 9	- Theil-Sen trend slope	36
	Cyclic Vegetation period**	- Overall cyclic fraction RUE 2003-2010 - Coefficient of variation [%] of the yearly cyclic fraction RUE	10 11	- Theil-Sen trend slope	37
	Dry season***	- Overall dryseason RUE 2003-2010 - Coefficient of variation [%] of the yearly dryseason RUE	14 15	- Theil-Sen trend slope	38
SMUE (Soil moisture use efficiency) Based on MERIS fAPAR and CCI soil moisture	Vegetation year*	- Overall vegetation year SMUE 2003-2010 - Coefficient of variation [%] of the yearly SMUE	17 18	- Theil-Sen trend slope	39
	Cyclic Vegetation period**	- Overall cyclic fraction SMUE 2003-2010 - Coefficient of variation [%] of the yearly cyclic fraction SMUE	20 21	- Theil-Sen trend slope	40
	Dry season***	- Overall dryseason SMUE 2003-2010 - Coefficient of variation [%] of the yearly dryseason SMUE	23 24	- Theil-Sen trend slope	41
TRMM Rainfall	Vegetation year*	- Average rainfall sum 2003-2010 - Coefficient of variation [%] of the yearly averages	25 26	- Theil-Sen trend slope - Epochal change 2003-2006 vs 2007-2010	42 46
	Cyclic Vegetation period**	- Average rainfall sum 2003-2010 - Coefficient of variation [%] of the yearly averages	27 28	- Theil-Sen trend slope - Epochal change 2003-2006 vs 2007-2010	43 47
CCI Soil moisture	Vegetation year*	- Average soil moisture 2003-2010 - Coefficient of variation [%] of the yearly averages	29 30	- Theil-Sen trend slope - Epochal change 2003-2006 vs 2007-2010	44 48
	Cyclic Vegetation period**	- Average soil moisture 2003-2010 - Coefficient of variation [%] of the yearly averages	31 32	- Theil-Sen trend slope - Epochal change 2003-2006 vs 2007-2010	45 49

* Full vegetation cycle starting at the local Start of Season (SoS) and ending after the dry season

** The period of the green peaks of the vegetation cycles

*** Season between the rainy seasons, in drylands usually with little or no vegetation growth

6.2.1.1 First order status indicators

The first order status products indicate the average and the variability of the underlying parameters (see Table 23: Overview of the organisation of the first order indicators and the related product numbers, first column) for the phenological periods (Table 23: Overview of the organisation of the first order indicators and the related product numbers, second column) through the eight vegetation years (n=8).

As average parameter, the arithmetic mean of the yearly parameters (e.g., vegetation year mean fAPAR 2003 – 2010) was calculated. For variability, coefficients of variation (CV) were derived in percent, i.e. the standard deviation is put in relation to the mean.

Deviating from this rule is the calculation of the status (average) of RUE and SMUE: instead of using the sometimes extremely varying yearly RUE and SMUE values (which went into the variability and trend calculations), RUE and SMUE average were directly derived by building the quotient of the respective NPP (proxy) and rainfall or soil moisture averages of the eight vegetation years for each of the three phenological integration periods.

All resulting status parameters, i.e., averages and CVs were classified into 26 classes each. The CV classes derived for every parameter were assigned the same colours as the averages, but in the opposite sequence. This reflects the fact that in drylands rainfall variability and thus essentially also the variability of primary productivity largely increases with decreasing mean annual rainfall. Examples of first order status products are shown in Figure 60 for test site 12, Southern Africa West.

6.2.1.2 First order trend indicators

The first order trend products indicate the trends of the underlying parameters (see Table 16 and Table 23, first column) for the phenological periods (Table 23, second column) through the eight vegetation years (n=8).

The trends were calculated with the Theil-Sen trend (TS) median slope trend analysis. The Theil-Sen trend method is a non-parametric linear trend estimator named after Henri Theil (1950) and Pranab K. Sen (1968), that estimates the strength of trends by determining the median of all differences between all values and all predecessors, i.e. of the slope estimates from all pairs of observation. The Theil-Sen method was chosen because of its resistance against outliers which makes it especially suited for trend estimations in short and noisy time series (Fensholt et al. 2013). Statistical trend significance was tested with a Mann-Kendall significance test generating z scores, which are thresholded to only include trend slopes above or below a selected minimum significance. The chosen confidence level was 90%, resulting in a z-sore of +/- 1.645 for a two-tailed test. I.e. for the trend to be significant at p=0.90, z-scores had to be larger than + 1.645 (positive trends) or smaller than – 1.645 for negative trends. The Mann-Kendall significance test as a non-linear trend indicator measures the significance (z-scores) of a monotonic trend but is commonly used as a trend test for the (linear) Theil-Sen trend slope estimator (Fensholt et al. 2013).

We also compared trend results of the OLS versus the Theil-Sen (TS) method, and found similar, but as expected not identical results. In some cases, OLS delivers more trends, in others TS.

The outputs of the trend analyses are trend slope images (raster files), where the slope values indicates the average absolute yearly trend. These continuous slope figures were classified into six positive and six negative trend slope classes each. One tenth of the trend slope class interval was taken as lower threshold for displaying trends. Examples of trend slope maps are illustrated in Figure 61.

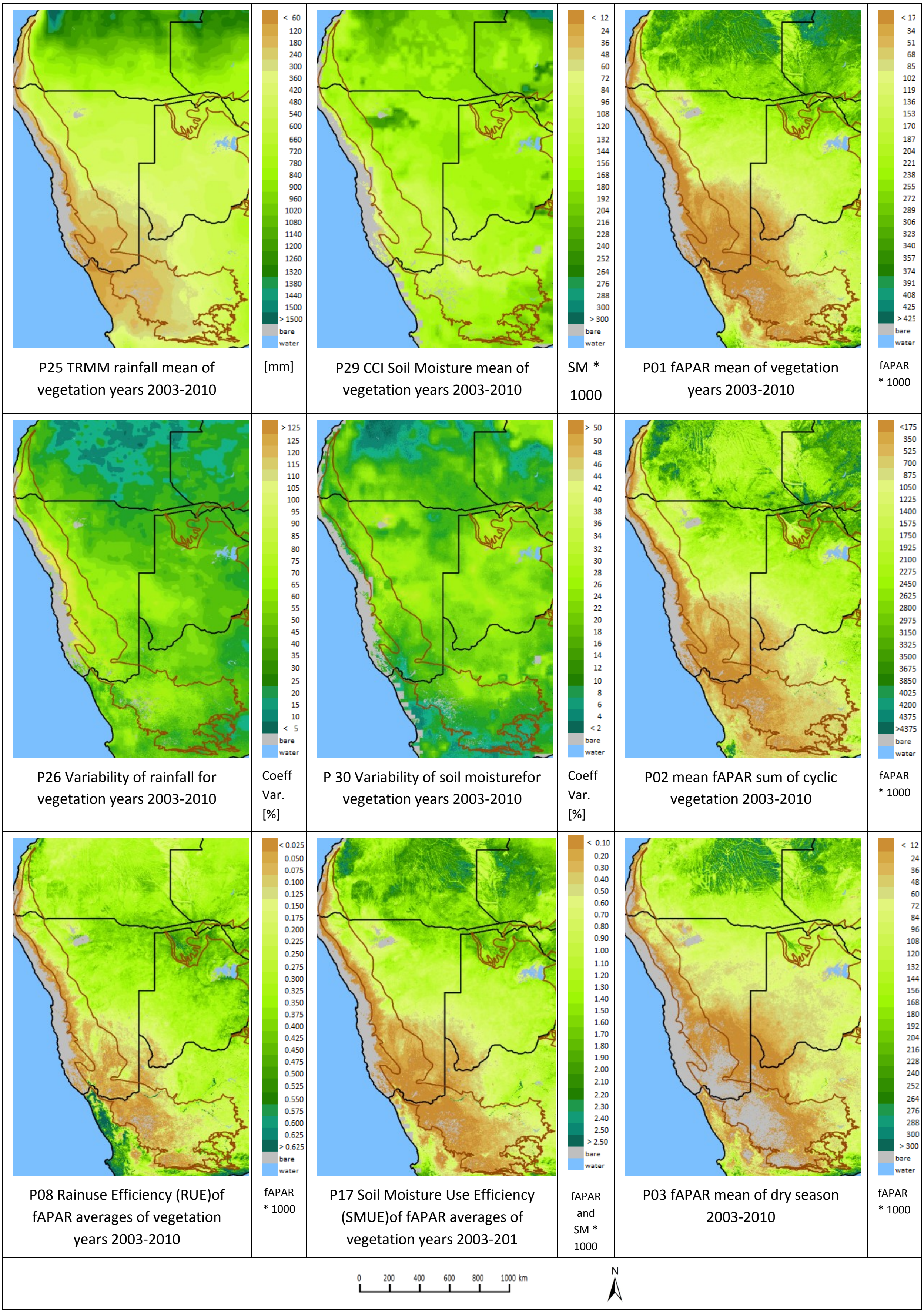

Figure 60: First order rainfall, soil moisture, fAPAR, RUE and SMUE products of site 12, Southern Africa West

6.2.1.3 *First order epochal change indicators*

Epochal difference products were derived for rainfall and soil moisture only. As already mentioned, trends in vegetation productivity are often co-occurring with epochal rainfall (and soil moisture) changes, and not just linked to steady trends of water availability. The epochal change products of the water parameters thus often better reflect the relation of vegetation trends to changing water budgets than year-by year water trends alone. The earlier mentioned “memory effect” of ecosystems is an expression of the relation between vegetation productivity and water availability beyond the current year.

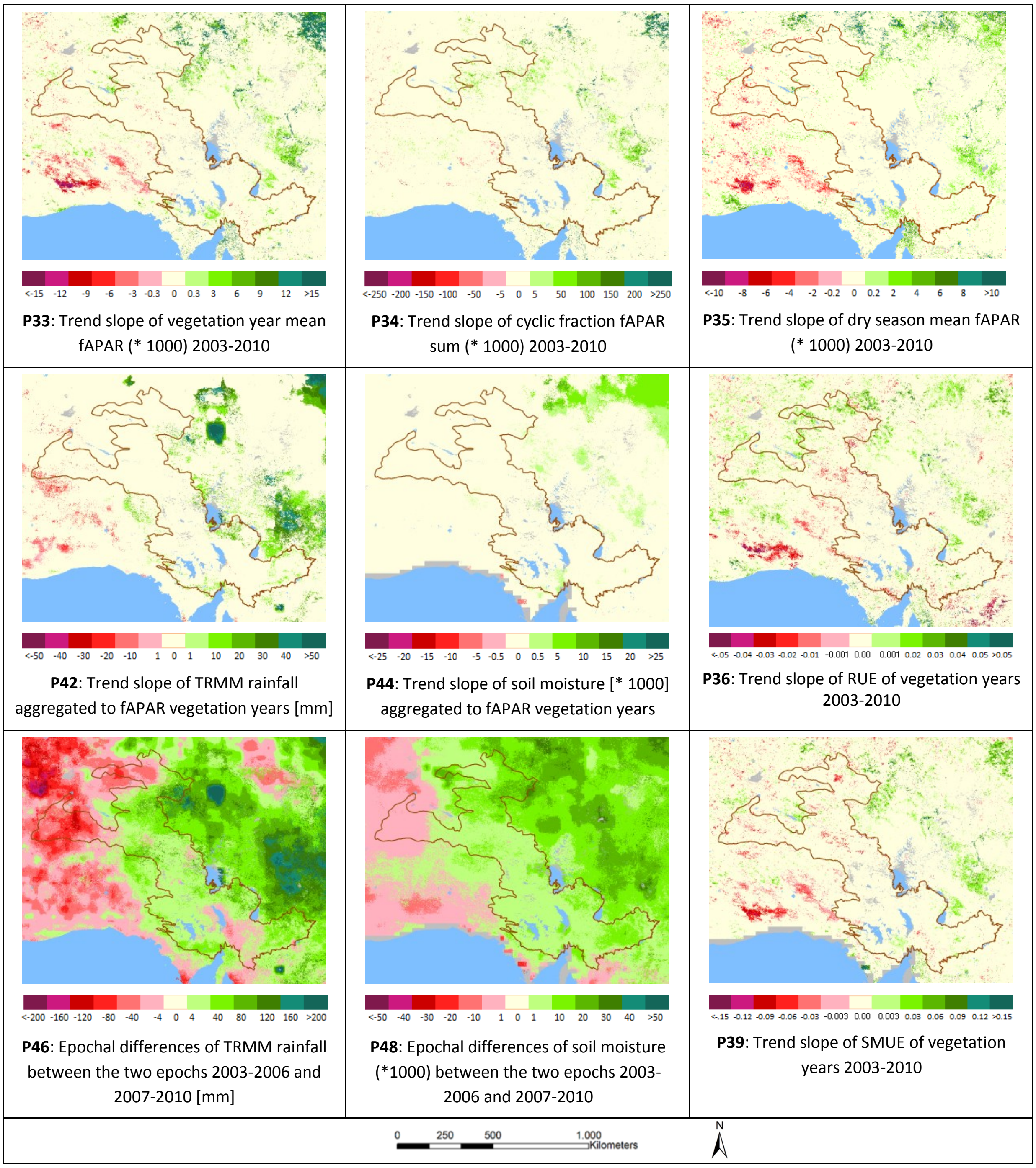

P33: Trend slope of vegetation year mean fAPAR (* 1000) 2003-2010

P34: Trend slope of cyclic fraction fAPAR sum (* 1000) 2003-2010

P35: Trend slope of dry season mean fAPAR (* 1000) 2003-2010

P42: Trend slope of TRMM rainfall aggregated to fAPAR vegetation years [mm]

P44: Trend slope of soil moisture [* 1000] aggregated to fAPAR vegetation years

P36: Trend slope of RUE of vegetation years 2003-2010

P46: Epochal differences of TRMM rainfall between the two epochs 2003-2006 and 2007-2010 [mm]

P48: Epochal differences of soil moisture (*1000) between the two epochs 2003-2006 and 2007-2010

P39: Trend slope of SMUE of vegetation years 2003-2010

Figure 61: fAPAR, RUE, SMUE and rainfall trends, rainfall and soil moisture epochal change products, site 20, Southern

For the epochal change products, the eight vegetation years were separated into two epochs, the first from 2003 to 2006, and the second from 2007 to 2010. The average amounts of rainfall and the average soil moisture of the two epochs were calculated and the resulting mean values of the first epoch were subtracted from the mean values of the second epoch. The resulting difference values were like the trend slopes classified into six positive and six negative difference classes each. They express the difference of the average rainfall/soil moisture between the two epochs. The class intervals are, as mentioned above, globally standardized and exhibit substantial epochal differences worldwide, the biggest reaching over 200 mm epochal decrease or increase of rainfall per year. Examples can be seen in Figure 61, third row.

6.2.2 Second Order Indicators

Second order dryland indicators are based on the first order indicators and contain more complex and abstract information. They show status, changes and trends of the most essential first order indicators in various relations to each other. Table 24 provides an overview about the relation of the second order indicators to the first order indicators and their contents.

Table 24: Overview of the systematic of the second order indicators (colours reflect product types)

Input first order indicators	Second order indicator	Status / Trend / Change	Prod. No.
- Vegetation year average greenness 2003-2010 - Mean percent of cyclic vegetation of vegetation year greenness* 2003-2010	Functional classes Relation between vegetation year greenness classes and the classified percentage of the cyclic vegetation of the yearly vegetation 2003-2010	Status indicator 2003-2010	50
- Epochal Vegetation year average greenness 2003-2006 and 2007-2010 - Epochal percent of cyclic vegetation of vegetation year greenness 2003-2006 and 2007-2010	Functional differences Epochal (2003-2006/2007-2010) difference map of the relation between vegetation year greenness classes and the classified percentage of the cyclic vegetation of the yearly vegetation	Epochal difference indicator 2003-2006 vs 2007-2010	51
- Trendslope of vegetation year greeness 2003-2010 - Trendslope of cyclic fraction greenness 2003-2010 - Trendslope of dry season greenness 2003-2010	Seasonal Trend Relations Relation between vegetation year greenness trends and seasonal greenness trends 2003-2010	Combined trend indicator 2003-2010	52
- Trendslope of vegetation year greeness 2003-2010 - Trendslope of vegetation year TRMM rainfall 2003-2010	TRMM Rainfall versus MERIS fAPAR vegetation year greenness trend	Combined trend indicator 2003-2010	53
- Trendslope of cyclic fraction greenness 2003-2010 - Trendslope of cyclic fraction TRMM rainfall 2003-2010	TRMM Rainfall versus MERIS fAPAR cyclic fraction greenness trend	Combined trend indicator 2003-2010	54
- Trendslope of dry season greenness 2003-2010 - Trendslope of vegetation year TRMM rainfall 2003-2010	TRMM Rainfall versus MERIS fAPAR dry season greenness trend	Combined trend indicator2003-2010	55
- Trendslope of GIMMS NDVI 1981-2002** - Trendslope of GPCP rainfall 1981-2002**	GPCP Rainfall versus GIMMS NDVI vegetation year greenness trend	Combined trend indicator 1981-2002	56

* This parameter was not included in the product suite as a dedicated first order indicator

** These longer term trend maps were not included as separate indicators in the product suite

For the second order indicators, with one exception (P52) no more than two first order indicators were combined per indicator to keep them simple. The latter, like all remaining second order MERIS based products (P52 – P55) is a trend relation product, where the trend directions (not considering the slopes) of two (P52:

three) variables are combined. Hence, the calculation method is also straight forward and fully repeatable with other data or for other periods.

Basically three types of second order products were generated, which are described in the following three sections 6.2.2.1 to 6.2.2.3.

6.2.2.1 Functional Classes – Status (P50) and Change (P51)

Only one second order status indicator was defined: P50 Functional Classes, constituting a combination of first order status indicator P01 Vegetation year average greenness 2003-2010, and the mean percent of cyclic vegetation of vegetation year greenness (sum) 2003-2010 (parameters (4) and (23) in Table 16).

All other second order products are change or trend products (P51 – P56).

Indicator product P50 was derived by dividing the two inputs into class intervals and combining the derived classes. The class intervals used are listed in Table 25. The Functional classes 1 to 5 for example include average vegetation year fAPAR values from 17 to 85 each (fAPAR * 1000), and are further subdivided into percentage classes of the cyclic vegetation of the yearly fAPAR sum ranging from ≤ 30 to > 60. The intervals of these percentages are somewhat lowered in the higher productivity classes 16 to 25.

The indicated class intervals were equally applied to all test sites. As this product is derived with a simple thresholding approach, it can be easily modified and is fully reproducible. For these reasons the second order products were all conceived as simple first order product combinations.

P50 was called “Functional Classes”, as it integrates the two major characteristics of vegetation productivity: amount and seasonal distribution. The results resemble to a high degree LC class patterns and may be used for land cover and ecosystems classifications.

The indicator map P50 is closely related to land use/cover patterns and also to soil type and terrain structures (see PUH chapter 3, section 3.5.5 for interpretation). Figure 62 provides an example.

P51 is an epochal change indicator of the above specified second order status product P50. This means, the inputs for P50 were calculated for the two epochs 2003-2006 and 2007-2010, respectively, and the resulting classes of the two epochs were subtracted from each other. The derived epochal differences are put in relation to each other only considering the direction of the change combinations (and not the size of the changes). An example of product P51 is shown in Figure 63 and can be compared with P52 (Figure 64), which exhibits the seasonal trend relation (see section 6.2.2.2). The change indicator (product no. 51) displays epochal (2003-2006 versus 2007-2010) changes between the aggregated classes of the two underlying first order indicators.

Table 25: Aggregations of input parameters for second order product P50: Functional classes

Functional classes	Average vegetation year greenness (= product P01)	Average percent of cyclic vegtation of yearly fAPAR sum
26	< 17 sparse vegetation	
1	17-85	< = 30
2		30 - 40
3		40 - 50
4		50 - 60
5		> 60
6	85-153	< = 30
7		30 - 40
8		40 - 50
9		50 - 60
10		> 60
11	153-221	< = 30
12		30 - 40
13		40 - 50
14		50 - 60
15		> 60
16	221-289	< = 25
17		25 - 35
18		35 - 45
19		45 - 55
20		> 55
21	> 289	< = 20
22		20 - 30
23		30 - 40
24		40 - 50
25		> 50

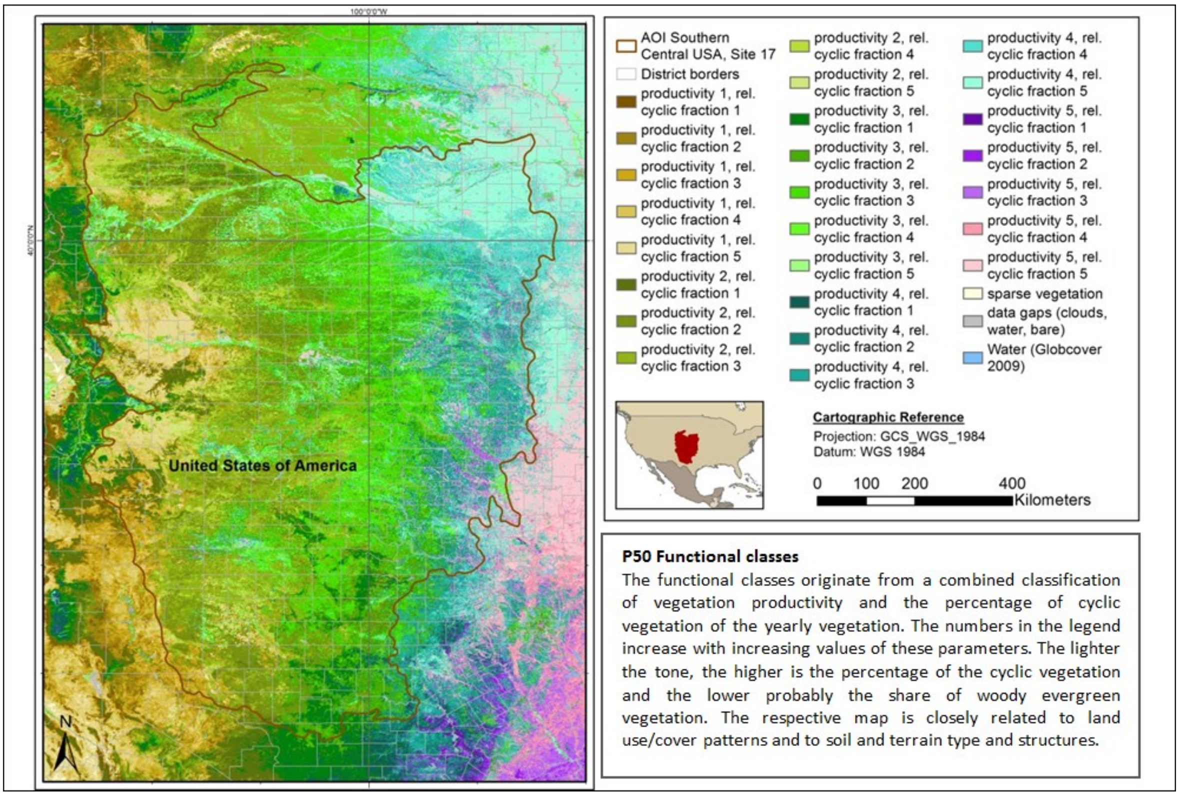

Figure 62: P50 Functional classes in test site 17, Southern Central USA

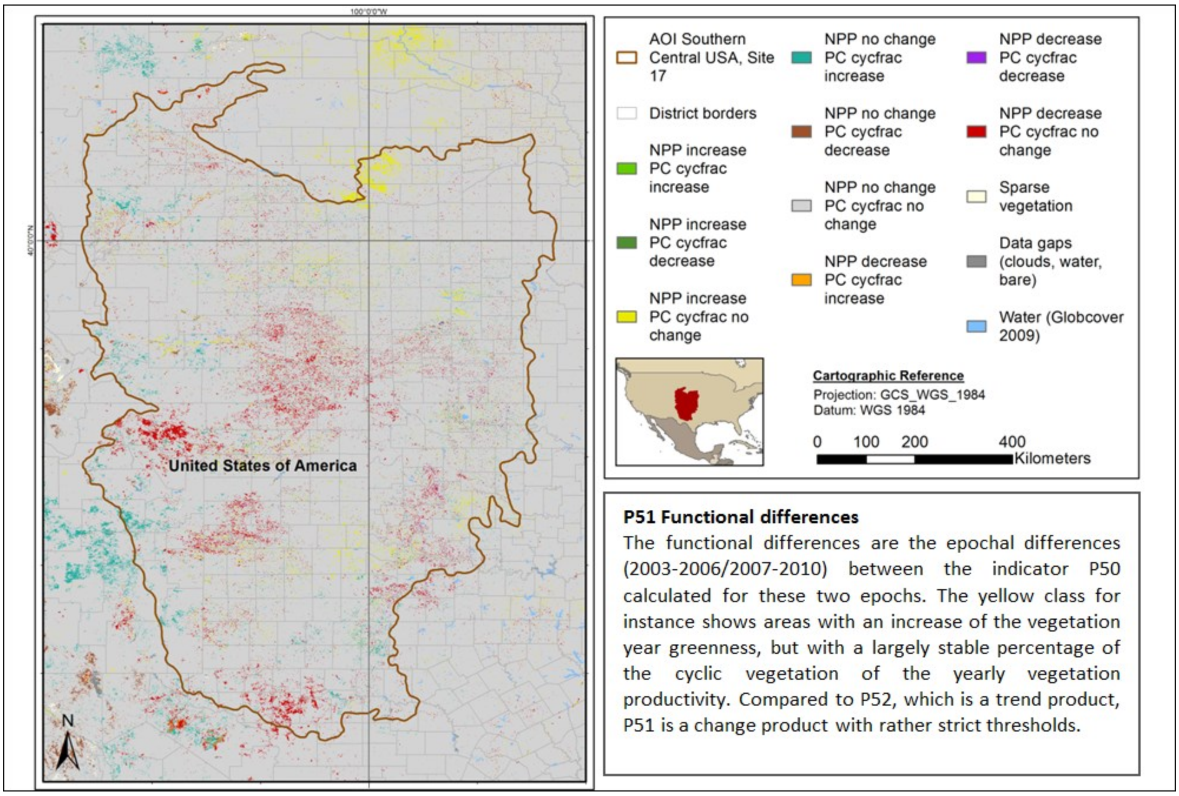

Figure 63: P51 Functional differences in test site 17, Southern Central USA

6.2.2.2 *Trend relation between vegetation year greenness and seasonal greenness (P52)*

The indicator product P52 combines the yearly (vegetation year) greenness trends with those of the cyclic vegetation and the dry season greenness. It has commonalities with P51, but the trend patterns deviate partly from the change patterns. Essentially this indicator shows the dynamics of the different basic vegetation types in relation to each other in the observation period. Developments such as bush encroachment or the extension of crop area may be captured by this indicator, the first by a relative increase of the dry season greenness, the latter by a relative increase of the cyclic vegetation productivity in relation to that of the dry season.

The two indicators P51 and P52 often exhibit different developments and changes, even though they both relate to changes of the seasonal composition of the vegetation. Trends in P52 may be too weak to pop out as changes in P51, and vice versa, making the two indicators more complementary than redundant.

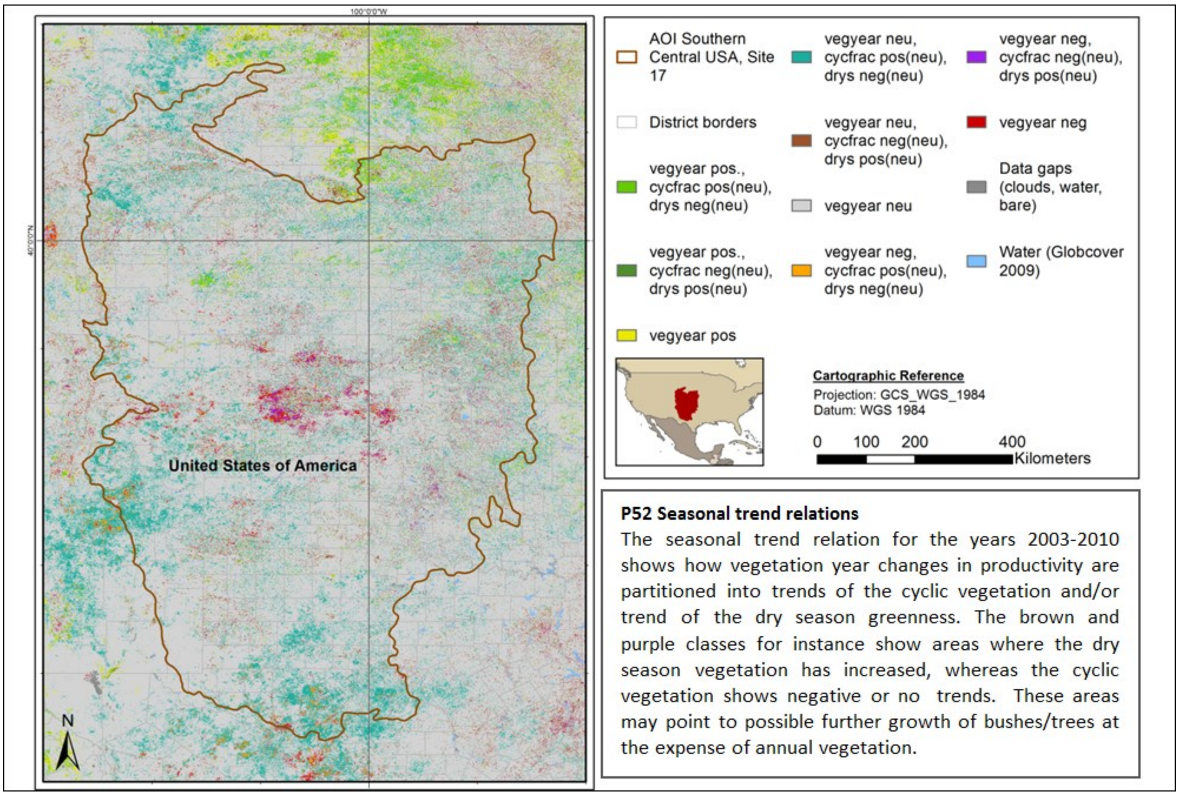

Figure 64: P52 Seasonal Trend Relation, test site 17, Southern Central USA

6.2.2.3 Direct relation between Rainfall and Vegetation Productivity (P53, P54, P55)

As an alternative to RUE/SMUE trends contained in the first order products, as well as to the so called "RESTREND" approach (see for instance Wessels, 2012), which assume linearity or even proportionality (RUE) between rainfall and NPP, assumption-free relation indicators between rainfall and NPP trends were generated. Indicators were prepared for the relation between rainfall and vegetation year greenness, cyclic vegetation, and respectively dry season greenness (P53, P54, P55). In addition, the same type of indicator was derived for a time span prior to the MERIS period (1981-2002), using GPCP rainfall data and NOAA GIMMS NDVI data.

These products were developed in order to integrate vegetation productivity trends and rainfall trends, and to highlight trend areas where rainfall and NPP proxy trends diverge. Consequently this type of products is a synoptic trend product combining the major driver of NPP trends in drylands, i.e. water, with NPP proxy trends. Negative NPP proxy tends which are not coinciding with negative rainfall trends (or areas with positive rainfall trends and missing positive or even negative NPP proxy trends) may point to potentially degraded areas, analogue to RUE, but showing separately the developments of each single parameter.

Rationale

RUE or SMUE indicators need to be generated and interpreted with care, as argued in section 5.4.1.1. RUE/SMUE trend indicators are provided by Diversity II, but they may actually not fulfill their original purpose of separating man-made changes from rainfall controlled variability of primary productivity. RUE trends are in large parts of the areas correlated with rainfall (both positively and negatively), and thus partly reflect rainfall changes/trends rather than normalizing for rainfall variability (see also Fensholt et al. 2013). The latter would be the prerequisite for RUE trends to indicate human induced land degradation or improvements.

In addition, land use changes, which at least at local scales occur rather abrupt, can hardly be retrieved with RUE trends. Also the RESTREND method (see for instance Wessels 2012), which interprets trends of regression residuals of rainfall and vegetation as human induced vegetation trends (productivity trends that are not explained by rainfall trends), relies on the assumption that rainfall and vegetation productivity are linearly related. While this may hold for shorter periods and certain ecosystems, vegetation has been found to exhibit different correlations with rainfall (at a given location) depending on the type and status of ecosystems and the duration of the observation (Ratzmann 2014).

These findings have led to the development of a group of second order indicators called "Direct relation between Rainfall and Vegetation Productivity", assumed to be a largely assumption-free indicator that directly relates rainfall and vegetation productivity trends to each other. "Largely assumption-free" means that they also must be interpreted with care, as an increase of rainfall amount may not necessarily lead to an increase of vegetation growth at the same place or time. For instance, increased rainfalls may come with higher intensities, possibly leading to spatial/temporal shifts of the effects via geomorphological and hydrological transportation and transition processes.

Even though many fAPAR trends seem to be related to rainfall trends, this nevertheless does not mean that all these trend areas, where trends can be explained by rainfall, are safe and stable. Desertification processes may be enhanced by natural fluctuations, and where negative vegetation productivity trends can be observed, there may always be the chance that processes start to get their own dynamics, or that human livelihoods are at risk. Therefore we tried to overcome the restriction to RUE, by showing all vegetation trends in these products along with the potentially related rainfall trends.

The general rule for the colour scheme of these products is that the stronger the mismatch between rainfall and fAPAR trend, respectively, the darker either the reddish tone for rainfall/fAPAR decreases or the green tone for increases. The lightest pink or green, respectively show areas without fAPAR trends even though the rainfall data show trends. The light green areas may be interpreted as resilient areas, which did not decrease in productivity in spite of rainfall decreases. The light pink regions, vice versa, may contain areas with missing response to increasing water availability.

Figure 65 displays the above mentioned products for test site 14, Patagonian Steppe in southern Argentina (upper row). TRMM rainfall trends are shown in the lower left for comparison. Notable here is that in particular within the study AOI there are widespread vegetation year fAPAR trends, partly without corresponding rainfall trends, even though the trends of the cyclic vegetation and the dry season are less pronounced. P37, RUE trends of the cyclic vegetation, is shown in the lower centre. The RUE trends partly resemble P54, but exhibit as expected significantly less trends, whereas P54 (and P53 and P55 accordingly) show all vegetation trends, no matter if they are RUE trends or not.

Figure 66 shows another example for this product type, in this case the rainfall to dry-season vegetation productivity relation for site 02, Northern Australia. Remarkable are the widespread positive dry season greenness trends, which do not seem to be triggered by extensive positive rainfall trends or changes, at least not during the eight vegetation years observed. For comparison indicator P56 is shown in Figure 67. As introduced above, this indicator relates the yearly (vegetation years) vegetation productivity to rainfall during the period preceding the MERIS data, which is covered by NOAA GIMMS NDVI data. As can be seen, the region with strong positives dry season trends during MERIS seemed to have strong positive rainfall trends in the years before, which did not lead everywhere to a respective vegetation response in the period prior to MERIS. So possibly, the dry season increases during MERIS are delayed responses of the woody vegetation to an increases rainfall budget the years before.

In Figure 68 the trend relation products for the MERIS period and the preceding 20 years are directly contrasted for test site 21, Southern Africa East.

P53: TRMM rainfall versus MERIS fAPAR vegetation year greenness trends 2003-2010 (see legend at lower right)

P54: TRMM rainfall versus MERIS fAPAR cyclic fraction greenness trends 2003 - 2010 (see legend at lower right)

P55: TRMM rainfall versus MERIS fAPAR dry season greenness trends 2003 – 2010 (see legend below)

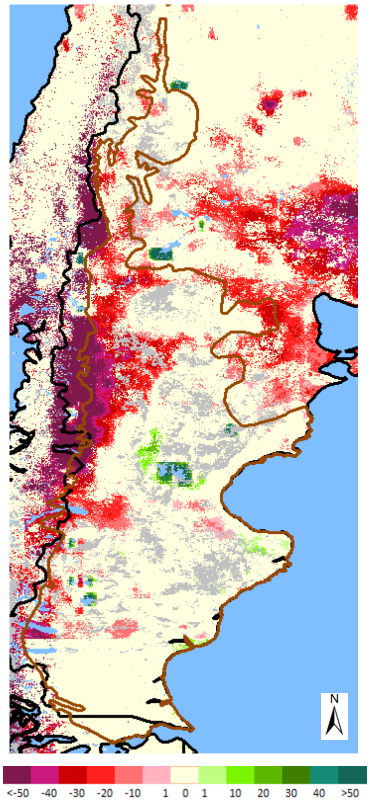

P42: Trend slope of TRMM rainfall aggregated to fAPAR vegetation years [mm]

P37: Rain Use Efficiency trend slopes of cyclic vegetation 2003-2010 (fAPAR * 1000)

trmm vegyear pos., fapar vegyear neg.	
trmm vegyear no (sig.) trend, fapar vegyear neg.	
trmm vegyear neg. fapar vegyear neg.	
trmm vegyear pos., fapar vegyear no (sig.) trend	
trmm vegyear neg., fapar vegyear no (sig.) trend	
trmm vegyear pos., fapar vegyear pos.	
trmm vegyear no (sig.) trend, fapar vegyear pos.	
trmm vegyear neg., fapar vegyear pos.	
trmm vegyear and fapar vegyear no (sig.) trend	
Data gaps (clouds, water, bare)	
Water (Globcover 2009)	

Legend of **P53**

trmm cyfrac pos., fapar cycfrac neg.	
trmm cyfrac no (sig.) trend, fapar cycfrac neg.	
trmm cyfrac neg. fapar cycfrac neg.	
trmm cyfrac pos., fapar cycfrac no (sig.) trend	
trmm cyfrac neg., fapar cycfrac no (sig.) trend	
trmm cyfrac pos., fapar cycfrac pos.	
trmm cyfrac no (sig.) trend, fapar cycfrac pos.	
trmm cyfrac neg., fapar cycfrac pos.	
trmm cyfrac and fapar cycfrac no (sig.) trend	
Data gaps (clouds, water, bare)	
Water (Globcover 2009)	

Legend of **P54**

trmm vegyear pos., fapar dry season neg.	
trmm vegyear no (sig.) trend, fapar dry season neg.	
trmm vegyear neg. fapar dry season neg.	
trmm vegyear pos., fapar dry season no (sig.) trend	
trmm vegyear neg., fapar dry season no (sig.) trend	
trmm vegyear pos., fapar dry season pos.	
trmm vegyear no (sig.) trend, fapar dry season pos.	
trmm vegyear neg., fapar dry season pos.	
trmm vegyear and fapar dry season no (sig.) trend	
Data gaps (clouds, water, bare)	
Water (Globcover 2009)	

Legend of **P55**

0 200 400 800 Kilometers

Figure 65: Relation between seasonal vegetation productivity and rainfall, site 14, Patagonian

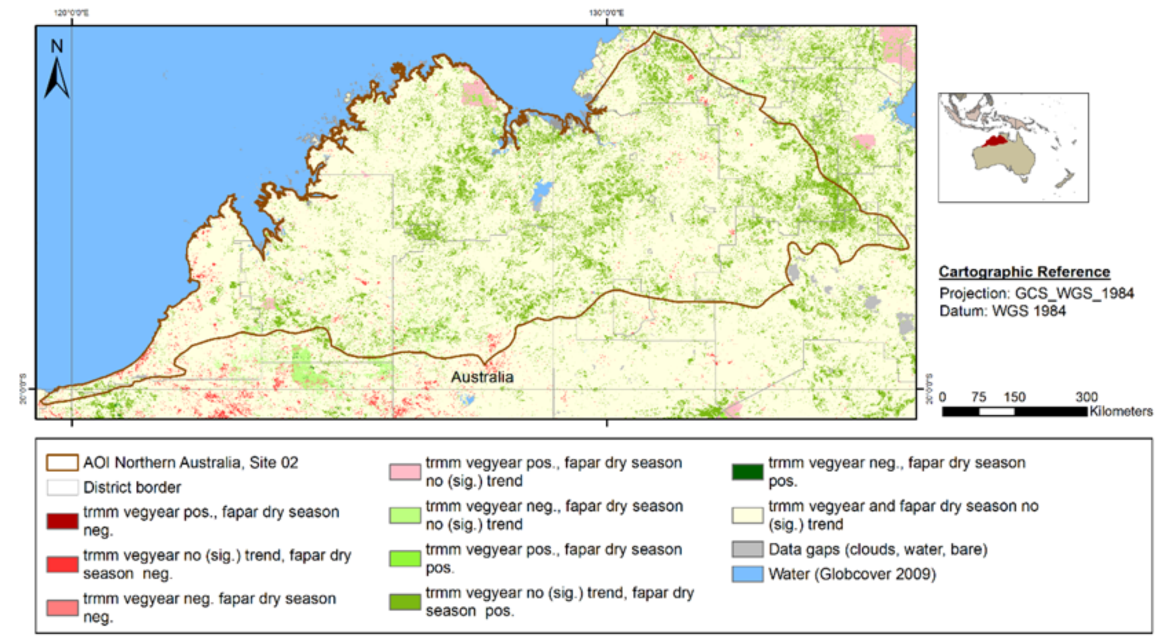

P55 TRMM rainfall versus MERIS fAPAR dry season greenness trends 2003-2010

This indicator shows the MERIS fAPAR based dry season vegetation trends for the vegetation years 2003-2010 in relation to the TRMM rainfall trends. This indicator combines all trends and thus highlights regions with rainfall and vegetation trends of equal direction and those of opposite directions. The light red areas e.g. exhibit areas without TRMM rainfall trends that show negative dry season fAPAR trends.

Figure 66: TRMM rainfall versus MERIS fAPAR dry season greenness trends 2003-2010, test site 02, Northern Australia

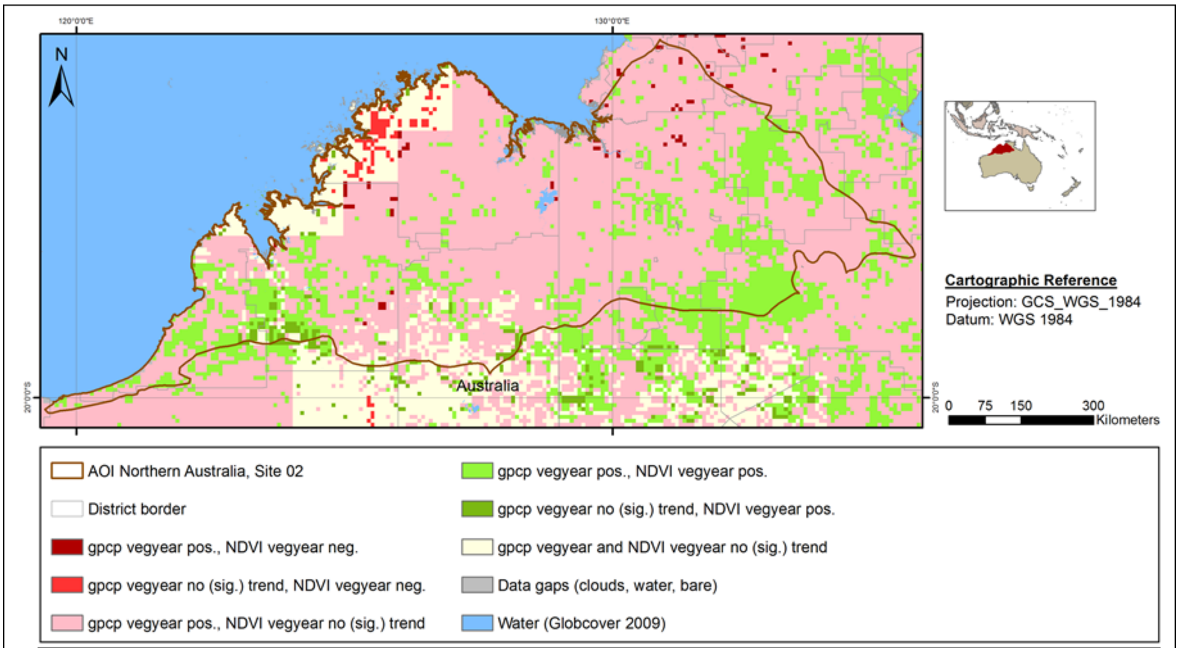

P56 GPCP rainfall versus GIMMS NDVI vegetation year greenness trends

This indicator shows the NOAA GIMMS based vegetation trends for the vegetation years 1981-2002 in relation to the GPCP rainfall trends. This product combines all trends and thus highlights regions with rainfall and vegetation trends of equal direction and those of opposite directions. The light pink areas e.g. exhibit positive GPCP rainfall trends, which are not matched by positive NDVI trends.

Figure 67: P56 Trend relations of GPCP rainfall and GIMMS NDVI data for vegetation years1982 – 2002

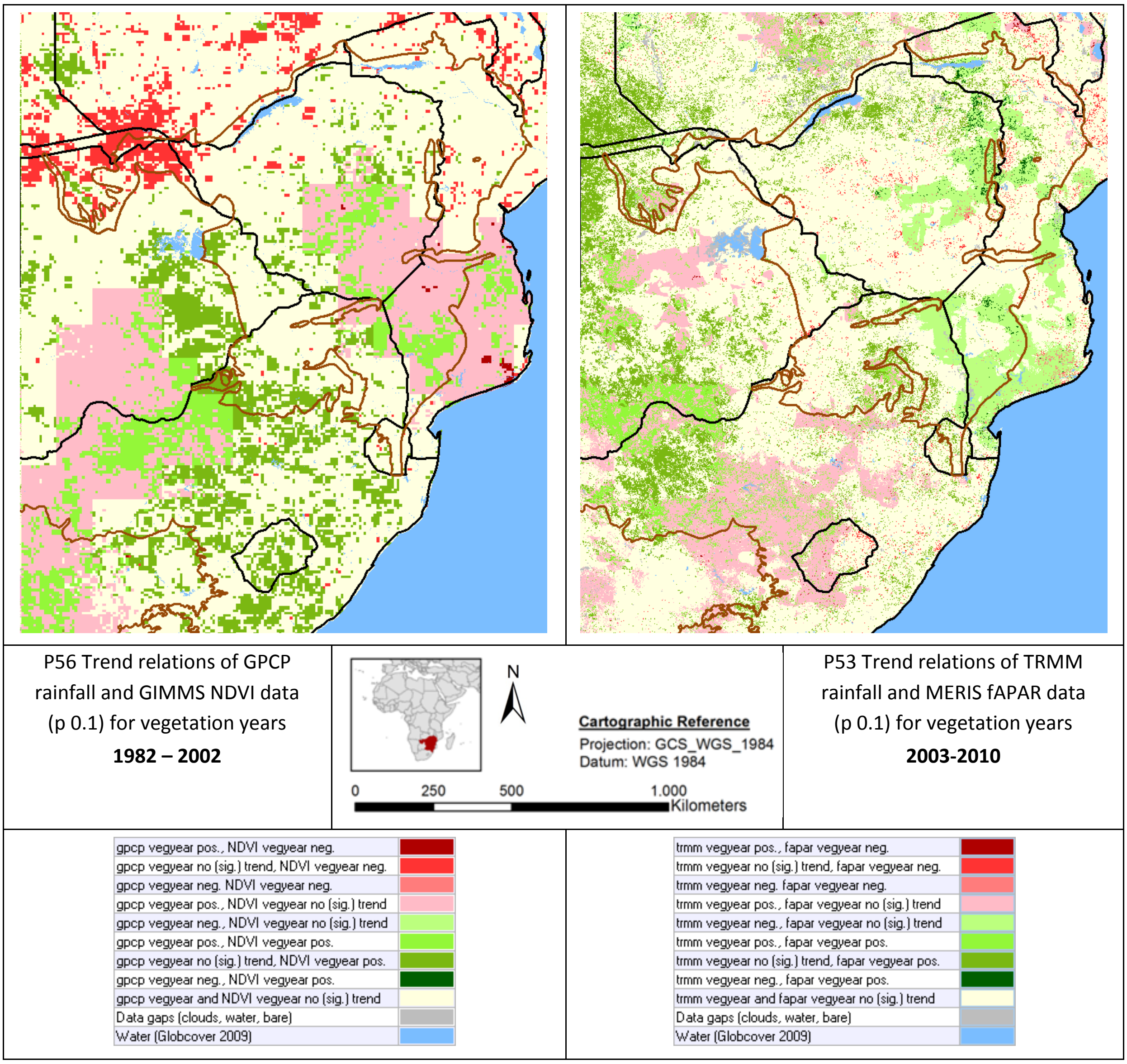

Figure 68: Trend relations of rainfall and NPP proxies (per vegetation year) for the two trend periods 1982-2002 and 2003-2010, respectively. Test site 21, Southern Africa East

6.2.3 Phenology Indicators

In addition to the first and second order products, which are all based on phenological and productivity parameters, explicit phenology products (maps) were generated in order to characterize the average conditions of major phenological properties of the test sites. Table 26 presents an overview of the map products. These products evolved directly from the phenological parameters, whose generation method is described in section 5.2.

Table 26: Phenology products

Phenology Product	Prod. No.
Median of the start times (half month number in the calendar year) of the vegetation year 2003-2010	57 (example in Figure 69)
Mean of the lengths of the vegetation seasons 2003-2010	58 (example in Figure 70)
Average start time (half month number in the calendar year) of the vegetation seasons (cyclic vegetation) 2003-2010	59 (example in Figure 71)

While the start of the vegetation year (P57) is situated at the very start of the vegetation signal rise at the end of the dry season (see Figure 55), the start time of the vegetation season is defined to be marked by the time when the vegetation rise has surpassed the baseline, i.e. the threshold between the (approximately) upper dry season level and the cyclic vegetation (see section 5.2.4). Figure 69 shows an example for the median start time of the vegetation year, and Figure 70 for the start of the growing season for test site 10, Southern Europe.

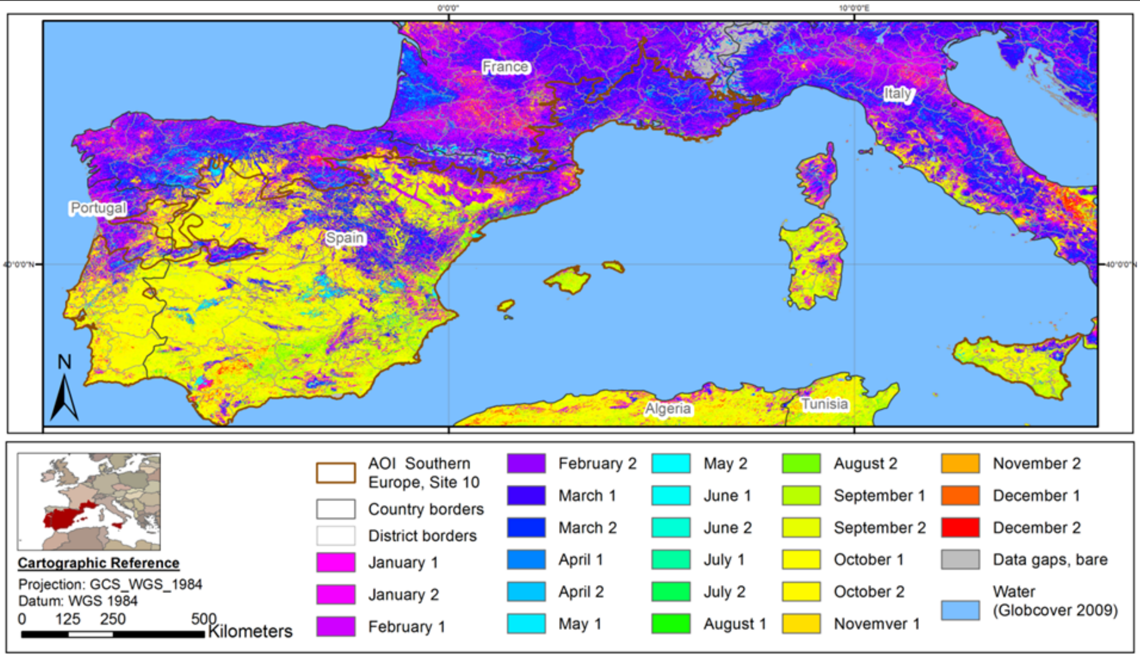

P57 Median start of vegetation year 2003-2010

The median value of the start of the vegetation year refers to the time when vegetation development is about to start, and is as such a very early indicator of the start of the vegetation season. The locally dominating start time, i.e. the most frequently occurring time period has been selected in cases where more than one start time (range) is being observed, considering their yearly fluctuations. This indicator shows the median value of the eight start times 2003-2010. The numbers behind the month names refer to the first and second half of each month, respectively.

Figure 69: P57 Median start of vegetation year 2003-2010, site 10, Southern Europe

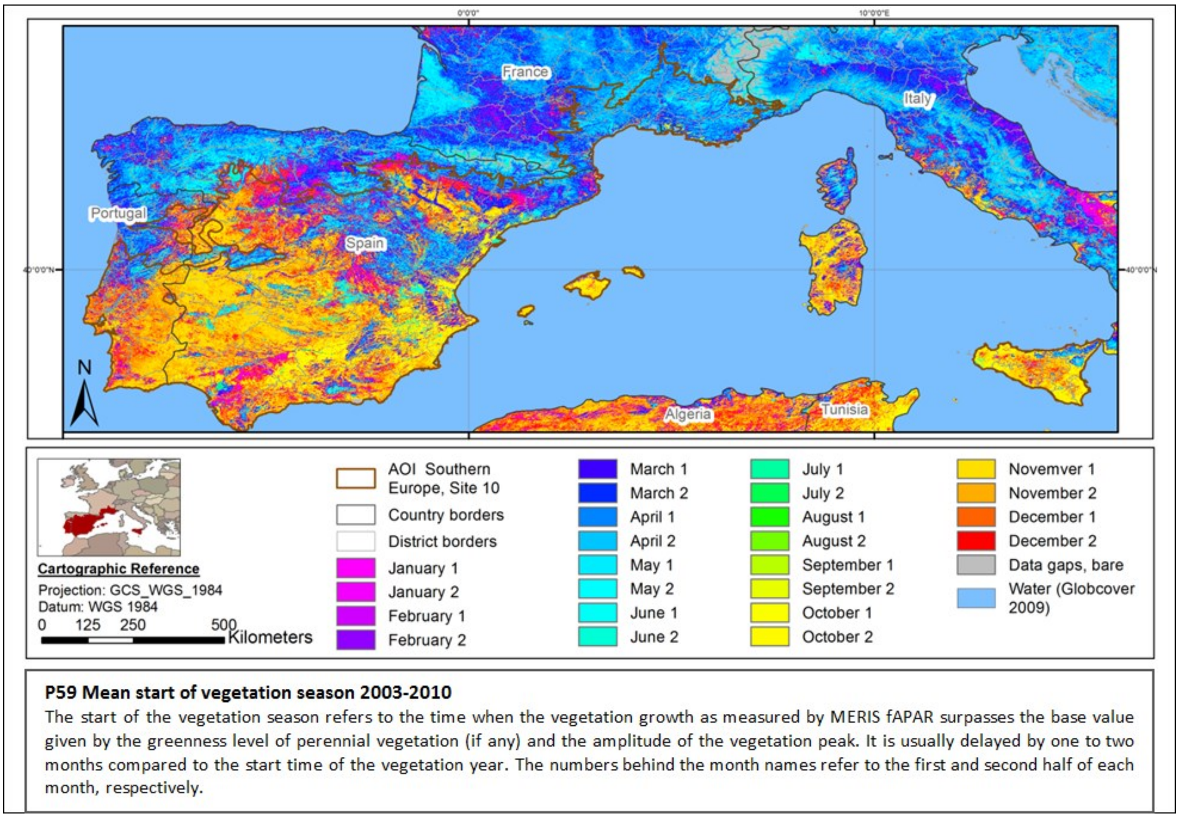

Figure 70: P59 Mean start of vegetation season 2003-2010, site 10, Southern Europe

The length of the vegetation season is given by the duration of the green peaks (or several green peaks within a vegetation year), without including very short and small peaks. The applied procedure is described in section 5.2.4.

Two map examples for the growing season length are shown in Figure 71 for site 01, Northern – Central Mexico and respectively Figure 72 for site 05, Eastern Mongolia Western Manchuria.

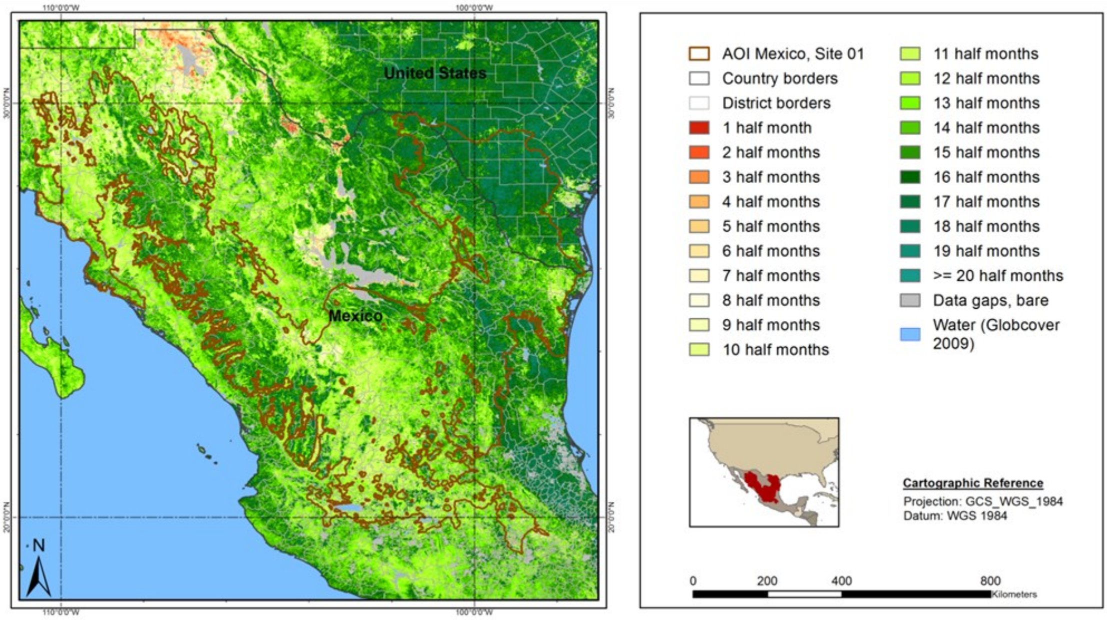

P58 Mean length of vegetation season 2003-2010
The mean length of the vegetation season (LOS) refers to the duration of the green peak(s) (cyclic fraction) of the vegetation within a vegetation year. It is negatively correlated with aridity, but by far not totally explained by the latter. The season, when the rain falls plays a role, and especially land cover/use, which determine largely the duration of the green period within given humidity ranges. In irrigated areas, LOS is +/-decoupled from climatic constraints.

Figure 71: P58 Mean length of vegetation season 2003-2010, site 01, Northern – Central Mexico

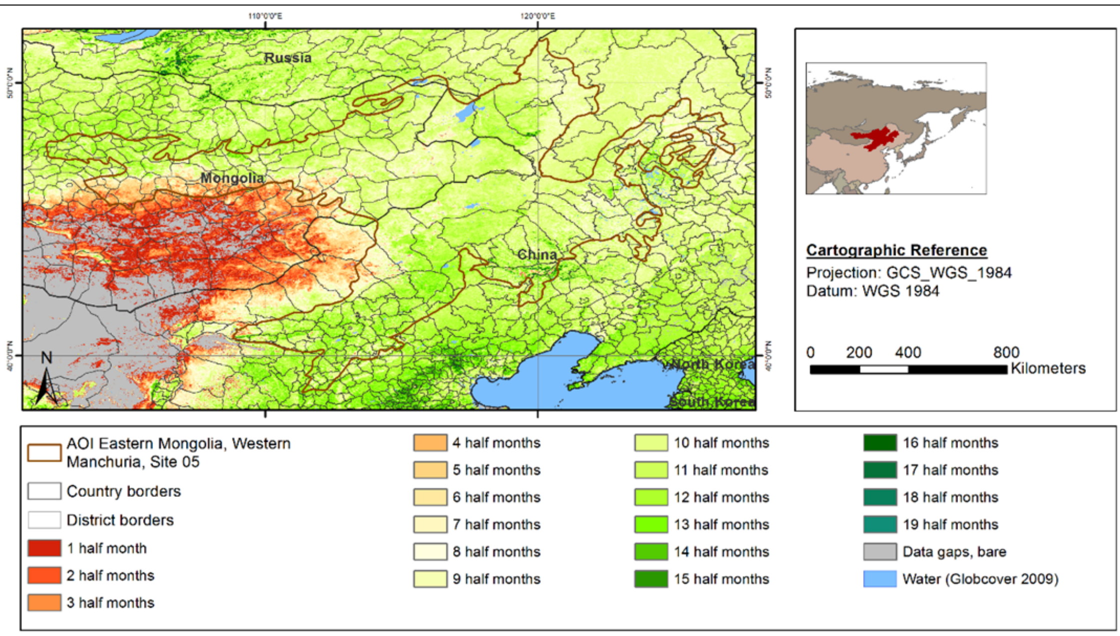

P58 Mean length of vegetation season 2003-2010
The mean length of the vegetation season (LOS) refers to the duration of the green peak(s) (cyclic fraction) of the vegetation within a vegetation year. It is negatively correlated with aridity, but by far not totally explained by the latter. The season, when the rain falls plays a role, and especially land cover/use, which determine largely the duration of the green period within given humidity ranges. In irrigated areas, LOS is +/-decoupled from climatic constraints.

Figure 72: P58 Mean length of vegetation season 2003-2010, site 05, Eastern Mongolia Western Manchuria

7 Relationships between RS Indicators and Biodiversity

This section intends to provide a theoretical basis about the inland water and dryland biodiversity indicators considered in this project.

7.1 Inland Waters Biodiversity indicators

The ecological or environmental variables play an extremely important role in the structure of biodiversity in inland waters. In fact, these factors can delineate entire physiological processes of aquatic species. The ecological freshwater guilds, which are basically groups of species that require the same environmental conditions and that have similar capabilities of exploring the same resources, represent an obvious example of this abiotic influence on the structuring of biodiversity. Species can be related according to their complex interactions at different levels, such as current velocity preferences, feeding areas and type of food, migration routes during reproductive season, and habitat type selection for spawning and tolerance capabilities to various stressors. Having into account the possibility of grouping species into ecological guilds, it is clear that there are obvious associations between the distribution of aquatic species and environmental variables, and consequently, it is expected a connection among the general patterns of species distribution and the abiotic gradients like water temperature, water depth and sediments present.

7.1.1 Water Temperature

Water temperature plays an exceptional role in influencing the biology of inland waters, through determination of thermal habitat distribution and physiological performance of many different species, particularly for ecthotermal organisms, i.e. organisms whose thermal homeostasis is regulated by changes in the environmental temperature (Langan et al. 2001; Arthington et al. 2010). Indeed, water temperature has been referenced as one crucial variable for determining the structure of freshwater fish communities (Crisp 1996), and surveys of lakes along geographical gradients have also shown that temperature is amongst the most important factors in accounting for variability in the distribution and assemblage structure of macroinvertebrates (Heino et al. 2009). This factor can also directly influence the physiology of macroinvertebrates, as demonstrated by Vaughn (2010), where it was discovered that temperature governs the rates at which mussel species clear material from the water column and excrete ammonia and phosphorus. Additionally, it was also found that different mussel species have different optimal temperatures, influencing the species composition and the consequent nutrient recycling (Spooner & Vaughn 2008; Vaughn, 2010).

Because of this huge effect of water temperature on biodiversity, Olden & Naiman (2010) call for a clearer elucidation of the negative impacts caused by thermal changes in shaping ecological patterns and processes in riverine ecosystems (Arthington et al. 2010). The human impact factors and global climate change are the most influent events that can change water temperature and consequently the biodiversity levels of inland waters (Lake et al. 2000; Xenopoulos et al. 2005). The inter-linkage of drivers and effects is depicted in Figure 73. On one hand, many human activities in the landscape have modified riverine thermal regimes, and dams in particular generate modified thermal regimes by selectively releasing hypolimnetic (cold) or epilimnetic (warm) water from thermally stratified reservoirs, to the detriment of entire assemblages of native organisms (Arthington et al. 2010). On the other hand, climate change can cause major changes in water temperature, affecting biodiversity at different scales of biological organisation (i.e. genes, species and ecosystems) at habitat, local, regional, and global scales (Heino et al. 2009).

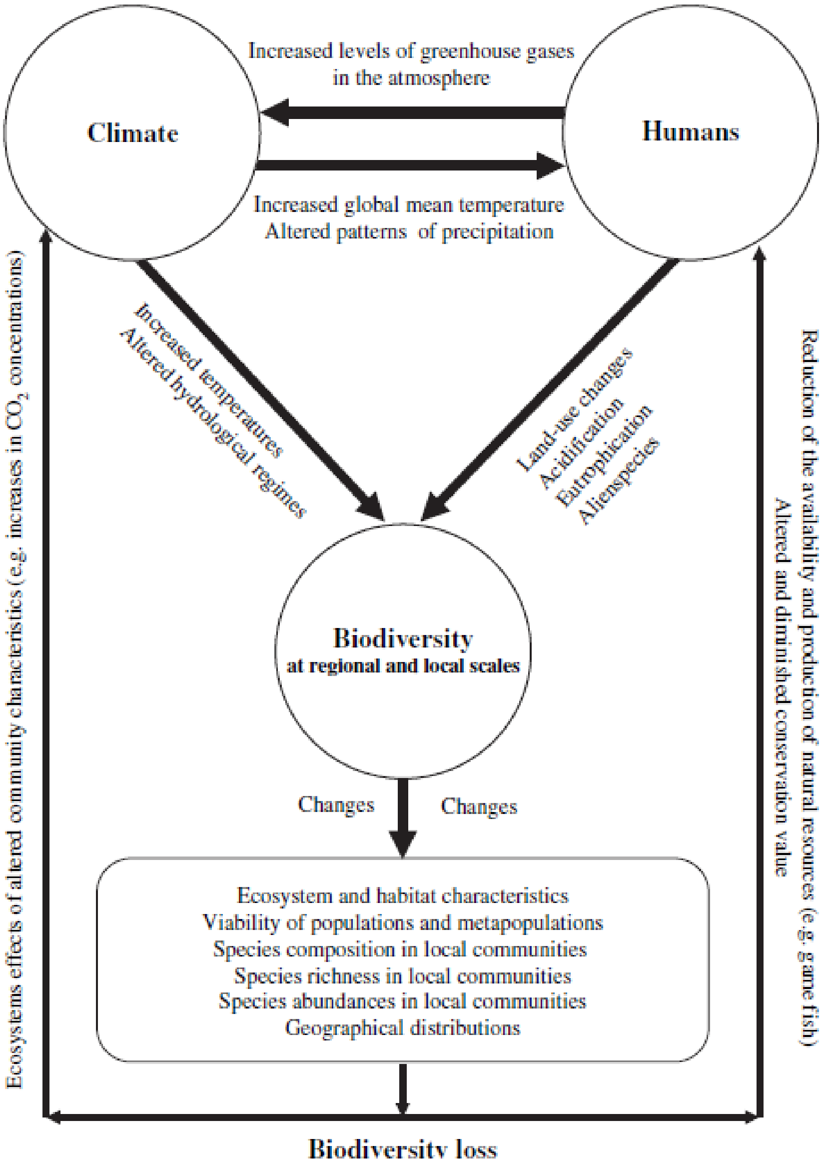

Figure 73: Schematic diagram showing the relationships between climate change and other major anthropogenic influences and their effects on biodiversity. The two major factors resulting directly from climate change and the four major anthropogenic factors have both individual and interactive effects on biodiversity in freshwater ecosystems (adapted from Kappelle et al. 1999; Heino et al. 2009).

The modified temperature regimes can cause delays in fishes spawning, disruptions in patterns of insect emergence, reductions of benthic standing crop, and direct extirpations of temperature-specific water species (Bunn & Arthington 2002; Figure 74). Additionally, increases in temperature may be especially relevant in boreal regions by increasing the invasion probability and establishment of exotic species that typically originate from more southerly regions (Bunn & Arthington 2002). This can have dramatic consequences for local native species, biotic communities and ecosystem processes (Rahel & Olden, 2008), since exotic species constitute an input of predation, competition and a source of parasites and diseases to which native species are unfamiliar with (Wrona et al. 2006; Heino et al. 2009; Kornis et al. 2013).

These examples demonstrate the strong relationships between water temperature and biodiversity, highlighting also the need for a complete understanding about how levels of variation in this biodiversity indicator can affect the global patterns of species diversity.

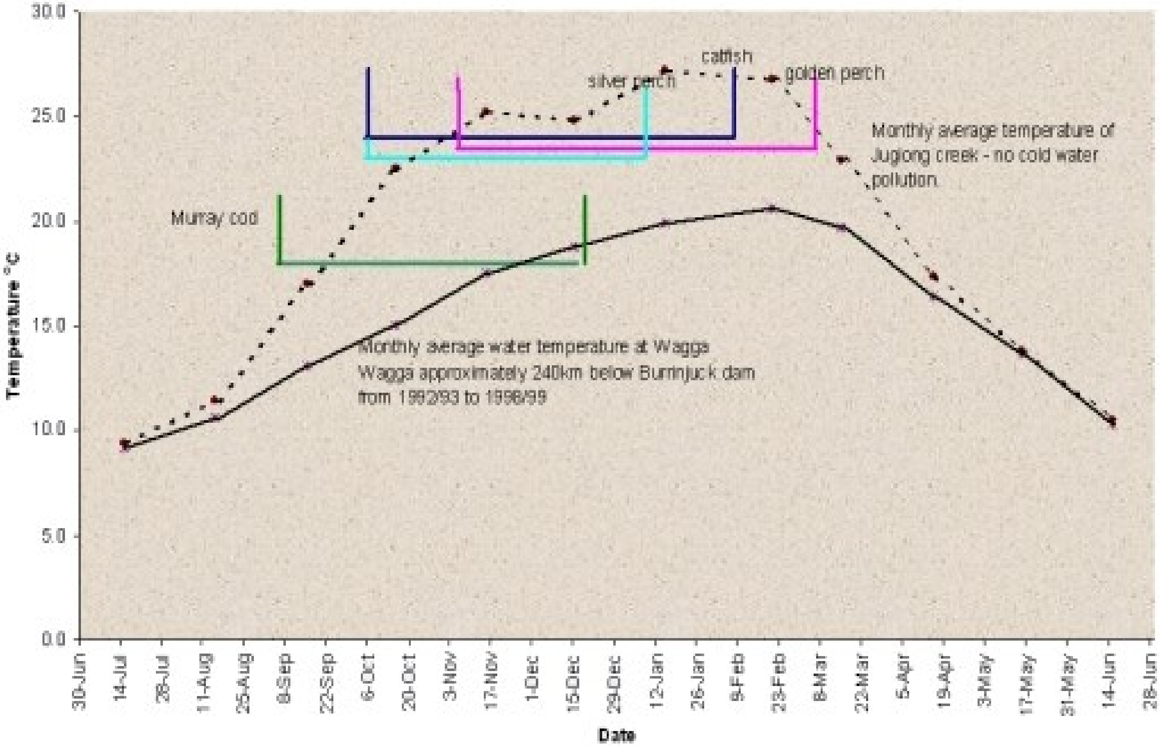

Figure 74: Observed water temperatures in comparison to fish spawning envelopes. The solid line shows the temperature of the Murrumbidgee River at Wagga Wagga where cold water pollution occurs. The dotted line shows water temperature at Jugiong Creek at Jugiong where there is no cold water pollution (adapted from New South Wales, 2006).

7.1.2 Suspended Sediment

Water sediments could be an important biodiversity indicator for assessing the quality of inland waters, especially because they have a clear relationship with water temperature, a very important factor for the stability of freshwater biodiversity. In fact, it is argued that the interactions between temperature and sediments are the most common interaction type of all. A study developed by Piggot et al. (2012) concluded that these two factors have a strong connection, influencing differently the metabolism and abundance of many invertebrates from several taxonomic groups. The levels of food productivity in lakes can also increase when high nutrients and high temperature are combined (Piggot et al. 2012). For these reasons, water sediments are inevitably related not only with water temperature but also with other events that can cause variations in this indicator and consequently on biodiversity, like the global climate change (Figure 75). However, the amount of water sediments per itself can have relevant consequences in the quality of inland waters. Excessive levels of sediments can be inappropriate for the maintenance of freshwater biodiversity. As an example, the clear-water and turbid-water represent the two most important regimes affecting the productivity of inland waters (Folke et al. 2004). In the clear-water regime, phosphorus inputs, phytoplankton biomass, and recycling of phosphorus from sediments are relatively low, while in the turbid-water regime, these same variables are relatively high. These higher levels can provide lower ecosystem services because of abundant toxic cyanobacteria, anoxic events, and fish kills (Smith 1998; Folke et al. 2004). In addition, increasing levels of water sediments can result from the augment of human activities, through the release of contaminants from land based sources via rivers and the atmosphere to the ocean where they may accumulate and recycle in sediments and organisms (Schiedek et al. 2007; Figure 75). Many of these contaminants are ecologically harmful and thus are also referred to as pollutants or hazardous substances, with major potential to alter ecosystem services and patterns of biodiversity (Schiedek et al. 2007). More information is required for a better comprehension of the effects caused by water sediments, and associated biodiversity indicators, on the global biodiversity.

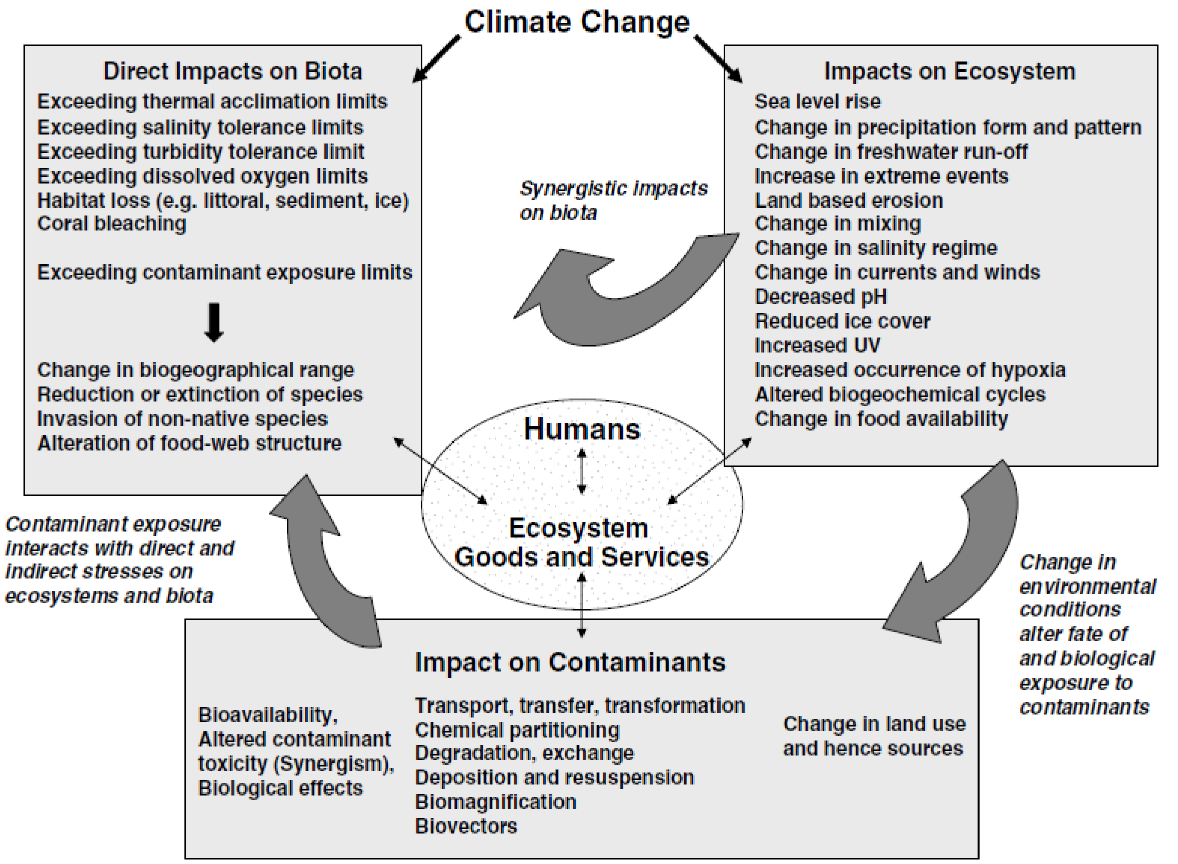

Figure 75: Overview of climate change impacts on ecosystem and biota, and how they interact with contaminants, and their fate and effects (from Schiedek et al. 2007).

7.1.3 Chlorophyll

The measurement and distribution of chlorophyll have been of interest to scientists, researchers, and aquatic resource managers, especially because the presence of chlorophyll is a direct indicator of the presence of phytoplankton (Figure 76), i.e. photosynthetic organisms (Agostinho et al. 2008). The distribution of phytoplankton allows researchers to draw conclusions about water quality, composition, and ecological status, and thus, this parameter can be used as an indicator organism for the health of inland waters.

Surface waters with high chlorophyll levels are normally high in nutrients, such as phosphorus and nitrogen, causing the algae to grow or bloom. After the bloom of algae populations, oxygen levels become depleted, which leads to the eutrophication of inland waters and the extirpation of entire fish communities. Additionally, the dynamics of chlorophyll and phytoplankton in most large rivers of the world is altered by human activities, such as pollutants and cultural eutrophication (Wehr & Descy 1998). This picture is further complicated when systems are highly regulated and their hydrological dynamics is arranged according to human needs (Billen et al. 1994; Sellers & Bukaveckas 2003; Sabater et al. 2008). For these reasons, the present amounts of chlorophyll in inland waters could be a useful biodiversity indicator, not only for assessing general biodiversity levels but also to provide important information concerning possible lakes that might be monitored for excessive phytoplankton growth.

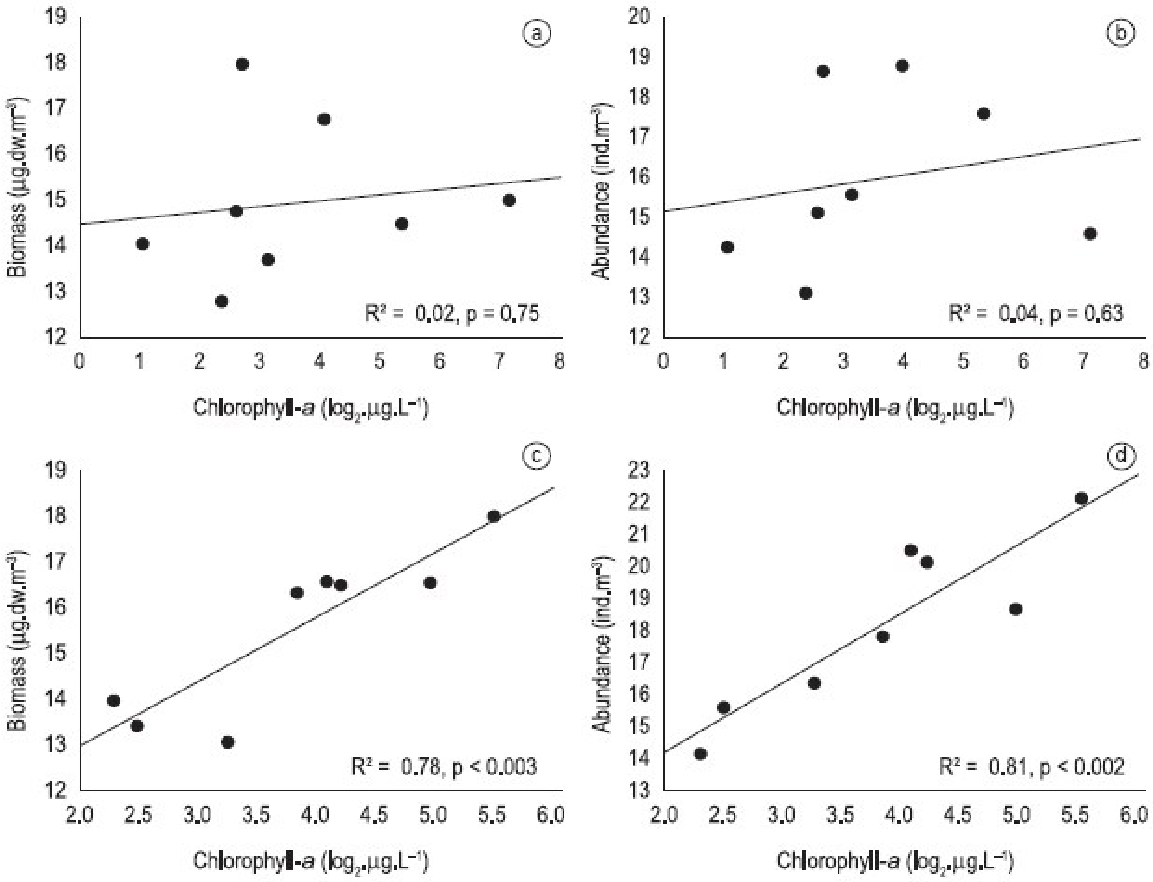

Figure 76: Association of the total density and zooplanctonic biomass with chlorophyll-a concentration in lakes during the dry (a and b) and rainy (c and d) seasons (adapted from Bonecker et al, 2012).

7.2 Relationships between Dryland Indicators and Biodiversity

In the Diversity II Products User Handbook (Gangkofner et al., 2015), results of comparisons between faunal species richness data and various Diversity II dryland products as well as halfmonthly fAPAR time series data are presented and discussed. Plant species richness and vegetation productivity proxies have not been explicitly contrasted in Diversity II, though at least in one extreme case, i.e. the Succulent Karoo, an outstanding floral biodiversity hotspot in western South Africa, we could recognise a clear relationship between NPP and RUE proxy indicators and biodiversity. This example is shown in Figure 77 (left, blue ellipse), along with the soil moisture status map to the right. A large area with spring horizons directly south of the Etosha Pan (marked with a blue ellipse on the right hand site of Figure 77) with numerous surface water ponds exhibits significantly increased soil moisture compared to the surroundings. So this hot spot of faunal biodiversity can be related best or even only to the soil moisture data.

Ecological or environmental variables play an important role in the structure of biodiversity in drylands. In fact, climatic variables such as temperature and precipitation are fundamental for the species physiological processes, influencing the geographical distribution of the species and consequently the biodiversity patterns of a region. For these reasons, biodiversity indicators that have a strong connection with these environmental variables, such as the Net Primary Production (NPP), can be very crucial for establishing relationships with species diversity measures.

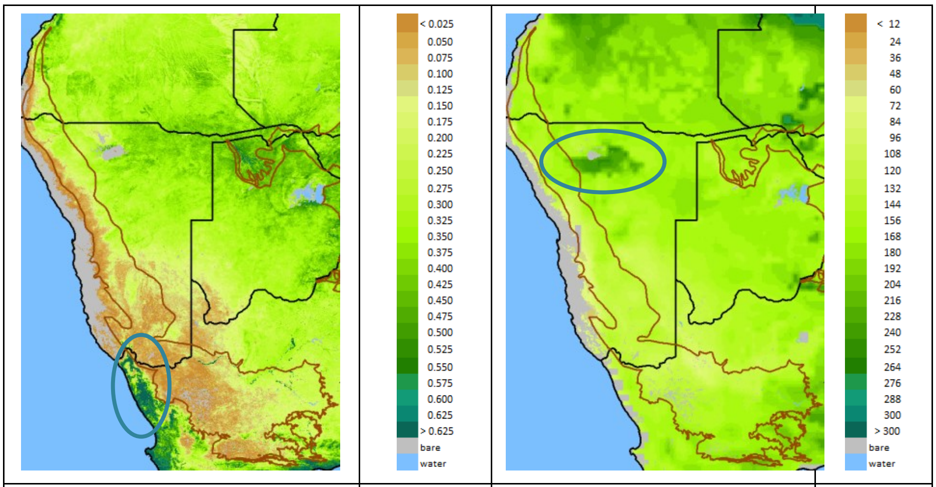

P08 Rain Use Efficiency (RUE)of fAPAR averages of vegetation years 2003-2010	fAPAR multiplied with 1000	P29 CCI Soil Moisture mean of vegetation years 2003-2010	SM multiplied with 1000

Figure 77: Biodiversity highlights in Southern Africa: Succulent Karoo (shown in RUE map in blue ellipse on the left), Area south to the Etosha Pan (shown in soil moisture map in the blue ellipse on the right)

7.2.1 Relation between Biodiversity and Primary Productivity

When looking at the literature, this issue is debated around some mainstream concepts, which all have their supporters and opponents. Overall, the relationship between vegetation productivity and floral or faunal biodiversity is highly scale dependent (see for instance Chase and Leibold, 2002) and biome/region specific and cannot be characterised with generalised linear relationships. The relationship further depends on the type of creatures and species (e.g. plants versus animals, mammals versus birds versus amphibians, etc.), on the range of environmental conditions analysed (e.g., complete spectrum of growing conditions or only arid regions) and on land cover/land use and land management practices.

Overall, i.e. across the entire spectrum of NPP (all climate regions), the degree of biodiversity has been shown to increase with humidity, except for humid temperate climates. However it may be argued that the latter are the most influenced by human uses and are therefore possibly already more affected by a biodiversity loss.

Figure 78 illustrates the number of flowering plants in different aridity zones and in humid climates. It can be concluded that biodiversity (measured in this way) overall increases with increasing water availability and thus with increasing NPP within drylands. Nevertheless, at local and regional scales, such relations may look different, as the following sections shortly summarise from a myriad of studies in this field.

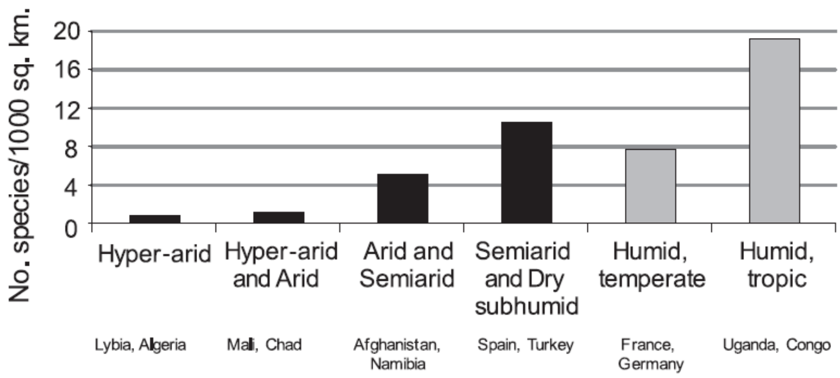

Figure 78: Number of Species of Flowering Plants in Selected Countries across the Aridity Gradient (per 1,000 sq. km). Each column represents a mean of two countries. Selected dryland countries are at least 95% dryland, either of one subtype, or two of roughly similar dimensions. Grey columns indicate non-dryland countries. Source: Millennium Assessment (http://www.millenniumassessment.org/documents/document.291.aspx.pdf), compiled from CIA (Central Intelligence Agency), 2004: The World Fact Book, https://www.cia.gov/redirects/ciaredirect.html, and from WRI (World

Resources Institute), 2004: EarthTrends, the Environmental Information Portal [Online], Drylands, People, and Ecosystem Goods and Services: A Web-based Geospatial Analysis (pdf version), by R.P. White and J. Nackoney.

7.2.1.1 Hump-shape theory

At very low levels of primary productivity, plant diversity was found to increase with increasing productivity, whereas from intermediate to high productivity levels, decreases have been observed (Oindo et al. 2002). Overall, this relationship is often described as producing a unimodal 'hump-shaped' curve, e.g. by Huston 1979 (cited by Oindo et al. 2002 in a study in Kenya), or by Oba et al. (2001), who analysed grazing areas in arid zones of Kenya. They found that optimum herbaceous species richness in these areas corresponded to a biomass level of 400-500 g/m², and declined when biomass exceeds 500 g/m². Further on, these authors compared open grazing land to grazing exclosures and observed that "*seasonal grazing exclosures may increase species richness to a certain level, but the decline in species richness with age of exclosures indicates that long-term exclusion of grazing may not necessarily increase species richness in arid-zone grazing lands*" (Oba et al., 2001, P. 836). Bhattarai et al. (2004) tested and confirmed the humped-back hypothesis in the arid Trans-Himalayan mountain grassland with a seasonal grazing system and found that species richness was highest at 120 ± 40 g/m². However, these hump-shaped curves of the relationship between primary productivity and plant species richness seem to be observable especially when broad spectra of ecological conditions are analysed. Different results were obtained by Chase and Leibold (2002) for the diversity of plants and benthic animals in ponds versus watersheds: the small scale (ponds) distribution of diversity with productivity exhibited the hump shape, while at the regional scale (watersheds) the authors observed a linear relation between primary productivity and species richness (Figure 80).

7.2.1.2 Theory of linear relation between biodiversity and primary productivity

Given the importance of ecosystem services to the resilience of species diversity, NPP can be used as a proxy for understanding patterns of biodiversity loss, habitat fragmentation and also climate change (Chase and Leibold 2002). NPP has been used as a consistent biodiversity indicator for evaluating general patterns in biodiversity distribution. It has been claimed that higher species diversity is normally related with higher values of primary productivity and these relationships were demonstrated for different taxa, such as tree species (Kale and Roy, 2012; Figure 79), invertebrates (Chase and Leibold 2002; Figure 80), birds and mammals (Luck 2007; Figure 81), at both local and regional scales. These patterns were confirmed for total species richness of particular regions and also for wider units of biodiversity, like the value of the ecosystem services of entire biomes (Costanza et al., 2007; Figure 82).

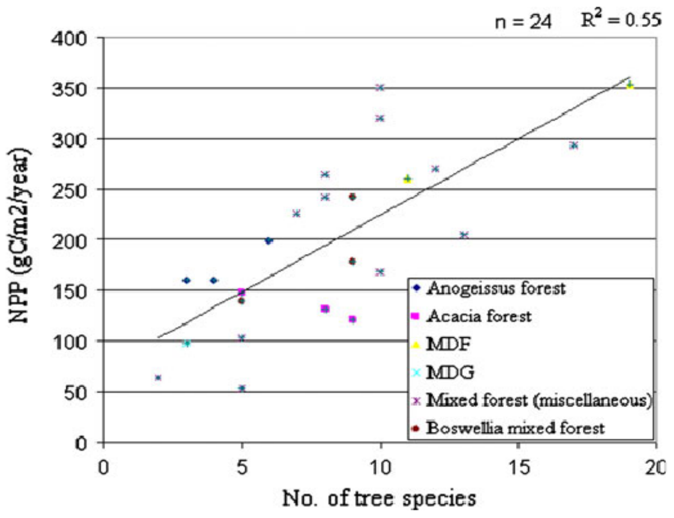

Figure 79: NPP and tree diversity relationship (source: Kale and Roy 2012).

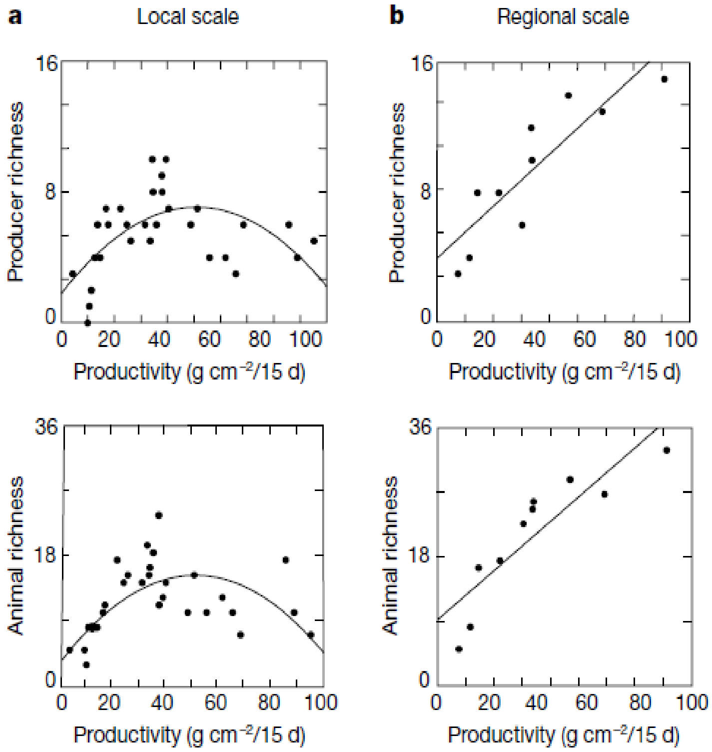

Figure 80: Results from the survey of pond species diversity relative to *in situ* primary productivity at local and regional scales. Top panels: producers (vascular plants and macroalgae); bottom panels: benthic animals (e.g. insects, crustaceans, amphibians). a) Local species diversity within-ponds (N . 30). Both relationships are significantly unimodel (P, 0:05). The line represents the estimated quadratic function. b) Regional species diversity within-watershed. For both producers (regression: N. 10, R2. 0:74, P, 0:001) and benthic animals (regression: N . 10, R2 . 0:75, P , 0:001) regional species diversity was linearly related to primary productivity (source: Chase and Leibold 2002).

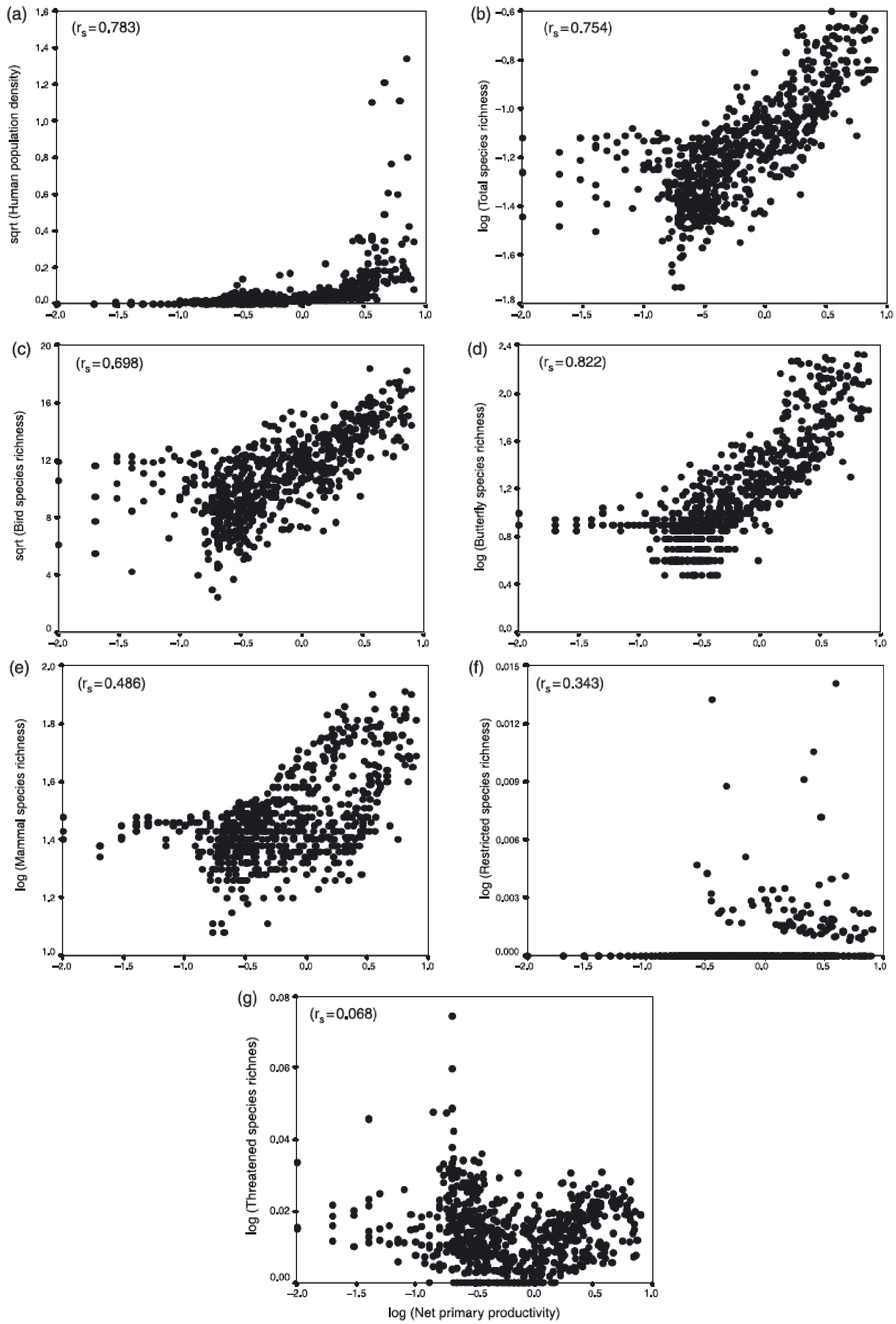

Figure 81: The relationship between log10 NPP and (a) square-root of human population density, (b) log10 total species richness (weighted index), (c) square-root bird species richness, (d) log10 butterfly species richness, (e) log10 mammal species richness, (f) log10 restricted species richness, and (g) log10 threatened species richness. Sample grain is 1 grid squares (n = 683) (from Luck 2007).

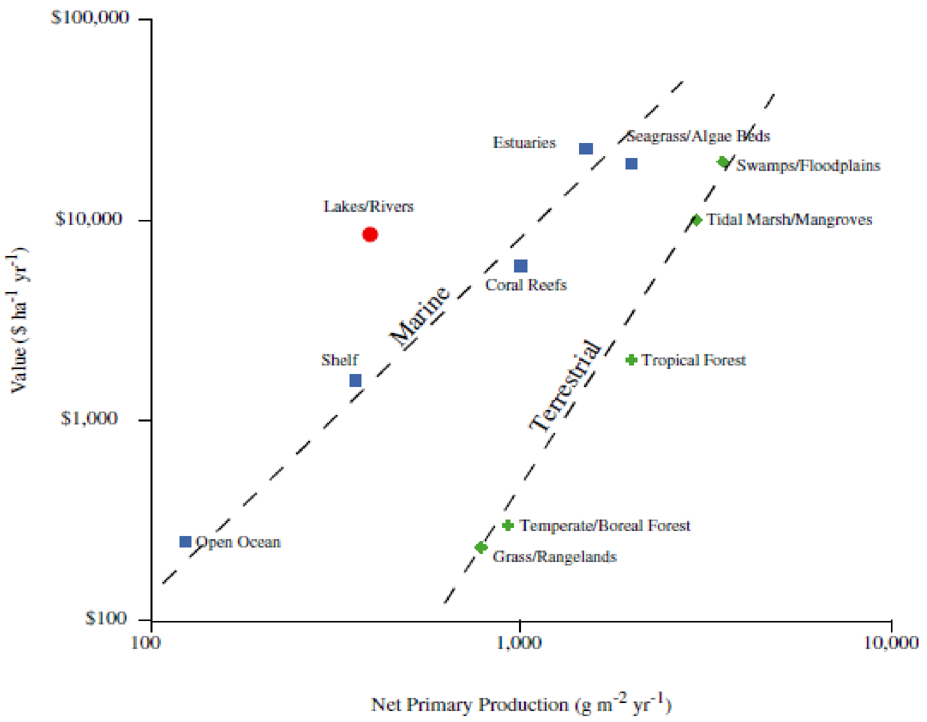

Figure 82: Relationship between NPP and the value of ecosystem services by biome (from Costanza et al. 1998).

7.2.1.3 Opponents of the hump-shape and the linear theories

The wide spread hump-shape theory as well as the linear relation (between biodiversity and NPP) theory are challenged by several authors, for instance Whittaker 2010, who argues that overall such study results depend among other factors heavily on the scale and sampling design. Also Adler et al. (2011, p. 1750) state: *"We addressed such concerns by conducting standardized sampling in 48 herbaceous-dominated plant communities on five continents. We found no clear relationship between productivity and fine-scale (meters−2) richness within sites, within regions, or across the globe"*. Further on, as Jenkins (2015) points out, often biomass as the most common proxy for productivity is used for these assessments. According to Jenkins, this may cause error and uncertainty in the resulting relation between NPP and biodiversity due to the fundamental difference between biomass and productivity and variable ratios between the two among and within ecosystems. Based on studies in worldwide grasslands, Cadotte et al. (2008, p. 17012) in turn "*show that the amount of phylogenetic diversity within communities explained significantly more variation in plant community biomass than other measures of diversity, such as the number of species or functional groups*", where *phylogenetic diversity "is the measures the magnitude of the divergences among species that have evolved since a common ancestor" (*Cadotte et al., 2008, p. 17012). These authors emphasize the importance of evolutionary history for biodiversity studies and conclusions.

7.2.1.4 Interpretation of EO derived greening trends

Given the spatial variability of relationships found between productivity (or biomass) and plant species richness, it becomes clear that also greening processes observed with satellite data are not necessarily positive with regard to biodiversity per se. Herrmann et al. (2013) investigated the greening of the Sahel since the drought years in the 1970s and 1980s that has been commonly observed with NOAA AVHRR NDVI data and is largely related to increased rainfalls since. They compared the woody vegetation species composition of several test plots in in the Sudanian zone of central Senegal for the years 1983 and 2010 and found: "*While increases in woody vegetation densities could be confirmed at about half of the greening sites, these increases occurred only in the shrub layer. A loss of trees was evident at all greening and control sites. Moreover, our data pointed to a loss in species richness and a shift towards more xeric species compositions at almost all sites. Discussions with the local population largely confirmed these observations. Our findings from central Senegal* *contrast with other findings of increasing field tree densities resulting from farmer managed natural regeneration in other parts of West Africa".*

The authors developed the diagram shown in Figure 83, which symbolises possible pathways of greening, where they observed changes in the sense of the blue arrow: greening, but towards a "green desert" made up of less diverse and valuable, but abundant shrub species.

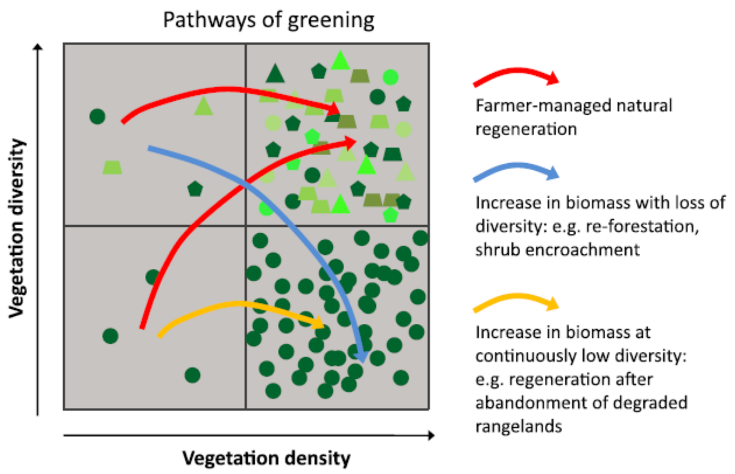

Figure 83: Conceptualized pathways of greening. Point symbols represent different woody species; arrows indicate possible pathways of change towards "greener" conditions. Source: Herrmann et al. 2013

Even in the rather short period of the MERIS data, we could frequently observe positive trends of the dry season greenness levels (without such trends in the cyclic vegetation, i.e. the peak vegetation during the rainy season(s)), which may give hints to the over-proportional thriving of woody vegetation, which in turn might be related to bush encroachment and potentially to invasive species.

Detailed studies of these relationships, especially with validations using in situ data would be of high interest.

7.2.1.5 Implications for the Diversity II derived indicators

NPP and RUE (type) proxy indicators displaying primary production and productivity (per unit water) patterns, gradients and hotspots potentially bear a lot of spatial information on biodiversity, which however is not deducible in a simple and consistent way from the NPP and RUE proxy figures. The individual Diversity II indicator products represent different facets of biodiversity, which could not be readily confronted with plant biodiversity data due to the profound lack of access to such data at suitable regional scales. In addition, the project concentrated on validations based on faunal diversity, which is nevertheless based on the existence of habitats which are made up by primary production and productivity to a large extent.

It would be of high interest to confront the derived indicators with in situ derived compositional biodiversity (species richness) information, where such information can be found. The aim would be to empirically link EO based indicators to dryland biodiversity, specifically in the context of land degradation and bush encroachment, test and prove its indicator function for the diversity of plant composition, and gain a more profound basis for the definition of further work.

7.2.2 Relation between Land Use, Degradation and Biodiversity

Maitima et al. (2009) investigated in a broad study the linkages between land use change, land degradation and biodiversity across East Africa. While wildlife is in general on strong decline e.g. in Kenya and Uganda due to land use intensification related to heavy population pressure, the authors also found that it cannot in general be concluded that grazing or cropping necessarily reduces the primary biodiversity and productivity.

Table 27: Total number of plant species, herbaceous (grasses and herbs) species and total plant biomass (gm-2) between grazed and un-grazed sites. * Means significantly different at (p < 0.05), t-test. Sample size was 245 plant species. Source: Kamau, 2004, from Maitima 2009.

	Grazed	Not grazed	p-value
Total species numbers	184	125.5	0.03*
Herbaceous species numbers	91.5	49.5	0.03*
Total biomass	91.63	887.8	0.04*
Herbaceous biomass	429.09	387.24	0.48

According to Table 27, grazing in Embu, Kenya, led to an increase in species numbers and herbaceous biomass, where it is unclear however how the amount of total biomass in grazed areas comes about (as it is smaller than that of the herbaceous biomass). The authors argue "*that the off-take of biomass through grazing in the area is moderately high and appears to reduce competition for resources between different plant species, thus increasing the number of species that can coexist in grazed sites compared to areas with no grazing*" (Maitima et al., 2009, p. 313). In other sites, pastures (planted and native) supported more weeds than other land uses and only occasionally were homes to plant species of conservation value. Likewise, the authors found different impacts of land use structures in croplands on biodiversity, where partly croplands at the Kilimanjaro (perennial poly-culture) supported more species including a significant number of indigenous species (and "only" 50% weeds) than nearby woodlots, bushland or pasture. In contrast, annual croplands in Embu exhibited the highest number of species, which however include to 90% weeds. In these and other cases farming practices led to significant losses of indigenous plants species including valuable medicinal plants. These mixed findings may find their expression in the relation between land use intensity and biodiversity shown in Figure 84, where the Shannon–Wiener diversity index[2] plotted against increasing land use intensity.

Further on, Maitima et al. found remarkable declines in soil productivity due to soil erosion, decrease of organic matter, degradation of soil structure and a reduction of nutrient availability. In addition, increases in toxicity due to acidification and salinisation especially on irrigated farmland were observed. Their overall conclusion is

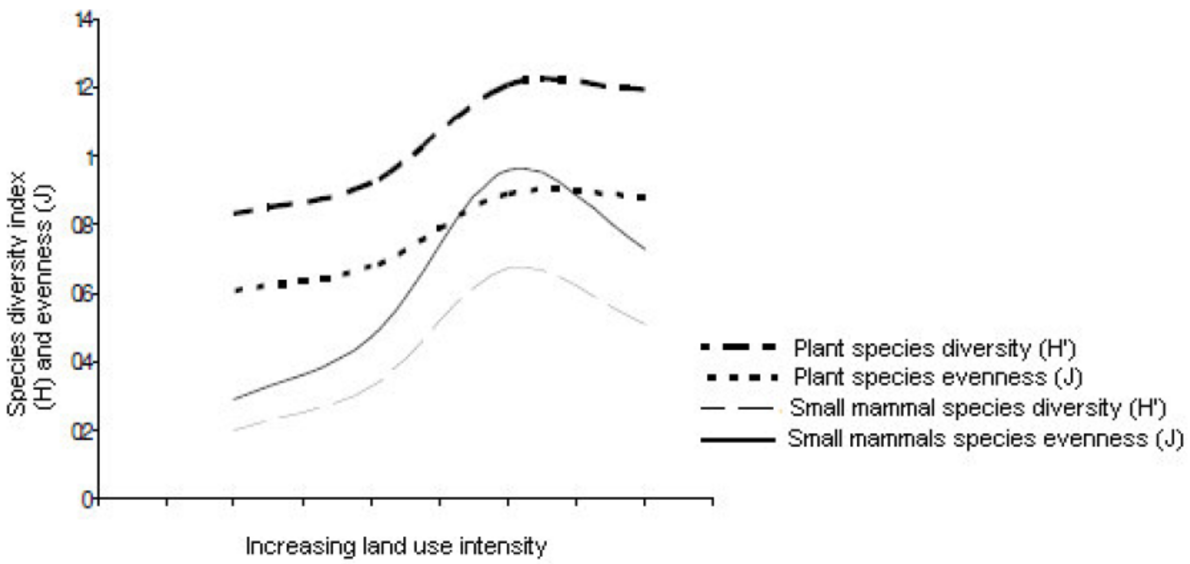

Figure 84: Shannon-Wiener diversity index (H) and evenness (J) of plant and small mammals. Source: Mugatha et al., 2003, from Maitima 2009.

[2] https://en.wikipedia.org/wiki/Diversity_index

When studying the NPP/RUE relation with biodiversity at a more detailed scale, many more factors than just humidity play a role. (Gardiner, B, 2010) establishes the relation between biodiversity, NPP, RUE, and resilience to climate change in a quite instructive way in the context of (drylands) rangeland management. In this context, the economic aim is to maximise RUE, as at the farm level, a maximum RUE minimises the volume and costs of purchased inputs. Gardiner describes these relationships as follows:

- For minimising runoff and soil erosion, sufficient vegetation ground cover (including dead and detached litter) is required. While 70% ground cover is the generally specified target in higher rainfall regions, much less than 70% ground cover may be found in conservatively grazed semi-arid woodlands. The higher the run-off, the less water is available for vegetation growth.
- Soil evaporation is reduced by litter, thus the more litter is built and maintained, the lower is the soil moisture loss (= lower RUE) by evaporation.
- A certain minimum green dry matter (1.5 t/ha corresponding to 5 – 15 cm of retained pasture height) is desirable in all seasons and all locations to make maximum use of the photosynthetic radiation, and to convert even small rainfall events into biomass.
- "*If pastures are to make maximum use of all incident rainfall, a variety of functional types of plants are likely to be more successful at maximising plant productivity and RUE than just one or two species*"(Gardiner, 2010, p. 4). Thus, the higher the biodiversity and the more different the phenological schedules of plants including perennials, the more use can be made of rainfall throughout the year.
- Woody, perennial plants have further functions that contribute to plant and animal productivity: they reduce wind speed and thus excessive evapotranspiration, damage to plants, and they reduce deep drainage below pasture root zones.
- Maintenance of optimal soil health is provided by keeping these factors above certain levels, as they all contribute to optimal levels of soil carbon and organic matter and soil structure, and to the reduction of soil surface crusting (Gardiner 2010), the latter being a major adverse factor of dryland soils.

These relationships explain why and how NPP, RUE and Biodiversity are interrelated. While water availability in dryland ecosystems is the major driver for NPP, it can be seen that the usability of the incoming water for NPP within the ecosystem can be maintained and significantly enhanced by the practices referred to above. On the temporal scale, increasing rainfall will trigger increasing NPP, but the above described processes will further contribute and lead to self-enhancing productivity and biodiversity conditions under optimal conditions. Vice versa, the resilience of dryland ecosystems against less favourable rainfall conditions or variability will increase where soils are healthy and biodiversity is high.

7.2.2.1 Implications for EO based mapping and monitoring

The above described interrelations between land use and biodiversity and those between field-level land management and biodiversity can only be assessed and monitored with high to very high resolution remote sensing data and in situ studies. Biodiversity on a species level can hardly be directly measured with EO, but conditions conducive for high or acceptable levels of biodiversity are detectable with EO data, and also habitat mapping is among frequently performed remote sensing applications. Further on, structural aspects of biodiversity, i.e. landscape and habitat heterogeneity, fragmentation or connectivity and proximity to potential threads can be examined (Kuenzer at al., 2014). Remote sensing studies of those topics require additional thematic data including for instance vegetation and land cover, crop area boundaries, cropping and grazing systems, traffic infrastructure, demographic data, protection status, etc. Such studies may be performed at different scales, but with regard to EO data, high or very high resolution data are preferable. In drylands, the usage of both wet season and dry season EO coverages are indispensable, which at least at the current cost level often restricts such analyses to time intervals of several years (see for instance Secade et al., 2014).

It can be expected that those tasks can be (partly) approached in less costly ways with the future Sentinel data, especially Sentinel 2 and associated “big data” processing environments, or the growth of open satellite-image archives such as Landsat (Skidmore et al., 2015). Nevertheless, we claim that moderate resolution and time series based NPP or RUE proxies and derived indicators can assist and supplement such work. Therefore ways should be found how to link low-cost and high frequency moderate resolution type monitoring approaches like the one performed in Diversity II to finer scale national or provincial mapping programmes in multi-scale approaches.

7.2.3 Functional Biodiversity

Noss (1990) expanded the three primary attributes of biodiversity recognized by Franklin et al. (1981), i.e. composition, structure, and function, into a hierarchical indicator scheme for monitoring purposes. Composition addresses measures of species and genetic diversity, structure the physical organisation and pattern of systems (e.g., patches, fragmentation) at landscape scale, while function “*involves ecological and evolutionary processes, including gene flow, disturbances and nutrient cycling*” (Noss, 1990, p. 357). Noss emphasized that according to Franklin (1988) the growing concern over compositional diversity has not been accompanied by an adequate awareness of structural and functional diversity.

In remote sensing this concept has been adopted for instance in a recent review of Kuenzer at al. (2014), or by Alcaraz-Segura et al. (2013) and by Ivits et al. (2013). The latter two derive ecosystem functional types (EFT) from EO time series data, specifically from derived phenological and productivity information. Both approaches are not geared specifically to drylands, and have led to continental-scale EFTs.

At a finer scale, many examples of remote sensing applications to map structural biodiversity (and “ecosystem services”) exist, such as the mapping of riparian areas requested by EEA in the frame of the Copernicus Initial Operations land (GIO land) components (http://calvalportal.ceos.org/documents/10136/373179/GIOland_LPVE_GBU.pdf/5366e72e-b6aa-4f27-b578-470ef084a15d).

Figure 85 shows a comparison of the EFTs (Ivits et al., 2013) to the functional classes (P50) derived in Diversity II. The derivation and legend of P50 are explained in section 6.2.2.1. The scale difference between the two approaches is clearly visible, where P50 shows a much stronger differentiation, as it was conceived for the regional scale. P50 was in addition adapted to drylands, leading to a sub-maximum structuring of humid areas. Consequently, in humid areas, this indicator would have to be modified to capture more specifically functional ecological traits of humid areas. Nevertheless rough commonalities between the patterns on both maps can be recognised.

Diversity II contributes quite obviously to the functional aspects of biodiversity, which are expressed in a simple most way using less parameters than Ivits et al. or Alcaraz-Segura et al. (2013): Diversity II indicator P50 is a combination of NPP status (average of vegetation years) and the percentage of the cyclic vegetation (green peak without perennial basis, see Figure 55) of the vegetation year production and or biomass. Alcaraz-Segura et al., based on MODIS EVI (enhanced Vegetation Index) data in contrast used EVI annual mean, EVI seasonal coefficient of variation, and date of the maximum EVI value. The EVI seasonal coefficient of variation is a descriptor of the differences in carbon gains between seasons according to the authors.

Diversity II P50 was geared to exhibit in addition to ecosystem mean production specifically the share of (mostly woody) perennial vegetation of the total production. It is based on the assumption that strong fAPAR signals during the dry season are related to perennially green vegetation, which in drylands can be assumed to be made up by woody plants. According to Clarke (2008), total perennial woody vegetation species richness, i.e. the diversity of woody-perennial vegetation is a sound surrogate of biodiversity in Australian rangelands, and we claim that this may apply to drylands in general given the important functional properties of woody vegetation. However, this indicator will also encompass woody vegetation related to bush encroachment, which is usually unwanted, and thus can only be interpreted with regional and local knowledge. On the longer run, the dynamics of such seasonal fractions of the vegetation can give valuable hints as to potential functional shifts of the vegetation. Used as status maps, P50 may be further evaluated with regards to the number of units occurring (spatial diversity), or in approaches for local scaling of NPP and RUE (see Prince at al., 2009).

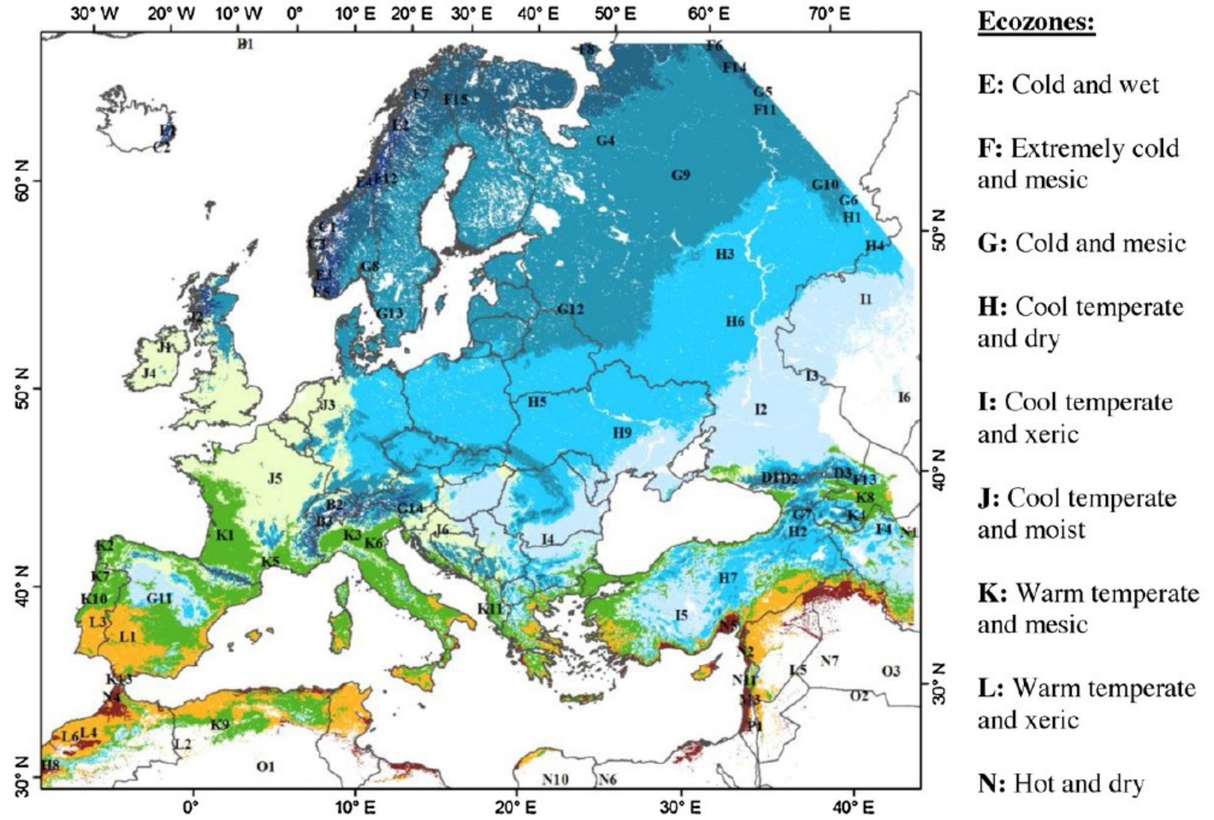

(a) European subset of the Global Environmental Classification with the nine ecozones (colours) and 73 strata (shown by numbered capital letters). Source: Ivits et al. 2013

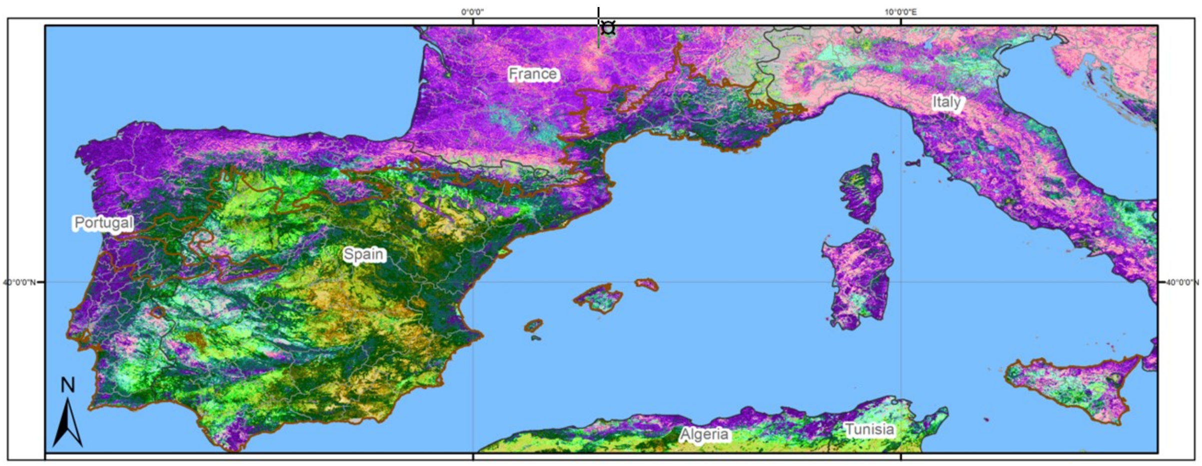

(b) Diversity II Indicator products P50: function classes (legend: section 6.2.2.1)

Figure 85: (a) Ecosystem Functional Types derived by Ivits et al. (2013) and (b) Diversity II Functional Units

8 Overview of Algorithms

The following table provides an overview on all algorithms described in this ATBD for the different processing steps.

Table 28: Overview on processing and algorithms

Chapter	Processing Step	Algorithm	Reference	Maturity	Validation	Selection
3	**Pre-processing**					
3.1	Improved Geolocation using Amorgos	Amorgos	SOTIS et al., 2011	Mature	Validated (Bicheron et al., 2011)	YES
3.2	Radiometric Correction	CoastColour Calibration		BEAM Implementation	CoastColour	YES (Drylands)
		MERIS FR bulk reprocessing				YES (Lakes)
		Equalisation	Bouvet & Ramino, 2010	BEAM Implementation	Bouvet and Ramino, 2010	YES
		Smile Correction				
3.3	Cloud Screening	Spectral threshold methods	Brockmann et al. 2011	Implemented in ESA ground segment		NO
		Bayesian probability	Merchant et al, 2005 Mackie et al, 2010a Mackie et al, 2010b		Merchant et al, 2005 Mackie et al, 2010a Mackie et al, 2010b	NO
		Cloud Probabililty	Preusker, 2006	BEAM processor	Preusker, 2006	NO
		Multi-temporal screening	Shi et al., 2007		Shi et al., 2007	NO
		Multi-sensor approach	Kokhanovsky et al., 2008 Shi et al., 2007		Kokhanovsky et al., 2008 Shi et al., 2007	NO

Chapter	Processing Step	Algorithm	Reference	Maturity	Validation	Selection
		Probabilistic Approach (IdePix)	LC-CCI ATBD, 2012	Implemented and used for BC processing chains	PixBox Validation, further validation focusing on dryland	YES
3.4	Land and water separation	Single band thresholds	Brockmann & Santer, 2011; MERIS Product Handbook 2011;	Applied in standard MERIS processing	Brockmann & Santer, 2011	NO
		Band comparison				
		NDWI	McFeeters, 1996	Mature, applicability needs to be tested	Haibo et al., 2011	NO
		Mixed Pixel Identification	Ruescas et al. (2011): Aquamar ATBD	Mature, applied in BC processing chains, CoastColour processing	Visual inspection, Ruescas et al., 2011	YES
3.5	Identification of optically shallow waters	Temporally consistent ratio_490	This ATBD, Section 3.5.2	Mature	This ATBD, Section 3.5.2	YES
		Semianalytical model for bottom depths and water properties	Lee, 1998, 1999	Not applicable for unsupervised MERIS archive processing		NO
		Bathymetry estimation: unmixing	Bierwirth, 1993			NO
		Bathymetry: band ratios	Lyzenga, 1978 Stumpf et al., 2003			NO
		Bathymetry and seabed mapping: radiative transfer model	Dierssen, 2003			NO
		Bathymetry MERIS	Philpot, 1989 Minghelli-Roman et al., 2007		Minghelli-Roman et al., 2007	NO

Chapter	Processing Step	Algorithm	Reference	Maturity	Validation	Selection
		Water properties in shallow waters	Green et al., 2000 Cannizzaro & Carder, 2006 Giardino et al., 2011			NO
		Seabed classification	Giardino et al., 2011 Kenny et al., 2003 Louchard et al., 2003 Vahtmäe & Kutser, 2007			NO
Not reported	Atmospheric Correction over Land	GlobAlbedo atmospheric correction	GlobAlbedo ATBD, 2010		GlobAlbedo ATBD, 2010	
		SCAPE-M for land	Guanter et al., 2008		Guanter et al., 2008	
		ATCOR 2/3	ATCOR, 2011			
		Durchblick	Holzen-Popp, T. et al., 2001	No longer maintained	Holzen-Popp, T. et al., 2001	
3.6.2	Atmospheric Correction over Inland Water	MERIS lakes and C2R	Doerffer & Schiller, 2008	Implemented in ESA ground segment, BEAM processors	MVT	NO
		CoastColour	Doerffer et al., 2012	Implemented in CC processing, ongoing	Doerffer et al., 2012	YES
		SCAPE-M for inland waters	Guanter et al., 2007, 2008	Implemented in BEAM	Guanter et al. 2010	NO
		Bottom-of-Rayleigh		Implemented in BEAM	(Mark William Matthews et al., 2012)m	YES
		Normalizing at-sensor radiances	Matthews et al. (2010) Binding et al. (2010).			NO
3.6.1.3	Adjacency Effect	ICOL	Santer et al. 2010a, Santer	Published and	a) Validated against Mermaid,	NO

Chapter	Processing Step	Algorithm	Reference	Maturity	Validation	Selection
	Correction		et al. 2010b	implemented as processor in BEAM	NOMAD data sets and AERONET Stations (Santer et al. 2010), b) validation against ground truth (Odermatt et al. 2010)	
		SIMEC	Knaeps et al. 2010, Sterckx et al., 2010	Published	AERONET and in-situ, Sterckx et al. 2012 Cross comparison between ICOL and SIMEC	NO
3.7.1	Drylands Auxiliary Data: Soil Moisture Data	WACMOS data set (ESA project)	Dorigo et al. 2012	These SM data constitutes the CCI SM data set, which is under development in the CCI project	Cross comparisons to the other efficiency products performed	YES
3.7.2	Drylands Auxiliary Data: Hydro-Meteorological Data	GPCP data set, NOAA	http://www.esrl.noaa.gov/psd/data/gridded/data.gpcp.html , Fensholt communication	Often used in global studies		YES
		TRMM data set, NASA, JAXA	Fensholt communication	“the best currently available rainfall data”	Comparison with station data in Australia	preferred
		CMORPH data set, NOAA	http://www.cpc.ncep.noaa.gov/products/janowiak/cmorph.shtml	Controversially discussed in the literature, but adds rainfall data with a better spatial resolution	Cross comparison with TRMM rainfall	No
		CPC Air Temperature data set	http://iridl.ldeo.columbia.edu/SOURCES/.NOAA/.NCEP/.CPC/.GHCN_CAMS/.gridded/.dataset_documentation.html	Not assessed	NA	NO

Chapter	Processing Step	Algorithm	Reference	Maturity	Validation	Selection
		MOD16 (ET) Evapotranspiration data set	GMAO (http://www.ntsg.umt.edu/project/mod16#data-product); Lu and Zhuang 2010	Not assessed	Data seem to be somewhat inconsistent as regards correlation with rainfall data and seasonality	NO
3.7.3	Drylands Auxiliary Data: AVHRR NDVI	NOAA AVHRR GIMMS3g NDVI data set	GIMMS research group Users e.g. Prince et al., 2009; Julien et al., 2011; Fensholt and Proud, 2012; Wessels et al., 2012	Yes, data has been reprocessed several times and is generally regarded as mature	Known limits, but long time series	YES, for comparison and indicator P56
4	**Algorithms Lakes Processing**					
4.1.1	Differentiation of water types	Separation by Ecoregion		Done for different applications/areas using different parameters for classification	no	NO
		Optical Water Type classification using Fuzzy Logic	(Moore et al., 2014)	Used in several applications	(Moore et al., 2014)	YES
		Applicability ranges of water constituents	Odermatt, 2012	Compiled from a large number of reviewed papers		NO
4.1.3	WQ retrieval algorithms	C2R / CC	Doerffer and Schiller (2008a)	Further developed within CoastColour Project, Doerffer et al., 2012	MVT studies, Marcoast Validation, CoastColour validation activities	YES
		FUB	Schroeder et al., 2007	Used in many applications, especially Baltic Sea and nordic lakes	Schroder et al., 2005, further MVT studies, Marcoast Validation, Odermatt, 2012b	YES

Chapter	Processing Step	Algorithm	Reference	Maturity	Validation	Selection
		MIP	Heege and Fischer, 2004	Used for operational services by EOMAP, not publicly available		NO
		HYDROPT	Van Der Woerd et al., 2008	Not publicly available		NO
		Linear matrix inversion approaches	Giardino et al., 2007; Brando et al., 2012	Used for operational services in coastal areas by CSIRO	Giardino et al., 2007; Brando et al., 2012	NO
		FLH / MCI	Gower et al., 1999; Gower et al., 2005	Applicable for very high concentrations	Application to inland waters: (Matthews et al., 2010; Binding et al., 2011	NO
		MPH	(Mark William Matthews et al., 2012; Mark William Matthews & Odermatt, 2015)	Implemented in BEAM	(Mark William Matthews et al., 2012; Mark William Matthews & Odermatt, 2015)	YES
		Band ratio algorithms	Several algos are available, described in Taylor and Matthews, 2011; Selected algorihms: Gitelson et al., 1993; (CDOM) Doxaran et al., 2002 (TSM)	Gitelson et al., 1993 applied in different lakes		NO
4.1.5	Lakes Water Temperature	ARC-Lake project	http://www.geos.ed.ac.uk /arclake/ARC-Lake-ATBD-v1.0.pdf	For lakes > 500 km²; per lake average product	(MacCallum & Merchant, 2010)	YES
4.2	Water Quantity Auxiliary Datasets	SRTM Water Body	SWBD Product Specific Guidance	Mature, some errors detected; missing for high		YES

Chapter	Processing Step	Algorithm	Reference	Maturity	Validation	Selection
				latitudes		
		SAR Water Body Data Set	Santoro & Wegmüller, 2014	Mature	Validated (Kirches et al., 2014)	YES
		LEGOS Hydroweb	(Crétaux et al., 2011)	Mature	(Crétaux et al., 2011)	YES
		ESA river and lake dataset	http://tethys.eaprs.cse.dmu.ac.uk/RiverLake/shared/main	Not used due to the relatively low number of lakes available		NO
5	**Algorithms Drylands Processing**					
5.1	Indices for NPP	fAPAR	Gobron and Verstraete (2009); Gobron, 2011 Fensholt et al., 2004	Mature	Gobron et al. (2008); Pinty et al. (2008); further foreseen within DIVERSITY II	YES
		NDVI	Günther, K.P., and Maier, S. (1999).	Mature	Several studies	YES
5.1.7	Temporal Integration	Discussion of aggregation period	Recommendation by Fensholt to capture also very short growing periods	Biweekly aggregation periods for biophysical time series data are commonly applied		YES
5.2	Phenology and NPP proxies	Processing suite for derivation of phenological and productivity parameters, developed in ERDAS	Concepts partly from Timesat (Eklundh and Jönsson, 2012)., Phenolo (Ivits et al., 2013); Existing concepts have been extended	Mature	Extensive and intensive internal validation by plotting time series and checking the breakpoints	YES
5.3	Aggregation of SM and rainfall	Specific models developed in ERDAS	Timelag observed via data analyses	Mature	Extensive and intensive internal validation	YES

Chapter	Processing Step	Algorithm	Reference	Maturity	Validation	Selection
5.4	Indices for Water Use efficiency	RUE (Rain Use Efficiency based on rainfall and NPP)	Le Houérou, 1984 Fensholt et al. (various cited papers)	Derived with th known limitations		YES
		SMUE (Soil Moisture Use Efficiency based on soil moisture and NPP)	Novelty	Derived with th known limitations	Partly compared to published maps of land degradation (Prince at al. 2009)	YES
		WUE (Water Use Efficiency based on evapotranspiration and NPP)		Will be derived with the constraints derived in the project	Internal analysis and comparison to RUE	NO
6.2.1	First order Dryland Indicators	Processing suite for generation of discrete products, developed in ERDAS	Information requirements of UNCCD and CBD; numerous papers on using NPP and RUE for mapping land condition	Mature	Comparison of indicators to faunal species richness in five validation sites Extensive and intensive internal validation Comparisons to various work from the literature in the PUH	YES
6.2.2	Second order Dryland Indicators	Processing suite for generation of discrete products, developed in ERDAS	Mostly novel ideas; P50 has references in Ivits et al 2013 (ecosystem functional types), Kuenzer at al. (2014), Alcaraz-Segura et al. (2013)	Mature with regard to technical generation	Relevance, usability and utility of second order indicators needs to be assessed. Close resemblance of indicator P50 to LC and land capability classes.	YES
6.2.3	Phenology Indicators	Processing suite for generation of discrete products, developed in	Timesat (Eklundh and Jönsson, 2012) , Ivits et al. 2013, etc.	Mature	Internal validation, comparison to published maps	YES

Chapter	Processing Step	Algorithm	Reference	Maturity	Validation	Selection
		ERDAS				

9 References

Adams, J.B., Smith, M.O., & Gillespie, A.R. (1989). Simple models for complex natural surfaces: a strategy for the hyperspectral era of remote sensing. In *Proceeding of IGARSS* (pp. 16–21). Vancouver.

Ammenberg, P., Flink, P., Lindell, T., Pierson, D. C., & Strombeck, N. (2002). Bio-optical modelling combined with remote sensing to assess water quality. *International Journal of Remote Sensing*, *23*(8), 1621.

Aoki, T., Hori, M., Motoyoshi, H., Tanikawa, T., Hachikubo, A., Sugiura, K., … Takahashi, F. (2007). ADEOS-II/GLI snow/ice products — Part II: Validation results using GLI and MODIS data. *Remote Sensing of Environment*, *111*(2–3), 274 – 290. http://doi.org/http://dx.doi.org/10.1016/j.rse.2007.02.035

Baret, F., Hagolle, O., Geiger, B., Bicheron, P., Miras, B., Huc, M., … Leroy, M. (2007). LAI, fAPAR and fCover global products derived from VEGETATION: Part 1: Principles of the algorithm. *Remote Sensing of Environment*, *110*(3), 275 – 286. http://doi.org/http://dx.doi.org/10.1016/j.rse.2007.02.018

Bicheron, P., Amberg, V., Bourg, L., Petit, D., Huc, M., Miras, B., … Arino, O. (2011). Geolocation Assessment of MERIS GlobCover Orthorectified Products. *IEEE Transactions on Geoscience and Remote Sensing*, *49*(8), 2972–2982.

Bierwirth, P. N., Lee, T., & Burne, R. V. (1993). Shallow sea-floor reflectance and water depth derived by unmixning multispectral imagery. *Photogrammetric Engineering & Remote Sensing*, *59*(3), 331–338.

Binding, C. E., Greenberg, T. a., Jerome, J. H., Bukata, R. P., & Letourneau, G. (2010a). An assessment of MERIS algal products during an intense bloom in Lake of the Woods. *Journal of Plankton Research*, *33*(5), 793–806. http://doi.org/10.1093/plankt/fbq133

Binding, C. E., Greenberg, T. A., Bukata, R. P., Smith, D. E., & Twiss, M. R. (2012). The MERIS MCI and its potential for satellite detection of winter diatom blooms on partially ice-covered Lake Erie. *Journal of Plankton Research*, *34*(6), 569–573. http://doi.org/10.1093/plankt/fbs021

Binding, C. E., Greenberg, T. a., Jerome, J. H., Bukata, R. P., & Letourneau, G. (2010b). An assessment of MERIS algal products during an intense bloom in Lake of the Woods. *Journal of Plankton Research*, *33*(5), 793–806. http://doi.org/10.1093/plankt/fbq133

Blomqvist,P., Kautsky, L., Pihl, L., & Wennhage, H. (2003). Förslag till indikatorer för biologisk mångfald i vatten (”Proposal for biodiversity indicators in water”). SEPA.

Bouvet, M., & Ramino, F. (2010). *Equalization of MERIS L1B products from the 2nd reprocessing* (No. ESA TN TEC-EEP/2009.521). ESA. Retrieved from mbouvet@esa.int

Brajard, J., Santer, R., Crépon, M., & Thiria, S. (2012). Atmospheric correction of MERIS data for case-2 waters using a neuro-variational inversion. *Remote Sensing of Environment*, *126*(null), 51–61. http://doi.org/10.1016/j.rse.2012.07.004

Brenguier, J.-L., Pawlowska, H., Schüller, L., Preusker, R., Fischer, J., & Fouquart, Y. (2000).

Radiative Properties of Boundary Layer Clouds: Droplet Effective Radius versus Number Concentration. *Journal of the Atmospheric Sciences*, *57*(6), 803–821. http://doi.org/10.1175/1520-0469(2000)057<0803:RPOBLC>2.0.CO;2

Brito, J., Campos, J., Gangkofner, U., Odermatt, D., Philipson, P., & Brockmann, C. (2015). *Products Quality Report v4*. ESA DUE Project Diversity II. Retrieved from http://www.diversity2.info/products/documents/

Brockmann, C., Ruescas, A., & Stelzer, K. (2011). *Ocean Colour Climate Change Initiative ATBD pixel identification* (No. v1.0) (p. 37). Brockmann Consult.

Bulgarelli, B., Kiselev, V., & Zibordi, G. (2014). Simulation and analysis of adjacency effects in coastal waters: a case study. *Appl. Opt.*, *53*(8), 1523–1545. http://doi.org/10.1364/AO.53.001523

Cannizzaro, J. P., & Carder, K. L. (2006). Estimating chlorophyll a concentrations from remote-sensing reflectance in optically shallow waters. *Remote Sensing of Environment*, *101*(1), 13–24. http://doi.org/10.1016/j.rse.2005.12.002

Carlson, T. N., & Ripley, D. A. (1997). On the relation between NDVI, fractional vegetation cover, and leaf area index. *Remote Sensing of Environment*, *62*(3), 241–252. http://doi.org/10.1016/S0034-4257(97)00104-1

Cervino, M., Levizzani, V., Serafini, C., Bartoloni, A., Mochi, M., Colandrea, P., & Greco, B. (2000). Cloud fraction within GOME footprint using a refined cloud clearing algorithm. *Advances in Space Research*, *25*(5), 993–996. http://doi.org/10.1016/S0273-1177(99)00462-7

Colapicchioni, A. (2004). KES: knowledge enabled services for better EO information use. In *Geoscience and Remote Sensing Symposium, 2004. IGARSS '04. Proceedings. 2004 IEEE International* (Vol. 1, p. -179). http://doi.org/10.1109/IGARSS.2004.1368988

Costanzo, S., Hawkey, J., & Kelsey, H. (2012). *Chilika Lake - 2012 Ecosystem Health Report Card* (http://www.chilika.com/documents/publication_1398815110.pdf) (p. 6). Cambridge, Maryland: University of Maryland Center for Environmental Science.

Crétaux, J.-F., Jelinski, W., Calmant, S., Kouraev, A., Vuglinski, V., Bergé-Nguyen, M., … Maisongrande, P. (2011). SOLS: A lake database to monitor in the Near Real Time water level and storage variations from remote sensing data. *Advances in Space Research*, *47*(9), 1497 – 1507. http://doi.org/http://dx.doi.org/10.1016/j.asr.2011.01.004

Dierssen, H., R.Zimmerman, R Leathers, T Valerie Downes, & Curtis David. (2003). Ocean colour remote sensing of seagrass and bathymentry in the Bahamas Banks by {HR} airborne imagery. *Limnology and Oceanography*, *48*(1(part 2)), 444–455.

Doerffer, R., Brockmann, C., Röttgers, R., Moore, T. S., & Dowell, M. D. (2012). Optical water type based algorithms for CoastColour. In *3rd MERIS/(A)ATSR & OLCI/SLSTR Preparatory Workshop*. Frascati, Italy.

Doerffer, R., & Schiller, H. (2007). The MERIS case 2 water algorithm. *International Journal of Remote Sensing*, *28*(3), 517–535. http://doi.org/Ja

Doerffer, R., & Schiller, H. (2008a). *Lake Water Algorithm for BEAM ATBD* (MERIS Lakes

ATBD) (p. 17). Geesthacht, Germany: GKSS.

Doerffer, R., & Schiller, H. (2008b). *MERIS Regional Coastal and Lake Case 2 Water Project Atmospheric Correction ATBD* (MERIS Lakes ATBD) (p. 42). Geesthacht, Germany: GKSS.

Dorigo, W., de Jeu, R., Chung, D., Parinussa, R., Liu, Y., Wagner, W., & Fernández-Prieto, D. (2012). Evaluating global trends (1988–2010) in harmonized multi-satellite surface soil moisture. *Geophysical Research Letters*, *39*(18), L18405. http://doi.org/10.1029/2012GL052988

Eklundh, L., & Jönsson, P. (2012). *TIMESAT 3.1 Software Manual* (Software Manual) (p. 82). Lund, Sweden: Lund University.

EUMETSAT. (2006). *Final report for the study on visula scenes analysis of AVHRR data* (No. 2). EUMETSAT.

Fell, F., & Fischer, J. (2001). Numerical simulation of the light field in the atmosphere–ocean system using the matrix-operator method. *Journal of Quantitative Spectroscopy and Radiative Transfer*, *69*(3), 351–388. http://doi.org/10.1016/S0022-4073(00)00089-3

Fensholt, R. (in preparation). Assessment of land degradation/recovery in the African Sahel from long-term Earth Observation based vegetation and precipitation trends.

Fensholt, R., Langanke, T., Rasmussen, K., Reenberg, A., Prince, S. D., Tucker, C., … Wessels, K. (2012). Greenness in semi-arid areas across the globe 1981–2007 — an Earth Observing Satellite based analysis of trends and drivers. *Remote Sensing of Environment*, *121*, 144–158. http://doi.org/10.1016/j.rse.2012.01.017

Fensholt, R., & Proud, S. R. (2012). Evaluation of Earth Observation based global long term vegetation trends — Comparing GIMMS and MODIS global NDVI time series. *Remote Sensing of Environment*, *119*, 131–147. http://doi.org/10.1016/j.rse.2011.12.015

Fensholt, R., & Rasmussen, K. (n.d.). Analysis of trends in the Sahelian “rain-use efficiency” using GIMMS NDVI, RFE and GPCP rainfall data. *Remote Sensing of Environment*, *115*(2), 438–451. http://doi.org/10.1016/j.rse.2010.09.014

Fensholt, R., Sandholt, I., & Rasmussen, M. S. (2004). Evaluation of MODIS LAI, fAPAR and the relation between fAPAR and NDVI in a semi-arid environment using in situ measurements. *Remote Sensing of Environment*, *91*(3-4), 490–507. http://doi.org/10.1016/j.rse.2004.04.009

Fensholt, R., Sandholt, I., Rasmussen, M. S., Stisen, S., & Diouf, A. (2006). Evaluation of satellite based primary production modelling in the semi-arid Sahel. *Remote Sensing of Environment*, *105*(3), 173–188. http://doi.org/10.1016/j.rse.2006.06.011

Fischer, J., & Grassl, H. (1984). Radiative transfer in an atmosphere—ocean system: an azimuthally dependent matrix-operator approach. *Applied Optics*, *23*(7), 1032. http://doi.org/10.1364/AO.23.001032

Fischer, J., Schüller, L., & Preusker, R. (1999). *Cloud Albedo and Cloud optical Thickness ATBD* (MAPP ATBD). Berlin, Germany: Freie Universität Berlin.

Gangkofner, P., Ratzmann, G., Brito, J., Campos, J., Philipson, P., Hahn, N., & Brockmann, C. (2015). *Products User Handbook Drylands v2.6*. ESA DUE Project Diversity II. Retrieved from http://www.diversity2.info/products/documents/

Garand, L., & Weinman, J. A. (1986). A Structural-Stochastic Model for the Analysis and Synthesis of Cloud Images. *Journal of Climate and Applied Meteorology*, *25*(7), 1052–1068. http://doi.org/10.1175/1520-0450(1986)025<1052:ASSMFT>2.0.CO;2

Gardiner, B. (2010). Rainfall use efficiency, natural resource management and profitable production in the rangelands. In *Proceedings of the 16th Biennial Conference of the Australian Rangeland Society* (p. 7). Perth: D.J. Eldridge and C. Waters.

GEO BON. (2011). *Adequacy of Biodiversity Observation Systems to support the CBD 2020 Targets* (Report for the Convention on Biological Diversity) (p. 106). Pretoria.

Giardino, C., Candiani, G., Bresciani, M., Lee, Z., Gagliano, S., & Pepe, M. (2012). BOMBER: A tool for estimating water quality and bottom properties from remote sensing images. *Computers & Geosciences*, *45*, 313–318. http://doi.org/10.1016/j.cageo.2011.11.022

Gitelson, A., Garbuzov, G., Szilagyi, F., Mittenzwey, K. H., Karnieli, A., & Kaiser, A. (1993). Quantitative remote sensing methods for real-time monitoring of inland waters quality. *International Journal of Remote Sensing*, *14*(7), 1269–1295.

Gobron, N. (2011). *Envisat's Medium Resolution Imaging Spectrometer (MERIS) - Algorithm Theoretical Basis Document: FAPAR and Rectifed Channels over Terrestrial Surfaces* (No. JRC65248). Ispra (Italy): European Commission ,Joint Research Centre, Institute for Environment and Sustainability.

Gobron, N., Pinty, B., Aussedat, O., Taberner, M., Faber, O., Melin, F., … Snoeij, P. (2008). Uncertainty estimates for the FAPAR operational products derived from MERIS — Impact of top-of-atmosphere radiance uncertainties and validation with field data. *Remote Sensing of Environment*, *112*(4), 1871–1883. http://doi.org/10.1016/j.rse.2007.09.011

Gobron, N., & Verstraete, M. (2009). *FAPAR: Fraction of Absorbed Photosynthetically Active Radiation* (Assessment of the status of the development of the standards for the terrestrial essential climate variables No. T10) (p. 24). Rome: GTOS.

Gomez-Chova, L., Camps-Valls, G., Calpe-Maravilla, J., Guanter, L., & Moreno, J. (2007). Cloud-Screening Algorithm for ENVISAT/MERIS Multispectral Images. *Geoscience and Remote Sensing, IEEE Transactions on*, *45*(12), 4105–4118. http://doi.org/10.1109/TGRS.2007.905312

Gómez, J., Alonso, C., & García, A. (2011). Remote sensing as a tool for monitoring water quality parameters for Mediterranean Lakes of European Union water framework directive (WFD) and as a system of surveillance of cyanobacterial harmful algae blooms (SCyanoHABs). *Environmental Monitoring and Assessment*, *181*(1-4), 317–334. http://doi.org/10.1007/s10661-010-1831-7

Gons, H. J. (2004). Effect of a waveband shift on chlorophyll retrieval from MERIS imagery of inland and coastal waters. *Journal of Plankton Research*, *27*(1), 125–127. http://doi.org/10.1093/plankt/fbh151

Goodman, A. H., & Henderson-Sellers, A. (1988). Cloud detection and analysis: A review of recent progress. *Atmospheric Research*, *21*(3-4), 203–228. http://doi.org/10.1016/0169-

8095(88)90027-0

Gordon, H. R. (1997). Atmospheric correction of ocean color imagery in the earth observing system era. *Journal of Geophysical Research*, *102*(D14), 17081–17106 ST – Atmospheric correction of ocean.

Grey, W. M. F., North, P. R. J., & Los, S. O. (2006). Computationally efficient method for retrieving aerosol optical depth from ATSR-2 and AATSR data. *Appl. Opt.*, *45*(12), 2786–2795. http://doi.org/10.1364/AO.45.002786

Guanter, J. f. L. . f, R.-V. A. b. O. D. c. G. C. d. S. S. e. E. V. f. H. T. g. D.-G. J. A. h. M. (2010). Atmospheric correction of ENVISAT/MERIS data over inland waters: Validation for European lakes. *Remote Sensing of Environment*, *114*(3), 467–480.

Guanter, L., Del Carmen González-Sanpedro, M., & Moreno, J. (2007). A method for the atmospheric correction of ENVISAT/MERIS data over land targets. *International Journal of Remote Sensing*, *28*(3-4), 709–728. http://doi.org/10.1080/01431160600815525

Guanter, L., Gómez-Chova, L., & Moreno, J. (2008). Coupled retrieval of aerosol optical thickness, columnar water vapor and surface reflectance maps from ENVISAT/MERIS data over land. *Remote Sensing of Environment*, *112*(6), 2898–2913. http://doi.org/10.1016/j.rse.2008.02.001

Guanter, L., Ruiz-Verdú, A., Odermatt, D., Giardino, C., Simis, S., Estellés, V., … Moreno, J. (2010). Atmospheric correction of ENVISAT/MERIS data over inland waters: Validation for European lakes. *Remote Sensing of Environment*, *114*(3), 467–480. http://doi.org/10.1016/j.rse.2009.10.004

Günther, K. P., & Maier, S. (1999). *AVHRR compatible NDVI* (p. 18). Wessling, Germany.

Härmä, P., Vepsäläinen, J., Hannonen, T., Pyhälahti, T., Kämäri, J., Kallio, K., … Koponen, S. (2001). Detection of water quality using simulated satellite data and semi-empirical algorithms in Finland. *Science of the Total Environment*, *268*(1–3), 107–121. http://doi.org/10.1016/S0048-9697(00)00688-4

Herdendorf, C. E. (1982). Large Lakes of the World. *Journal of Great Lakes Research*, *8*(3), 379–412. http://doi.org/10.1016/S0380-1330(82)71982-3

Hori, M., Aoki, T., Stamnes, K., & Li, W. (2007). ADEOS-II/GLI snow/ice products — Part III: Retrieved results. *Remote Sensing of Environment*, *111*(2–3), 291 – 336. http://doi.org/http://dx.doi.org/10.1016/j.rse.2007.01.025

Hu, B., Lucht, W., & Strahler, A. H. (1999). The interrelationship of atmospheric correction of reflectances and surface BRDF retrieval: a sensitivity study. *IEEE Transactions on Geoscience and Remote Sensing*, *37*(2), 724 –738. http://doi.org/10.1109/36.752189

IOCCG, & Lee, Z. P. (2006). *Remote Sensing of Inherent Optical Properties: Fundamentals, Tests of Algorithms, and Applications* (p. 122 ST – Remote Sensing of Inherent Optical Prope). IOCCG.

Julien, Y., Sobrino, J., Mattar, C., Ruescas, A., Jimenez-Munoz, J., Soria, G., … Cuenca, J. (2011). Temporal analysis of normalized difference vegetation index (NDVI) and land surface temperature (LST) parameters to detect changes in the Iberian land cover between 1981 and

2001. *International Journal of Remote Sensing*, *32*(7), 2057–2068. http://doi.org/10.1080/01431161003762363

Kallio, K., Koponen, S., Ruiz-Verdu, A., Heege, T., Soerensen, K., Pyhalahti, T., & Doerffer, R. (2007). *Development of MERIS Lake Water Algorithms - Validation Protocol* (No. v1.0) (p. 14).

Kallio, K., Kutser, T., Hannonen, T., Koponen, S., Pulliainen, J., Vepsalainen, J., & Pyhalahti, T. (2001). Retrieval of water quality from airborne imaging spectrometry of various lake types in different seasons. *The Science of The Total Environment*, *268*(1-3), 59–77.

Kaufman, Y. J., & Sendra, C. (1988). Algorithm for automatic atmospheric corrections to visible and near-IR satellite imagery. *International Journal of Remote Sensing*, *9*(8), 1357–1381. http://doi.org/10.1080/01431168808954942

Kenny, A. J., Cato, I., Desprez, M., Fader, G., Schüttenhelm, R. T. E., & Side, J. (2003). An overview of seabed-mapping technologies in the context of marine habitat classification. *{ICES} Journal of Marine Science: Journal Du Conseil*, *60*(2), 411–418. http://doi.org/10.1016/S1054-3139(03)00006-7

Kirches, G., Brockmann, C., Boettcher, M., Peters, M., Bontemps, S., Lamarche, C., … Defourny, P. (2014). *Land Cover CCI Product User Guide Version 2* (No. Version 2.4) (p. 87). Louvain, Belgium: UCL Geomatics.

Kirches, G., Brockmann, C., Boettcher, M., Smollich, S., Bontemps, S., Lamarche, C., … Defourny, P. (2012). *Land Cover Climate Change Initiative PVR* (No. v1) (p. 121). UCL Geomatics.

Kirches, G., Krueger, O., Boettcher, M., Bontemps, S., Lamarche, C., Verheggen, A., … Defourny, P. (2012). *Land Cover CCI Algorithm Theoretical Basis Document* (No. Version 2.1) (p. 217). Louvain, Belgium: UCL Geomatics.

Kokhanovsky, A., von Hoyningen-Huene, W., Burrows, J. P., Colin, O., Rosaz, J.-M., & Mathot, E. (2008). The determination of the Cloud Fraction in the SCIAMACHY Pixels using MERIS. In *Proc. of the 2nd MERIS/(A)ATSR User Workshop* (p. 8). Frascati, Italy.

Koponen, S., Attila, J., Pulliainen, J., Kallio, K., Pyh‰lahti, T., Lindfors, A., … Hallikainen, M. (2007). A case study of airborne and satellite remote sensing of a spring bloom event in the Gulf of Finland. *Continental Shelf Research*, *27*(2), 228–244.

Koponen, S., Ruiz-Verdu, A., Heege, T., Heblinski, J., Sorensen, K., Kallio, K., … Peters, M. (2008). *Development of MERIS lake water algorithms* (p. 65).

Kotchenova, S. Y., Vermote, E. F., Matarrese, R., & Klemm, F. J. (2006). Validation of a vector version of the 6S radiative transfer code for atmospheric correction of satellite data. Part I: path radiance. *Applied Optics*, *45*(26), 6762–74.

Kratzer, S., & Vinterhav, C. (2010). Improvement of MERIS level 2 products in Baltic Sea coastal areas by applying the Improved Contrast between Ocean and Land processor (ICOL) – data analysis and validation *. *Oceanology*, *52*(2 August 2009).

Lee, Z., Carder, K. L., Mobley, C. D., Steward, R. G., & Patch, J. S. (1998). Hyperspectral remote sensing for shallow waters. I. A semianalytical model. *Appl. Opt.*, *37*(27), 6329–6338. http://doi.org/10.1364/AO.37.006329

Lee, Z., Carder, K. L., Mobley, C. D., Steward, R. G., & Patch, J. S. (1999). Hyperspectral remote sensing for shallow waters: 2. Deriving bottom depths and water properties by optimization. *Appl. Opt.*, *38*(18), 3831–3843. http://doi.org/10.1364/AO.38.003831

Lehner, B., & Döll, P. (2004). Development and validation of a global database of lakes, reservoirs and wetlands. *Journal of Hydrology*, *296*(1–4), 1–22. http://doi.org/10.1016/j.jhydrol.2004.03.028

Liou, K. N. (1992). *Oxford Monographs on Geology and Geophysics: Theory, Observation and Modeling*. Oxford University Press.

Lopez, G., Muller, J.-P., Potts, D., Shane, N., Kharbouche, S., Fisher, D., … Guanter, L. (2013). *GlobAlbedo Algorithm Theoretical Basis Document* (No. v.4.12) (p. 313). University College London. Retrieved from http://www.globalbedo.org/docs/GlobAlbedo_Albedo_ATBD_V4.12.pdf

Louchard, E. M., Reid, R. P., Stephens, F. C., Davis, C. O., Leathers, R. A., & Downes, T. V. (2003). Optical remote sensing of benthic habitats and bathymetry in coastal environments at Lee Stocking Island, Bahamas: A comparative spectral classification approach. *Limnology and Oceanography*, *48*(1 part 2), 511–521.

Luo, Y., Trishchenko, A. P., & Khlopenkov, K. V. (2008). Developing clear-sky, cloud and cloud shadow mask for producing clear-sky composites at 250-meter spatial resolution for the seven MODIS land bands over Canada and North America. *Remote Sensing of Environment*, *112*(12), 4167–4185.

Lu, X., & Zhuang, Q. (2010). Evaluating evapotranspiration and water-use efficiency of terrestrial ecosystems in the conterminous United States using MODIS and AmeriFlux data. *Remote Sensing of Environment*, *114*(9), 1924–1939. http://doi.org/10.1016/j.rse.2010.04.001

Lyapustin, A., & Wang, Y. (2009). The time series technique for aerosol retrievals over land from MODIS. In D. A. A. Kokhanovsky & P. G. de Leeuw (Eds.), *Satellite Aerosol Remote Sensing over Land* (pp. 69–99). Springer Berlin Heidelberg. Retrieved from http://link.springer.com/chapter/10.1007/978-3-540-69397-0_3

Lyzenga, D. (1981). Remote sensing of bottom reflectance and water attenuation parameters in shallow water using aircraft and Landsat data. *International Journal of Remote Sensing*, *2*(1), 71–82. http://doi.org/10.1080/01431168108948342

Lyzenga, D. R. (1978). Passive remote sensing techniques for mapping water depth and bottom features. *Appl. Opt.*, *17*(3), 379–383. http://doi.org/10.1364/AO.17.000379

MacCallum, S., & Merchant, C. (2010). *ATSR Reprocessing for Climate Lake Surface Temperature: ARC-Lake Validation Report* (No. v1.0) (p. 42). Univ. of Edinburgh. Retrieved from http://www.geos.ed.ac.uk/arclake/ARC-Lake-Vaidation-Report-v1.0.pdf

MacCallum, S., & Merchant, C. (2013). *ATSR Reprocessing for Climate Lake Surface Temperature: ARC-Lake Algorithm Theoretical Basis Document* (No. v1.4) (p. 98). Univ. of Edinburgh. Retrieved from http://www.geos.ed.ac.uk/arclake/ARC-Lake-ATBD-v1.4.pdf

Mackie, S., Embury, O., Old, C., Merchant, C. J., & Francis, P. (2010). Generalized Bayesian cloud detection for satellite imagery. Part 1: Technique and validation for night-time imagery over land and sea. *International Journal of Remote Sensing*, *31*(10), 2573–2594. http://doi.org/10.1080/01431160903051703

Mackie, S., Merchant, C. J., Embury, O., & Francis, P. (2010). Generalized Bayesian cloud detection for satellite imagery. Part 2: Technique and validation for daytime imagery. *International Journal of Remote Sensing*, *31*(10), 2595–2621. http://doi.org/10.1080/01431160903051711

Maritorena, S., Morel, A., & Gentili, B. (1994). Diffuse reflectance of oceanic shallow waters: Influence of water depth and bottom albedo. *Limnology and Oceanography*, *39*(7), 1689–1703 ST – Diffuse reflectance of oceanic sha.

Matthews, M. W. (2011). A current review of empirical procedures of remote sensing in inland and near-coastal transitional waters. *International Journal of Remote Sensing*, *32*(21), 6855–6899. http://doi.org/10.1080/01431161.2010.512947

Matthews, M. W., Bernard, S., & Robertson, L. (2012). An algorithm for detecting trophic status (chlorophyll-a), cyanobacterial-dominance, surface scums and floating vegetation in inland and coastal waters. *Remote Sensing of Environment*, *124*(0), 637 – 652. http://doi.org/10.1016/j.rse.2012.05.032

Matthews, M. W., Bernard, S., & Winter, K. (2010). Remote sensing of cyanobacteria-dominant algal blooms and water quality parameters in Zeekoevlei, a small hypertrophic lake, using MERIS. *Remote Sensing of Environment*, *114*(9), 2070–2087 ST – Remote sensing of cyanobacteria–do.

Matthews, M. W., & Odermatt, D. (2015). Improved algorithm for routine monitoring of cyanobacteria and eutrophication in inland and near-coastal waters. *Remote Sensing of Environment*, *156*, 374–382. http://doi.org/10.1016/j.rse.2014.10.010

Merchant, C. J., Harris, a. R., Maturi, E., & Maccallum, S. (2005). Probabilistic physically based cloud screening of satellite infrared imagery for operational sea surface temperature retrieval. *Quarterly Journal of the Royal Meteorological Society*, *131*(611), 2735–2755. http://doi.org/10.1256/qj.05.15

Merchant, C., Llewellyn-Jones, D., Saunders, R. W., Rayner, N., & Kent, E. (2005). Sea Surface Temperature for Climate from the ATSRs. In *Proceedings of the MERIS (A)ATSR Workshop 2005 (ESA SP-597)* (pp. 26–40). Frascati, Italy.

Mobley, C. D. (1994). *Light and Water*. San Diego: Academic Press Inc.

Moore, T. S., Dowell, M. D., Bradt, S., & Ruiz Verdu, A. (2014). An optical water type framework for selecting and blending retrievals from bio-optical algorithms in lakes and coastal waters. *Remote Sensing of Environment*, *143*(0), 97–111. http://doi.org/10.1016/j.rse.2013.11.021

Morel, A., & Gentili, B. (1991). Diffuse reflectance of oceanic waters: Its dependence on Sun angle as influenced by the molecular scattering contribution. *Appl. Opt.*, *30*(30), 4427–4438 ST – Diffuse reflectance of oceanic wat.

Moses, W. J., Gitelson, A. A., Berdnikov, S., & Povazhnyy, V. (2009). Satellite Estimation of

Chlorophyll-a Concentration Using the Red and NIR Bands of MERIS - The Azov Sea Case Study. *Geoscience and Remote Sensing Letters, IEEE*, *6*(4), 845–849 ST – Satellite Estimation of Chlorophyll–.

Odermatt, D., Gangkofner, U., Danne, O., Ruescas, A. B., Zühlke, M., & Brockmann, C. (2015). *Technical Specifications v3*. ESA DUE Project Diversity II.

Odermatt, D., Giardino, C., & Heege, T. (2010). Chlorophyll retrieval with MERIS Case-2-Regional in perialpine lakes. *Remote Sensing of Environment*, *114*(3), 607–617. http://doi.org/10.1016/j.rse.2009.10.016

Odermatt, D., Kiselev, V., Heege, T., Kneubühler, M., & Itten, K. I. (2008). Adjacency effect considerations and air/water constituent retrieval for Lake Constance. In *Proc. 2nd MERIS/AATSR workshop* (p. 8). Frascati, Italy: ESA/ESRIN.

Odermatt, D., Pomati, F., Pitarch, J., Carpenter, J., Kawka, M., Schaepman, M., & Wüest, A. (2012). MERIS observations of phytoplankton blooms in a stratified eutrophic lake. *Remote Sensing of Environment*, *126*(0), 232 – 239. http://doi.org/http://dx.doi.org/10.1016/j.rse.2012.08.031

Odermatt, M. a. D. a. G. A. b. B. V. E. c. S. (2012). Review of constituent retrieval in optically deep and complex waters from satellite imagery. *Remote Sensing of Environment*, *118*, 116–126.

Pawlowska, H., Brenguier, J.-L., Fouquart, Y., Armbruster, W., Bakan, S., Descloitres, J., … Schüller, L. (2000). Microphysical and radiative properties of stratocumulus clouds: the {EUCREX} mission 206 case study. *Atmospheric Research*, *55*(1), 85 – 102. http://doi.org/http://dx.doi.org/10.1016/S0169-8095(00)00058-2

Phulpin, T., Derrien, M., & Brard, A. (1983). A two-dimensional histogram procedure to analyze cloud cover from NOAA satellite high-resolution imagery. *Journal of Climate and Applied Meteorology*, *22*(8), 1332–1345.

Pinty, B., Lavergne, T., Kaminski, T., Gobron, N., & Taberner, M. (2008). Validation of the MERIS FAPAR L2 products against independent estimates derived from the MODIS and MISR surface albedo operational products. In *Proc. of the 2nd MERIS/(A)ATSR User Workshop* (p. 8). Frascati, Italy.

Plummer, S. E. (2008). The GLOBCARBON Cloud Detection System for the Along-Track Scanning Radiometer (ATSR) Sensor Series. *IEEE Transactions on Geoscience and Remote Sensing*, *46*(6), 1718 –1727. http://doi.org/10.1109/TGRS.2008.916200

Preusker, R., Hünerbein, A., & Fischer, J. (2008). *MERIS Global Land Surface Albedo Maps - ATBD Cloud Detection* (No. Issue 4) (p. 24). Freie Universität Berlin. Retrieved from http://www.brockmann-consult.de/albedomap/pdf/atbd_cloud_detection_amap__5.pdf

Prince, S. D., Becker-Reshef, I., & Rishmawi, K. (2009). Detection and mapping of long-term land degradation using local net production scaling: Application to Zimbabwe. *Remote Sensing of Environment*, *113*(5), 1046–1057. http://doi.org/10.1016/j.rse.2009.01.016

Rahman, H., & Dedieu, G. (1994). SMAC : a simplified method for the atmospheric correction of satellite measurements in the solar spectrum. *International Journal of Remote Sensing*, *15*(1), 123–143.

Rathke, C., & Fischer, J. (2002). Evaluation of four approximate methods for calculating infrared radiances in cloudy atmospheres. *Journal of Quantitative Spectroscopy and Radiative Transfer*, *75*(3), 297 – 321. http://doi.org/http://dx.doi.org/10.1016/S0022-4073(02)00012-2

Robinson, I. S. (2004). *Measuring the Oceans from Space: The principles and methods of satellite oceanography* (1st ed.). Springer.

Rossow, W. B., & Schiffer, R. A. (1999). Advances in Understanding Clouds from ISCCP. *Bulletin of the American Meteorological Society*, *80*(11), 2261–2287. http://doi.org/10.1175/1520-0477(1999)080<2261:AIUCFI>2.0.CO;2

Ruescas, A. B., Brockmann, C., Stelzer, K., Tilstone, G. H., & Beltran, J. (2014). *DUE CoastColour Validation Report* (p. 58). Geesthacht, Germany: Brockmann Consult. Retrieved from http://www.coastcolour.org/documents/DEL-27%20Validation%20Report_v1.pdf

Ruiz-Verdu, R., Koponen, S., Heege, T., Doerffer, R., Brockmann, C., Kallio, K., … Pulliainen, J. (2008). Development of MERIS lake water algorithms: Validation results from Europe. In *Proc. 2nd MERIS/AATSR workshop* (p. 8). Frascati, Italy: ESA/ESRIN.

Sandlund, O.T, & Viken, A. (1997). *Report of the Trondheim conferences on biodiversity. Workshop of Freshwater biodiversity.* Norway: Norwegian Institute for Nature Research, Directorate for nature Management.

Santer, R., Carrère, V., Bubuisson, P., & Roger, J. C. (1999). Atmospheric correction over land for MERIS. *International Journal of Remote Sensing*, *20*(9), 1819–1840 ST – Atmospheric correction over land f.

Santer, R., Carrère, V., Dessailly, D., Dubuisson, P., & Roger, J. C. (1997). *Pixel Identification ATBD* (MERIS ESL ATBD 2.17). Wimereux, France: Université du Littoral Côte d'Opale, Wimereux, France.

Santer, R., Ramon, D., Vidot, J., & Dilligeard, E. (2007). A surface reflectance model for aerosol remote sensing over land. *International Journal of Remote Sensing*, *28*(3-4), 737–760. http://doi.org/10.1080/01431160600821028

Santer, R., & Schmechtig, C. (2000). Adjacency effects on water surfaces: primary scattering approximation and sensitivity study. *Appl. Opt.*, *39*(3), 361–375.

Santer, R., & Zagolski, F. (2009). *ICOL Improve Contrast between Ocean & Land* (p. 15). Wimereux, France: Université du Littoral Côte d'Opale, Wimereux, France.

Santoro, M., & Wegmuller, U. (2014). Multi-temporal Synthetic Aperture Radar Metrics Applied to Map Open Water Bodies. *Selected Topics in Applied Earth Observations and Remote Sensing, IEEE Journal of*, *7*(8), 3225–3238. http://doi.org/10.1109/JSTARS.2013.2289301

Saunders, R. W., & Kriebel, K. T. (1988). A review of: "An improved method for detecting clear sky and cloudy radiances from AVHRR data." *International Journal of Remote Sensing*, *9*(8), 1393–1394. http://doi.org/10.1080/01431168808954944

Scheuerell, S. J., & Mahaffee, W. F. (2004). Compost Tea as a Container Medium Drench for

Suppressing Seedling Damping-Off Caused by Pythium ultimum. *Phytopathology*, *94*(11), 1156–1163. http://doi.org/10.1094/PHYTO.2004.94.11.1156

Schiller, H., Brockmann, C., Krasemann, H., & Schönfeld. (2008). A method for detection and classification of clouds over water. In *Proceedings of MERIS-AATSR Workshop*. ESRIN, Italy.

Schiller, H., Brockmann, C., Krasemann, H., & Schönfeld, W. (2008). A method for the detection and classification of clouds over water. In *Proc. of the 2nd MERIS/(A)ATSR User Workshop*. Frascati, Italy.

Schroeder, T., Behnert, I., Schaale, M., Fischer, J., & Doerffer, R. (2007a). Atmospheric correction algorithm for MERIS above case-2 waters. *International Journal of Remote Sensing*, *28*(7), 1469–1486. http://doi.org/10.1080/01431160600962574

Schroeder, T., Behnert, I., Schaale, M., Fischer, J., & Doerffer, R. (2007b). Atmospheric correction algorithm for MERIS above case-2 waters. *International Journal of Remote Sensing*, *28*(7), 1469–1486 ST – Atmospheric correction algorithm f.

Sebego, R., Arnberg, W., & Ringrose, S. (2002). Relation between cold cloud data, NDVI and mopane in Eastern Botswana. In *ISPRS Archives – Volume XXXIV-6/W6* (p. 13). Dar es Salaam. Retrieved from http://www.isprs.org/proceedings/XXXIV/6-W6/

Sen, P. K. (1968). Estimates of the regression coefficient based on Kendall's tau. *Journal of the American Statistical Association*, *63*, 1379–1389.

Shi, T., Clothiaux, E. E., Yu, B., Braverman, A. J., & Groff, D. N. (2007). Detection of daytime arctic clouds using {MISR} and {MODIS} data. *Remote Sensing of Environment*, *107*(1–2), 172 – 184. http://doi.org/http://dx.doi.org/10.1016/j.rse.2006.10.015

Simpson, J. J., & Gobat, J. I. (1996). Improved cloud detection for daytime AVHRR scenes over land. *Remote Sensing of Environment*, *55*(1), 21–49. http://doi.org/10.1016/0034-4257(95)00188-3

Simpson, J. J., Schmidt, A., & Harris, A. (1998). Improved Cloud Detection in Along Track Scanning Radiometer (ATSR) Data over the Ocean. *Remote Sensing of Environment*, *65*(1), 1–24. http://doi.org/10.1016/S0034-4257(98)00025-X

Sotis, G., Balducci, F., & Campbell, R., Goryl, P. (2011). *ENVISAT-1 Products Specifications Colume 11: MERIS Products Specifications, PO-RS_MDA-GS-2009, Issue 6/a* (p. 248).

Stamnes, K., Li, W., Eide, H., Aoki, T., Hori, M., & Storvold, R. (2007). ADEOS-II/GLI snow/ice products — Part I: Scientific basis. *Remote Sensing of Environment*, *111*(2–3), 258 – 273. http://doi.org/http://dx.doi.org/10.1016/j.rse.2007.03.023

Steinmetz, F., Deschamps, P.-Y., & Ramon, D. (2011). Atmospheric correction in presence of sun glint: application to MERIS. *Optics Express*, *19*(10), 9783. http://doi.org/10.1364/OE.19.009783

Sterckx, S., Knaeps, S., Kratzer, S., & Ruddick, K. (2014). SIMilarity Environment Correction (SIMEC) applied to {MERIS} data over inland and coastal waters. *Remote Sensing of Environment*, (0), -. http://doi.org/http://dx.doi.org/10.1016/j.rse.2014.06.017

Theil, H. (1950). A rank-invariant method of linear and polynomial regression analysis. In *I, II, III, Nederl. Akad. Wetensch.* (Vol. Proc. 53, pp. 386–392, 521–525, 1397–1412).

Vermote, E. F., & Kotchenova, S. (2008). Atmospheric correction for the monitoring of land surfaces. *Journal of Geophysical Research*, *113*(D23), D23S90. http://doi.org/10.1029/2007JD009662

Vina, A. (2004). *Remote estimation of leaf area index and biomass in corn and soybean*. University of Lincoln, Nebraska.

Wessels, K. J., van den Bergh, F., & Scholes, R. J. (2012). Limits to detectability of land degradation by trend analysis of vegetation index data. *Remote Sensing of Environment*, *125*, 10–22. http://doi.org/10.1016/j.rse.2012.06.022